

# **Experimental and computational study of S segregation in Fe**

by

**Pieter Egbert Barnard**

**B.Sc Hons**

*A thesis presented in fulfilment of the requirements of the degree*

**MAGISTER SCIENTIAE**

**in the Department of Physics**

**at the University of the Free State**

**Republic of South Africa**

**Supervisor: J.J. Terblans**

**Co-supervisor: H.C. Swart**

**Co-supervisor: M.J.H. Hoffman**

June 2012



**All glory and honour to my heavenly Father**



# Acknowledgements

I would like to thank the following people:

- *Prof. J.J. Terblans* as my promoter for his help and guidance during this study.
- *Prof. H.C. Swart* for his help and guidance during this study.
- *Prof. M.J.H. Hoffman* for useful discussions.
- *Dr. B.G. Anderson* and his research group at Sasol for their advice and help.
- My mother, *Hester Barnard*, whom have given me the greatest support during this study.
- The *personnel at the department of electronics* for their assistance with the apparatus.
- The *personnel at the department of instrumentation* for their assistant with the apparatus.
- The *personnel at the Physics Department* for the useful discussions and interest they have shown during this study.
- To *the students in my group* for useful discussions during group meetings.



# Keywords

Activation energy  
Auger Electron Spectroscopy (AES)  
Binding energy  
Density Functional Theory (DFT)  
Diffusion mechanism  
Fe(100)  
Fe(110)  
Fe(111)  
Fick`s model  
Guttmann`s model  
Iron (Fe)  
Lattice strain  
Linear heating  
Migration energy  
Pre-exponential factor  
Quantum ESPRESSO  
Segregation energy  
Sulfur (S)  
Surface stability  
Vacancy formation energy  
X-Ray Diffraction



# Abstract

A systematic study was conducted to investigate the diffusion and segregation of S in bcc Fe using (i) DFT modelling and (ii) the experimental techniques Auger Electron Spectroscopy (AES) and X-Ray diffraction (XRD). The aim of this study was to obtain the activation energies for the segregation of sulfur (S) in bcc iron (Fe), both computationally and experimentally in order to explain the diffusion mechanism of S in bcc Fe as well as the influence the surface orientation has on surface segregation.

The Quantum ESPRESSO code which performs plane wave pseudopotential Density Functional Theory (DFT) calculations was used to conduct a theoretical study on the segregation of S in bcc Fe. To determine the equilibrium lattice sites of S in bcc Fe, the tetrahedral-interstitial, octahedral-interstitial and substitutional lattice sites were considered. Their respective binding energies were calculated as -1.464 eV, -1.660 eV and -3.605 eV, indicating that the most stable lattice site for S in bcc Fe is the substitutional lattice site. The following mechanisms were considered for the diffusion of S in bcc Fe: tetrahedral-interstitial, octahedral-interstitial, nearest neighbour (nn) substitutional and next nearest neighbour (nnn) substitutional with migration energies,  $E_m$ , of respectively 4.438 kJ/mol (0.046 eV), 22.48 kJ/mol (0.233 eV),  $9.938 \pm 6.754$  kJ/mol ( $0.103 \pm 0.007$  eV) and  $96.49 \pm 0.579$  kJ/mol ( $1.000 \pm 0.006$  eV). According to the binding and migration energy calculations, S will diffuse via a substitutional mechanism with a migration energy of  $9.938 \pm 6.754$  kJ/mol ( $0.103 \pm 0.007$  eV).

The three low-index planes of bcc Fe were investigated to determine the stability, the vacancy formation energy and the activation energy for each surface. Structural relaxation calculations showed that the surfaces in order of decreasing stability are: Fe(110) > Fe(100) > Fe(111) which is in agreement with surface energy calculations obtained from literature. The formation of a vacancy in bcc Fe was modelled as the formation of a Schottky defect in the lattice. Using this mechanism, the vacancy formation energies,  $E_{vac}$ , for the Fe(110), Fe(100) and Fe(111) surfaces were respectively calculated as 267.4 kJ/mol (2.772 eV), 256.8 kJ/mol (2.662 eV) and 178.2 kJ/mol (1.847 eV). The activation energy,  $Q$ , of S diffusing via the substitutional mechanism for the Fe(100), Fe(110) and Fe(111) surfaces were respectively calculated as 277.4 kJ/mol (2.875 eV), 266.8 kJ/mol (2.765 eV) and 188.1 kJ/mol (1.950 eV). Thus it was found that the vacancy formation energy is dependent on the surface orientation and thus the structural stability of the Fe crystal. Experimental values for the

activation energy of S in bcc Fe (232 kJ/mol (2.40 eV) and 205 kJ/mol (2.13 eV)) were obtained from literature confirming the nearest neighbour substitutional diffusion mechanism of S in bcc Fe. No indication is given regarding the orientation of the crystal in which the value of 232 kJ/mol (2.40 eV) was obtained while the value of 205 kJ/mol (2.13 eV) is for a Fe(111) crystal orientation.

For the experimental investigation of the Fe/S system polycrystalline bcc Fe samples were studied. These samples were prepared by a new doping method by which elemental S is diffused into Fe. In order to prepare the samples by this method a new system was designed and build. Auger depth profile analysis confirms the successful doping of Fe with S using the newly proposed doping method. It was found that the S concentration was increased by 89.38 % when the doping time was doubled from 25 s to 50 s. An Fe sample doped for 50 s was annealed at 1073 K for 40 days after which the effects induced by S and the annealing of the sample were investigated by Secondary Electron Detector (SED) imaging. Results showed a  $36\pm 11$  % decrease in the grain sizes of the polycrystalline Fe sample due to the presence of S. It was found that the re-crystallization rate of Fe is increased due to the presence of S.

Using XRD, the Fe (100), Fe(211), Fe(110), Fe(310) and Fe(111) orientations were detected for both the un-doped and the annealed S doped Fe samples. The annealed sample showed the following percentage changes in the concentrations of the respective orientations compared to the un-doped sample: -5.180, +2.030, +16.41, +0.400, -13.66. Taking the calculated trend in surface stability for the three low-index orientations of Fe into consideration, it was found that the more stable Fe(110) orientation had increased in concentration during annealing, while the less stable Fe(100) and unstable Fe(111) orientations had decreased in concentration during annealing.

AES measurements on the two samples were performed using the linear programmed heating method. The segregation parameters of S for the un-doped Fe sample are:  $D_0=4.90\times 10^{-2}$  m<sup>2</sup>/s,  $Q=190.8$  kJ/mol (1.978 eV),  $\Delta G=-134$  kJ/mol (-1.39 eV) and  $\Omega_{Fe/S}=20$  kJ/mol (0.21 eV). The segregation parameters of P obtained for the un-doped Fe sample are:  $D_0=0.129$  m<sup>2</sup>/s,  $Q=226.5$  kJ/mol (2.348 eV). For the S doped Fe sample the segregation parameters of S were determined as:  $D_0=1.79\times 10^{-2}$  m<sup>2</sup>/s and  $Q=228.7$  kJ/mol (2.370 eV),  $\Delta G=-145$  kJ/mol (-1.50 eV) and  $\Omega_{Fe/S}=8$  kJ/mol (0.08 eV). These results showed that for the doped sample, with an increased concentration in the stable Fe(110) and a decreased concentration in the less stable Fe(100) and unstable Fe(111) orientations, a higher activation energy was obtained. Comparing the measured activation energies to the calculated values indicates that the diffusion of S occurs via a vacancy mechanism, where the S atom occupies a substitutional lattice site. Despite the fact that polycrystalline samples were analysed, the activation energies are still in the same order as the

calculated activation energies of the single crystals. This confirms the theoretical prediction of a substitutional diffusion mechanism of S in bcc Fe.

During this study the diffusion mechanism of S was determined as the substitutional diffusion mechanism whereby a S atom would diffuse from a substitutional lattice site to a nearest neighbour vacancy. The different Fe orientations considered in the calculations can be arranged from highest to lowest activation energy as Fe(110)>Fe(100)>Fe(111). These calculations are in agreement with the AES results which showed an increased activation energy for the doped sample having a higher Fe(110) concentration and lower Fe(111) and Fe(100) concentrations.



# Table of content

<b>1.</b>	<b>Introduction</b>	<b>19</b>
1.1.	Aim of this study	19
1.2.	Layout of this thesis	20
1.3.	References	21
<b>2.</b>	<b>Literature review</b>	<b>23</b>
	References	30
<b>I</b>	<b>Theory</b>	<b>33</b>
<b>3.</b>	<b>Diffusion theory</b>	<b>35</b>
3.1.	Introduction	35
3.2.	Fick`s first diffusion law	36
3.3.	Fick`s second diffusion law	39
3.4.	Diffusion mechanism	42
3.4.1.	Interstitial mechanism	42
3.4.2.	Vacancy/substitutional mechanism	45
3.4.3.	Interstitialcy mechanism	47
3.4.4.	Interstitial-substitutional mechanism	48
3.5.	Influence of temperature on diffusion	49
3.6.	Summary	51

3.7.	References	51
<b>4.</b>	<b>Segregation theory</b>	<b>53</b>
4.1.	Introduction	53
4.2.	Kinetics of surface segregation	53
4.3.	Equilibrium surface segregation	60
4.3.1.	Equilibrium conditions	60
4.3.2.	Surface-bulk equilibrium	62
4.3.3.	Equilibrium model for a ternary system	64
4.4.	Summary	67
4.5.	References	67
<b>5.</b>	<b>Density functional theory (DFT) fundamentals</b>	<b>69</b>
5.1.	Introduction	69
5.2.	Bloch theorem	70
5.3.	Brillouin zone sampling	73
5.4.	Hohenberg-Kohn	75
5.5.	The self-consistent loop for solving the Kohn-Sham equation	77
5.5.1.	Mixing schemes for obtaining the electron density	79
5.5.2.	The Kohn-Sham equation and the effective potential	80
5.5.3.	Solving the Kohn-Sham equation	84
5.5.4.	Metallic smearing/broadening	87
5.6.	Exchange-Correlation energy functional	89
5.6.1.	Local density approximation (LDA)	89
5.6.2.	Generalized gradient approximation (GGA)	90
5.7.	Pseudopotentials	93
5.8.	Nudged elastic band	94

5.9. Summary	97
5.10. References	97
<b>II Experimental</b>	<b>99</b>
<b>6. Sample preparation</b>	<b>101</b>
6.1. Introduction	101
6.2. Doping methodology	101
6.3. Experimental set-up	108
6.4. Experimental procedure	112
6.4.1. Doping of Fe with S	112
6.4.2. Annealing of Fe-S sample	113
6.5. Summary	114
6.6. References	114
<b>7. Experimental techniques</b>	<b>117</b>
7.1. Introduction	117
7.2. X-Ray Diffraction	117
7.2.1. Principle of operation	117
7.2.2. Apparatus	120
7.2.3. System settings	121
7.3. Auger Electron Spectroscopy	123
7.3.1. Principle of operation	123
7.3.2. Apparatus	125
7.3.3. System configuration and calibration	128
7.3.4. Electron beam size determination	130

7.3.5.	Temperature measurements	132
7.4.	Auger quantification	135
7.4.1.	Palmberg method	135
7.4.2.	Segregated layer/monolayer quantification	136
7.4.3.	Quantification of homogenous samples	143
7.5.	Experimental procedure for segregation measurements	147
7.6.	Summary	148
7.7.	References	148
<b>III</b>	<b>Results and discussion</b>	<b>151</b>
<b>8.</b>	<b>Experimental results</b>	<b>153</b>
8.1.	Introduction	153
8.2.	Sample composition	153
8.3.	Doping of Fe with S	155
8.4.	Grain growth and surface effects of polycrystalline Fe	162
8.5.	Surface segregation measurements	180
8.6.	Summary	192
8.7.	References	193
<b>9.</b>	<b>Computational results</b>	<b>195</b>
9.1.	Introduction	195
9.2.	Computational details	195
9.3.	Bulk Fe calculations	197
9.3.1.	Binding energy	197
9.3.2.	Lattice strain	201

9.3.3.	Charge density	202
9.3.4.	Reaction pathways and activation energy calculations	206
9.4.	Fe(100), Fe(110) and Fe(111) surface calculations	218
9.4.1.	Relaxation of Fe surfaces	222
9.4.2.	Vacancy formation energy, $E_{vac}$	224
9.4.3.	Segregation energy, $\Delta G$ , of Fe(100)	230
9.5.	Summary	233
9.6.	References	234
<b>10.</b>	<b>Conclusion and future work</b>	<b>237</b>
<b>V</b>	<b>Appendix</b>	<b>239</b>
<b>A</b>	<b>Density Functional Theory</b>	<b>241</b>
A.1.	Introduction	241
A.2.	Hohenberg-Kohn theorems	241
A.3.	Hellman-Feynman force theorem	246
A.4.	References	249
<b>B</b>	<b>Computational parameters optimization</b>	<b>251</b>
B.1.	Introduction	251
B.2.	Overview of computational parameters	252

B.3. Optimization of a single unit cell	253
B.3.1. Convergence of the total energy with respect to $E_{cut}$	254
B.3.2. Convergence of the total energy with respect to the k-point grid size	255
B.3.3. Determination of the magnetic state	256
B.3.4. Determination of the smearing scheme for metallic systems	258
B.3.5. Determination of the smearing width (degauss value)	259
B.3.6. Determination of the equilibrium lattice parameter and bulk modulus	260
B.4. Optimization parameters for Supercell calculations	262
B.4.1. Cell size determination	262
B.4.2. Calculation of the required vacuum spacing of surface structures	264
B.5. References	266

## **C Publications and conference contributions 267**

# Chapter 1: Introduction

The movement of atoms in materials can be used to design new materials that are very specific in use. This is especially important for metals, which are used in industrial processes such as catalysis and steel making. Under high temperatures, movement of atoms becomes rapid and atoms can move out of the bulk and occupy positions on the surface or in the grain boundaries of the metal. This movement of atoms onto the surface or grain boundaries is known as segregation. Segregation of atoms in metals can be beneficial to the function of the metal, but more often the segregated atoms have negative effects on the function of the metal. This is true for iron (Fe) which is used as a catalyst in the Fischer-Tropsch process for the production of hydrocarbons [1]. The presence of sulfur (S) impurities on the Fe surface causes the Fe catalyst to be deactivated [2]. S also has a negative effect on the mechanical strength of industrial steels by causing the Fe to become brittle due to the presence of S in the grain boundaries [3; 4; 5; 6].

## 1.1. Aim of this study

This study aims to investigate the diffusion of S in Fe by:

1. Performing theoretical calculation to determine the diffusion mechanism and the bulk activation energy of diffusion for S in bcc Fe(100), Fe(110) and Fe(111).
2. Developing a new method for the preparation of S doped Fe samples which can be used to confirm the findings obtained by the theoretical calculations.
3. Conducting AES measurements on the prepared samples to determine the diffusion parameters of S in bcc polycrystalline Fe.

## 1.2. Layout of this thesis

This thesis consists of 10 chapters and two appendixes, A and B, at the back of the thesis. Below is a short description of each chapter.

*Chapter 2:* This chapter gives a literature review of previous work that has been done on the Fe/S system.

*Chapter 3:* The basic concepts of diffusion are given in this chapter. The two laws of Fick are derived and the mechanisms of diffusion for various systems are discussed.

*Chapter 4:* Fick's model describing the kinetics of surface segregation and Guttmann's model describing the equilibrium of surface segregation are discussed. It is shown how these two models can be used in combination to obtain all the segregation parameters from Auger electron spectroscopy data.

*Chapter 5:* The important concepts needed to perform the Density Functional Theory calculations presented in this study are discussed. The chapter is focussed on providing a practical understanding of the technique and is not focussed on the detailed mathematics of DFT.

*Chapter 6:* The newly proposed method and preparation chamber for the doping of Fe using S is described. The experimental procedure, used to prepare the samples analysed in this study, is described.

*Chapter 7:* Auger electron spectroscopy and X-Ray diffraction, the two experimental techniques used to obtain data for the Fe/S system in this study are discussed. The apparatus used to obtain the data is shown along with a description of the apparatus. It is also shown how elemental concentrations can be obtained from Auger data using one of three quantification methods.

*Chapter 8:* Experimental results obtained for the diffusion and segregation of S in bcc Fe are presented in this chapter.

*Chapter 9:* The computational results obtained using DFT are presented in this chapter.

*Chapter 10:* A conclusion of the study is given in this chapter along with a scope on future work that is planned.

### 1.3. References

- [1]. B.H. Davis, *Catal. Today* 141 (2009) 25.
- [2]. W. Arabczyk, D. Moszyński, U. Narkiewicz, R. Pelka, M. Podsiadły, *Catal. Today* 124 (2007) 43.
- [3]. J.S. Braithwaite, P. Rez, *Acta. Mater.* 53 (2005) 2715.
- [4]. P. Rez, J.R. Alvarez, *Acta. Mater.* 47 (1999) 4069.
- [5]. N.H. Heo, *Scripta Mater.* 51 (2004) 339.
- [6]. J. Ouder, *Mater. Sci. Eng* 42 (1980) 101.



## Chapter 2: Literature review

The study presented in this thesis is motivated by the use of iron (Fe) as a catalytic converter for the production of hydrocarbons in the Fischer-Tropsch process used by Sasol. This process has been in use at Sasol since 1955, when only the fixed bed reactors were used until 1993 when the first slurry phase reactor (SPR) was commissioned [1]. In the work of Adesina [1] conducted in 1996, South Africa was considered as one of the largest Fischer-Tropsch synthesis countries with a total of 4 thousand tons of production capacity per year from the three Sasol plants. The largest Fe based catalyst fixed bed reactor is in use by Sasol in Sasolburg South Africa, while Shell in Malaysia is running the largest cobalt (Co) based catalyst fixed bed reactor according to the work of Espinoza *et. al.* [2]. It is well known that the presence of sulfur (S) causes the Fe catalyst to be deactivated [3]. According to literature the S impurities originates from the synthesis gas [4; 5]. Also there is a large tendency for S to bind to metallic species and thus there is always a certain concentration of S in the Fe even before exposure to the synthesis gas. The exact mechanism of the Fischer-Tropsch process is unclear with the possibility of both a carbon (C) and a oxygen (O) mechanism that can be responsible for hydrogen production [6]. The key point to be noticed here is that irrespective of the mechanism for the Fischer-Tropsch process, the fact remains that the presence of S impurities on the Fe catalyst surface prevents the binding of the active molecules in the synthesis gas to the catalyst surface.

Apart from the unwanted effect of catalytic poisoning caused by S impurities in the Fischer-Tropsch process. The presence of S in Fe also causes the unwanted effect of grain boundary embrittlement [7; 8; 9]. Grain boundary embrittlement caused by the S impurities leads to the mechanical failure of machinery operated at high temperatures [10]. In order to prevent the negative influence S has on Fe, a thorough study on the segregation and diffusion of S in Fe is required. Such a study would provide the foundation for modifications to the system by which one can engineer the system in order to get the required properties of the material.

The negative effects caused by S in Fe is primarily concerned with the surface, be it the free surface of the material or the grain boundaries. The use of surface sensitive techniques such as X-Ray Photoelectron Spectroscopy (XPS) in the study of reaction rates on surfaces and properties of catalysts is discussed by Sinfelt [11]. The use of surface science techniques in combination to computational techniques such as Density Functional Theory (DFT) or *ab initio* calculations, kinetic Monte Carlo (kMC) and molecular dynamics (MD) simulations to study surface phenomena

with specific relevance to catalysis have been investigated by Stampfl *et al.* [12]. A discussion of surface sensitive techniques such as Auger Electron Spectroscopy (AES), X-Ray Photoelectron Spectroscopy (XPS) and Low Energy Electron Diffraction (LEED) in the study of metal surfaces, with the focus on heterogeneous catalysis is given by Briggs and Seah [13]. Presented in the remainder of this chapter is a summary of experimental and theoretical research conducted on Fe and Fe containing S impurities.

Previous studies in literature have been conducted on pure Fe surfaces to calculate properties such as lattice relaxations, surface energies, magnetic properties and work functions using DFT. Supercell structures are used consisting of a number of atomic layers, sufficient enough to allow for a bulk and a surface region of the structure under study. A vacuum spacing is used to allow the simulation of a surface and avoid the interaction of periodically repeated cells. The discussion here is limited to the three low-index planes of bcc Fe, namely the Fe(100), Fe(110) and Fe(111) surfaces.

Calculations of the surface energies revealed that the physical stability of the three surfaces from most stable to least stable are:  $\text{Fe}(110) \geq \text{Fe}(100) > \text{Fe}(111)$  [14; 15; 16]. This stability of the structures are also seen in the structural relaxation calculations. The relaxation of the three iron surfaces revealed that the most stable surface is the Fe(110) surface, which has geometrical parameters similar to the bulk [14; 15; 16]. The second most stable surface was found to be the Fe(100) surface and the Fe(111) surface was found to be the most unstable surface [14; 15; 16]. The values calculated by the different authors for the degree of lattice relaxation differed slightly, but the general trend of layers expanding and contracting remained the same. For the Fe(100) surface the following pattern was observed for the first four atomic layers: -, +, +, -, where + refers to the expansion of an atomic layer and - refers to the contraction of atomic layers [14; 15; 16]. For the first 3 atomic layers of the Fe(110) surface the pattern observed for lattice relaxations were: -, +, -. There were variations in the relaxation for the third atomic layer, with Błonski *et al.* [15] claiming the expansion of the third layer. The unstable Fe(111) surface showed the following pattern for lattice relaxation: -, -, +, - [14; 15; 16]. An investigation of the work function of the three surfaces revealed that the Fe(100) surface had the smallest value, with the value of Fe(111) being only slightly larger and the Fe(110) surface having the largest value. For all three surfaces the magnetic character of Fe was found to increase at the surface due to the abrupt termination of the crystal and the reduced coordination of the surface atoms. Values indicated that the largest increase was observed in the Fe(100) surface and the smallest increase was found in the Fe(110) surface [14; 15; 16]. The results obtained above form a foundation for studies concerning the adsorption and also the segregation of impurities on Fe surfaces. Table 2.1 gives a summary of the

results found for the lattice relaxations, surface energies, magnetization and the work functions of the three low index Fe surfaces.

**Table 2.1:** Summary of the properties for the Fe(100), Fe(110) and Fe(111) surfaces obtained from literature.

	Fe(100)	Fe(110)	Fe(111)
<b>Lattice relaxation</b>	-, +, +, - [14; 15; 16]	-, +, - [14; 16]/-, +, + [15]	-, -, +, - [14; 15; 16]
<b>Surface energies (J/m<sup>2</sup>)</b>	2.27 [16]; 2.25 [15]; 2.47 [14]	2.29 [16]; 2.25 [15]; 2.37 [14]	2.52 [16]; 2.54 [15]; 2.58 [14]
<b>Work function (eV)</b>	3.86 [15]; 3.91 [14]	4.81 [15]; 4.76 [14]	3.90 [15]; 3.95 [14]
<b>Magnetization (μB)</b>	2.95 [14]	2.59 [14]	2.81 [14]

For the adsorption of S onto the surface of Fe, the following observations were made. For Fe(100) the S adsorbs in a 0.5 monolayer c(2×2) structure on the surface with the hollow site being the most stable position for the S atom, the bridge and atop sites were calculated as a transition and a second order saddle point respectively [17]. Todorova *et. al.* [18] considered the formation of a p(2×2) S structure on Fe(100), with the hollow site being the most stable position for adsorbed S. The c(2×2) structure of adsorbed S agrees with experimental data obtained by LEED [19]. For the Fe(110) surface the adsorption of S was found to be most stable in the four fold hollow site [18; 20] forming a p(2×2) surface structure [21]. On the Fe(111) surface a p(1×1) structure was formed by segregated S [22]. Construction of charge density distribution plots for S adsorbed onto the Fe(100) and Fe(110) surfaces revealed that an increase in charge density is seen between the S atom and the Fe surface [17; 21]. An investigation of the magnetic properties indicated that there is an increase in the magnetization of the adsorbed S atom [23] and a decrease in the magnetization of the surfaces, indicating the formation of a Fe-S bond [17]. Todorova *et. al.* [18] also performed calculations to determine the diffusion parameters of S on the Fe(100) and Fe(110) surfaces. They found that S had an activation energy,  $Q$ , of 115 kJ/mol (1.20 eV) for the Fe(100) surface compared to the activation energy of 49.2 kJ/mol (0.51 eV) for the Fe(110) surface. The pre-exponential factors,  $D_0$ , for the respective surfaces were calculated as  $4.83 \times 10^{12} \text{ s}^{-1}$  and  $3.84 \times 10^{12} \text{ s}^{-1}$ . The diffusion parameters indicated that the diffusion of S on the Fe(110) surface would occur much faster compared to diffusion of S on the Fe(100) surface.

Briant [24] found that there exists competitive segregation between S and Phosphorus (P) at grain boundaries in bcc Fe. The grain boundary embrittlement due to S segregation has been reported [9]. The segregation of S and P to the tilt boundary of Fe(210) was also investigated by Braithwaite *et. al.* [7] who found that both impurities caused a decrease in the cohesion of Fe leading to grain boundary embrittlement. This is in agreement with the experimental findings of Heo [9] who observed grain boundary embrittlement in Fe due to the presence of S and P. Interstitial impurities C, and boron (B) have been shown to cause an increasing effect on cohesion in Fe. Rez *et. al.* [8] performed first principle calculations using full potential linearised augmented plane wave (FLAPW) and layer Korringa Kohn Rostoker (KLLR) codes to investigate the changes in the *d* states due to the impurities C, B, S and P. They determined that the interstitial impurities C and B caused a reduction in the *d*-band energy of the neighbouring Fe atoms, which led to fewer filled anti-bonding states resulting in an increased cohesion of the Fe atoms. The substitutional impurities S and P led to an increased energy of the *d*-bands which indicated that there are more filled anti-bonding states present which led to a reduced cohesion of Fe.

Tacikowski *et. al.* [9] conducted studies on polycrystalline Fe samples having different concentrations of S and C in order to determine the influence of non-metal impurity atom concentrations on grain boundary population. For the four different samples, pure Fe, Fe-C, Fe-S and Fe-C-S, the grain sizes of the samples decreased from pure Fe to Fe-C, with Fe-S having the smallest grain size despite the fact that the C concentration were three times higher than that of the S concentration. The grains in the Fe-C-S sample seemed to be closer in size to the Fe-C sample than to that of the Fe-S sample. They concluded that re-crystallization in the early stages is controlled by C and that the initial segregation of C to the grain boundaries is displaced by the segregation of S.

Grabke *et. al.* [19] performed segregation studies on Fe(100) to investigate the segregation of non-metal impurities. At temperatures below 923 K the impurities C and nitrogen (N) were observed to segregate, but at 923 K the segregation of S was observed to form a c(2×2) structure on the Fe(100) surface. At 1073 K a maximum surface concentration of S was observed independent of the S bulk concentration. They determined that the segregation of S in Fe(100) would be observed for bulk concentrations as low as 0.01 ppm, but that such measurements would not be time effective. They were able to determine the segregation energy of C in Fe(100) as -85 kJ/mol (-0.88 eV).

G. Panzner and B. Egert [25] performed studies on  $\alpha$ -iron and iron sulphide surfaces (FeS, FeS<sub>2</sub>) to determine the bonding state of S on the different surfaces. For the Fe(100) sample containing 3 wt. % silicon (Si) and 20 ppm S, the Si segregated first, but was replaced by S at 900 K to produce a

c(2×2) equilibrium surface structure. This replacement of the Si from the surface is explained by a high S segregation energy as compared to a smaller Si segregation energy. From core level analysis the electron binding energies of the S 2p peak are in the range 162.2-161.7 eV, which indicates that the S atoms are negatively charged as a result of the charge transfer of electrons from Fe to S. This charge transfer effect is more pronounced in FeS and FeS<sub>2</sub> as observed by the increasing binding energy of the S 2s and S 2p core level going from FeS<sub>2</sub> to FeS. From the S (LMM) Auger spectra the interactions involving the Fe 3d electrons can be analyzed. These peaks show a five peak structure indicating the interaction of S and Fe. For segregated S in Fe this effect is stronger as compared to the Fe sulfide surfaces.

Fujita *et. al.* [26] studied the segregation of S in Fe(100) and the effect S has on the oxidation of the Fe crystal. They performed linear heating segregation measurements and observed the segregation of impurities C, O and S. C segregated at the lower temperatures of 573-673 K. At temperatures above 673 K S segregation became more dominant reaching full surface coverage at temperatures of 973-1073 K. They explained the initial segregation of C and the later segregation of S as being due to their respective activation energies. According to their literature values C has an activation energy of 123 kJ/mol (1.27 eV) compared to the value of 232 kJ/mol (2.40 eV) for S. Thus the C segregation process occurs much faster than the segregation of S in bcc Fe. To determine whether the segregated S can prevent the oxidation of Fe, they conducted three experiments. The first was to measure the oxidation of a sputter cleaned Fe sample. The second experiment was to observe the oxidation of an Fe sample that had segregated S on the surface, which was half sputter cleaned. The third experiment was the oxidation of an Fe sample containing segregated S at full coverage. They found that the presence of S on the Fe surface prevented the initial oxidation of the surface. Two models could be used to clarify this, the first was that the electronegative S atoms attract electrons from the metal substrate. This results in less unbound electrons at the surface, which may decrease surface reactivity and stabilize the surface. The second model was that the electronegative S atom on the surface becomes negative due to the transfer of electrons from the metal to the S atom. This causes each S atom to create an electric dipole perpendicular to the surface. Thus an electrostatic force is induced between two neighbouring dipoles resulting in a positive potential energy. This causes a repulsive interaction between segregants, forcing them to occupy the hollow sites on the surface. Thus the surface is fully saturated and the adsorption of other species cannot occur.

M.M Eisl *et. al.* [27] conducted a study to determine the diffusion properties of S and N in polycrystalline bcc Fe by using the method of linear programmed heating described by Viljoen *et. al.* [28]. Pure Fe samples were heated from 373 K to 1123 K at a rate of 0.004 K/s and 0.0075 K/s respectively. They found that N is the dominant segregant at temperatures in the range

523-673 K. From Scanning Auger Microscope (SAM) maps it was observed that a homogenous surface distribution was obtained for N on the surface. At temperatures above 673 K, S starts to segregate and displaces the N from the surface. They explained this effect by the segregation energies for Fe single crystals which is given by Grabke *et. al.* [29] as -190 kJ/mol (-1.97 eV) for S, and -110 kJ/mol (-1.14 eV) for N. The large energy decrease experienced by the crystal due to the segregation of S provides a structure that is energetically more stable and would thus be favoured over the segregation of N. In contrast to the segregation of N, the initial segregation of S does not produce a homogenous distribution on the surface, instead the S is observed as small spots and lines on the surface. From this they concluded that the segregation of N is primarily a result of bulk diffusion while the diffusion of S is of a more complex mechanism. Initially the S diffuses via grain boundaries causing the small spots and lines, at 873 K the S saturates the Fe surface with both grain boundary and bulk diffusion now taking place. They determined the activation energy,  $Q$ , of diffusion as 145 kJ/mol (1.50 eV) and the pre-exponential factor,  $D_0$ , as  $1.07 \times 10^{-6}$  m<sup>2</sup>/s, performing a second run delivered different parameters with a  $D_0$  value of 0.16 m<sup>2</sup>/s and a  $Q$  value of 232 kJ/mol (2.40 eV). They explained that the increase in the activation energy and the pre-exponential factor was the result of grain growth, since at high temperatures re-crystallisation of the Fe occurs.

Arabczyk *et. al.* [22] performed segregation studies on a Fe(111) surface at constant temperatures in the temperature range of 770-1000 K. They measured an activation energy of 2.13 eV for the diffusion of S in bcc Fe. Other reported activation energies for S diffusion in bcc Fe single crystals are: 202 kJ/mol (2.09 eV), 232 kJ/mol (2.40 eV) and 222 kJ/mol (2.30 eV) [30].

Hong *et. al.* [31] performed calculations using molecular orbital theory to study the segregation of S in Fe(100) via a substitutional diffusion mechanism. They found that the inclusion of S in the calculation of the Fe coordination number causes a reduction in the spin polarization and produces binding energies close to experimental values. For S in a bulk substitutional site, the S 3s orbital interacts with occupied  $a$ -symmetry orbitals resulting in a closed shell repulsion. On the surface the S 3p orbitals are symmetrically allowed to mix with the S 3s orbital, reducing the repulsion. The 3s orbital is thus largely responsible for S binding more strongly to the surface than in the bulk of Fe, with a surface binding energy of -3.98 eV and a bulk binding energy of -3.10 eV. They calculated the vacancy formation energy in Fe as 76.2 kJ/mol (0.79 eV) and the segregation energy as -161 kJ/mol (-1.67 eV). They contributed half of the segregation energy to the difference in surface and bulk binding energies of S and the other half to the vacancy formation energy of Fe.

For the calculation of activation energies for substitutional diffusing elements it is important to obtain the vacancy formation energy of bcc Fe. Calculations have been performed by numerous

authors [32; 33; 34; 35; 36] with values in good agreement with experimental findings. Terblans [37; 38; 39; 40] proposed that the vacancy formation energy is dependent on the surface orientation by considering the formation of vacancies to occur via a Schottky defect mechanism. This method is different from the conventional method in which the vacancy formation energy is calculated, where the formation of vacancies were considered to be independent of the surface orientation. No literature, previous to the work of Terblans, could be obtained where the surface orientation of the crystal was taken into account for the calculation of the vacancy formation energy. Terblans was able to successfully calculate the vacancy formation energies in Cu and Al single crystals [37; 38]. For the Cu single crystals the vacancy formation energies are from largest to smallest: Cu(110)=148 kJ/mol (1.54 eV), Cu(100)=129 kJ/mol (1.34 eV), Cu(111)=103 kJ/mol (1.07 eV). For the low-index planes of Aluminium the vacancy formation energies in order of the largest to smallest are: Al(110)=116 kJ/mol (1.20 eV), Al(100)=128 kJ/mol (1.33 eV), Al(111)=144 kJ/mol (1.49 eV).

The literature study revealed that the segregation of impurities in bcc Fe segregate to the surface and grain boundaries at high temperatures. The interstitial impurities C and N are seen to segregate in the lower temperature range of 673-973 K for both polycrystalline and single crystals forming a  $c(2 \times 2)$  structure on the Fe(100) surface. At higher temperatures the substitutional impurities S and P are seen to dominate the surface, especially S dominance on the surface is seen at high temperatures, 973-1073 K. It was determined that interstitial impurities such as C have activation energies which are smaller than those of substitutional impurities S and P resulting in the faster diffusion of interstitial species. The segregation of S on the Fe surface dominates the surface forming a  $c(2 \times 2)$  structure on the Fe(100) surface, with little other impurities visible on the surface, this was explained by the large segregation energy (-190 kJ/mol (-1.97 eV)) of S in bcc Fe(100). From the computational literature information the stability of the different surfaces of Fe could be obtained. The influence of the crystal surface orientation on vacancy formation energies was also discussed by looking at Cu and Al, providing valuable information regarding substitutional diffusion in crystalline solids.

To the best knowledge of the author no previous computational study was done to systematically investigate the diffusion of S in bcc Fe to determine the various diffusion paths and equilibrium lattice sites for S in bcc Fe. It is the aim of this study to compute the activation energy of diffusion for S in the low-index orientations of bcc Fe and the segregation energy of S in a bcc Fe(100). Experimental work, including AES, will also be performed in order to confirm the predictions made by DFT modelling.

## References

- [1]. A.A. Adesina, *Appl. Catal. A-Gen.* 138 (1996) 345.
- [2]. R.L. Espinoza, A.P. Steynberg, B. Jager, A.C. Vosloo, *Appl. Catal. A- Gen.* 186 (1999) 13.
- [3]. W. Arabczyk, D. Moszyński, U. Narkiewicz, R. Pelka, M. Podsiadły, *Catal. Today* 124 (2007) 43.
- [4]. J.A. Kritzinger, *Catal. Today* 71 (2002) 307.
- [5]. U. Narkiewicz, *Appl. Surf. Sci.* 134 (1998) 63.
- [6]. B.H. Davis, *Catal. Today* 141 (2009) 25.
- [7]. J.S. Braithwaite, P. Rez, *Acta. Mater.* 53 (2005) 2715.
- [8]. P. Rez, J.R. Alvarez, *Acta. Mater* 47 (1999) 4069.
- [9]. N.H. Heo, *Scripta Mater.* 51 (2004) 339.
- [10]. J. Ouder, *Mater. Sci. Eng* 42 (1980) 101.
- [11]. J.H. Sinfelt, *Surf. Sci.* 500 (2002) 923.
- [12]. C. Stampfl, M.V. Ganduglia-Pirovano, K. Reuter, M. Scheffler, *Surf. Sci.* 500 (2002) 368.
- [13]. D. Briggs, M.P. Seah, (Eds.), *Practical surface analysis by Auger and X-ray Photoelectron Spectroscopy*, John Wiley & Sons, New York, 1983.
- [14]. P. Błonski, A. Kiejna, *Surf. Sci.* 601 (2007) 123.
- [15]. P. Błonski, A. Kiejna, *Vacuum* 74 (2004) 179.
- [16]. M.J.S. Spencer, A. Hung, I.K. Snook, I. Yarovsky, *Surf. Sci.* 513 (2002) 389.
- [17]. S.G. Nelson, M.J.S. Spencer, I.K. Snook, I. Yarovsky, *Surf. Sci.* 590 (2005) 63.
- [18]. N. Todorova, M.J.S. Spencer, I. Yarovsky, *Surf. Sci.* 601 (2007) 665.
- [19]. H.J. Grabke, W. Paulitschke, G. Tauber, H. Viehhaus, *Surf. Sci.* 63 (1977) 377.
- [20]. M.J.S. Spencer, I.K. Snook, I. Yarovsky, *J. Phys. Chem. B* 110 (2006) 956.
- [21]. M.J.S. Spencer, A. Hung, I.K. Snook, I. Yarovsky, *Surf. Sci.* 540 (2003) 420.
- [22]. W. Arabczyk, M. Militzer, H.-J. Müssig, J. Wieting, *Scripta Metall. Mater.* 20 (1986) 1549.
- [23]. T. Kishi, S. Itoh, *Surf. Sci.* 363 (1996) 100.
- [24]. C.L. Briant, *Acta. Metall.* 36 (1988) 1805.
- [25]. G. Panzner, B. Egert, *Surf. Sci.* 144 (1984) 651.
- [26]. D. Fujita, T. Ohgi, T. Homma, *Appl. Surf. Sci.* 200 (2002) 55.
- [27]. B.M. Reichl, M.M. Eisl, T. Weis, H. Störi, *Surf. Sci.* 331-333 (1995) 243.
- [28]. E.C. Viljoen, J. du Plessis, *Surf. Sci.* 431 (1999) 128.

- [29]. H.J. Grabke, H. Viehhaus, Surface segregation of nonmetal atoms on metal surfaces. in: P.A. Dowben, A. Miller, (Eds.), Surface segregation phenomena, CRC Press, Boca Raton, Florida, 1990.
- [30]. S. Mrowec, Defects and diffusion in solids: An Introduction, Elsevier, New York, 1980.
- [31]. S.Y. Hong, A.B. Anderson, Phys. Rev. B. 38 (1988) 9417.
- [32]. T. Ohnuma, N. Soneda, M. Iwasawa, Acta. Mater 51 (2009) 5947.
- [33]. P.A.T. Olsson, Comp. Mater. Sci. 47 (2009) 135.
- [34]. C.Q. Wang, Y.X. Yang, Y.S. Zhang, Y. Jia, Comp. Mater. Sci. 50 (2010) 291.
- [35]. J.-M. Zhang, G.-X. Chen, K.-W. Xu, Physica B 390 (2007) 320.
- [36]. G. Lucas, R. Schäublin, Nucl. Instrum. Meth. B. 267 (2009) 3009.
- [37]. J.J. Terblans, Surf. Interface Anal. 33 (2002) 767.
- [38]. J.J. Terblans, Surf. Interface Anal. 35 (2003) 548.
- [39]. J.J. Terblans, W.J. Erasmus, E.C. Viljoen, J. du Plessis, Surf. Interface Anal. 28 (1999) 70.
- [40]. J.J. Terblans, G.N. van Wyk, Surf. Interface Anal. 35 (2003) 779.



Part I  
Theory



# Chapter 3: Diffusion theory

## 3.1. Introduction

A very general definition for solid state diffusion can be given as the transfer of atoms from one part of a system to another as a result of the random motion of the individual atoms in the system [1]. All the atoms in the system are constantly oscillating around their respective equilibrium positions. If sufficient energy is added to the system these oscillations become large enough to give rise to atomic jumps and the atoms are said to diffuse [2; 3]. A very basic example to explain the diffusion process is the mixing of iodine in water. At first when the iodine is poured into the water a large concentration of iodine is observed at the point of entry. As time evolves the iodine diffuses throughout the water and after sufficient time has passed a homogenous distribution of iodine is observed [1]. Although this example is given for two fluids, the same effect occurs in solids where a homogenous distribution is obtained if the process is allowed to take place at a high temperature for a sufficient amount of time. From the iodine example above it is convincing to believe that diffusion is caused by a concentration gradient between two or more solids or liquids. This is how the two laws of Fick [1; 2; 3; 4] describes diffusion, the first law describes the diffusion of atoms in terms of a concentration gradient alone, while the second law describes the change in concentration as a time evolving process. The two laws of Fick are derived in this chapter along with other basic concepts of the diffusion process. These include the diffusion mechanisms that are possible for a range of different systems. A short description is also given on the Arrhenius equation [4] which gives the relation between the diffusion coefficient,  $D$ , the pre-exponential factor,  $D_0$ , and the activation energy,  $Q$ .

## 3.2. Fick`s first diffusion law

Fick`s first law predicts the flow rate of atoms as a result of a concentration gradient between the different atoms in the system. In one-dimension Fick`s first law is given by equation 3.1 [2; 3; 4]

$$J = -D \frac{\partial C}{\partial x} \quad (3.1)$$

where  $J$  is the flux of atoms and,  $\frac{\partial C}{\partial x}$ , the concentration gradient with  $C$  the concentration and  $x$  the position of atoms. For the derivation of equation 3.1, consider two atomic planes at positions  $x$  and  $x+\Delta x$  shown in figure 3.1, with  $M_x$  and  $M_{x+\Delta x}$  representing the number of atoms per unit area at the respective positions. The distance  $\Delta x$  represents the distance over which atoms can diffuse, the inter atomic distance. All the diffusing atoms are taken to be of the same type.

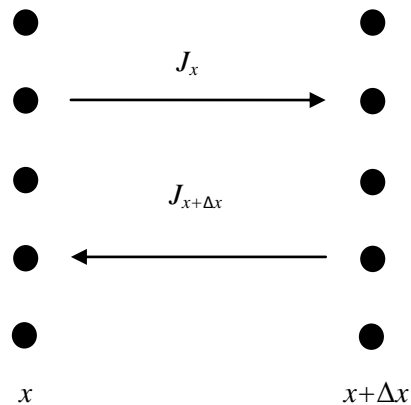


**Figure 3.1:** Diffusion between two atomic planes at positions  $x$  and  $x+\Delta x$  with  $M_x$  and  $M_{x+\Delta x}$  representing the number of atoms per unit area of the respective positions. From position  $x$  to position  $x+\Delta x$  there is a flux of  $J_x$  and in the opposite direction from  $x+\Delta x$  to  $x$ , there is a flux of  $J_{x+\Delta x}$ .

Assuming that atoms can only diffuse a distance equal to the inter atomic distance, the flux of atoms diffusing from  $x$  to  $x+\Delta x$  is given by equation 3.2

$$J_x = \frac{1}{2} \Gamma M_x. \quad (3.2)$$

Here,  $\Gamma$ , is the mean jump frequency giving the average number of times an atom changes lattice sites per second. The factor of a half arises due to the assumption that half of the atoms would diffuse to the right and the other half would diffuse to the left for the two dimensional case considered here [4]. In the opposite direction, from  $x+\Delta x$  to  $x$ , the flux is given by equation 3.3

$$J_{x+\Delta x} = \frac{1}{2} \Gamma M_{x+\Delta x}. \quad (3.3)$$

Subtracting equation 3.2 from equation 3.3 and multiplying by,  $\frac{(\Delta x)^2}{(\Delta x)^2}$ , results in an expression for the total flux,  $J$

$$\begin{aligned} J &= \left( \frac{1}{2} \Gamma M_{x+\Delta x} - \frac{1}{2} \Gamma M_x \right) \left( \frac{(\Delta x)^2}{(\Delta x)^2} \right) \\ &= \frac{1}{2} \Gamma (\Delta x)^2 \frac{(M_{x+\Delta x} - M_x)}{(\Delta x)^2}. \end{aligned} \quad (3.4)$$

Using the relation,  $\Delta C = \frac{\Delta M}{\Delta x}$ , leads to equation 3.5

$$\begin{aligned}
 J &= -\frac{1}{2}\Gamma(\Delta x)^2 \frac{\Delta C}{\Delta x} \\
 &= -D \frac{\partial C}{\partial x}.
 \end{aligned}
 \tag{3.5}$$

The diffusion coefficient,  $D$ , in equation 3.5 is given by equation 3.6

$$D = \frac{1}{2}\Gamma(\Delta x)^2.
 \tag{3.6}$$

For the three-dimensional case equation 3.6 becomes

$$\begin{aligned}
 J &= -\frac{1}{6}\left(\Gamma_x d_x^2 \frac{\partial C}{\partial x} + \Gamma_y d_y^2 \frac{\partial C}{\partial y} + \Gamma_z d_z^2 \frac{\partial C}{\partial z}\right) \\
 &= -\left(D_{xx} \frac{\partial C}{\partial x} + D_{yy} \frac{\partial C}{\partial y} + D_{zz} \frac{\partial C}{\partial z}\right)
 \end{aligned}
 \tag{3.7}$$

where the symbol,  $d$ , has been used for the inter atomic distance. The three dimensional diffusion coefficient is given by equation 3.8

$$D_{ii} = \frac{1}{6}\Gamma_i d_i^2.
 \tag{3.8}$$

The subscript,  $i$ , is used to indicate the crystal directions in each of the Cartesian coordinates  $x$ ,  $y$  and  $z$ . Cubic solids are considered as isotropic and thus the diffusion coefficient in all three directions are the same i.e.

$$D_{xx} = D_{yy} = D_{zz}. \quad (3.9)$$

Inserting equation 3.8 into equation 3.7 and taking the system to be isotropic leads to equation 3.10 [2; 3; 4]

$$\begin{aligned} J &= -\frac{1}{6}\Gamma d^2 \left[ \frac{\partial C}{\partial x} + \frac{\partial C}{\partial y} + \frac{\partial C}{\partial z} \right] \\ &= -D\nabla C. \end{aligned} \quad (3.10)$$

The following is important when Fick's first law is considered

- It is only valid for ideal solutions without any free energy gradients such as temperature, pressure, electrostatic or vibrational gradients.
- It applies only to ideal solutions, thus the thermodynamic activity coefficient is unity for all concentrations.
- $D$  is independent of concentration [4].

### 3.3. Fick's second diffusion law

It is not always possible to determine the flux of atoms, for a gas in the presence of a solid the problem is relatively easy, but it becomes more complicated if two solids are considered. This is where it becomes more practical to make use of Fick's second law generally known as the diffusion equation. Here time is included and the equation describes the kinetic behaviour of the system

under study. Thus the non-steady state for an isotropic material is studied using Fick's second law, where the concentration is now both time and position dependant [4]. Fick's second law is given by equation 3.11 [2; 3; 4; 5]

$$\frac{\partial C}{\partial t} = D \frac{\partial^2 C}{\partial x^2} \quad (3.11)$$

where  $t$  is the time of diffusion. Fick's second law is derived as follow: consider the rectangular volume divided into two parts by a thin membrane of thickness  $\delta x$  and area  $A$  as shown in figure 3.2.

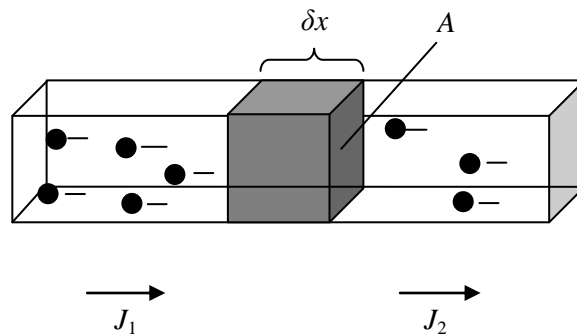


**Figure 3.2:** A rectangular volume, separated by a thin membrane of thickness  $\delta x$  and area  $A$ , used to illustrate a time dependant diffusion process as given by Fick's second diffusion law.

The number of atoms entering the membrane is given by  $J_1 A \delta t$  and the number of atoms leaving the membrane by  $J_2 A \delta t$ . Thus the change in the number of atoms,  $\Delta N$ , is given by

$$\begin{aligned} \Delta N &= J_1 A \delta t - J_2 A \delta t \\ &= A \delta t (J_1 - J_2). \end{aligned} \quad (3.12)$$

The change in concentration of atoms inside the volume of the membrane is given by equation 3.13

$$\frac{\Delta N}{A\delta x} = \delta C. \quad (3.13)$$

Making use of equation 3.13 and dividing equation 3.12 by  $A\delta x$  results in equation 3.14

$$\frac{\Delta N}{A\delta x} = \delta C = \frac{A \delta t (J_1 - J_2)}{A\delta x}$$

$$\frac{\delta C}{\delta t} = \frac{(J_1 - J_2)}{\delta x}. \quad (3.14)$$

Since the membrane is very thin the flux leaving the volume  $J_2$  can be expressed as

$$J_2 = J_1 + \frac{\partial J}{\partial x} \delta x. \quad (3.15)$$

Substituting equation 3.15 into equation 3.14 results in the continuity equation, equation 3.16

$$\frac{\delta C}{\delta t} = -\frac{\partial J}{\partial x}. \quad (3.16)$$

Substituting Fick's first law, equation 3.5, into equation 3.16 leads to Fick's second law, given by equation 3.17 [5]

$$\frac{\delta C}{\delta t} = D \frac{\partial^2 C}{\partial x^2}. \quad (3.17)$$

In three dimensions for an isotropic material equation 3.17 becomes equation 3.18 [2; 3; 4; 5]

$$\frac{\partial C}{\partial t} = D \nabla^2 C . \quad (3.18)$$

This second order differential equation, equation 3.18, can be solved for different initial and boundary conditions, depending on the system under study. The semi-infinite solution to equation 3.17 is described in chapter 4, Segregation theory.

## 3.4. Diffusion mechanisms

Fick's second law from the preceding section, section 3.3, describes the diffusion process as a concentration gradient evolving in time. This allows information regarding the kinetics of the diffusion process to be obtained, giving information on how fast a certain diffusion process will occur but gives no direct information regarding the diffusion path of the atoms. Apart from knowing the rate of the diffusion process it is also important to know by which mechanism diffusion occurs. Different rates are expected for the different diffusion mechanisms as will be seen in this section. Information regarding the diffusion mechanism enables the researcher to modify a material in order to obtain certain desired properties.

### 3.4.1. Interstitial mechanism

The interstitial diffusion mechanism is commonly found in systems where the diffusing atom is much smaller in size compared to the matrix atoms [2; 3; 4]. The diffusion of C in  $\alpha$ - and  $\gamma$ - iron [3] as well as the diffusion of the gases He, H<sub>2</sub>, N<sub>2</sub> and O<sub>2</sub> in pure metals are examples of the

interstitial diffusion mechanism [4]. Figure 3.3 gives a schematic representation of the interstitial diffusion process in crystalline solids.

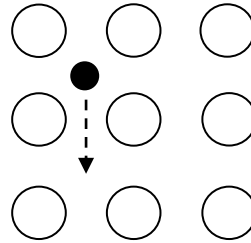


**Figure 3.3:** Interstitial mechanism of diffusion, here the diffusing atom is smaller in size than that of the matrix atoms and the diffusing atom moves from one interstitial lattice site to a nearest neighbour empty interstitial lattice site as indicated by the arrow.

In figure 3.3 the black atom represents the atom in the interstitial site of the lattice. This atom can diffuse to any empty nearest neighbour interstitial site. It is not limited to one atomic jump alone and can diffuse over large distances depending on the energy barrier and the energy available in the system. In order for the interstitial atom to diffuse the lattice needs to distort to allow a channel by which the atom can diffuse. Figure 3.4 illustrates this, atoms 1 and 2 needs to change position (indicated by the solid arrows) and in doing so they provide a channel by which the atom can jump from one interstitial site to a nearest neighbour interstitial site [2; 3; 4]. The presence of the surrounding atoms, especially atoms 1 and 2, causes an energy barrier between the initial and final positions of the atom. An amount of energy equal to this barrier, the migration energy,  $E_m$ , is required by the atom to diffuse. Since it was not necessary to create an empty lattice site to which the interstitial atom can diffuse, the migration energy is equal to the activation energy of diffusion. If a vacancy first needed to be created to which the interstitial atom can diffuse, an additional energy term,  $E_{vac}$ , the vacancy formation energy would have to be added to the migration energy term to get the total activation energy of diffusion [3].

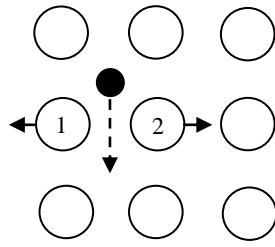


**Figure 3.4:** Illustration of the interstitial diffusion mechanism. The diffusing atom, the atom in black, requires a certain amount of energy to overcome the energy barrier created by the surrounding lattice atoms, called the migration energy,  $E_m$ .

If the diffusing atom is large relative to the matrix atoms, the energy requirements for an interstitial diffusion process becomes too large and another diffusion mechanism becomes dominant [3]. The interstitial sites are those sites in the matrix lattice that are energetically favourable for the diffusing atom. For example in the bcc crystal structure the interstitial positions are either tetrahedral or octahedral positions as illustrated in figures 3.5(a) and 3.5(b) respectively [2].

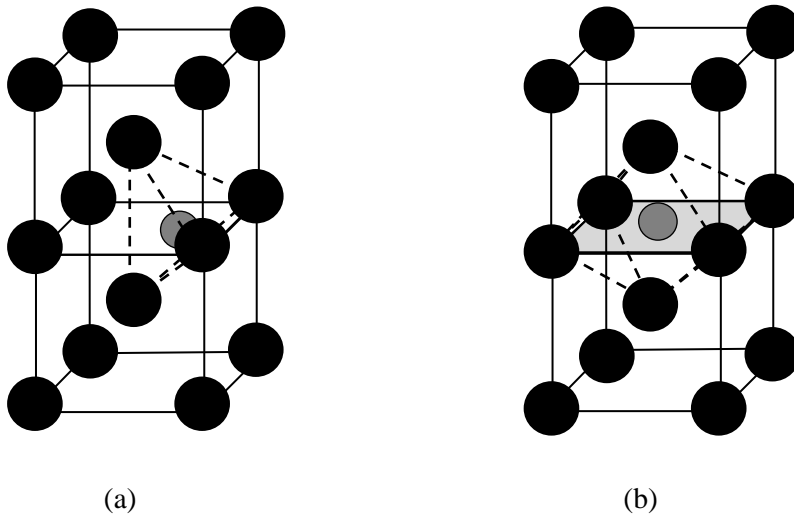


**Figure 3.5:** Energetically favourable sites for interstitial atoms in a bcc crystal structure: (a) tetrahedral site and (b) octahedral site.

The activation energy of diffusion for this mechanism is very small and atoms can diffuse over large distances before being trapped by crystal defects i.e. surfaces, grain boundaries, vacancies etc. Trapping of impurities at grain boundaries in sufficient numbers can lead to grain boundary embrittlement [4].

### 3.4.2. Vacancy/Substitutional mechanism

The substitutional mechanism of diffusion requires that a substitutional site be vacant in the nearest neighbour position of the diffusing atom. Thus before a substitutional atom can diffuse an empty lattice site or a vacancy needs to be created. This additional energy required for the creation of a vacancy, the vacancy formation energy  $E_{vac}$ , is added to the migration energy of diffusion,  $E_m$ , to get the total activation energy,  $Q$ , for the substitutional diffusion process. The fraction of vacancies at a specific temperature can be calculated using equation 3.19 [4; 6]

$$n_v = n_o \exp\left(\frac{-E_{vac}}{RT}\right) \quad (3.19)$$

where,  $n_v$  is the number of vacancies,  $n_o$  the number of lattice sites,  $E_{vac}$  is the vacancy formation energy,  $T$  the temperature in Kelvin and  $R$  is the universal gas constant with a value of 8.314 J/K/mol. Equation 3.6, needs to be adapted to incorporate the probability,  $X_v$ , that a particular lattice site is vacant and thus becomes [4]

$$D = \frac{1}{2} \Gamma (\Delta x)^2 X_v \quad (3.20)$$

where  $X_v$  is given by equation 3.21

$$X_v = \frac{n_v}{n_0} \exp\left(\frac{-E_{vac}}{RT}\right). \quad (3.21)$$

Similar to the interstitial diffusion mechanism, the lattice has to distort to allow the atom to diffuse into an empty lattice site. This is shown by the solid arrows in figure 3.6 which illustrates the substitutional diffusion mechanism.

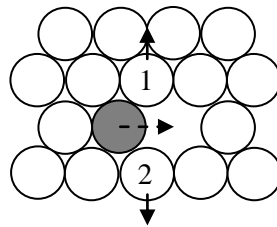


**Figure 3.6:** Substitutional diffusion mechanism for crystalline solids. For the atom in grey to diffuse into the adjacent vacancy, atoms 1 and 2 needs to change their positions (indicated by the two solid arrows) in order to allow the diffusing atom to pass into the vacancy.

This mechanism is commonly found in fcc metals, but has also been observed in bcc and hcp metals as well as in oxides and ionic compounds. In comparison with interstitial diffusion, the substitutional diffusion mechanism is slower due to the vacancy that needs to be created first before the atom can diffuse [3].

### 3.4.3. Interstitialcy mechanism

If an atom large in comparison to the atoms of the matrix, occupies an interstitial lattice site the interstitialcy diffusion mechanism can be expected to occur. Energy required by an atom to diffuse via the interstitial diffusion mechanism is too large and instead the interstitial atom will diffuse by displacing one of the nearest neighbour atoms. The displaced atom will then displace one of its nearest neighbour atoms continuing the diffusion process [2; 3], this is illustrated in figure 3.7.

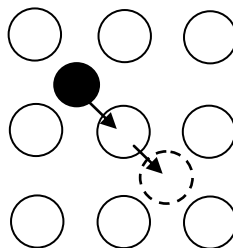


*Figure 3.7: Interstitialcy diffusion mechanism where the diffusing atom replaces one of its nearest neighbour atoms.*

Interstitialcy diffusion has been observed for the AgBr system where the diffusing Ag atom is comparable in size to the Br atom and does not cause large distortion of the lattice by occupying an interstitial site [2; 3; 4]. Normally this mechanism is not expected, since the energy required for a large atom to be in an interstitial position is too high. For systems that have been exposed to radiation or high energy particle damage, where lattice defects are created, this mechanism is a strong possibility [2; 3].

### 3.4.4. Interstitial-substitutional mechanism

An atom located in an interstitial position diffuses through the crystal via an interstitial mechanism and can occasionally fill a vacancy or replace one of the lattice atoms. This mechanism of diffusion is known as an interstitial-substitutional diffusion mechanism. As mentioned above two possibilities exist; one is the filling of a vacancy and the other is the substitution of a matrix atom. They are respectively called the dissociative and the kick-out mechanisms as illustrated in figure 3.8 and 3.9 [2].

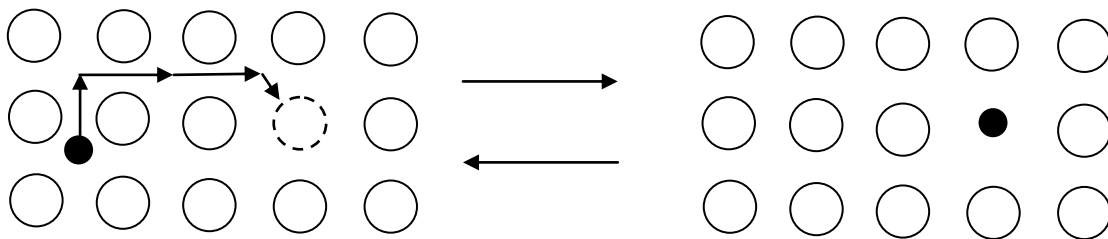


**Figure 3.8:** Dissociative interstitial-substitutional diffusion mechanism which explains the fast diffusion of Cu in Ge.

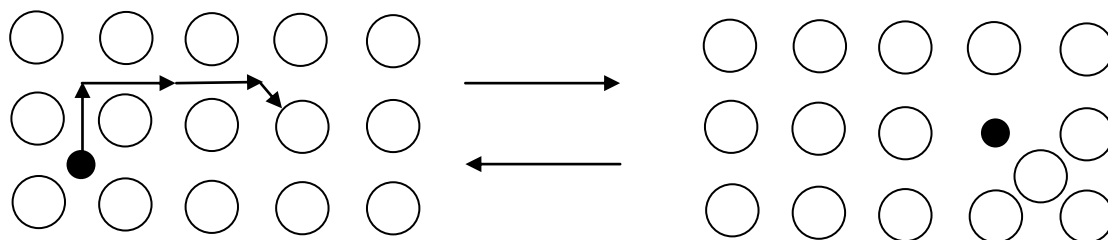


**Figure 3.9:** Kick-out interstitial-substitutional diffusion mechanism responsible for the diffusion of Au, Pt and Zn in Si.

Diffusion of Cu in Ge as well as diffusion of foreign metallic elements in Pb, Sn, Nb, Ti and Zr is due to the dissociative mechanism. Diffusion of Au, Pt and Zn in Si is a result of the kick-out mechanism. Fick's diffusion equations need to be adapted to incorporate the reaction terms, since

there are three species involved in this mechanism [2]. A discussion of this topic will not be done here, a detailed discussion thereof can be found in the references [7; 8].

### 3.5. Influence of temperature on diffusion

The temperature dependence of diffusion can generally be described by the Arrhenius relation given by equation 3.22 [2; 4]

$$D = D_0 \exp\left(\frac{-Q}{RT}\right) \quad (3.22)$$

where,  $Q$ , is the activation energy of diffusion,  $D_0$  is a temperature independent quantity called the pre-exponential factor. The activation energy,  $Q$ , is the sum of the vacancy formation energy and the migration energy,  $E_m$ , given by equation 3.23.

$$Q = E_m + E_{vac} . \quad (3.23)$$

For atoms diffusing via the interstitial diffusion mechanism, no vacancy is required and the activation energy is equal to the migration energy. The pre-exponential factor is given by equation 3.24

$$D_0 = D'_0 \exp\left(\frac{-\Delta S}{R}\right) \quad (3.24)$$

where,  $\Delta S$  is the entropy of diffusion and  $D'_0$  is given by equation 3.25 [2; 3]

$$D'_0 = \left[ \gamma a_0^2 \nu \exp \left( \frac{\Delta S}{R} \right) \right] \quad (3.25)$$

The term  $\gamma$  is a geometric factor, which is equal to 1 for substitutional diffusion,  $a$  is the interlattice parameter and,  $\nu$  is the vibrational frequency. Plotting  $\ln D$  over  $\frac{1}{T}$  from equation 3.22 gives a straight line with a gradient of  $\frac{-Q}{R}$  and a y-intercept of  $\ln D_0$ . This temperature dependence of the rate constant,  $D$ , implies that a energy barrier between the initial and the final states of diffusion is present and can be overcome by the addition of energy to the system, for example thermal energy [4]. The energy barrier between the initial and the final states is shown in figure 3.10.

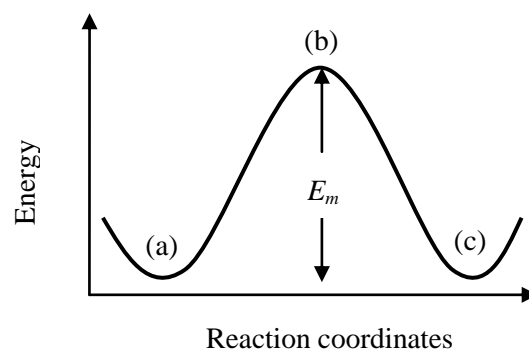
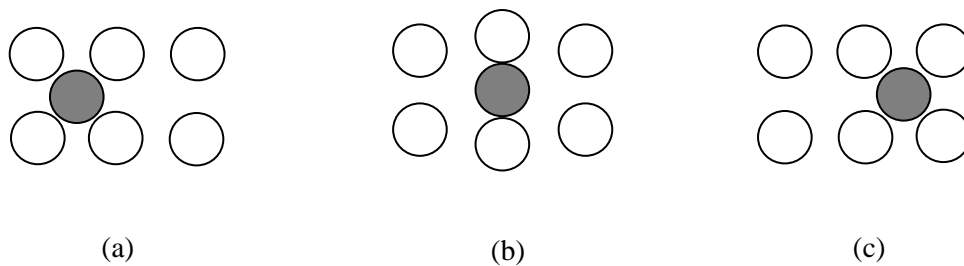


**Figure 3.10:** The temperature dependence of diffusion, showing how energy is required to overcome the diffusion barrier. From an initial state, (a), to a final state, (c), where state (b) represents the transition state.

## 3.6. Summary

This chapter described the basic theoretical concepts of diffusion. The two laws of Fick were derived in full due to their importance and use in later chapters. Fick's first law described diffusion in terms of a concentration gradient, while Fick's second law was able to give a description of a time evolving diffusion process. The second law of Fick can be solved for different initial and boundary conditions to describe the kinetics of diffusion and segregation. Various diffusion mechanisms were discussed along with examples for each of the mechanisms. The Arrhenius equation which describes the rate of diffusion is explained in short to illustrate the presence of an energy barrier for a diffusion reaction.

## 3.7. References

- [1]. J. Crank, *The mathematics of diffusion*, Oxford university press, London, 1975.
- [2]. P. Heitjans, J. Karger, (Eds.), *Diffusion in condensed matter*, Springer, Berlin, 2005.
- [3]. P.G. Shewmon, *Diffusion in solids*, McGraw-Hill Book Company, New York, 1963.
- [4]. R.J. Borg, G.J. Dienes, *Introduction to solid state diffusion*, Academic Press, New York, 1988.
- [5]. D.A. Porter, K.E. Easterling, *Phase transformations in metals and alloys*, Chapman & Hall, 1981.
- [6]. D.R. Askeland, *Material science and engineering*, Stanley Thornes, Cheltenham, 1998.
- [7]. C.R.A. Catlow, C.M. Freeman, B. Vessal, S.M. Tomlinson, M. Leslie, *J. Chem. Faraday Trans. 87* (1991) 1947.
- [8]. S. Fritzsche, R. Haberlandt, J. Kärger, H. Pfeifer, K. Heinzinger, *Chem. Phys. Letters* 198 (1992) 283.



# Chapter 4: Segregation theory

## 4.1. Introduction

This chapter describes two models which can be used to extract the segregation parameters from AES data. For the kinetics of surface segregation a solution of Fick's second law is derived for the case of linear programmed heating. The equilibrium of surface segregation is described by the model of Guttmann. The combination of these two models are used to obtain all the segregation parameters for the system under study.

## 4.2. Kinetics of surface segregation

The kinetics of surface segregation determines the rate at which atoms move to the surface of a material. For a description of the kinetics of surface segregation Fick's second law can be solved for specific initial and boundary conditions. The initial condition is that the concentration,  $C$ , of the segregating specie is constant at time  $t=0$ . The boundary condition assumes that the rate of atomic movement is independent of the number of atoms on the surface and thus it is assumed that there is always a clean surface present. Mathematically these conditions are given by equation 4.1

$$\begin{aligned} C &= 0, & x &= 0, & t &> 0 \\ C &= C_0, & x &> 0, & t &= 0 \end{aligned} \quad (4.1)$$

where  $x$  is the position in the sample and  $C_0$  is the initial concentration. Fick's second law derived in chapter 3, Diffusion theory, is given by equation 4.2

$$\frac{\partial C}{\partial t} = D \frac{\partial^2 C}{\partial x^2}. \quad (4.2)$$

where  $D$  is the diffusion coefficient. Solving Fick's second law for the initial and boundary conditions given by equation 4.1 leads to equation 4.3 [1]

$$C = C_0 \operatorname{erf}\left(\frac{x}{2\sqrt{Dt}}\right). \quad (4.3)$$

Equation 4.3 describes the concentration,  $C$ , of the segregating specie at position  $x$  in the material after time  $t$ . From equation 4.3 the flux of atoms moving through  $x=0$  is given by equation 4.4 [1]

$$D \left( \frac{\partial C}{\partial x} \right)_{x=0} = \frac{DC_0}{\sqrt{\pi Dt}} \quad (4.4)$$

To obtain the total amount of the segregating specie which has left the crystal through an area  $A$  at  $x=0$  in time  $t$  is found by integrating equation 4.5.

$$A \frac{DC_0}{\sqrt{\pi Dt}} \quad (4.5)$$

which results in equation 4.6.

$$M_t = 2AC_0 \left( \frac{Dt}{\pi} \right)^{\frac{1}{2}}. \quad (4.6)$$

The surface concentration of the segregated layer of thickness  $d$  is found by dividing the total amount of the material which have diffused through an area  $A$ , equation 4.6, by the area times the thickness of the segregated layer. The concentration of the segregated layer,  $C_s$ , on the surface is thus given by equation 4.7 [1]

$$C_s = \frac{\left[ 2AC_0 \left( \frac{Dt}{\pi} \right)^{\frac{1}{2}} \right]}{Ad}. \quad (4.7)$$

Since the surface concentration is independent of the flux of segregating atoms, any value can be added to the starting value of  $C_s$ . The bulk concentration,  $C_B$ , was added to  $C_s$  resulting in the final expression for the semi-infinite solution, equation 4.8 [1]

$$C_s = C_B \left[ 1 + \frac{2}{d} \left( \frac{Dt}{\pi} \right)^{\frac{1}{2}} \right]. \quad (4.8)$$

An equation describing surface segregation where the temperature was increased linearly (linear programmed heating) can be derived starting from equation 4.8. An enrichment factor,  $\beta$ , independent of the bulk concentration is given by equation 4.9 [2]

$$\beta = \frac{C_s - C_B}{C_B} = \left[ \frac{2}{d} \left( \frac{Dt}{\pi} \right)^{\frac{1}{2}} \right]. \quad (4.9)$$

The rate at which  $\beta$  is going to change is given by equation 4.10

$$\frac{d\beta}{dt} = \left[ \frac{1}{d} \left( \frac{D}{\pi} \right)^{\frac{1}{2}} \left( \frac{1}{t_B} \right)^{\frac{1}{2}} \right] \quad (4.10)$$

where the increase in  $\beta$  is given as a function of  $t_B$  and not  $t$ , since the temperature was linearly increased resulting in a varying diffusion coefficient. The term  $t_B$  describes the amount of time required by the diffusion coefficient,  $D$ , to obtain the concentration profile for a linear temperature run given in terms of the number of atoms which have segregated to the surface. From equation 4.9 the term  $t_B$  is given by equation 4.11

$$t_B = \left( \frac{\beta d}{2} \right)^2 \left( \frac{\pi}{D} \right). \quad (4.11)$$

To obtain a analytical solution of  $\beta$ , equation 4.11 is substituted into equation 4.10 to obtain equation 4.12

$$\partial\beta = \frac{1}{d} \left( \frac{D}{\pi} \right)^{\frac{1}{2}} \partial t \left( \frac{2}{\beta d} \right) \left( \frac{D}{\pi} \right)^{\frac{1}{2}}. \quad (4.12)$$

The temperature,  $T$ , is given by equation 4.13

$$T = T_0 + \alpha t \quad (4.13)$$

where  $\alpha$  is the rate at which the temperature was increased. The well known Arrhenius equation [3], equation 4.14, gives the rate of a diffusion process at a specified temperature

$$D = D_0 \exp\left(\frac{-Q}{RT}\right) \quad (4.14)$$

where  $D_0$  is the pre-exponential factor given by equation 3.24 in chapter 3,  $Q$  the activation energy and  $R$  the universal gas constant with a value of 8.314 J/K/mol. Using equation 4.13 and substituting the Arrhenius equation, equation 4.14, into equation 4.12 results in the integral expression, equation 4.15 [2; 4]

$$\frac{1}{2}\beta^2 = \frac{2}{\pi} \left(\frac{D_0}{\alpha d^2}\right) \int_{T_0}^{T_{\text{final}}} \exp\left(\frac{-Q}{RT}\right) dT. \quad (4.15)$$

The following approximation can be made to the integral in equation 4.15

$$\int_{T_0}^{T_{\text{final}}} \exp\left(\frac{-Q}{RT}\right) dT = \left[ \frac{RT^2}{Q} \exp\left(\frac{-Q}{RT}\right) \right] \quad (4.16)$$

resulting in equation 4.17 [4]

$$\beta^2 = \frac{4}{\pi} \frac{D_0}{\alpha d^2} \left[ \frac{RT^2}{Q} \exp\left(\frac{-Q}{RT}\right) \right]. \quad (4.17)$$

Equation 4.17 was fitted to the experimental data in chapter 8, Experimental results, in order to extract the values for the pre-exponential factor,  $D_0$ , and the activation energy,  $Q$ . Figure 4.1 gives example fits of equation 4.17 for 4 different activation energies with a  $D_0$  value of  $1.0 \times 10^{-4}$  m<sup>2</sup>/s. Figure 4.2 provides example fits of equation 4.17 for a  $Q$  value of 120 kJ/mol (1.24 eV) for a range of  $D_0$  values. The values for the parameters used in the calculations are:  $d=3.68 \times 10^{-10}$  m,  $C_B=6 \times 10^{-6}$  fractional concentration and  $\alpha=0.01$  K/s.

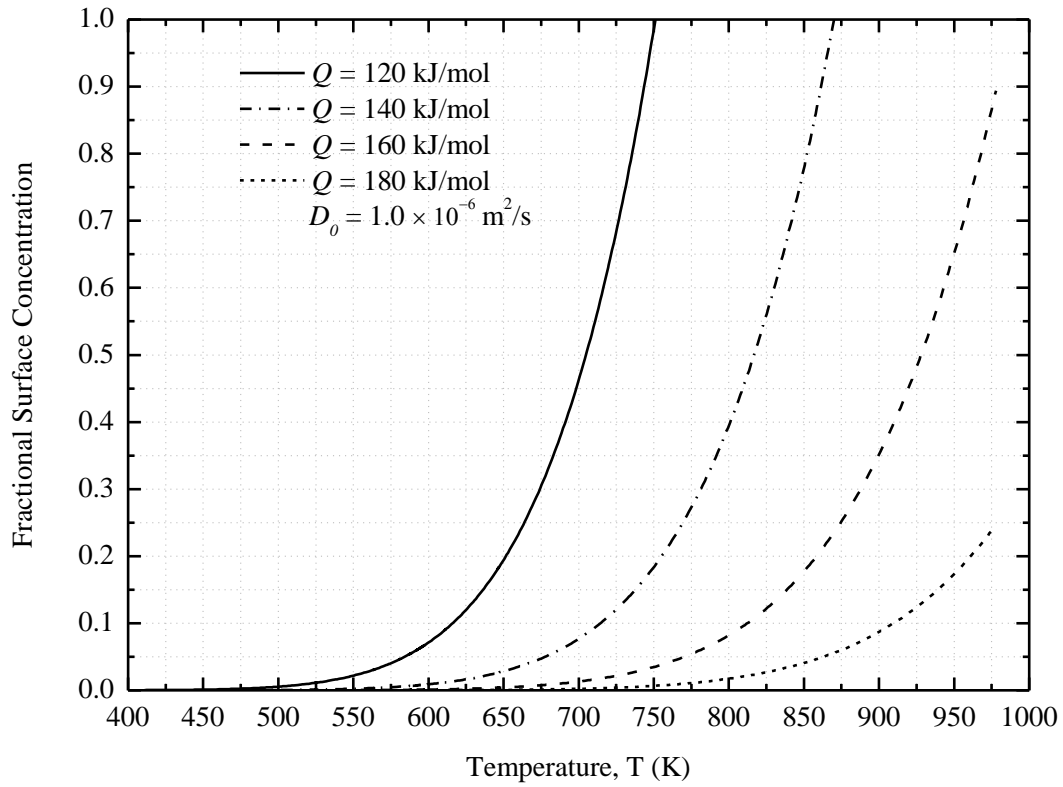


**Figure 4.1:** Example fits of Fick's linear programmed heating model for four different activation energy values and a  $D_0$  value of  $1.0 \times 10^{-6} \text{ m}^2/\text{s}$ .

Figure 4.1 illustrates the influence of the activation energy on the segregation profile. The smaller activation energies results in a faster diffusion process since less energy is required for the diffusion process to occur.

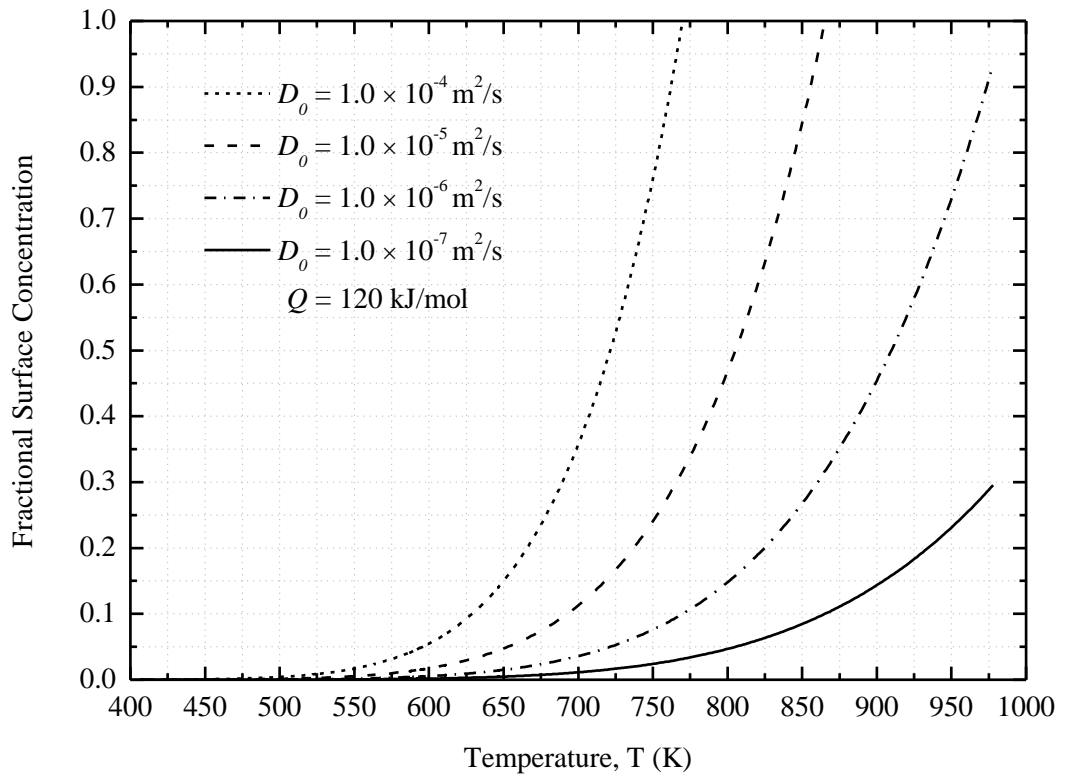


**Figure 4.2:** Example fits of Fick's model for four different pre-exponential values and a activation energy of 120 kJ/mol (1.24 eV).

Figure 4.2 illustrates the influence the pre-exponential value has on the segregation profile. For larger values of  $D_0$  a faster diffusion rate is observed. Thus for a fast diffusion process, a large  $D_0$  and a small  $Q$  value is required.

## 4.3. Equilibrium surface segregation

### 4.3.1. Equilibrium conditions

Equilibrium surface segregation of a closed system consisting of  $p$  phases can be considered as the lowering of the systems total energy, expressed by equation 4.18 [1; 5]

$$(\delta E)_{S,V,n_i} = \sum_{\nu=1}^p \delta E^{\nu} \geq 0 \quad (4.18)$$

The term  $\delta E^{\nu}$  is given by equation 4.19

$$\delta E^{\nu} = T^{\nu} \delta S - P^{\nu} \delta V + \delta G^{\nu} \quad (4.19)$$

where  $T$  is the temperature,  $S$  the entropy,  $V$  the volume and  $P$  the pressure of phase  $\nu$ . If the pressure and temperature is the same for all the phases (constant T and P), equation 4.19 becomes equation 4.20

$$\delta E^{\nu} = \delta G^{\nu} \quad (4.20)$$

This reduces equation 4.18 to

$$(\delta E)_{n_i} = \delta G_{n_i} \geq 0. \quad (4.21)$$

Thus the equilibrium segregation or the minimization of the total energy can be described in terms of the Gibbs free energy at constant  $P$  and  $T$ . Equation 4.22 gives the Gibbs free energy for a  $m$  component system in terms of the chemical potential  $\mu$

$$G = \sum_{\nu=1}^p \sum_{i=1}^m n_i^{\nu} \mu_i^{\nu} \quad (4.22)$$

where  $n_i^{\nu}$  is the number of moles of specie  $i$  in phase  $\nu$ . Using the product rule of differentiation, the variation in the Gibbs free energy is given by equation 4.23

$$\delta G = \sum_{\nu=1}^p \left[ \sum_{i=1}^m \delta n_i^{\nu} \mu_i^{\nu} + \sum_{i=1}^m n_i^{\nu} \delta \mu_i^{\nu} \right]. \quad (4.23)$$

Thus the equilibrium condition of surface segregation in a closed system can be written in terms of the chemical potential given by equation 4.24

$$\sum_{\nu=1}^p \left[ \sum_{i=1}^m \delta n_i^{\nu} \mu_i^{\nu} + \sum_{i=1}^m n_i^{\nu} \delta \mu_i^{\nu} \right] \geq 0. \quad (4.24)$$

### 4.3.2. Surface-bulk equilibrium

For the derivation of the surface bulk equilibrium a closed system of the two phases is considered for which the following assumptions are valid [5].

- The surface is considered as finite in size with a finite number of atoms. i.e.  $n^\phi = \text{constant}$
- The bulk phase is considered infinite in size with an infinite number of atoms. i.e.  $n^B = \infty$
- Atoms can move freely between the bulk and surface phases

For a system of two phases, the bulk ( $B$ ) and surface phase ( $\phi$ ), equation 4.23 becomes equation 4.25

$$\delta G = \left[ \sum_{i=1}^m \delta n_i^\phi \mu_i^\phi + \sum_{i=1}^m \delta n_i^B \mu_i^B \right] + \left[ \sum_{i=1}^m n_i^\phi \delta \mu_i^\phi + \sum_{i=1}^m n_i^B \delta \mu_i^B \right]. \quad (4.25)$$

The second square bracket is the well known Gibbs-Duhem [6] expression which is equal to zero and thus equation 4.25 reduces to equation 4.26

$$\delta G = \left[ \sum_{i=1}^m \delta n_i^\phi \mu_i^\phi + \sum_{i=1}^m \delta n_i^B \mu_i^B \right]. \quad (4.26)$$

From the first assumption above stating that the number of atoms are constant, the following mathematical expression can be formulated

$$\sum_{i=1}^m n_i^\phi = n^\phi. \quad (4.27)$$

The physical meaning of equation 4.27 is that if an atom is removed from the surface another atom will fill its position and thus a constant number of atoms are maintained on the surface. The total change in the number of surface atoms is given by equation 4.28

$$\delta n_1^\phi + \delta n_2^\phi + \cdots + \delta n_m^\phi = 0. \quad (4.28)$$

The  $m^{\text{th}}$  term in equation 4.28 can be expressed in terms of all the other  $m-1$  terms, equation 4.29

$$\delta n_1^\phi + \delta n_2^\phi + \cdots + \delta n_{m-1}^\phi = -\delta n_m^\phi. \quad (4.29)$$

Substituting equation 4.29 into equation 4.26 and performing some mathematical manipulations delivers equation 4.30

$$\left[ \sum_{i=1}^{m-1} (\mu_i^\phi - \mu_i^B - \mu_m^\phi + \mu_m^B) \delta n_i^\phi \right] \geq 0. \quad (4.30)$$

Since  $m-1$  terms are independent of  $\delta n_i^\phi$ , equation 4.30 can only be a valid mathematical statement if the inside bracket is equal to zero as expressed in equation 4.31 [1]

$$(\mu_i^\phi - \mu_i^B - \mu_m^\phi + \mu_m^B) = 0. \quad (4.31)$$

Equation 4.31 is the requirement for the surface bulk equilibrium expressed in terms of the chemical potential.

### 4.3.3. Equilibrium model for a ternary system

From equation 4.31, the equilibrium conditions for a 3 component system is given by equations 4.32 and 4.33

$$\mu_1^\phi - \mu_1^B - \mu_3^\phi + \mu_3^B = 0 \quad (4.32)$$

$$\mu_2^\phi - \mu_2^B - \mu_3^\phi + \mu_3^B = 0. \quad (4.33)$$

The solution of these expressions using the regular solution model are given in terms of the surface concentrations of components 1 and 2 by equation 4.34 and 4.35 respectively, a complete derivation can be found in the work of McMahan [7]

$$X_1^\phi = \frac{X_1^B \exp\left(\frac{\Delta G_1}{RT}\right)}{1 - X_1^B + X_1^B \exp\left(\frac{\Delta G_1}{RT}\right) - X_2^B + X_2^B \exp\left(\frac{\Delta G_2}{RT}\right)} \quad (4.34)$$

$$X_2^\phi = \frac{X_2^B \exp\left(\frac{\Delta G_2}{RT}\right)}{1 - X_2^B + X_2^B \exp\left(\frac{\Delta G_2}{RT}\right) - X_1^B + X_1^B \exp\left(\frac{\Delta G_1}{RT}\right)} \quad (4.35)$$

where  $\Delta G_1$  and  $\Delta G_2$  is respectively given by equation 4.36 and 4.37

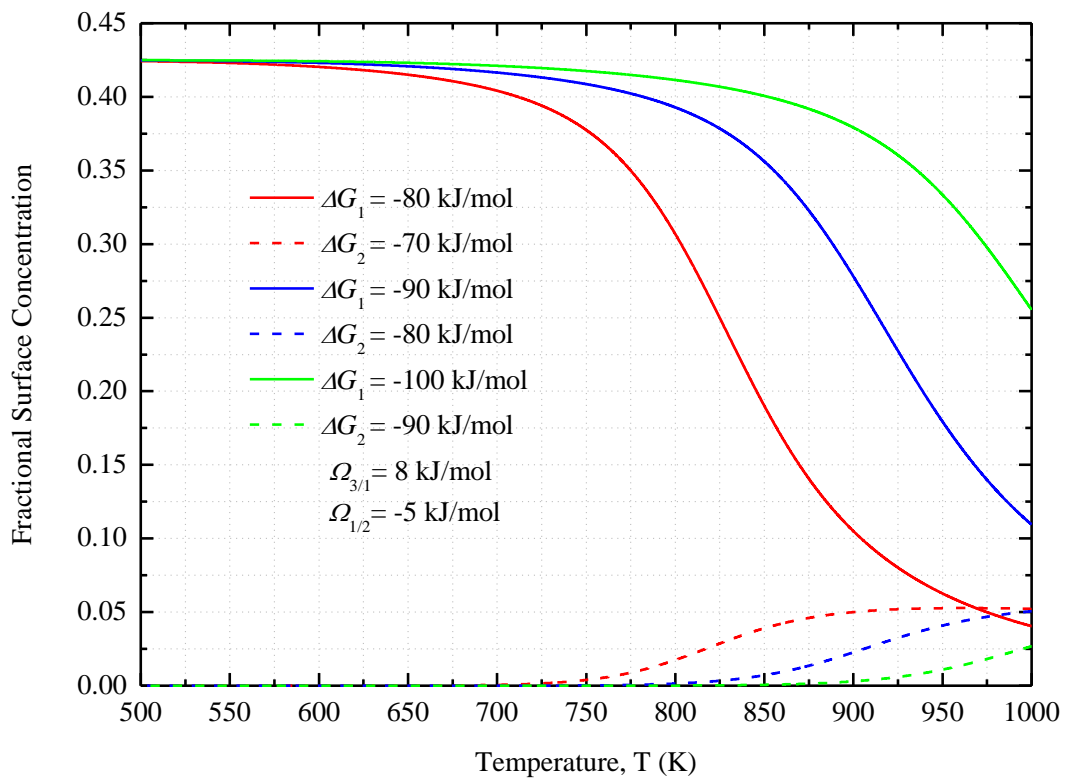
$$\Delta G_1 = \Delta G_1^\circ + 2\Omega_{13}(X_1^\phi - X_1^B) + \Omega'(X_2^B - X_2^\phi) \quad (4.36)$$

$$\Delta G_2 = \Delta G_2^\circ + 2\Omega_{23}(X_2^\phi - X_2^B) + \Omega'(X_1^B - X_1^\phi). \quad (4.37)$$

The terms  $\Delta G_1^\circ$  and  $\Delta G_2^\circ$  are the standard segregation energies of components 1 and 2 and the term  $\Omega_{ij}$  is the interaction energy for the respective components. The term  $\Omega'$  is given by equation 4.38

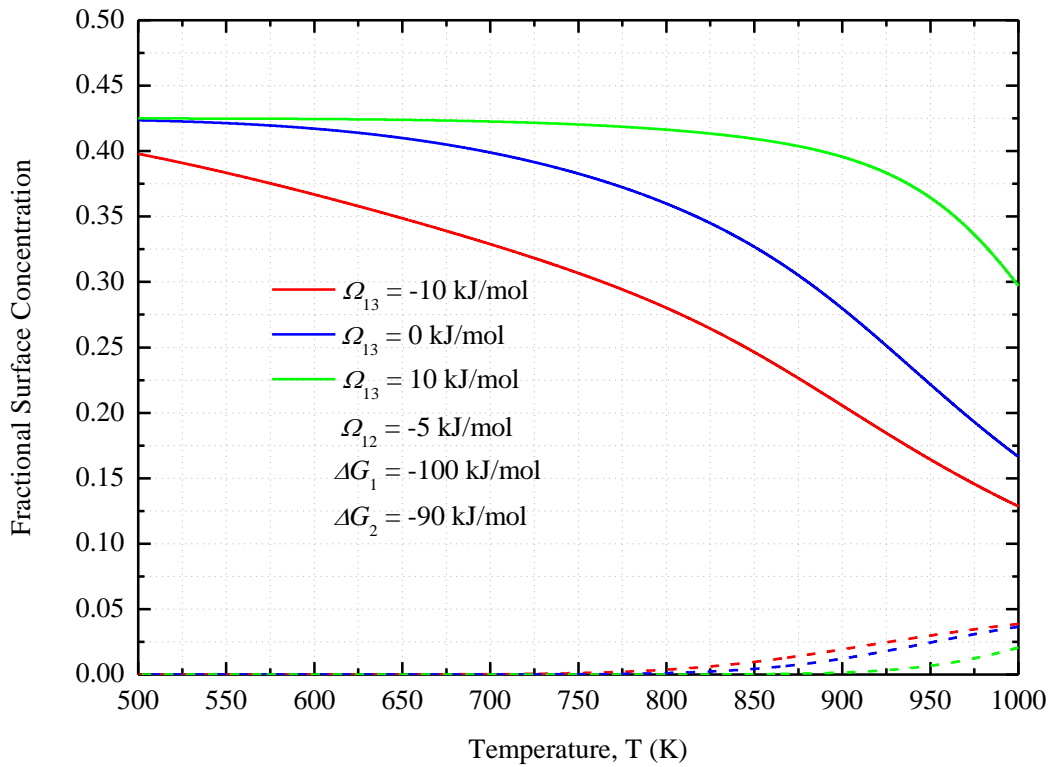
$$\Omega' = \Omega_{12} - \Omega_{13} - \Omega_{23}. \quad (4.38)$$

Figure 4.3 shows the fitting of the Guttman model for a range of segregation energies maintaining a difference of 10 kJ/mol (0.1 eV) between the segregation energies of components 1 and 2. The interaction parameter between components 1 and 3 was chosen as 8 kJ/mol (0.08 eV) and between components 1 and 2 an interaction parameter of -5 kJ/mol (-0.05 eV) was chosen. For component 2 and 3 a zero interaction parameter was chosen.



**Figure 4.3:** Fit of the Guttman equilibrium segregation model for different segregation energies with the interaction parameter kept constant.

Figure 4.4 gives the interaction parameters -10, 0 and 10 kJ/mol (0.1 eV) for components 1 and 3 with a constant interaction of -5 kJ/mol (-0.05 eV) for components 1 and 2. Constant segregation energies of 100 kJ/mol (1.04 eV) and -90 kJ/mol (-0.9 eV) for component 1 and 2 respectively were used in figure 4.4.



**Figure 4.4:** Fit of the Guttman equilibrium segregation model for different interaction parameters between the segregant and matrix atoms while the segregation energies were kept constant.

From figures 4.3 and 4.4 it can be concluded that for smaller segregation energies and interaction parameters, the segregated atoms will desegregate into the bulk material at higher temperatures.

## 4.4. Summary

In this chapter the derivation of two models which can be used in combination to describe both the kinetic and equilibrium regions of surface segregation were performed. The linear programmed temperature version of the semi-infinite solution describes a theoretical model by which the pre-exponential factor,  $D_0$ , and the activation energy,  $Q$ , can be obtained simultaneously. From the conditions of surface bulk equilibrium, the Guttmann model can be derived which can be used to extract the energies of segregation and the interaction parameters for a ternary system. These two models were fitted on all experimental data presented in chapter 8, Experimental results, in order to obtain the segregation parameters of S and P in bcc polycrystalline Fe.

## 4.5. References

- [1]. J. du Plessis, Surface segregation, Sci-Tech publications, Bloemfontein, 1990.
- [2]. E.C. Viljoen, Lineêre verhittingstudie van oppervlaksegregasie on binêre allooie, Dissertation, Bloemfontein, 1995.
- [3]. D.R. Askeland, The science and engineering of materials, Stanley thornes, Cheltenham, 1998.
- [4]. W.J. Erasmus, Die segregasie van Sb na die lae indeksoppervlakke van Cu enkelkristalle, Dissertation, Bloemfontein, 1999.
- [5]. J.J. Terblans, Modelling en eksperimentele ondersoek van Sb-oppervlak segregasie in Cu-enkelkristalle, Dissertation, Bloemfontein, 2001.
- [6]. C.H.P. Lupis, Chemical thermodynamics of materials, Elsevier Science Publishing Co., Inc., New York, 1983.
- [7]. C.J.J. McMahon, L. Marchut, J. Vac. Sci. Technol. 15 (1978) 450.



# Chapter 5: Density functional theory (DFT) fundamentals.

## 5.1. Introduction

Electronic structure calculations has undergone a great deal of development since the first quantitative calculations of H. D. Hartree, who formulated the self-consistent field (SCF) theory [1; 2]. Other great contributions in the field are those of Walter Kohn and John A. Pople who received the 1998 Noble Prize in chemistry [3]. Density functional theory (DFT), a more recent method of electronic structure calculations, uses the ground state electron density,  $n(\vec{r})$ , of the system under study to solve the Schrödinger-like Kohn-Sham equation [4] self consistently. This delivers properties such as the forces, energies, stresses etc. DFT is capable of providing accurate information on a range of material properties and has been used with great success to solve problems related to but not limited to catalysis, embrittlement of materials and the study of surface phenomena.

Though the technique has been used with great success, it does have some drawbacks which needs to be taken into consideration. The biggest disadvantage of DFT compared to classical computational techniques, such as molecular dynamics and Monte Carlo, is the computational time that is needed by DFT calculations. Typically smaller systems is studied by DFT as compared to classical computational techniques. The extra time required by DFT calculations comes with an increased accuracy for some values as compared to classical computational techniques. Also it should be noted that DFT solves a Schrödinger-like equation to obtain the ground state electron density from which energies, forces etc. can be computed. It does not solve the Schrödinger equation itself which would provide the exact ground state of the system [1; 5]. This causes some uncertainty in the values being calculated and requires that calculations be confirmed by experimental results [5]. Another problem experienced is the calculation of excited states for which techniques like time dependant density functional theory (TD-DFT) has been developed [1; 5; 6]. Despite the drawbacks mentioned above, DFT is capable of providing accurate results of physical properties in complex materials [5].

This chapter aims to present the basic concepts of DFT in order to provide a good understanding of the technique and its implementation in practical calculations. The chapter does not attempt to give full mathematical explanations of DFT, but rather to provide a practical insight into the theoretical concepts of DFT. The explanation is based on the plane wave pseudopotential method (PWPP) as implemented in the Quantum ESPRESSO code [7]. Some of the most important theoretical concepts that will be discussed are: the use of plane waves and the k-point grid, the Hohenberg-Kohn theorems which forms the foundation of DFT. The Schrödinger-like Kohn-Sham equation that simplified the many body problem into a system of independent particles. The use of the Nudged Elastic Band (NEB) and the Climbing Image Nudged Elastic Band (CI-NEB) methods for the calculation of minimum energy paths which describes the diffusion of atoms.

## 5.2. Bloch theorem

The Bloch theorem is discussed here to illustrate the concept of plane waves, lattice periodicity and the use of Fourier expansions, all of which are important in practical DFT calculations. For the derivation of the Bloch theorem the assumption is made that all the cells in the crystal are identical and thus the crystal is periodic. The wavefunction,  $\psi$ , from one cell to the next will only differ by a phase factor  $pa$ , where  $a$  is the lattice parameter of the cell and  $p$  is a constant. This periodicity of the crystal structure is expressed mathematically by equation 5.1

$$\psi_{\bar{k}}(x + pa) = \psi_{\bar{k}}(x) e^{i\bar{k}pa}. \quad (5.1)$$

The subscript  $\bar{k}$  refers to the wave vector associated with a specific wavefunction. Equation 5.1 is Bloch's theorem for a one dimensional case, for a three dimensional case equation 5.1 becomes equation 5.2 [1; 8]

$$\psi_{\bar{k}}(\bar{r} + \bar{R}) = \psi_{\bar{k}}(\bar{r}) e^{i\bar{k} \cdot \bar{R}} \quad (5.2)$$

where,  $\bar{R}$ , is a lattice translation vector. Multiplying equation 5.2 on both sides by  $e^{-i\bar{k}\cdot\bar{r}}$  and rearranging the terms results in equation 5.3

$$\psi_{\bar{k}}(\bar{r}) = \left[ \psi_{\bar{k}}(\bar{r} + \bar{R}) e^{-i\bar{k}\cdot(\bar{r} + \bar{R})} \right] e^{i\bar{k}\cdot\bar{r}} \quad (5.3)$$

Equation 5.3 illustrates the periodicity of the Bloch function,  $\psi_{\bar{k}}(\bar{r})$ , and since the cell function,  $u_{\bar{k}}(\bar{r})$ , is also a periodic function [1; 8] .i.e.

$$u_{\bar{k}}(\bar{r} + \bar{R}) = u_{\bar{k}}(\bar{r}) . \quad (5.4)$$

Bloch's wavefunction can also be written in the form given by equation 5.5 [1; 5; 8]

$$\psi_{\bar{k}}(\bar{r}) = \frac{1}{\sqrt{\Omega}} u_{\bar{k}}(\bar{r}) e^{i\bar{k}\cdot\bar{r}} \quad (5.5)$$

where  $u_{\bar{k}}(\bar{r})$  has the same periodicity as the lattice. The factor  $\frac{1}{\sqrt{\Omega}}$  is introduced to ensure normalization of the wavefunction, where  $\Omega$  is the volume of the crystal. Since  $u_{\bar{k}}(\bar{r})$  is periodic it can be represented by a Fourier sum as expressed in equation 5.6 [5; 8]

$$u_{\bar{k}}(\bar{r}) = \sum_{\bar{G}} C_{\bar{k}}(\bar{G}) e^{i\bar{G}\cdot\bar{r}} \quad (5.6)$$

where  $\bar{G}$  is a reciprocal lattice vector. Substituting equation 5.6 into equation 5.5 leads to equation 5.7 [5; 8]

$$\psi_{\bar{k}}(\bar{r}) = \frac{1}{\sqrt{\Omega}} \sum_{\bar{G}} C_{\bar{k}}(\bar{k} + \bar{G}) e^{i(\bar{k} + \bar{G})\bar{r}} \quad (5.7)$$

which is equivalent to equation 5.5. Equation 5.7 is an expansion of plane waves of the form  $e^{i(\bar{k} + \bar{G})\bar{r}}$ , with expansion coefficients  $C_{\bar{k}}(\bar{k} + \bar{G})$ . These  $\bar{k} + \bar{G}$  vectors of the plane waves can be visualized in k-space as illustrated in figure 5.1 by the vector in red.

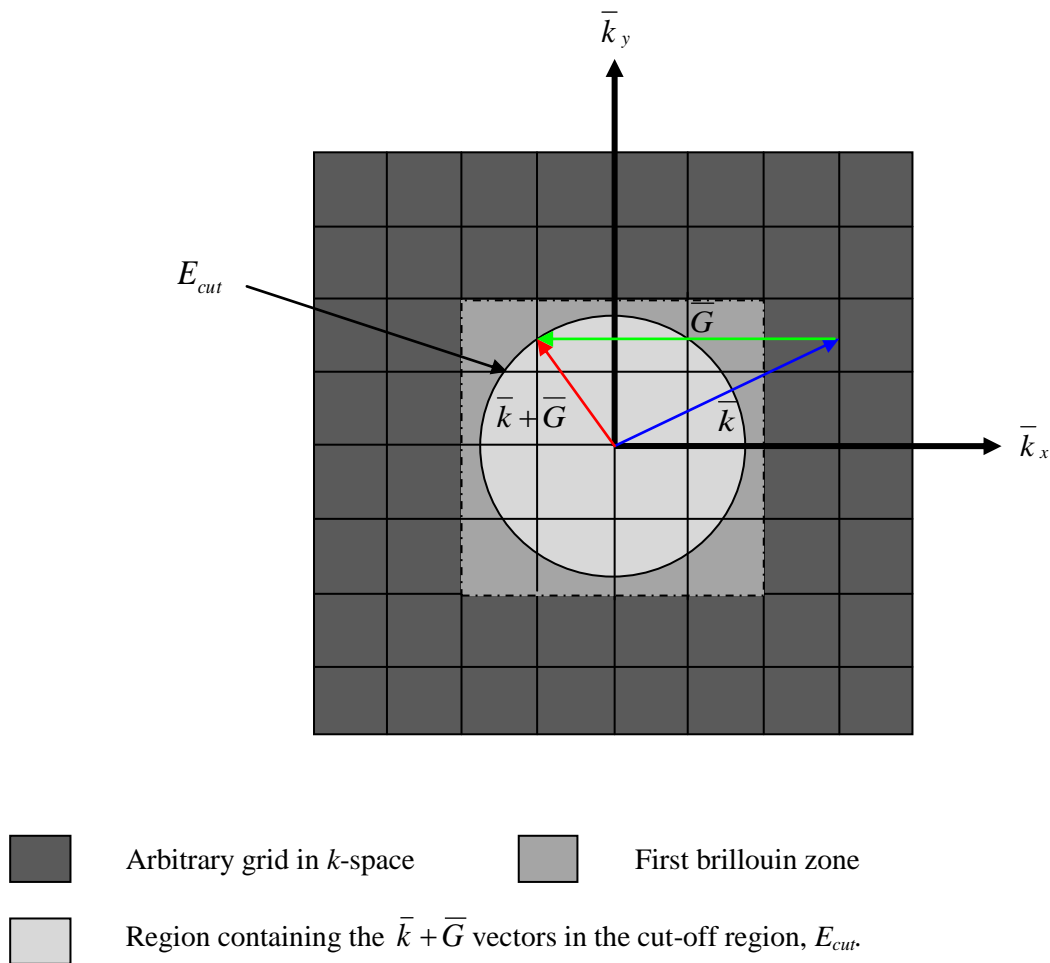


**Figure 5.1:** Grid in  $k$ -space for the plane waves,  $\psi_{\bar{k}}(\bar{r})$ , illustrating the  $\bar{k} + \bar{G}$  wave vectors of the plane waves. The circle contains all the  $\bar{k} + \bar{G}$  vectors in the cut-off region,  $E_{cut}$ .

In practical DFT calculations plane waves, similar in form to equation 5.7, are used to simulate the atomic wavefunctions in a material. Equation 5.7 allows for the use of Fast Fourier Transforms

(FFT) to solve the Kohn-Sham equation, which shortens computational time significantly. The solution of the Kohn-Sham equation is discussed in section 5.5.3. In practice contributions of the higher Fourier components can often be neglected depending on the amount of fine structure and oscillations in the wave function and thus a certain cut-off value,  $E_{cut}$  can be chosen as indicated by the circle in figure 5.1. The cut-off value is traditionally expressed in units of energy, Rydberg (Ry), and is obtained by performing a convergence test [1; 5]. Thus the  $E_{cut}$  region in k-space has to be large enough to include as many plane waves as possible but not too large where insignificant terms are included. Also the volume cannot be too small since this will exclude important information of the plane waves. For an example on how to choose the number of plane waves,  $E_{cut}$ , by means of a convergence test see Appendix B.

### 5.3. Brillouin zone sampling

Brillouin zone summation is used in the calculation of the electron density,  $n(\vec{r})$ , which is used to obtain the total energy of the system under study. The charge density is calculated by equation 5.8 [9]

$$n(\vec{r}) = \sum_k \sum_{i=1}^N |\psi_{\vec{k},i}^-(\vec{r})| \quad (5.8)$$

where  $i$  refers to the occupied state (band) and  $k$  refers to the wave vector. The function  $\psi_{\vec{k},i}^-(\vec{r})$  is given by equation 5.7. Using the Born von Karman boundary condition, the function  $\psi_{\vec{k},i}^-(\vec{r})$  can be written as

$$\psi_{\vec{k},i}^-(\vec{r}) = \psi_{\vec{k},i}^-(\vec{r} + L_1\vec{m}_1) = \psi_{\vec{k},i}^-(\vec{r} + L_2\vec{m}_2) = \psi_{\vec{k},i}^-(\vec{r} + L_3\vec{m}_3) \quad (5.9)$$

where  $\vec{m}$  is a vector given the distance between two k-points and  $L$  is the number of k-points in the length of the unit cell. Thus the total number of allowed k-points for the three dimensional structure is given by equation 5.10 [9]

$$L = L_1 L_2 L_3 \quad (5.10)$$

Instead of performing a sum over an infinite number of k-points, a few “special points” is chosen for brillouin zone summation. Two commonly used schemes for brillouin zone summation are the Chadi-Cohen [10] and the Monkhorst-Pack [11] schemes. The Monkhorst-Pack scheme is the more popular one of the two and is the scheme used in all calculations presented in this thesis. Monkhorst-Pack brillouin zone summation makes use of an evenly spaced grid in k-space of the first brillouin zone as illustrated in figure 5.2.

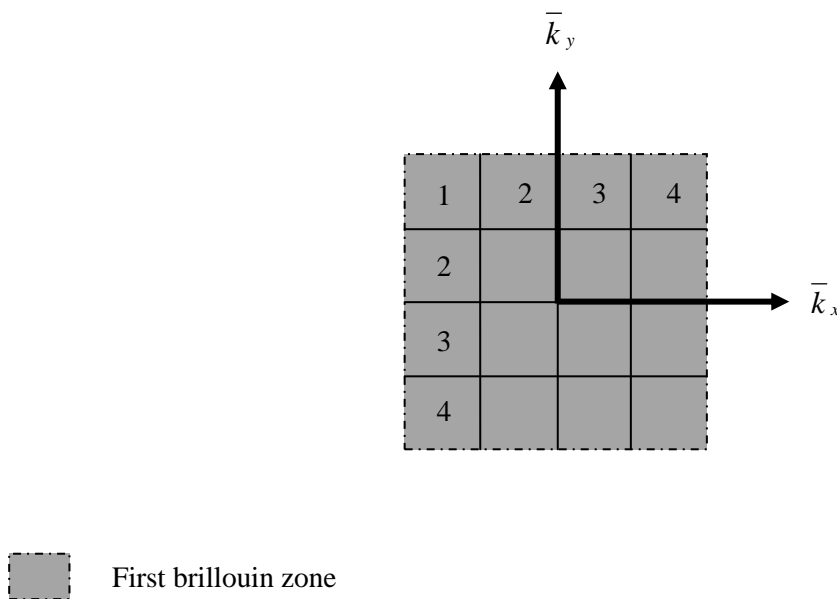


**Figure 5.2:** Two dimensional 4x4 Monkhorst-Pack k-point grid in the first Brillouin zone.

The grid can also be shifted in order to break symmetry and allow for faster convergence of the k-points. Shifting the grid by 1x1 will cause a displacement of half a k-point in each direction and thus breaking the symmetry. More k-points results in a more dense mesh which requires more Fourier components. It is thus desirable to obtain the minimum values of  $L_1$ ,  $L_2$  and  $L_3$ , where  $L$

now represents the Monkhorst pack k-points, which provides the ground state energy of the system under study by means of a convergence test.

The explanation on plane waves in section 5.2 and the above explanation on k-points is vital to any DFT calculation in order to optimize the system. The discussion is done in this chapter to emphasize the importance of these two parameters and also to aid in the understanding of topics that will be discussed later in this chapter. These two parameters are not the only optimization parameters that needs to be considered. The equilibrium lattice parameter, bulk modulus and size of the crystal cell are also important. If a metallic system is studied, optimization of the smearing scheme, the smearing width or the degauss factor and the magnetic state (starting magnetization) also needs to be optimized. Apart from metallic smearing which is discussed in section 5.4.4, the other parameters are not discussed in this thesis. In Appendix B examples of how to optimize a system with respect to each of these parameters are given.

## 5.4. Hohenberg-Kohn theorems

Hohenberg and Kohn formulated two theorems which form the foundation of density functional theory [1]. The theorems state that any property of a many body system can be represented as a functional of the ground state electron density  $n(\vec{r})$ . Thus in principle a function of position,  $n(\vec{r})$ , determines all the information of the many body wavefunction for the ground state and all excited states. The two theorems are valid for any system of interacting particles in an external potential where the Hamiltonian is given by equation 5.11 [1]

$$\hat{H}_i = -\frac{\hbar^2}{2m_e} \sum_i \nabla_i^2 - \sum_{i,I} \frac{Z_I e^2}{|\vec{r}_i - \vec{R}_I|} + \frac{1}{2} \sum_{i \neq j} \frac{e^2}{|\vec{r}_i - \vec{r}_j|} - \sum_I \frac{\hbar^2}{2M_I} \nabla_I^2 + \frac{1}{2} \sum_{I \neq J} \frac{Z_I Z_J e^2}{|\vec{R}_I - \vec{R}_J|}. \quad (5.11)$$

where,  $\frac{\hbar^2}{2m_e} \sum_i \nabla_i^2$  is the kinetic energy of the electrons, the second term,  $\sum_{i,I} \frac{Z_I e^2}{|\vec{r}_i - \vec{R}_I|}$ , is the potential acting on the electrons due to the nuclei, the electron-electron interaction is given by

$\frac{1}{2} \sum_{i \neq j} \frac{e^2}{|\bar{r}_i - \bar{r}_j|}$ . Using the Born-Oppenheimer approximation, which states that the mass of the ions

are large compared to the mass of the electrons and thus  $\frac{1}{M_I}$  is a negligible quantity leading to a

zero value for the fourth term. The final term,  $\frac{1}{2} \sum_{I \neq J} \frac{Z_I Z_J e^2}{|\bar{R}_I - \bar{R}_J|}$ , is the classical nuclei-nuclei

interaction term. Only a brief discussion of the two theorems will be given in this chapter, for a full derivation refer to appendix A.

**Theorem 1:** For any system of interacting particles in an external potential,  $V_{ext}(\bar{r})$ , the potential  $V_{ext}(\bar{r})$ , is determined uniquely, except for a constant, by the ground state electron density  $n(\bar{r})$ .

**Corollary 1:** Since the Hamiltonian is thus fully determined, except for a constant shift in the energy, it follows that the many body wavefunction for all states (ground and excited) are determined. Therefore all properties of the system are completely determined given only the ground state electron density  $n(\bar{r})$ .

**Theorem 2:** A universal functional,  $F(E[n])$  in terms of the energy,  $E(n)$ , in terms of the electron density can be defined, valid for any external potential  $V_{ext}(\bar{r})$ . For any particular external potential,  $V_{ext}(\bar{r})$ , the exact ground state energy of the system is the global minimum value of this functional,  $F(E[n])$ , and the electron density  $n(\bar{r})$  that minimizes the functional is the exact ground state electron density  $n(\bar{r})$ .

**Corollary 2:** The functional  $F(E[n])$  alone is sufficient to determine the exact ground state energy and electron density. In general, excited states of the electron must be determined by other means. Thermal equilibrium properties such as specific heat are determined directly by the free-energy functional of the electron density

[1; 6; 9].

## 5.5. The self-consistent loop for solving the Kohn-Sham equation.

The Kohn-Sham equation is similar to the Schrödinger equation that is solved self-consistently for an effective potential,  $V_{eff}^{\sigma}(\vec{r})$ , in order to obtain properties such as the total energy, force, stress etc. This section presents the self-consistent loop by which the Kohn-Sham equation is solved. Figure 5.3 [1] gives the self-consistent loop used in order to solve the Kohn-Sham equation, see also the accompanying paragraph and the table of symbols, table 5.1. In subsection 5.5.1, calculation of the electron density is briefly discussed. Subsection 5.5.2 deals with the effective potential and the derivation of the Kohn-Sham equation. The solution of the Kohn-Sham equation for plane waves is discussed in subsection 5.5.3 and in subsection 5.5.4 metallic smearing is discussed.

**Table 5.1:** Symbols used in the Kohn-Sham loop of figure 5.3

$n^{\uparrow\downarrow}(\vec{r})$	Electron density with spin up ( $\uparrow$ ) and spin down ( $\downarrow$ ) electrons.
$V_{eff}^{\sigma}(\vec{r})$	Effective potential of the Kohn-Sham equation, where $\sigma$ refers to the spin of the electrons.
$V_{ext}(\vec{r})$	External potential of electron-ion interactions.
$V_{Hartree}[n]$	Hartree potential, that includes the electron-electron interactions.
$V_{xc}^{\sigma}[n^{\uparrow}, n^{\downarrow}]$	Exchange-correlation potential. Deals with the exchange and correlation effects of electrons in the system.
$f_i$	Smearing scheme for metallic systems (Methfessel-Paxton, Fermi etc.) see Appendix B for examples of different schemes.

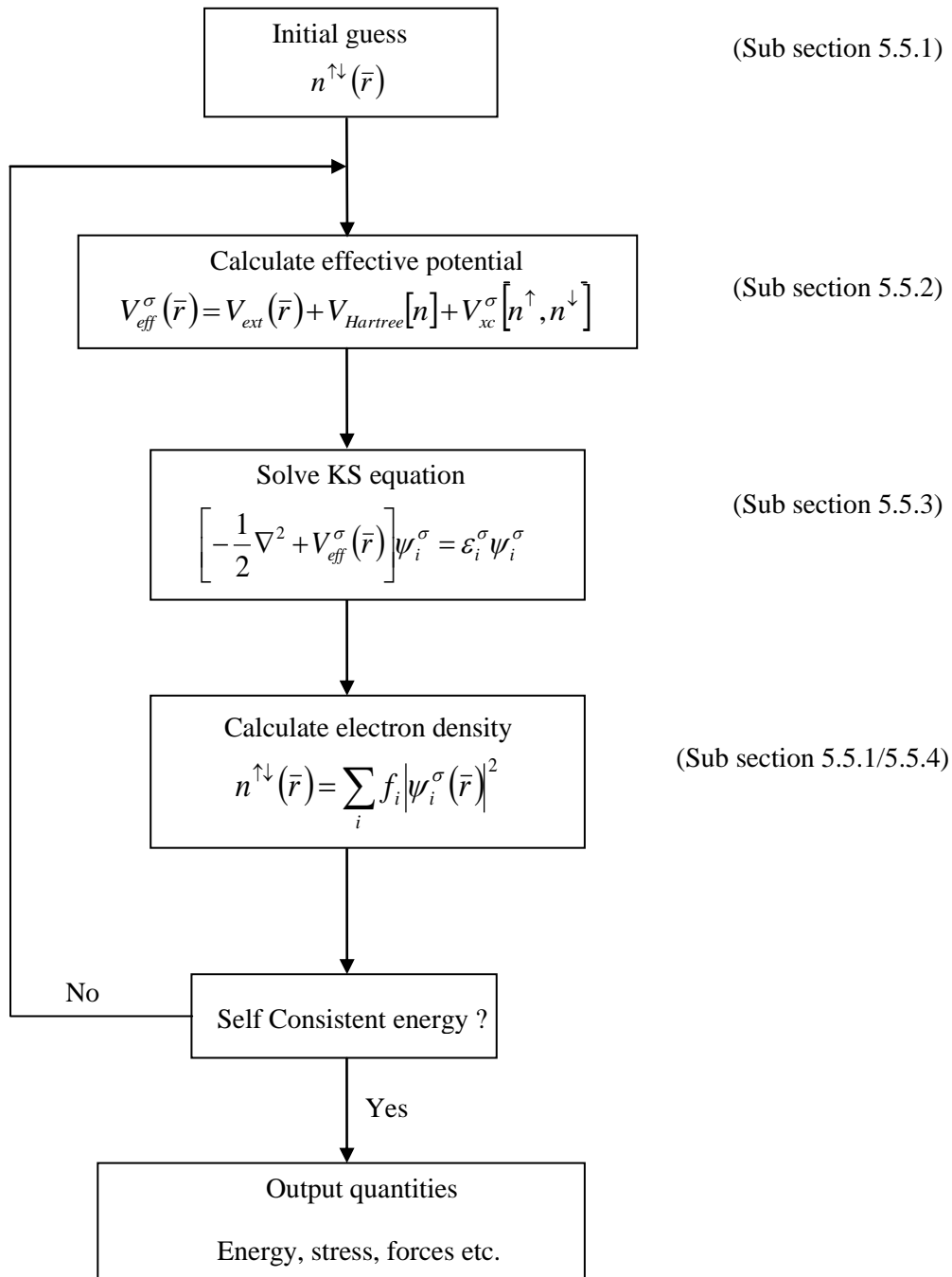


**Figure 5.3:** Schematic of the self-consistent Kohn-Sham loop used in Density Functional Theory to calculate the properties of materials.

An Initial guess is made for the electron density of spin up and spin down electrons. The effective potential, consisting of the external potential, the Hartree potential and the exchange-correlation potential is then calculated from the electron density. Both the Hartree potential and the exchange-correlation potential are functionals of the electron density. The effective potential is then used to solve the Kohn-Sham equation in order to obtain the total energy of the system. Using a mixing scheme, a new electron density and thus effective potential is calculated from the total energy and the loop is repeated. When the energy converges to the specified convergence criteria, the system is said to be self-consistent.

### 5.5.1. Mixing schemes to obtain the electron density

An initial guess is made for an input value of the electron density. This value is then used to calculate the total energy of the system. If the total energy is not within a certain criteria for convergence the electron density is updated and the process is repeated until convergence is achieved. Various schemes exist for updating the electron density. The simplest is linear mixing which forms a linear combination of the input electron density,  $n_i^{in}$ , and the output electron density,  $n_i^{out}$ , to calculate a new input value,  $n_{i+1}^{in}$ . Mathematically the linear mixing scheme is given by equation 5.12 [1]

$$n_{i+1}^{in} = n_i^{out} + (1 - \alpha n_i^{in}) \quad (5.12)$$

where  $\alpha$  is the fractional component of the previous electron density,  $n_i^{out}$ , that is used to calculate the new electron density,  $n_{i+1}^{in}$ . This scheme is effective and robust, but is more time consuming as compared to numerical methods [1]. Another mixing scheme is the numerical, Broyden scheme given by equation 5.13 [1]

$$n_{i+1}^{in} = n_i^{out} - J^{-1}(n_i^{out} - n_i^{in}). \quad (5.13)$$

With each iteration the Jacobian,  $J$ , is improved, making this mixing scheme less time consuming compared to the linear scheme. The linear scheme offers the advantage that little information on the system is needed to compute a new electron density [1]. For a more complete explanation of mixing schemes refer to the book, *Electronic structure - Basic theory and applications* [1].

## 5.5.2. The Kohn-Sham equation and the effective potential

The difficult many body problem for a system of particles was simplified by Kohn and Sham by treating the system as independent particles. To account for the exchange and correlation effects of the many body system they included the exchange-correlation potential [4]. This section explains how the many body problem was simplified by Kohn and Sham by deriving the Kohn-Sham equation and obtaining an expression for the effective potential,  $V_{eff}^{\sigma}(\vec{r})$ .

The many body problem has a Hamiltonian of the form given by equation 5.14 [1]

$$\hat{H} = \hat{T} + \hat{V}_{int} + \hat{V}_{ext} + E_{II} \quad (5.14)$$

where,  $\hat{T}$  is the kinetic energy operator,  $\hat{V}_{int}$  is the internal potential operator,  $\hat{V}_{ext}$  is the external potential operator and  $E_{II}$  is the ion-ion interaction energy term. For the system of independent particles the Hamiltonian is given by equation 5.15, where the subscript KS refers to the Kohn-Sham Hamiltonian [1]

$$\hat{H}_{KS}^{\sigma} = \hat{V}_{Hartree}(\vec{r}) + \hat{V}_{ext}(\vec{r}) + \hat{V}_{XC}(\vec{r}). \quad (5.15)$$

The term  $\hat{V}_{xc}(\bar{r})$  contains all the interactions of the many body system,  $\hat{V}_{ext}(\bar{r})$  is as defined in table 5.1 and  $\hat{V}_{Hartree}(\bar{r})$  is given by equation 5.16 [1]

$$\hat{V}_{Hartree} = \frac{\partial E_{Hartree}}{\partial n(\bar{r}, \sigma)} = \frac{\partial}{\partial n(\bar{r}, \sigma)} \left[ \frac{1}{2} \int \frac{n(\bar{r})n(\bar{r}')}{|\bar{r} - \bar{r}'|} \right] \quad (5.16)$$

which is the interaction energy of the electrons. Two important assumptions were made to derive equation 5.15. The first assumption is that the exact ground state electron density can be represented by the ground state electron density of a system of non-interacting particles. The second assumption is that a Hamiltonian having the usual kinetic energy operator and a effective potential to account for the many body effects can be used. For a complete understanding of equation 5.15, the derivation thereof is done below. According to the second assumption made above, the Hamiltonian is given by equation 5.17 [1; 6; 9], where Hartree atomic units were used ( $\hbar = m_e = e = 4\pi\epsilon_0$ )

$$\hat{H} = -\frac{1}{2}\nabla^2 + \hat{V}_{eff}^{\sigma}(\bar{r}). \quad (5.17)$$

For a system of  $N$  electrons having spin up and spin down states, there will be an electron in each orbital,  $\psi_i^{\sigma}(\bar{r})$ , of the ground state with the lowest eigenvalue of  $\epsilon_i^{\sigma}$ . The electron density for the system of independent particles is given by equation 5.18 [1; 6; 9]

$$n(\bar{r}) = \sum_{\sigma} n(\bar{r}, \sigma) = \sum_{\sigma} \sum_{i=1}^N \left| \psi_i^{\sigma}(\bar{r}) \right|^2. \quad (5.18)$$

The kinetic energy for the independent particles is given by equation 5.19 [1; 6; 9]

$$T_s = -\frac{1}{2} \sum_{\sigma} \sum_{i=1}^N \langle \psi_i^{\sigma}(\vec{r}) | \nabla^2 | \psi_i^{\sigma}(\vec{r}) \rangle = -\frac{1}{2} \sum_{\sigma} \sum_{i=1}^N \int |\nabla \psi_i^{\sigma}(\vec{r})|^2 d^3 r. \quad (5.19)$$

Using the Hohenberg-Kohn expression, given by equation 5.20, which described the energy as a functional of the electron density

$$E_{HK}[n] = T[n] + E_{in}[n] + \int V_{ext}(\vec{r}) n(\vec{r}) d^3 r + E_{II}. \quad (5.20)$$

The Kohn-Sham energy can be written as a functional of the electron density with the inclusion of the exchange-correlation energy to take into account the many body effects.

$$E_{KS}(\vec{r}) = T_s[n] + E_{Hartree}[n] + \int V_{ext}(\vec{r}) n(\vec{r}) d^3 r + E_{II} + E_{XC}[n]. \quad (5.21)$$

The last term in equation 5.21 is given by equation 5.22

$$E_{XC}[n] = F_{HK} - (T_s[n] + E_{Hartree}[n]) = \langle \hat{T} \rangle - T_s[n] + \hat{V}_{int} - E_{Hartree}[n]. \quad (5.22)$$

Minimization of the Kohn-Sham independent particle energy expression, equation 5.22, will result in the Kohn-Sham equation. The minimization can be done with respect to the electron density or the effective potential. The minimization is done here with respect to the density using the chain rule of differentiation with respect to the wavefunction,  $\psi_i^{\sigma*}(\vec{r})$ , which results in equation 5.23 [1; 9]

$$\frac{\partial E_{KS}}{\partial \psi_i^{\sigma*}(\vec{r})} = \frac{\partial T_s}{\partial \psi_i^{\sigma*}(\vec{r})} + \left[ \frac{\partial \int V_{ext}(\vec{r}) n(\vec{r}) d^3 r}{\partial n(\vec{r}, \sigma)} + \frac{\partial E_{Hartree}}{\partial n(\vec{r}, \sigma)} + \frac{\partial E_{II}}{\partial n(\vec{r}, \sigma)} + \frac{\partial E_{xc}}{\partial n(\vec{r}, \sigma)} \right] \frac{\partial n(\vec{r}, \sigma)}{\partial \psi_i^{\sigma*}(\vec{r})} = 0 \quad (5.23)$$

From equation 5.23 the following terms can be calculated individually by equations 5.24-5.27 [1; 9]

$$\frac{\partial E_H}{\partial n(\bar{r}, \sigma)} = 0 \quad (5.24)$$

$$\frac{\partial \int V_{ext}(\bar{r})n(\bar{r})d^3r}{\partial n(\bar{r}, \sigma)} = \int V_{ext}(\bar{r})\frac{\partial n(\bar{r})}{\partial n(\bar{r}, \sigma)}d^3r = \hat{V}_{ext}(\bar{r}) \quad (5.25)$$

$$\frac{\partial T_s}{\partial \psi_i^{\sigma*}(\bar{r})} = -\frac{1}{2}\nabla^2\psi_i^\sigma(\bar{r}) \quad (5.26)$$

$$\frac{\partial n(\bar{r}, \sigma)}{\partial \psi_i^{\sigma*}(\bar{r})} = \psi_i^\sigma(\bar{r}). \quad (5.27)$$

Substitution of equations 5.24 – 5.27 into equation 5.23, results in equation 5.28

$$\frac{\partial E_{KS}}{\partial \psi_i^{\sigma*}(\bar{r})} = -\frac{1}{2}\nabla^2\psi_i^\sigma(\bar{r}) + \left[ V_{ext}(\bar{r}) + \frac{\partial E_{Hartree}}{\partial n(\bar{r}, \sigma)} + \frac{\partial E_{xc}}{\partial n(\bar{r}, \sigma)} \right] \psi_i^\sigma(\bar{r}) = 0. \quad (5.28)$$

Written in terms of the potentials, equation 5.28 becomes [1; 9]

$$\frac{\partial E_{KS}}{\partial \psi_i^{\sigma*}(\bar{r})} = -\frac{1}{2}\nabla^2\psi_i^\sigma(\bar{r}) + \{ V_{ext}(\bar{r}) + V_{Hartree}[n] + V_{xc}[n] \} \psi_i^\sigma(\bar{r}) = 0 \quad (5.29)$$

where the term in curly brackets is the KS or the effective potential, equation 5.29 can be reduced to equation 5.30

$$\frac{\partial E_{KS}}{\partial \psi_i^{\sigma*}(\bar{r})} = \left[ -\frac{1}{2} \nabla^2 + V_{KS}^{\sigma} \right] \psi_i^{\sigma}(\bar{r}) = 0 \quad (5.30)$$

and in terms of the KS Hamiltonian equation 5.30 becomes equation 5.31

$$\frac{\partial E_{KS}}{\partial \psi_i^{\sigma*}(\bar{r})} = H_{KS}^{\sigma} \psi_i^{\sigma}(\bar{r}) = 0. \quad (5.31)$$

Solving equations 5.31, delivers the Kohn-Sham equation, equation 5.32 [1; 4; 6; 9]

$$\left( H_{KS}^{\sigma} - \varepsilon_i^{\sigma} \right) \psi_i^{\sigma}(\bar{r}) = 0 \quad (5.32)$$

### 5.5.3. Solving the Kohn-Sham equation

The Schrödinger-like Kohn-Sham equation for independent particles with electrons moving in an effective potential,  $V_{eff}(\bar{r})$ , is given by equation 5.33 [1]

$$\hat{H}_{eff}(\bar{r}) \psi_i(\bar{r}) = \left[ -\frac{\hbar^2}{2m_e} \nabla^2 + V_{eff}(\bar{r}) \right] \psi_i(\bar{r}) = \varepsilon_i \psi_i(\bar{r}). \quad (5.33)$$

Since the eigenfunction is a periodic function it can be represented as a Fourier expansion given by equation 5.34. A similar expression is given by equation 5.5 in section 5.2, where Bloch's theorem is discussed

$$\psi_i(\vec{r}) = \frac{1}{\sqrt{\Omega}} \sum_{\vec{q}} C_{i,\vec{q}} e^{i\vec{q}\cdot\vec{r}} \equiv \sum_{\vec{q}} C_{i,\vec{q}} |\vec{q}\rangle \quad (5.34)$$

where

$$|\vec{q}\rangle = \frac{1}{\sqrt{\Omega}} e^{i\vec{q}\cdot\vec{r}} \quad (5.35)$$

and

$$\begin{aligned} \langle \vec{q}' | \vec{q} \rangle &= \frac{1}{\Omega} \int_{\Omega} e^{-i\vec{q}'\cdot\vec{r}} \cdot e^{i\vec{q}\cdot\vec{r}} d^3\vec{r} \\ &= \frac{1}{\Omega} \int_{\Omega} e^{i[\vec{q}-\vec{q}']\cdot\vec{r}} d^3\vec{r} \\ &= \delta_{\vec{q},\vec{q}'} \end{aligned} \quad (5.36)$$

Inserting the expression for the eigenfunction, equation 5.34, into the Schrödinger-like equation, equation 5.33, and by multiplying on both sides of the equation by  $\langle \vec{q}' |$ , results in equation 5.37

$$\sum_{\vec{q}} C_{i,\vec{q}} \langle \vec{q}' | \hat{H}_{eff}(\vec{r}) | \vec{q} \rangle = \varepsilon_i \sum_{\vec{q}} C_{i,\vec{q}} \langle \vec{q}' | \vec{q} \rangle = \varepsilon_i C_{i,\vec{q}'} \quad (5.37)$$

Taking only the matrix elements of the kinetic energy operator, equation 5.37 can be written as

$$\sum_{\vec{q}} C_{i,\vec{q}} \langle \vec{q}' | -\frac{\hbar^2}{2m} \nabla^2 | \vec{q} \rangle = \frac{\hbar^2}{2m} \sum_{\vec{q}} C_{i,\vec{q}} |q|^2 \delta_{\vec{q},\vec{q}'} \quad (5.38)$$

The matrix elements for  $V_{eff}(\vec{r})$  can be evaluated as follow, since  $V_{eff}(\vec{r})$  is a periodic function it can also be expanded in Fourier components, thus

$$V_{eff}(\vec{r}) = \sum_m V_{eff}(\vec{G}_m) e^{i\vec{G}_m \cdot \vec{r}} \quad (5.39)$$

where  $\vec{G}_m$  is the reciprocal lattice vectors. The inverse of the above Fourier expansion, the Fourier expansion in terms of  $\vec{G}_m$ , can be written as

$$V_{eff}(\vec{G}_m) = \frac{1}{\sqrt{\Omega}} \int_{\Omega} V_{eff}(\vec{r}) e^{-i\vec{G}_m \cdot \vec{r}} d^3\vec{r}. \quad (5.40)$$

The matrix elements for the potential,  $V_{eff}(\vec{r})$ , becomes

$$\langle \vec{q}' | V_{eff}(\vec{r}) | \vec{q} \rangle = \sum_m V_{eff}(\vec{G}_m) \delta_{\vec{q}-\vec{q}', \vec{G}_m} \quad (5.41)$$

The only non-zero components of the matrix elements is when  $\vec{q}$  and  $\vec{q}'$  differs by some reciprocal lattice vector  $\vec{G}_m$ , as expressed in equation 5.42

$$\vec{q} - \vec{q}' = \vec{G}_m. \quad (5.42)$$

To accomplish this, the following relations needs to be defined

$$\vec{q} = \vec{k} + \vec{G}_m. \quad \text{and} \quad \vec{q}' = \vec{k} + \vec{G}_{m'}. \quad (5.43)$$

Inserting the expressions of equation 5.43 into equation 5.42, delivers equation 5.44

$$\bar{q} - \bar{q}' = \bar{G}_m - \bar{G}_{m'} = \bar{G}_{m''}. \quad (5.44)$$

Using equations 5.37 and 5.41, the Schrödinger equation, equation 5.33, for a given  $\bar{k}$  can be written as

$$\sum_{m'} H_{m,m'}(\bar{k}) C_{i,m'}(\bar{k}) = \varepsilon_i(\bar{k}) C_{i,m'}(\bar{k}) \quad (5.45)$$

where the matrix Hamiltonian is given by equations 5.46 and 5.47 [1]

$$H_{m,m'}(\bar{k}) = \langle \bar{k} + \bar{G}_m | \hat{H}_{eff}(\bar{r}) | \bar{k} + \bar{G}_{m'} \rangle \quad (5.46)$$

$$\hat{H}_{eff}(\bar{r}) = \frac{\hbar^2}{2m} |\bar{k} + \bar{G}_{m'}|^2 \delta_{m,m'} + V_{eff}(\bar{G}_m - \bar{G}_{m'}) \quad (5.47)$$

Thus the Kohn-Sham equation reduces to a matrix equation. For a more complete explanation of solving the Kohn-Sham equation in order to obtain an expression for the total energy, refer to the book *Electronic structure - Basic theory and applications* [1].

#### 5.5.4. Metallic smearing/broadening

For metallic systems the continuous distribution of electrons across the Fermi level needs to be taken into consideration, when summing over the k-point grid. Electrons can move across the Fermi level since there is no band gap present in metallic systems. To calculate the total energy in metallic systems, an fictitious electronic temperature is introduced, called metallic smearing or

broadening, into the system. The total energy of the system increases and the free energy of the system decreases with increasing smearing values. When both the total energy and the free energy is known for a specific smearing width, it is possible to calculate the true energy of the system. Figure 5.4 illustrates the use of smearing when performing calculations in metallic systems. The line given by TE is the total energy of the system, the free energy is given by FE and C gives the correction made to account for the continuous distribution of the electrons in metallic systems.

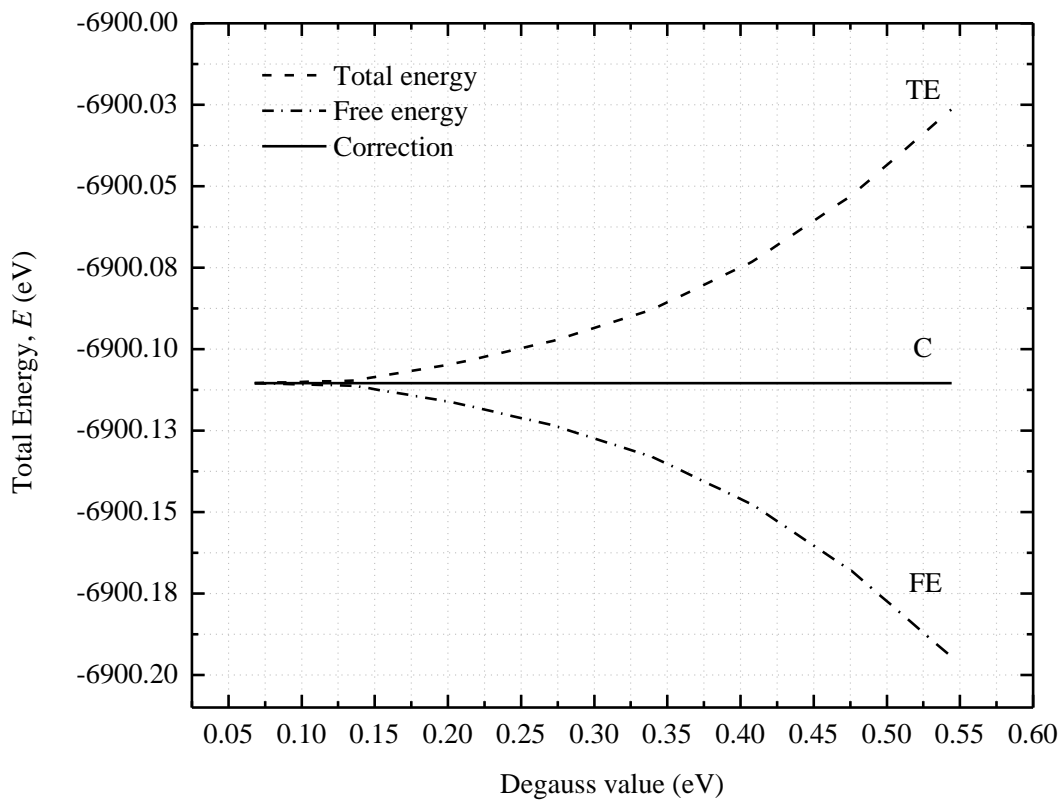


**Figure 5.4:** Illustration of the correction made in metallic system by the introduction of a fictitious electronic temperature to account for the discontinuous distribution of electrons in the system.

See Appendix B for an example on how to choose a smearing scheme. For a more detailed discussion on the various distribution functions refer to the book Electronic structure - Basic theory and applications [1].

## 5.6. Exchange-Correlation energy functional

Kohn and Sham reduced the difficult many body problem into an independent particle problem. To solve the Kohn-Sham equation the exchange-correlation energy functional is determined self consistently, since it is a functional of the density. Various functionals have been derived with great success, the most common of these are the LDA and the GGA functionals discussed in this section.

### 5.6.1. Local Density Approximation (LDA)

The LDA functional is based on the assumption that a solid has a charge density close to that of a homogeneous electron gas. For such a system the exchange and correlation effects are taken to be local in character. The functional is an integration over all space where the exchange correlation energy density is assumed to be the same as that found in a homogeneous electron gas with that density. The functional for a spin polarized system is given by equations 5.48 and 5.49 [1; 6; 9]

$$E_{XC}^{LSDA}[n^{\uparrow}, n^{\downarrow}] = \int d\bar{r} n(\bar{r}) \varepsilon_{XC}^{hom}(n^{\uparrow}(\bar{r}), n^{\downarrow}(\bar{r})) \quad (5.48)$$

$$= \int d\bar{r} n(\bar{r}) \left[ \varepsilon_X^{hom}(n^{\uparrow}(\bar{r}), n^{\downarrow}(\bar{r})) + \varepsilon_C^{hom}(n^{\uparrow}(\bar{r}), n^{\downarrow}(\bar{r})) \right] \quad (5.49)$$

For a spin un-polarized system the following simplification can be made to equations 5.48 and 5.49

$$n(\bar{r}) = \frac{n^{\uparrow}(\bar{r}) + n^{\downarrow}(\bar{r})}{2}. \quad (5.50)$$

The functional has been used with great success in systems that closely resembles a homogenous electron gas, such as Au and Al. The functional however fails to include the self interaction term

and care should be taken when applying the functional to atoms where self interaction could lead to inaccurate results [1].

## 5.6.2. Generalized Gradient Approximation (GGA)

The LDA served as the basis for the development of the GGA functional [1]; in this section the magnitude of the density gradient is included in the exchange-correlation energy. Equation 5.51 gives the expression for the GGA functional where spin has been taken into consideration [1; 6; 9]

$$E_{XC}^{GGA} = [n \uparrow, n \downarrow] = \int d\bar{r} n(\bar{r}) \varepsilon_{XC} \left( n^\uparrow(\bar{r}), n^\downarrow(\bar{r}), |\nabla n^\uparrow|, |\nabla n^\downarrow| \right)$$

$$E_{XC}^{GGA} = [n \uparrow, n \downarrow] = \int d\bar{r} n(\bar{r}) \varepsilon_X^{hom}(n) F_{XC} \left( n^\uparrow(\bar{r}), n^\downarrow(\bar{r}), |\nabla n^\uparrow|, |\nabla n^\downarrow| \right). \quad (5.51)$$

The term  $F_{XC} \left( n^\uparrow(\bar{r}), n^\downarrow(\bar{r}), |\nabla n^\uparrow|, |\nabla n^\downarrow| \right)$  can be divided into an exchange function,  $F_X$ , and a correlation function,  $F_C$ . The exchange function is given by equation 5.52 [1], where the lower order terms were calculated analytically

$$F_X = 1 + \frac{10}{81} s_1^2 + \frac{146}{2025} s_2^2 + \dots \quad (5.52)$$

$s_m$  is given by [1]

$$s_m = \frac{|\bar{\nabla}^m n|}{(2k_F)^m n} = \frac{|\bar{\nabla}^m n|}{2^m (3\pi^2)^{\frac{m}{3}} (n)^{\left(1+\frac{m}{3}\right)}} \quad m = 1, 2, 3, \dots \quad (5.53)$$

Making use of equation 5.54

$$n = \left( \frac{3}{4\pi r_s^3} \right) \quad (5.54)$$

and taking the first gradient as  $m = 1$ , reduces equation 5.53 for  $s$  into equation 5.55 [1]

$$s_1 = s = \frac{|\nabla r_s|}{2 \left[ \left( \frac{9\pi}{4} \right)^{\frac{1}{3}} \frac{1}{r_s} \right] r_s} \quad (5.55)$$

Different forms of  $F_x$  have been proposed where  $s = s_1$ . The three most widely used forms is that of Perdew and Wang (PW91) [12], Perdew, Burke and Enzerhof (PBE) [13] and Becke (B88) [14]. These three functions are illustrated in figure 5.5 [1].

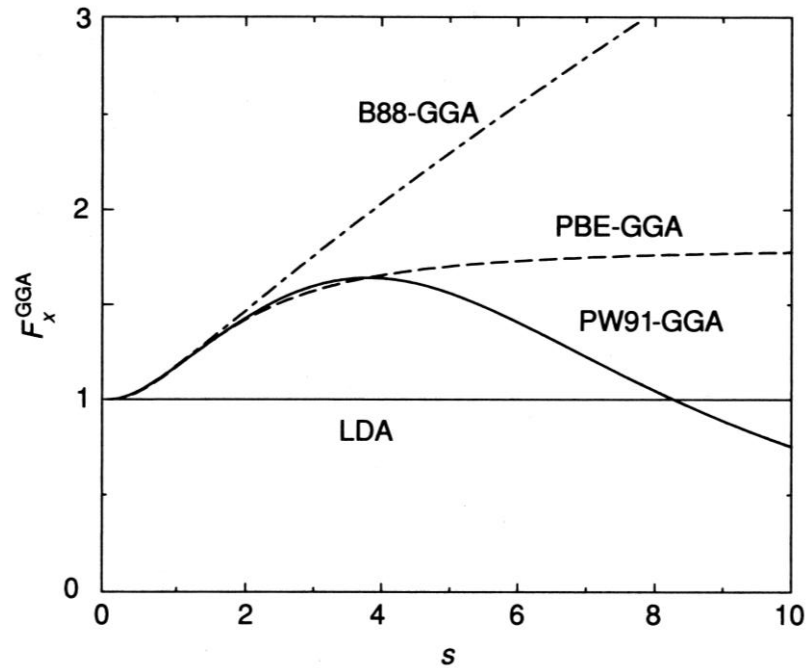


**Figure 5.5:** Plot of the exchange functionals for the PW91, PBE and B88 pseudopotentials.

The correlation is more difficult to express in terms of a functional and generally the contribution of  $F_C$  is less than  $F_X$ . An expression for the correlation function  $F_C$  is approximately given by equation 5.56 [1]

$$F_C = \frac{\varepsilon_C^{LDA}(n)}{\varepsilon_X^{LDA}(n)} (1 - 0.219,51 s_1^2 + \dots). \quad (5.56)$$

Figure 5.6 [1] shows the function  $F_C$  for the PBE-GGA functional which is almost identical to that of the PW91-GGA functional.

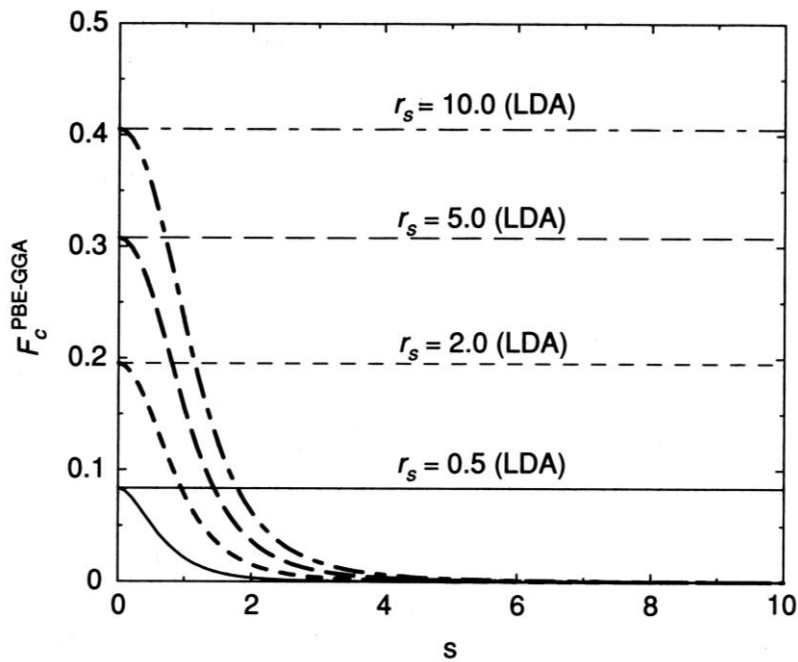


**Figure 5.6:** Plot of the correlation function for different values of  $r_s$  for the PBE pseudopotential.

Thus by looking at figures 5.5 and the fact that the correlation functional for the two pseudopotentials are very close below a certain  $s$  value [1] it can be concluded that the difference between the PW91 and the PBE functional are due to the difference in the functional  $F_X$ . For a

more detailed discussion, refer to the book Electronic structure - Basic theory and applications [1] as well as the sources [13; 15; 16] .

## 5.7. Pseudopotentials

Pseudopotentials are used to replace the all electron potential and reduce the calculation time significantly. The validity of using pseudopotentials is that outside of the core region,  $r_c$ , the form of the pseudopotential and the all electron potential are effectively the same, figure 5.7. This is true since it is only the valence electrons taking part in bond formation and thus these are the electrons of importance in electronic structure calculations [5]. Various pseudopotentials have been derived, which can be divided into two main groups, the “soft” or ultrasoft pseudopotentials or the “hard” potentials namely the norm-conserving pseudopotentials. The “soft” potentials are smoother and thus fewer components in the Fourier expansion are required [5], refer to section 5.2 for an explanation of the Fourier components in a plane wave. Whereas the “hard” potentials require more Fourier components [5], but could lead to improved results on the ultrasoft pseudopotentials in some cases. Figure 5.7 [17] shows a schematic representation of the pseudo wavefunction,  $\psi_{pseudo}$ , and pseudo potential,  $V_{pseudo}$ , in red as compared to the all-electron wavefunction,  $\psi_{all-electron}$ , and potential,  $V_{all-electron}$ , in blue. It can be seen that outside the core region,  $r_c$ , the two wavefunctions and potentials are effectively the same.

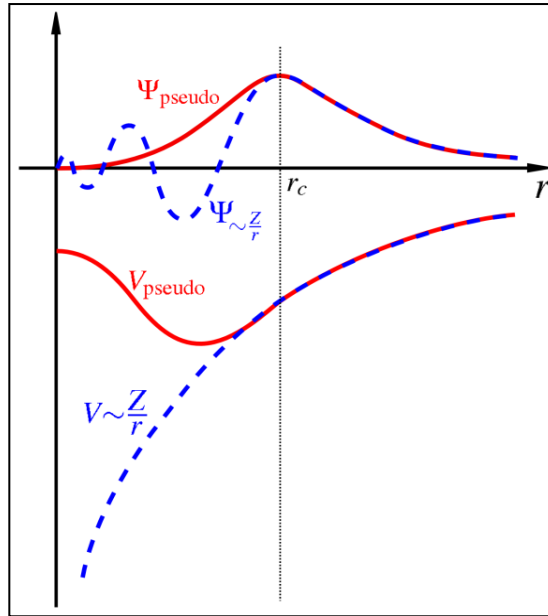


**Figure 5.7:** Schematic representation of the all-electron wavefunction and potential in blue as compared to the pseudo wavefunction and potential in red [17].

## 5.8. Nudged Elastic Band

The diffusion rate is given by the Arrhenius relation which was discussed in chapter 3, it is given here for completeness by equation 5.57

$$D = D_0 \exp\left(\frac{-E_{vac} + E_m}{RT}\right), \quad (5.57)$$

where  $D$  is the diffusion rate and  $D_0$  is the pre-exponential factor. In the exponent,  $E_{vac}$  is the vacancy formation energy and  $E_m$  is the migration energy.  $R$  is the universal gas constant and  $T$ , the temperature in Kelvin. In order to calculate a value for  $E_m$ , the nudged elastic band method is used in order to obtain the minimum energy path of a diffusing atom, see chapter 9 on computational

results. This section explains the Nudged Elastic Band (NEB) method and the modified Climbing Image Nudged Elastic Band (CI-NEB) method that was used to perform all migration energy calculation in this thesis.

The NEB [18] is used to determine the minimum energy path (MEP), for a transition from one stable state to the next. A number of images are chosen along a path, called the elastic band, from the initial to the final state. The atom then moves along the path according to the coordinates given by the images and is optimized with respect to the NEB force,  $\bar{F}_i^{NEB}$ . Figure 5.8 [18] shows the initial and final positions of a diffusion process, with the NEB path and the MEP respectively. When the NEB force is optimized the NEB path will be equal to the minimum energy path. The inset shows the NEB force with its parallel and perpendicular components.

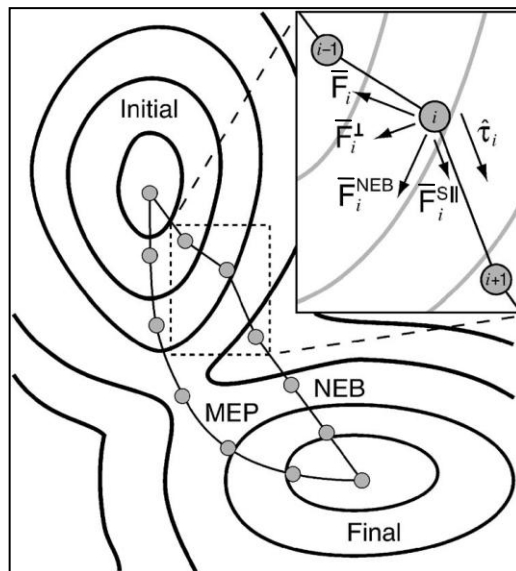


**Figure 5.8:** Illustration of the NEB method for finding the minimum energy path of a diffusing atom, the NEB force,  $\bar{F}_i^{NEB}$ , with its parallel and perpendicular components are given in the inset [18].

The NEB force is given by equation 5.58 [5; 18; 19]

$$\bar{F}_i^{NEB} = \bar{F}_i^\perp + \bar{F}_i^{S//} \quad (5.58)$$

where  $\bar{F}_i^\perp$  is the force projected perpendicular to the elastic band between two images, and is called the true force. The true force is experienced by the atom as a result of the potential energy surface in which it is located and is given by equation 5.59 [5; 18; 19]

$$\bar{F}_i^\perp = -\nabla E(\bar{R}_i) + (\nabla E(\bar{R}_i) \cdot \hat{\tau}_i) \hat{\tau}_i. \quad (5.59)$$

The force  $\bar{F}_i^{S//}$  is the spring force, a force parallel to the elastic band which is experienced by the images as a result of the elastic band. Equation 5.60 gives the expression for the parallel spring force [5; 18; 19]

$$\bar{F}_i^{S//} = k \left( |\bar{R}_{i+1} - \bar{R}_i| - |\bar{R}_i - \bar{R}_{i-1}| \right) \hat{\tau}_i \quad (5.60)$$

where  $\hat{\tau}_i$  is the unit vector along the direction,  $\bar{R}$ , of the path from one image to a neighboring image of higher energy and  $k$  is the elastic constant.

The elastic band is optimized in order to obtain the minimum energy path for the transition, this is done by minimizing the total force given by equation 5.58. The CI-NEB method [19] is further modified by allowing the image of highest energy, image  $l$ , to climb up the saddle point via a reflection in the force along the tangent  $\hat{\tau}_l$ . The force experienced by atom  $l$  is given by equation 5.61 [19]

$$\bar{F}_l^{CI} = \bar{F}_l - (2\bar{F}_l \cdot \hat{\tau}_l) \hat{\tau}_l. \quad (5.61)$$

This image,  $l$ , expressed in equation 5.61 does not experience any spring forces and can climb freely along the saddle point.

## 5.9. Summary

This chapter provided the basic concepts that is needed to perform practical DFT calculations. The importance of lattice periodicity and plane waves were illustrated in the derivation of the Bloch theorem. The use of a k-point grid to simplify summation over k-space was explained using the method of Monkhorst and Pack. It was shown how Kohn and Sham simplified the many body problem into a single particle problem by introducing an exchange-correlation term to account for the many body interactions. The Kohn-Sham self consistent loop was explained by investigating the various components in the loop including the solution of the Kohn-Sham equation. For the calculation of the minimum energy paths and diffusion barriers, the nudged elastic and climbing image nudged elastic band methods was explained. The chapter provided the necessary theoretical tools needed to perform the DFT calculations presented in chapter 9, Computational results.

## 5.10. References

- [1]. R.M. Martin, *Electronic structure: basic theory and Practical applications*, Cambridge University Press, Cambridge, 2004.
- [2]. J.S. Michael, F.R.S. Dewar, *The molecular orbital theory of organic chemistry*, McGraw-Hill Book Company, United States: New York, 1969.
- [3]. Nobelprize.org, *The Nobel Prize in Chemistry 1998, 2011*.
- [4]. W. Kohn, L.J. Sham, *Phys. Rev. B.* 140 (1965) 1133.
- [5]. D.S. Sholl, J.A. Steckel, *Density Functional Theory: A practical introduction* Wiley & sons, New Jersey, 2009.
- [6]. K. Burke, *The ABC of DFT*, Department of Chemistry, University of California Irvine, 2007.

- [7]. P. Gianozzi, et al., *J. Phys. Cond. Mat.* 21 (2009) 1.
- [8]. D.W. Snoke, *Solid State Physics essential concepts*, Pearson, San Francisco, 2009.
- [9]. P. Giannozzi, *Density Functional Theory for electronic structure calculations*, Italy: Pisa, 2005.
- [10]. D.J. Chadi, L. Cohen, *Phys. Rev. B* 8 (1973) 5747.
- [11]. H.J. Monkhorst, J.D. Pack, *Phys. Rev. B* 13 (1976) 5188.
- [12]. J.P. Perdew, Y. Wang, *Phys. Rev. B.* 45 (1992) 13244.
- [13]. J.P. Perdew, K. Burke, M. Ernzerhof, *Phys. Rev. Lett.* 77 (1996) 3865.
- [14]. A.D. Becke, *Phys. Rev. A.* 38 (1988) 3098.
- [15]. K. Burke, J.P. Perdew, M. Levy, *Semilocal Density Functionals for Exchange and Correlation: Theory and Application*, Tulane University, Los Angeles.
- [16]. J.P. Perdew, K. Burke, Y. Wang, *Phys. Rev. B* 54 (1996) 16533.
- [17]. W. Quester, Comparison of a wavefunction in the Coulomb potential of the nucleus (blue) to the one in the pseudopotential (red). The real and the pseudo wavefunction and potentials match above a certain cutoff radius  $r_c$ , 2006.
- [18]. D. Sheppard, R. Terrell, G. Henkelman, *J. Chem. Phys.* 128 (2008) 134106.
- [19]. G. Henkelman, B.P. Uberuaga, H. Jonsson, *J. Chem. Phys.* 113 (2000) 9901.

Part II  
Experimental



# Chapter 6: Sample preparation

## 6.1. Introduction

This chapter describes the method and equipment used in the preparation of S doped Fe samples (Fe-S). The preparation of Fe-S samples is commonly carried out by allowing a mixture of hydrogen and hydrogen sulfide gas ( $H_2/H_2S$ ) to flow over the surface of an Fe sample [1; 2; 3; 4]. It has been reported that the presence of hydrogen can lead to grain boundary embrittlement in Fe [5; 6; 7; 8]. Due to the negative effects caused by hydrogen and the inability of the experimental technique Auger electron spectroscopy to detect hydrogen, a new method for the preparation of Fe-S samples is proposed. This newly proposed doping method of Fe with elemental S was performed in the preparation chamber that was specifically built for the experiment. The various components of the preparation chamber are discussed.

## 6.2. Doping methodology

This section describes the methodology used in order to successfully prepare Fe-S samples by means of diffusing elemental S into Fe. Three conditions which had to be avoided during the doping process are stated below and discussed in this section.

1. Formation of iron sulfide phases ( $FeS$ ,  $FeS_2$ ) on the surface, which would result in sample damage.
2. Temperatures,  $T$ , exceeding the bcc Fe phase region,  $T > 912^\circ C$  (1185 K).
3. Concentration of S,  $C_{Sulfur}$ , exceeding the bcc Fe phase region,  $C_{Sulfur} > 0.033$  at. % (330 ppm).

The use of pure S instead of the  $H_2/H_2S$  mixture for the preparation of Fe-S samples will result in a cleaner Fe-S system. The side effects caused by the presence of hydrogen are eliminated and

ideally a binary system consisting of Fe and S can be obtained. There are also potential health and safety risks when working with the gases  $H_2$  and  $H_2S$ , and special precautions need to be taken. However using S is not just a simple exchange of  $H_2/H_2S$  for the pure S. S has a very low melting point of 392 K [9], far below the temperature where S will diffuse into Fe within a reasonable time period. Another problem faced is that when the S is heated to the point of evaporation, the majority of the S will condensate against the inside of the preparation chamber. The S that is deposited onto the surface of the Fe will simply evaporate off the surface during annealing, with little S diffusing into the Fe. Taking this into account eliminates the conventional method of using electron beam deposition to prepare Fe-S samples. The poisoning effect of S in metallic systems also prevents the use of electron beam deposition, since the whole system would be contaminated by S making it unsuitable for deposition of any other materials in the future.

Various tests were performed in order to find a valid method for the preparation of Fe-S samples using elemental S. It was found that the only method that did not result in damage of the Fe sample or complete evaporation of the S was to have a controlled process where the S is deposited onto a heated Fe surface. The process was carried out in an Ar gas atmosphere to ensure that no contamination of the sample occurred. The S source and Fe sample were heated separately at two different temperatures. The S was heated to above the boiling point ( $T > 718$  K) [9], while the Fe was kept at a high temperature (640 K) to ensure that the vapour making contact with the Fe surface can diffuse into Fe within a reasonable time period. Attempts were made to prepare Fe-S samples by simply placing a S flake onto the surface of the Fe sample and diffusing the S into Fe at a high temperature. Results indicated that an uneven distribution of S was obtained on the surface, with some areas of the surface completely free of S. The melted S, which remained on areas of the surface after doping, formed a thick layer which was difficult to remove and often resulted in sample damage.

Deposition of S onto a heated Fe surface proved to be a very effective method for the preparation of Fe-S samples. The concentration of S can be controlled by varying the time for which the sample is exposed to the S vapour. It was also found that the Fe sample needed to be exposed to the S vapour in intervals in order to allow the deposited S to diffuse into the Fe before more S was deposited onto the Fe surface. If the sample was exposed to the S vapour for too long, formation of sulphide phases could cause the sample to become damaged and unsuitable for the study of diffusion and segregation. This is the first condition stated, the second and third conditions are to ensure that Fe remained in the bcc Fe structure, since at temperatures exceeding  $912^\circ\text{C}$  (1185 K) and concentrations exceeding 0.033 at. % (330 ppm), Fe would no longer be in the pure  $\alpha$ -phase.

The second and third conditions are indicated in the phase diagram of figure 6.1 [10], with the second condition marked by point A and the third condition marked by point B.

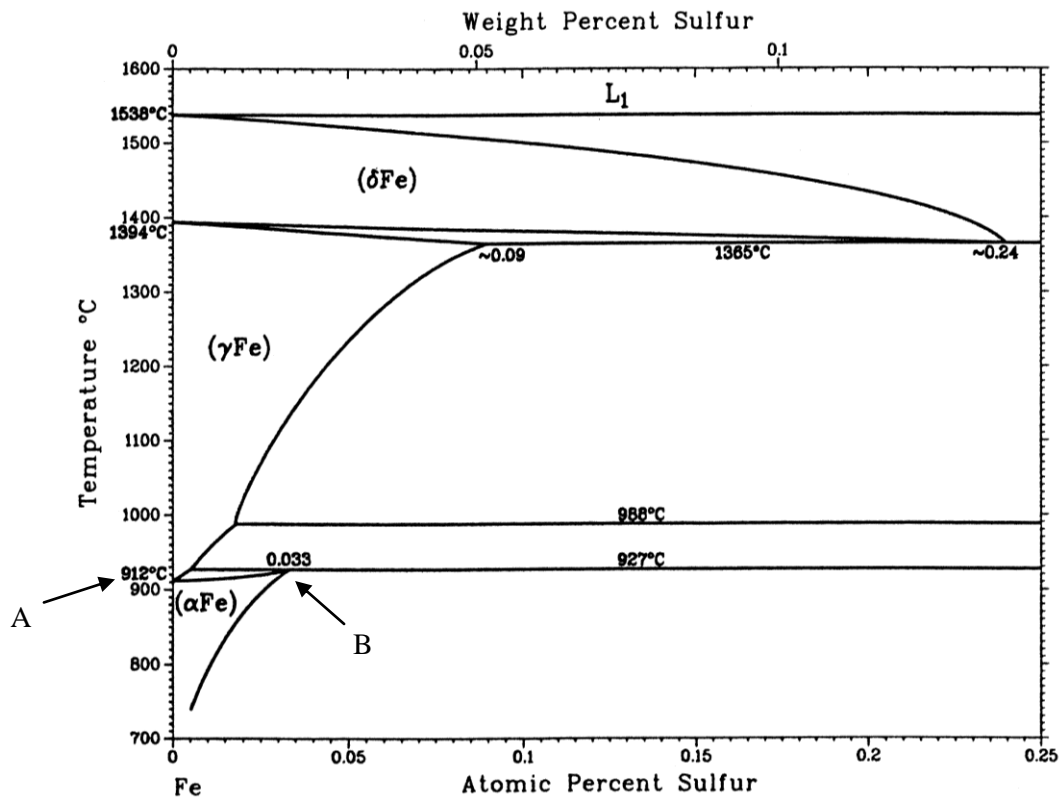


**Figure 6.1:** Phase diagram of the Fe-S system, showing that for bcc Fe the maximum temperature is 912°C (1185 K), point A, and the maximum S concentration is 0.033 at. % (330 ppm), point B.

The temperature of the Fe sample was measured by a type K thermocouple placed at the back of the Fe sample, between the sample and the heater. The temperature measured by the thermocouple was controlled by a operational amplifier temperature control unit. In chapter 7, Experimental results, the relationship between the temperature measured by the thermocouple at the back of the Fe sample and the surface temperature was established. It is shown that a polynomial fit of order six gave an good description of this temperature relationship. Using this polynomial model, the surface temperature of the Fe sample was determined from the temperature measured by the thermocouple at the back of the Fe sample.

Calculations were performed in order to obtain an estimated time for which the sample should be doped for in order to obtain the desired S concentration. This was done by solving Fick's second law for a finite sample with an infinite diffusion source, equation 6.1

$$C(x,t) = C_0 \left[ \sum_{n=0}^{\infty} (1)^n \operatorname{erfc} \left( \frac{(2n+1)L-x}{2\sqrt{Dt}} \right) + \sum_{n=0}^{\infty} (1)^n \operatorname{erfc} \left( \frac{(2n+1)L+x}{2\sqrt{Dt}} \right) \right] \quad (6.1)$$

where  $L$  is the thickness of the sample,  $x$  the depth into the sample,  $t$  the time of diffusion and  $D$  the diffusion coefficient of S in the polycrystalline Fe sample.  $C_0$  is the initial concentration of S which was taken to be a fraction of 1. Values for the diffusion parameters obtained from the work of Reichl *et. al.* [11] were used to calculate a value for  $D$  at a temperature of 640 K using the Arrhenius equation, equation 3.22, in chapter 3, Diffusion theory. Figure 6.2 shows examples of the diffusion profiles for S in Fe, calculated using equation 6.1.

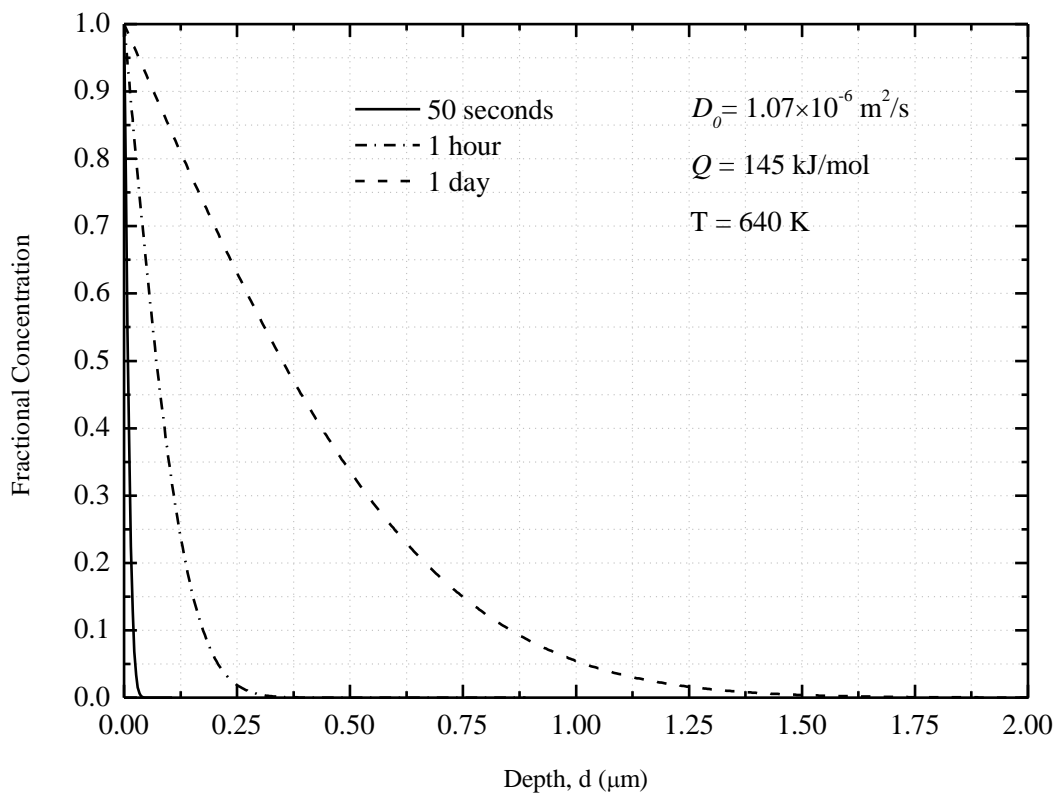


**Figure 6.2:** Solutions to Fick's second law for a finite system containing an infinite diffusion source, calculated for three different time periods at 640 K.

After the successful doping of an Fe sample with the required amount of S, the sample needs to be annealed in order to obtain a homogeneous distribution of S in Fe. To determine the amount of time that is needed, Fick's second law is solved for a finite sample with a limited diffusion source, equation 6.2 [12].

$$C(x,t) = C_0 \sum_{n=-\infty}^{\infty} \left[ \operatorname{erf} \left( \frac{h + 2nL - x}{2\sqrt{Dt}} \right) + \operatorname{erf} \left( \frac{h - 2nL + x}{2\sqrt{Dt}} \right) \right] \quad (6.2)$$

where  $h$  is the thickness of the diffusion source. For a complete derivation of both equation 6.1 and 6.2 refer to the book: The mathematics of diffusion [12]. Figure 6.3 shows the variation of the S concentration with a variation in depth, calculated for three different time periods at a temperature of 1073 K.

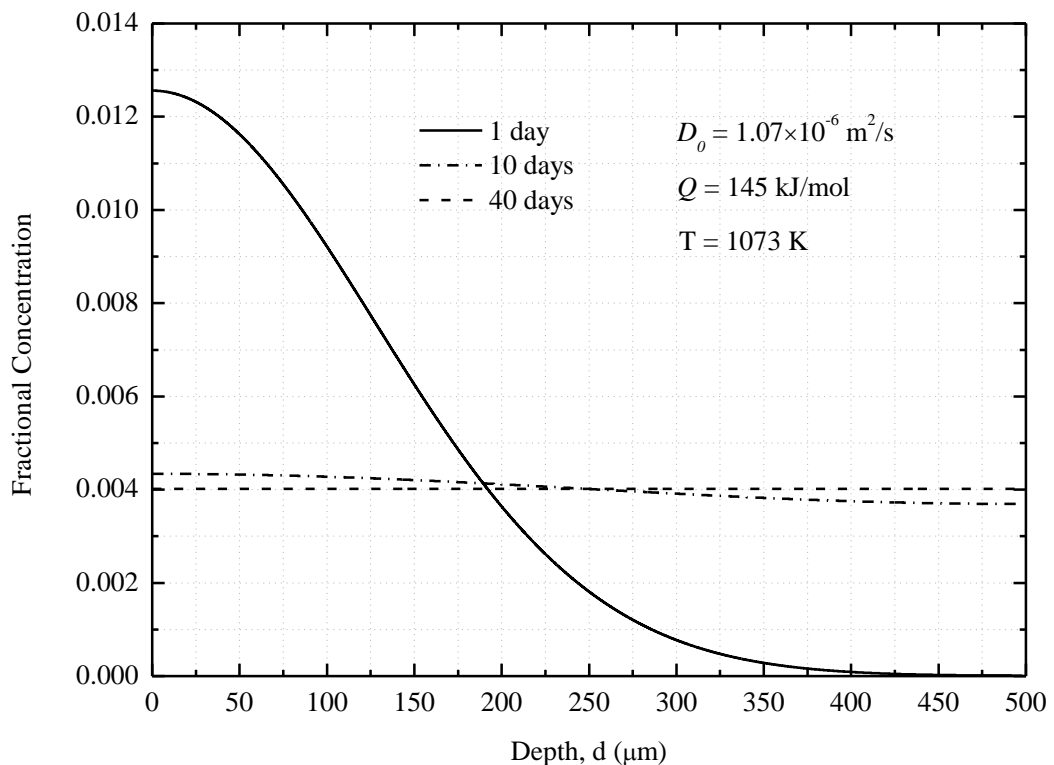


**Figure 6.3:** Solution to Fick's second law for a finite system with a limited diffusion source. The calculations were performed for three different time periods at a temperature of 1073 K.

From figure 6.3, the amount of time needed in order to obtain a homogenous distribution for S in Fe was calculated as 40 days at a temperature of 1073 K. The fractional concentration at the front end of the sample is given by  $C_0$  and the concentration at the back of the sample, of thickness  $L$ , is given by  $C_L$ . Taking the ratio  $\frac{C_L}{C_0}$  gives a value for the fractional homogeneity of S in the Fe sample. Equation 6.2 was solved for different time periods (number of days) with the results shown in figure 6.4. Two curves are shown in figure 6.4, one for a diffusion distance of 0.5 mm and one for a diffusion distance of 1.0 mm. The value of 0.5 mm is the thickness of the Fe sample, while the value of 1.0 mm is the distance at the edges of the sample which was not deposited with S during doping. During doping the cap of the heater, keeping the sample in place on the heater, prevented S from being deposited onto the edges (~1.0 mm) of the sample as shown in figure 6.5.

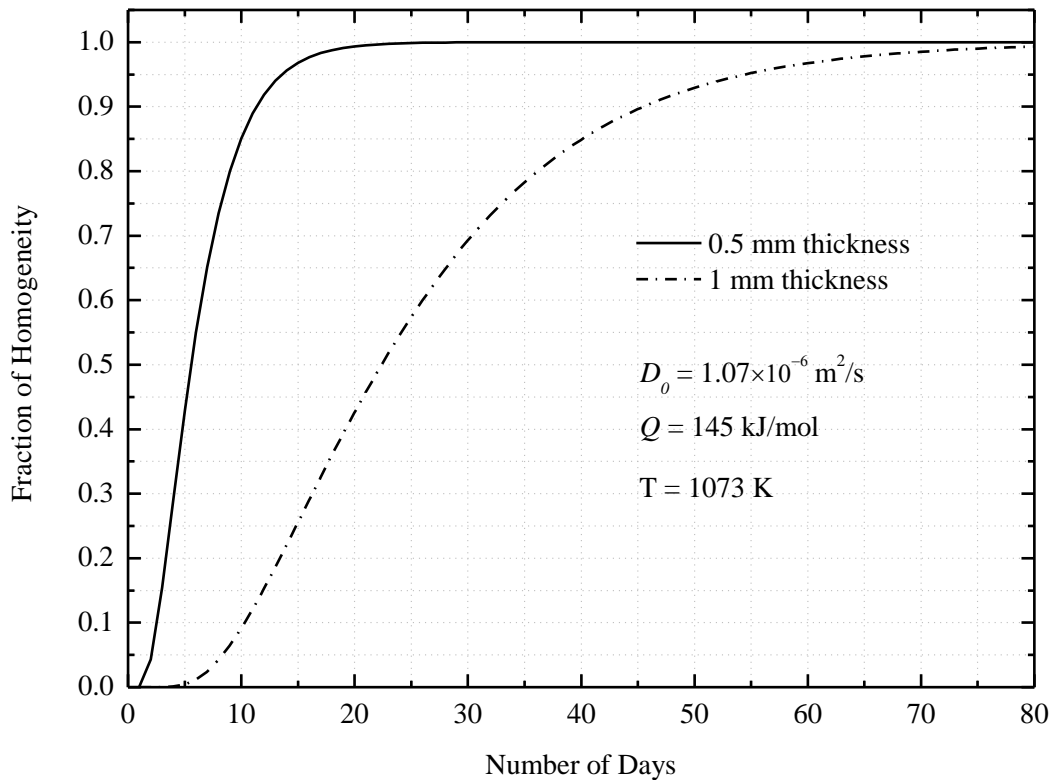


**Figure 6.4:** Solution to Fick's second law for a finite system with a limited diffusion source. The calculations were performed for different time periods (number of days), at a temperature of 1073 K.

From figure 6.4, an annealing time of 40 days would result in a 100 % homogeneity for the thickness of the sample, with a 84 % homogeneity along the edges of the sample. Figure 6.5 shows the area of the sample deposited with S in grey, with the outer edges not deposited with S in white. It is important to note that the 84 % homogeneity will only be on the outer edge of the sample, this value will increase to 100 % closer to the region deposited with S.

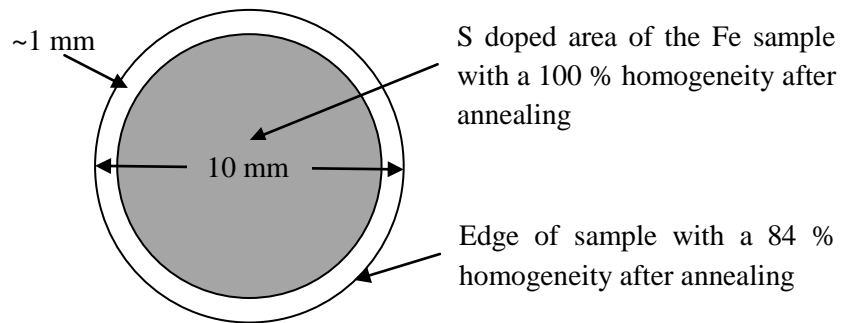


**Figure 6.5:** Schematic showing the homogeneity of the two different regions of the Fe-S sample after being annealed for 40 days at a temperature of 1073 K.

In order to dope Fe with S using the method described here, a preparation chamber had to be built that can effectively be used for the preparation of Fe-S samples. The remainder of this chapter describes this preparation chamber and how a controlled process was carried out in order to successfully prepare Fe-S samples.

### 6.3. Experimental setup

The experimental set-up used for the preparation of Fe-S samples by means of diffusing elemental S into Fe is shown in figures 6.6 and 6.7. Figure 6.6 shows the newly built preparation chamber from the outside while figure 6.7 shows an inside view of the preparation chamber. The various components of the system are discussed in this section and are also indicated in the figures.

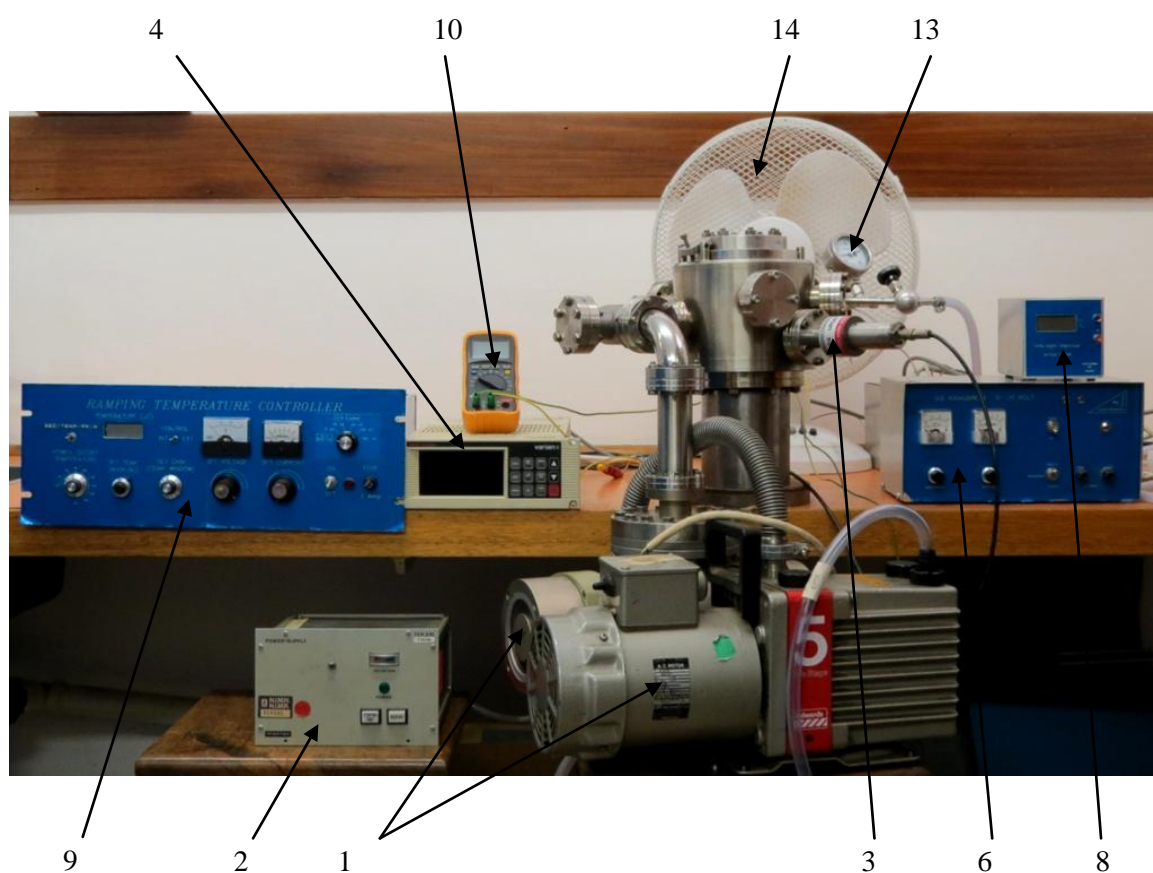
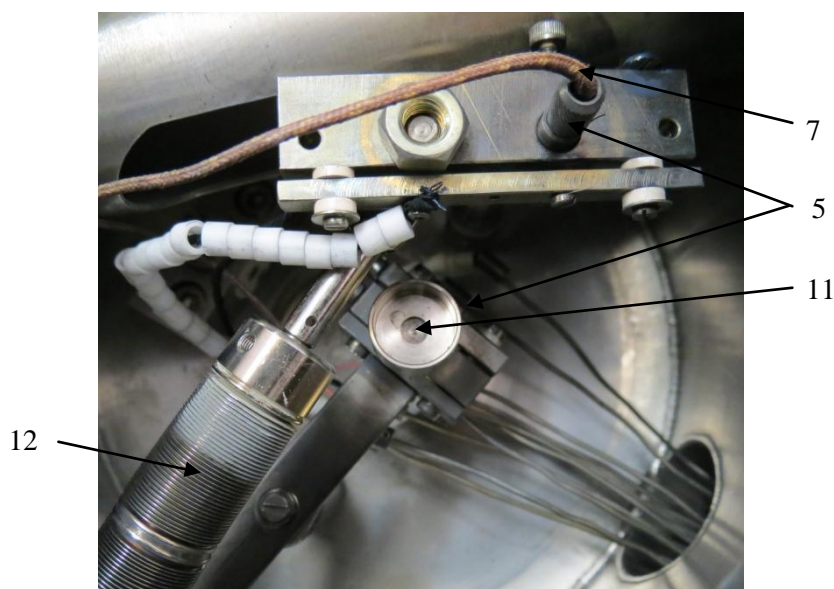


**Figure 6.6:** The newly designed and built Fe-S preparation chamber used for the preparation of Fe-S samples by diffusing elemental S into Fe. The components indicated in the figure are listed in the text.

The system shown in figure 6.6 consists of the following components:

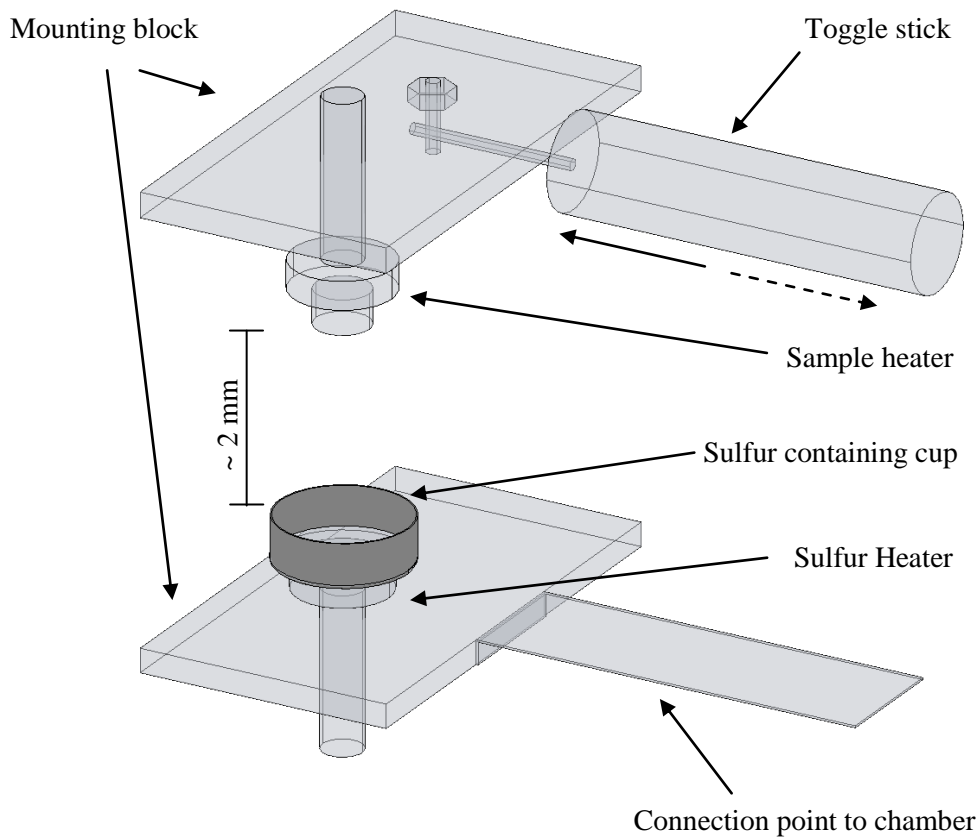
1. Rotary vane pump and turbo molecular pump combination, capable of reaching pressures down to  $10^{-8}$  Torr
2. Turbo molecular pump control unit.
3. Cold cathode pressure gauge, capable of measuring pressures in the range  $10^{-3}$ - $10^{-8}$  Torr.
4. Control unit for the cold cathode pressure gauge.
5. 2 Heaters consisting of a tungsten filament each.
6. Power supply for heating of the S heater.
7. Type K thermocouple placed at the back of the sample to measure temperature.
8. Thermocouple reference display unit.
9. Operational amplifier control unit for controlling the temperature.
10. Ammeter to measure the current supplied to the sample heater.
11. A stainless steel cup into which the S flakes are placed.
12. Toggle stick with which the Fe sample can be manipulated inside the chamber.
13. Analogue pressure gauge for measuring pressures in the range 750-1500 Torr.
14. Fans to prevent the system from overheating.

Figure 6.7 shows the internal components of the preparation chamber not visible in figure 6.6.



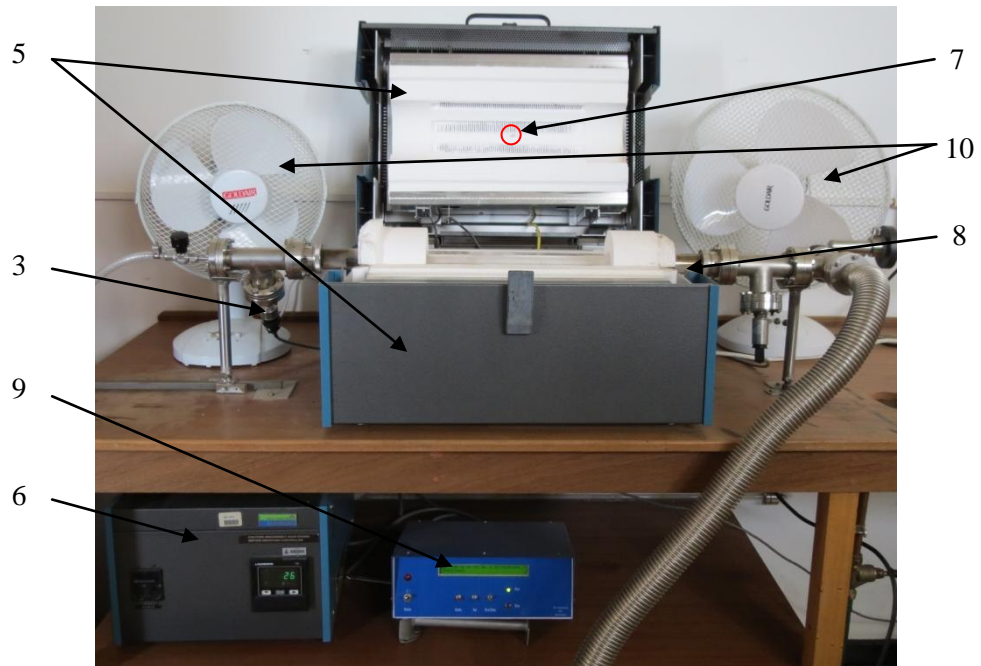
**Figure 6.7:** Internal view of the preparation chamber, showing the connections made for the sample and S heaters. The components indicated in the figure are listed in the text.

Figure 6.8 gives a schematic, showing the set-up of the two heaters inside the preparation chamber. The sample mounted onto the sample heater can be exposed to the S vapour in intervals. This is done by manipulating the toggle stick, illustrated in figure 6.8. The toggle stick is moved forward (solid arrow) in order to position the sample over the S vapour. To remove the sample from the S vapour, the toggle stick is pulled back (dashed arrow).



**Figure 6.8:** Schematic showing the set-up of the two heaters used respectively for the Fe sample and the S source. The directions in which the toggle stick can be moved in order to expose or remove the Fe sample from the S vapour are indicated by the solid and dashed arrows respectively. (not drawn to scale).

Once the required S concentration was successfully diffused into the Fe sample, the sample was annealed for 40 days in the annealing system shown in figure 6.9.



**Figure 6.9:** Annealing system used to obtain a homogenous distribution of S in Fe when annealed at a temperature of 1073 K for a time period of 40 days. The components indicated in the figure are listed in the text.

The annealing oven in figure 6.9 consists of the following components:

1. Rotary and turbo molecular pump combination (not shown in figure 6.9).
2. Turbo molecular pump control unit (not shown in figure 6.9).
3. Thermocouple pressure gauge capable of measuring pressures in the range  $760\text{-}10^{-3}$  Torr
4. Thermocouple pressure gauge control unit (not shown in figure 6.9).
5. Lindberg annealing oven.
6. Lindberg temperature control unit.
7. Thermocouple for temperature measurement.
8. Quartz tube into which the sample is placed.
9. Digital pressure gauge for pressures above atmosphere.
10. Fans for cooling the fittings of the quartz tube.

## 6.4. Experimental procedure

### 6.4.1. Doping of Fe with S

1. Samples were polished using silicon carbide (SiC) paper of grain size 15  $\mu\text{m}$  and subsequently cleaned in an ultrasonic ethanol bath. This creates an even surface onto which S can evaporate. Surfaces smoother than 15  $\mu\text{m}$  were found insufficient for the sticking of S to Fe.
2. The Fe sample was mounted onto the heating stage and the S flakes placed in the cup mounted onto the bottom heater.
3. The system was closed and allowed to pump down for a few days to remove the impurity gasses from the system.
4. The system was backfilled with Ar gas to a pressure of 1500 Torr and pumped out afterwards.
5. Step 3 was repeated 10 times to ensure that all impurity gasses were properly washed out from the system.
6. The system was once again backfilled with Ar gas to a pressure of 1500 Torr.
7. The heater containing the Fe sample was heated to 640 K. This temperature allows diffusion of S into Fe within a reasonable time period. Higher temperatures were avoided to prevent overheating of the glass windows of the preparation chamber.
8. The system was allowed to stabilize for 10 minutes, to ensure that the Fe sample was properly heated and that a stable temperature was obtained.
9. During the 10 min preheating of the Fe sample, the S was slowly heated to ensure that a total of two minutes is spent preheating the S flakes at a low temperature  $<393$  K.
10. The Fe sample was exposed to the S vapour ( $T > 718$  K) at intervals of 2 seconds with a 5 seconds resting period, for a total of 50 seconds. The process was monitored via the glass window at the top of the chamber (figure 6.7).
11. The electrical current to the two filaments were switched off immediately and the system pumped down to prevent over exposure of the Fe sample.
12. The sample was removed from the preparation chamber after it was allowed to cool to room temperature, and cleaned in an ultrasonic bath of ethanol.

### 6.4.2. Annealing of the Fe-S sample

1. The quartz tube of the annealing system was pumped out for 24 hours to remove any impurity gases.
2. The quartz tube was backfilled with Ar gas to a pressure of 1200 Torr.
3. The temperature of the annealing oven was slowly increased to a temperature of 1173 K to avoid drastic temperature changes that can cause damage to the quartz tube.
4. The quartz tube was cleaned by pumping out the impurity gasses and then backfilled with Ar gas. This procedure was repeated a number of times while the system was kept at a constant temperature of 1173 K for a period of 30 days. This was done to ensure that any contamination that might have been introduced into the quartz tube by previous users are completely removed.
5. After the 30 day time period, the annealing oven was slowly cooled to avoid damage to the quartz tube.
6. The quartz tube was opened and the doped sample was placed in the annealing oven along with 4 titanium (Ti) plates. The Ti plates were placed on either side of the Fe-S sample in an attempt to prevent oxidation of the sample.
7. The quartz tube was pumped out for a few hours to remove impurity gasses.
8. The quartz tube was backfilled with Ar gas to a pressure of 1200 Torr and again pumped out. This procedure was repeated 10 times to ensure that all impurity gasses were properly washed out from the system.
9. The temperature was slowly increased to a value of 373 K, where it remained for a total of 24 hours.
10. The temperature was slowly increased by 20 K, where it remained for a period of 24 hours.
11. Step 10 was repeated until a temperature of 453 K was reached. This was to ensure that the S diffuses into Fe and not evaporate into the quartz tube.
12. The temperature was slowly increased to a final temperature of 1073 K, where it remained constant for a total period of 40 days.
13. During annealing of the sample, the pressure in the quartz tube was kept at a value of 1200 Torr.
14. After 40 days the quartz tube was slowly cooled and the sample was removed from the system, ready for analysis.

The results for samples prepared using the experimental procedures described here are given in chapter 8, Experimental results.

## 6.5. Summary

The new method and equipment used for the preparation of Fe-S samples by means of diffusing elemental S into Fe was described in this chapter. It was found that the most effective method by which S can be diffused into the Fe sample was to deposit S onto a heated Fe surface. The equipment used and the experimental procedure that was carried out, are explained in detail. This method and the equipment can also be used for other low melting point materials such as indium (In). The advantage of preparing samples by this method is that the material gets diffused into the matrix material and thus when the sample is annealed, the probability for the material to evaporate from the matrix is reduced.

## 6.6. References

- [1]. M.M. Montagono, J. Cabané, Surf. Sci. 285 (1993) L468.
- [2]. Y. Niu, G.Y. Fu, P. Catello, F. Gesmundo, W.T. Wu, F. Viani, Corros. Sci. 39 (1997) 1811.
- [3]. T. Rosenqvist, B.L. Dunicz, Jom-J. Min. Met. Mat. S. June (1952).
- [4]. M.F. Pillis, L.V. Ramanathan, Mater. Res. 5 (2002) 349.
- [5]. T. Michler, J. Naumann, Int. J. Hydrogen Energ. 35 (2010).
- [6]. Y. Mine, S. Matsumoto, Z. Horita, Corros. Sci. 53 (2011) 2969.
- [7]. J.-S. Wang, Eng. Fract. Mech. 68 (2001) 647.
- [8]. I. Y.-Telitchev, O. Vinogradov, Comp. Mater. Sci. 36 (2006) 272.
- [9]. R.C. Weast, M.J. Astle, W.H. Beyer, (Eds.), Handbook of chemistry and physics, CRC Press, Inc., Boca Raton, Florida, 1983-1984.
- [10]. T.B. Massalski, H. Okamoto, P.R. Subramanian, L. Kacprzak, (Eds.), Binary alloy phase diagrams, W.W. Scott., Jr, 1990.

- [11]. B.M. Reichl, M.M. Eisl, T. Weis, H.Hutter, H.Störi, Fresenius J. Anal. Chem. 353 (1995) 762.
- [12]. J. Crank, The mathematics of diffusion, Oxford University Press, London, 1975.



# Chapter 7: Experimental techniques

## 7.1. Introduction

In this chapter the use of the experimental techniques AES and XRD are discussed. AES was used to study the diffusion and segregation of S in bcc polycrystalline Fe while XRD was used to study the influence S had on the crystal structure of the polycrystalline Fe samples. The principle of operation of each technique, the apparatus and the optimized experimental parameters used in the experiments are discussed. In order to obtain the elemental concentrations of the elements analysed, Auger quantification is also discussed in detail.

## 7.2. X-Ray Diffraction (XRD)

X-Ray diffraction was used to determine the crystal orientations present in the polycrystalline Fe samples. The results obtained using XRD are presented in chapter 8, Experimental results. The remainder of this section provides the basic concepts of XRD, with the focus on the diffractometer and the experimental parameters used to obtain the results.

### 7.2.1. Principle of operation

A short description is given here to explain the principle of operation behind XRD. This includes the derivation of Bragg's Law. XRD makes use of high energy X-Rays (up to 40 kV), diffracted by a crystal to obtain information regarding the periodicity of the crystal structure. For diffracted X-Rays differing with a whole number of wavelengths, the waves are said to be in phase and

constructive interference will occur. This will result in a strong XRD peak caused by a wave with an amplitude equal to the sum of the two diffracted wave amplitudes. If the diffracted X-Rays are out of phase, destructive interference will result in a zero amplitude of the two diffracted X-Rays and thus no peak is observed [1].

Consider the parallel atomic planes given in figure 7.1, showing the incident and diffracted X-Rays. The angle of incidence is given by  $\theta$ , where the angle  $2\theta$ , gives the experimentally measured angle.

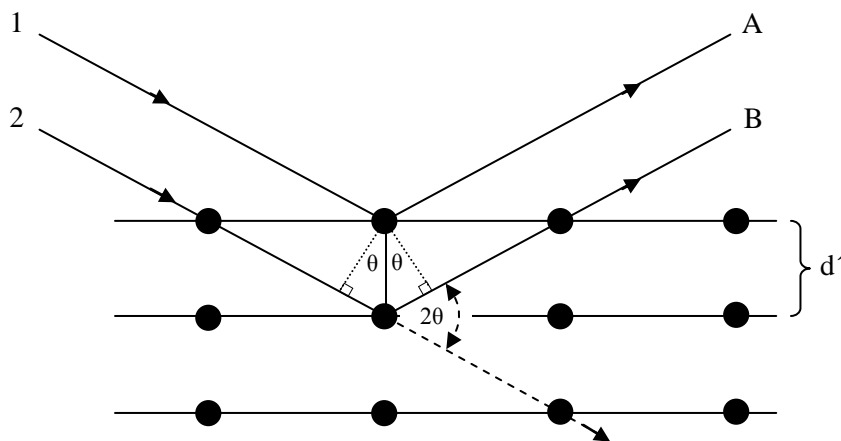


**Figure 7.1:** Schematic showing the diffraction of X-rays from two parallel crystal planes in order to illustrate the principle of operation behind the technique X-Ray Diffraction (XRD).

From figure 7.1, the total path difference,  $x$ , between the X-Rays marked 1 and 2 when they arrive at point A and B respectively is given by equation 7.1

$$x = 2d' \sin \theta . \quad (7.1)$$

For constructive interference to occur, the path difference has to be equal to a whole number of wavelengths,  $n\lambda$ , where  $n$  is a whole number. Inserting this condition into equation 7.1 results in equation 7.2 [1]

$$n\lambda = 2d' \sin\theta \quad n = 1, 2, 3 \dots \quad (7.2)$$

Equation 7.2 is Bragg's Law, which is the condition required for diffraction to occur. To ensure that different values of  $n$ , results in the same  $d$  value it is more convenient to make use of equation 7.3 [1]

$$\lambda = 2d \sin\theta \quad (7.3)$$

where

$$d = \frac{d'}{n} \quad (7.4)$$

Equation 7.3 was used in chapter 8, Experimental results, in order to determine the periodicity of the different grains detected in the polycrystalline Fe samples measured.

## 7.2.2. Apparatus

The *D8 ADVANCE* X-Ray diffractometer used in the analyses of the polycrystalline Fe samples is shown in figure 7.2.



*Figure 7.2: The D8 ADVANCE X-Ray diffractometer used for the determination of the crystal orientations present in polycrystalline Fe samples.*

The *D8 ADVANCE* diffractometer consists of the following components:

1. Copper (Cu) X-Ray source
2. LynxEye powder diffraction detector
3. Goniometer
4. Ni filter of 0.02 mm thickness
5. Rotating sample stage
6. Fixed slit of width 0.6 mm and rotary absorber

The experimental set-up of the sample relative to the X-Ray source and detector is shown in figure 7.3. The various components listed above are indicated in figure 7.3 [2].

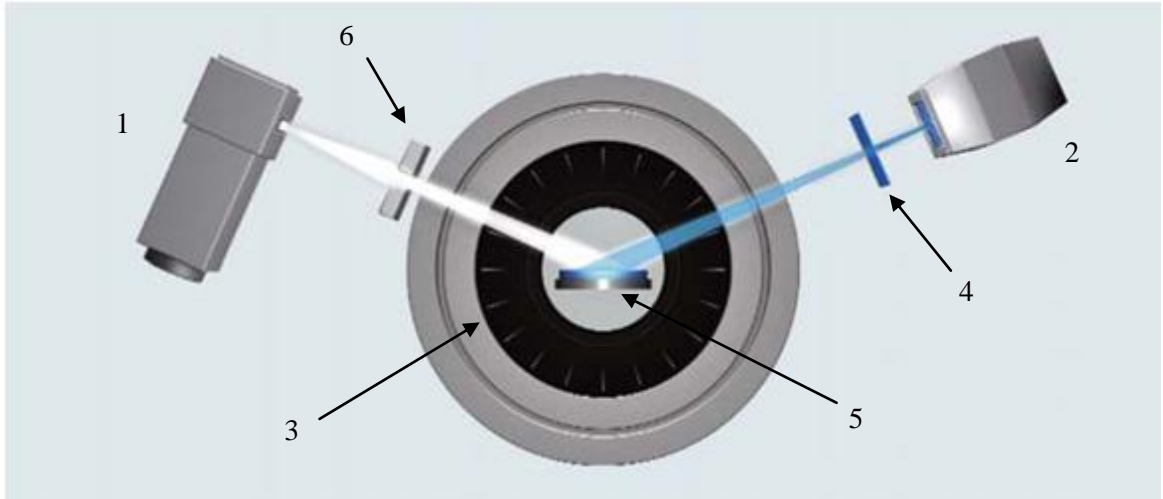


*Figure 7.3: Experimental set-up used for X-Ray diffraction, showing the position of the X-Ray source and detector relative to the sample being analysed.*

### 7.2.3. System settings

In order to obtain the maximum peak intensities of the crystal orientations present in the Fe samples and to minimize the background, a number of tests were performed to optimize the experimental parameters. The optimized parameters used in all the measurements conducted in this study are given in table 7.1. Figure 7.4 gives the XRD spectra obtained for an un-doped Fe sample using the experimental parameters given in table 7.1.

**Table 7.1:** Optimized parameters of the D8 ADVANCE X-Ray diffractometer used to determine the crystal orientations present in the Fe samples.

	<b>Parameter</b>	<b>Value</b>
<b>X-Ray source</b>	Voltage	40 kV
	Current	40 mA
	Slit width	0.6 mm
	Rotary absorber	On
<b>Detector</b>	Filter	Nickel (Ni) 0.02 mm
<b>Measurement settings</b>	Time per step	1 s
	Step size	0.0085 °
	Mode	Coupled two theta
	Rotation	On

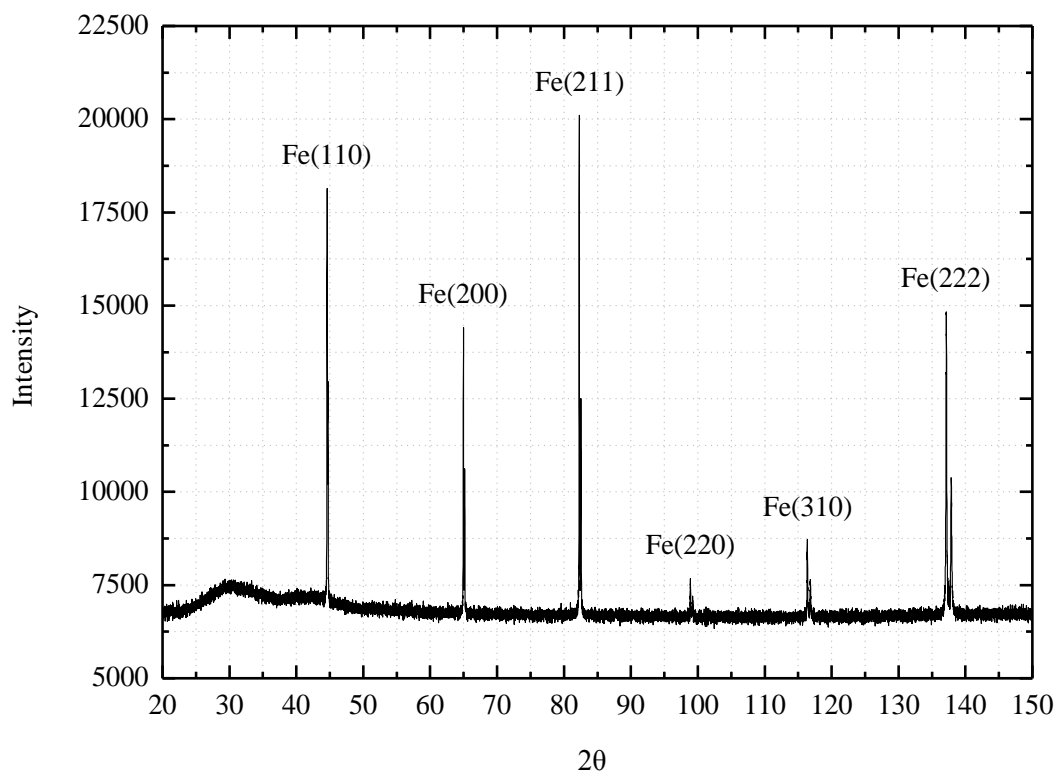


**Figure 7.4:** XRD spectra of a polycrystalline Fe sample measured using the experimental parameters given in table 7.1

From figure 7.4, XRD peaks are seen to form a doublet, this is especially noticeable at the higher values of  $2\theta$ . This doublet is due to the presence of both the  $K_{\alpha 1}$  and  $K_{\alpha 2}$  copper X-Rays which have wavelengths of respectively 1.540 Å and 1.544 Å [1]. These wavelengths are so close to one another that they are indistinguishable by the Ni filter.

## 7.3. Auger Electron Spectroscopy (AES)

Auger electron spectroscopy was used to obtain both qualitative and quantitative information on the Fe samples analysed. The diffusion of S in Fe was investigated by means of depth profile analysis and the effect S has on the grain sizes were investigated by obtaining SED images of the sample surface. Surface segregation of the non-metal impurities in polycrystalline bcc Fe were also studied using AES. The basic principle of operation for Auger electron spectroscopy, along with the two different spectrometers used and their respective experimental parameters are described in this section.

### 7.3.1. Principle of operation

Auger electron spectroscopy is the bombardment of a sample with high energy (3-25 keV) electrons, resulting in the ionization of a core energy level in the atoms. An electron from a higher energy level within the atom fills the ionized level and in doing so emits an amount of energy equal to the difference between the two energy levels. This emitted energy is transferred to a third electron, which is emitted as an Auger electron. The Auger process is illustrated in figure 7.5 [3; 4; 5].

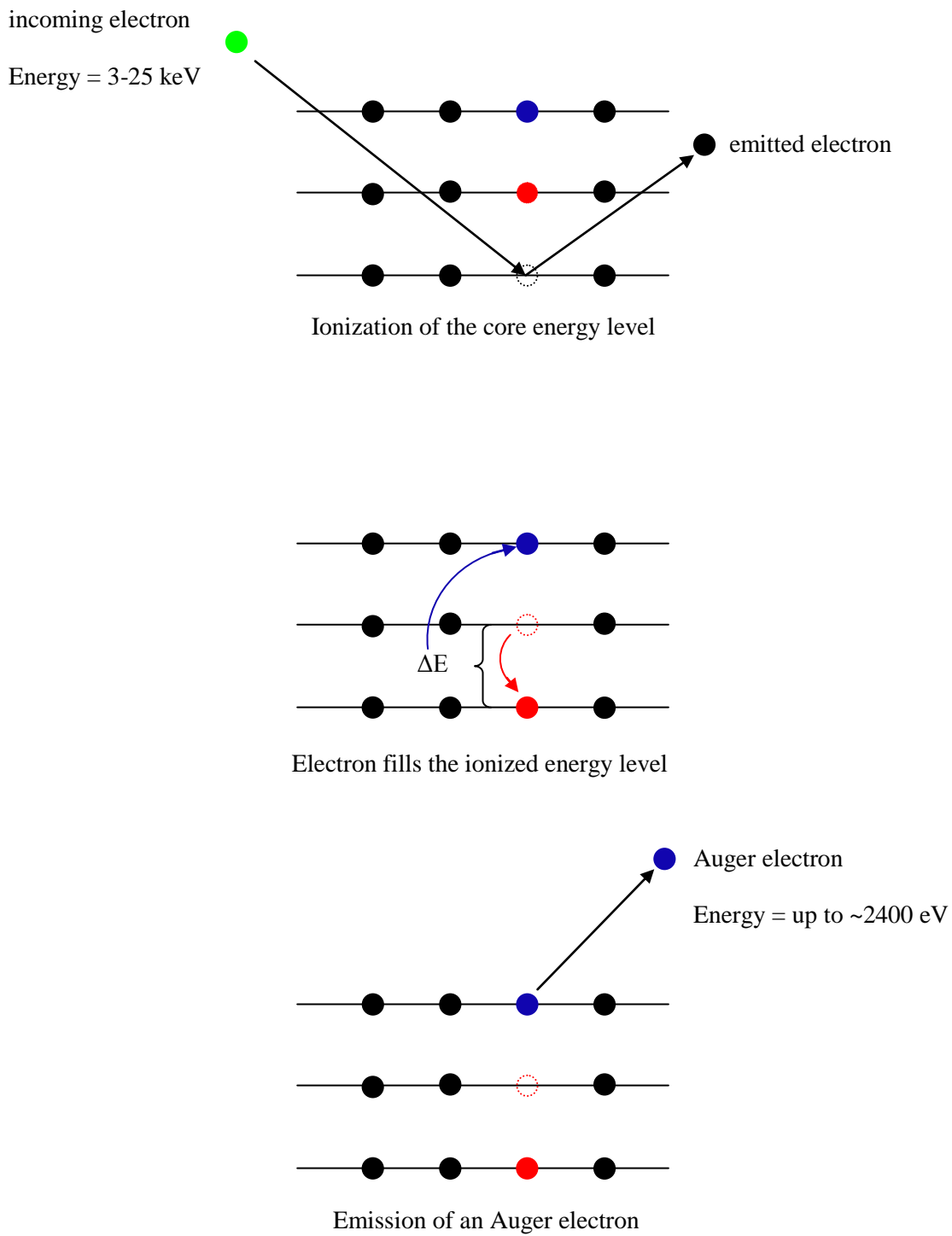


**Figure 7.5:** Illustration of the 3 steps for the emission of an Auger electron in order to explain the principle of operation for the technique Auger Electron Spectroscopy (AES).

It is evident from figure 7.5 that the energy of the Auger electron is independent of the primary electron beam energy and is only dependant on the energy difference between the ionized energy level and the energy level from which the electron, replacing the emitted electron, comes from. This energy difference is unique for each element and thus by analysing the energy of the Auger electron, the element being analysed can be identified. It should also be noticed that the Auger process requires 3 electrons, which is the reason Auger electron spectroscopy cannot be used to analyse samples containing H or He [5].

### **7.3.2. Apparatus**

This section describes the equipment and the experimental set-up used in Auger analysis of the Fe samples. Two different systems were used, the SAM 590 Auger system was used to study surface segregation, while the PHI 700 Auger Nanoprobe was used in depth profile analysis, elemental mapping and SED imaging. Both systems were manufactured by the Physical Electronics Company. Each system is specifically suited for its purpose, the SAM 590 Auger system is equipped with a heating stage and a PID control unit for temperature studies. The PHI 700 Auger Nanoprobe has a small beam diameter provided by the field emission tip of the electron gun which makes this system ideal for SED imaging. Figure 7.6 shows an image of the SAM 590 Auger system used to study the surface segregation of non-metal impurities in bcc Fe.



*Figure 7.6: The SAM 590 Auger system used in the study of non-metal impurity surface segregation in polycrystalline bcc Fe.*

The SAM 590 consists of the following components:

- Rotary and turbo molecular fore pumping combination
- Ion pump capable of reaching pressures down to  $\sim 10^{-9}$  Torr
- Physical electronics electron gun equipped with a LaB<sub>6</sub> filament (Model: 18-085)
- Single pass cylindrical mirror analyser, CMA (Model: 25-110)
- Physical electronics Auger system control (Model: 11-055)
- Physical electronics electron multiplier supply (Model: 20-075)
- Physical electronics lock-in amplifier (Model: 32-010)
- Perkin-Elmer ion gun (Model: 11-065)
- A heating stage fitted onto the sample stage for segregation studies
- Software package for controlling the voltages on the CMA plates via the control unit, and for data capturing

The PHI 700 Nanonprobe used in the study of depth profile analysis, elemental mapping and grain growth is shown in figure 7.7 [6].



**Figure 7.7:** The PHI 700 Auger Nanoprobe used for obtaining depth profiles, elemental maps and SED images of the polycrystalline bcc Fe samples.

The PHI 700 Auger Nanoprobe consists of the following components:

- Rotary and turbo molecular fore pumping combination
- Ion pump capable of reaching pressures down to  $\sim 10^{-9}$  Torr
- ULVAC PHI electron beam power supply (Model 18-197)
- ULVAC PHI electron gun control for the field emission tip (Model 20-630)
- Single pass cylindrical mirror analyser, CMA (Model: 25-140)
- ULVAC PHI ion gun control (Model 11-066)
- Smartsoft-AES version 4.1.3.2 software package for controlling the system and recording of data.

Figure 7.8 shows a schematic representation of the sample position relative to the electron and ion gun. The set-up is similar for the SAM 590 and PHI 700 Auger Nanoprobe with the sample in both systems positioned at an angle of 30 degrees relative to the ion and electrons guns. The only difference in set-up between the two systems is the position of the electron gun. For the SAM 590

Auger system the electron gun is positioned horizontally, while the electron gun of the PHI 700 Auger Nanoprobe is positioned vertically.

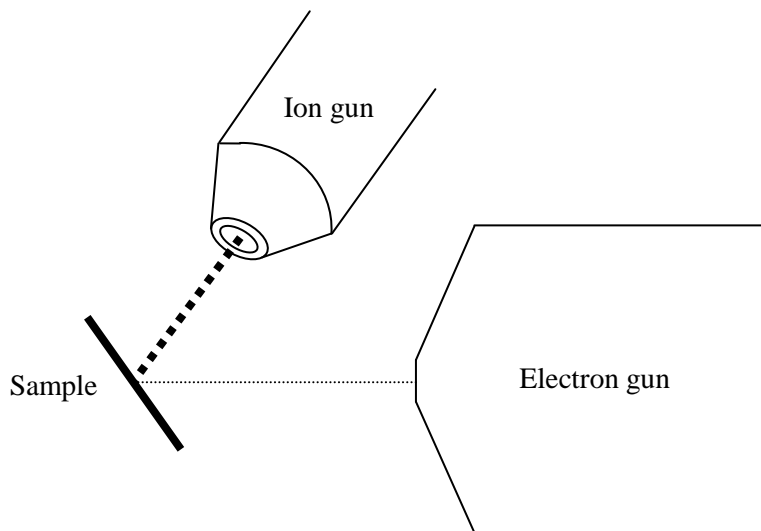


*Figure 7.8: Schematic of the sample position relative to the ion and electron gun in the AES systems. For both the SAM 590 and the PHI 700 Auger Nanoprobe spectrometers the sample was positioned at an angle of 30 degrees with respect to the ion and electron guns.*

### 7.3.3. System configuration and calibration

The systems were switched on and allowed to stand for a couple of hours to ensure that the electronic components are warmed up before measurements were started. If the electronic components of the system are not properly warmed up before being used, the Auger signal starts to drift during measurements due to a temperature change of the electronic components. The electrical current of both the electron gun and ion gun filaments were slowly increased to allow the filaments to degas. Once they reached the required electrical current the filaments remained at that current for one hour to ensure stability of the filaments before measurements were started. This procedure of filament degassing was only carried out for the SAM 590, since the filaments of the PHI 700 system is always kept on. Once the systems were ready, the 66 eV and 922 eV Auger peaks of a copper (Cu) standard were used to calibrate the energy scale for the respective systems. A number

of test were done in order to determine the optimum parameters for the Auger systems, ensuring that the maximum peak-to-peak heights were obtained and that the signal noise was reduced to a minimum. Table 7.2 contains the optimized parameters used in all measurements conducted on the SAM 590.

*Table 7.2: Optimized settings used on the SAM 590 system to ensure that the maximum Auger peak-to-peak heights are obtained and that the signal noise is reduced to a minimum.*

	<b>Parameter</b>	<b>Value</b>
<b>Electron gun settings</b>	Primary beam voltage	5 keV
	Primary beam voltage (elastic peak)	2 keV
	Emission current	0.15 mA
	Beam current	0.95 $\mu$ A
	Beam diameter	163.5 $\mu$ m
<b>Ion gun settings</b>	Argon beam voltage	2 kV
	Beam current	65 nA
	Beam current (with raster on)	12.5 nA
	Emission current	25 mA
	Pressure	2 mPa
	Raster size	2 $\times$ 2 mm
<b>Measurement settings</b>	Scan rate	5 eV/s
	Modulation voltage	2 eV
	Sensitivity	100
	Time constant (measurements)	0.1 s
	Time constant (elastic peak)	0.03 s
	Photomultiplier voltage (measurements)	2.350 keV
Photomultiplier voltage (elastic peak)	1.850 keV	

The settings used on the PHI 700 Auger Nanoprobe are tabulated in table 7.3.

**Table 7.3:** *Optimized settings used on the PHI 700 Auger Nanoprobe to ensure that the maximum Auger peak-to-peak heights are obtained and that the signal noise is reduced to a minimum.*

	<b>Parameter</b>	<b>Value</b>
<b>Electron gun</b>	Primary beam voltage	25 keV
	Primary beam voltage (elastic peak)	1 keV
	Emission current	280 $\mu$ A
	Beam current	0.5 nA
	Beam diameter	20 nm
<b>Ion gun</b>	Argon beam voltage	2 kV
	Beam current	2 $\mu$ A
	Beam current (with raster on)	2 $\mu$ A
	Emission current	12.5 mA
	Pressure	15 mPa
	Raster size	1 $\times$ 1 mm
	Sputter rate	27 nm/min
<b>Measurement settings</b>	Energy per step	1 eV
	Time per step	50 ms
	Number of differentiation points	13
	Photomultiplier voltage (measurements)	2.2 keV
	Photomultiplier voltage (elastic peak)	2.2 keV

### **7.3.4. Electron beam size determination**

The beam diameter determines the area on the sample from which the Auger electrons will be generated. For surface segregation studies a larger beam diameter is required in order to obtain information over a larger area on the sample. For the study of polycrystalline samples where different grain orientations are present it is important to obtain Auger information over a larger area to avoid local effects such as grain boundaries. The diameter of the electron beam for each of the systems used was determined by placing the electron beam in the centre of the Faraday cup and

scanning it across the side of the cup. This provides information of the electron beam current intensity as a function of distance, shown in figure 7.9 for the electron beam of the SAM 590.

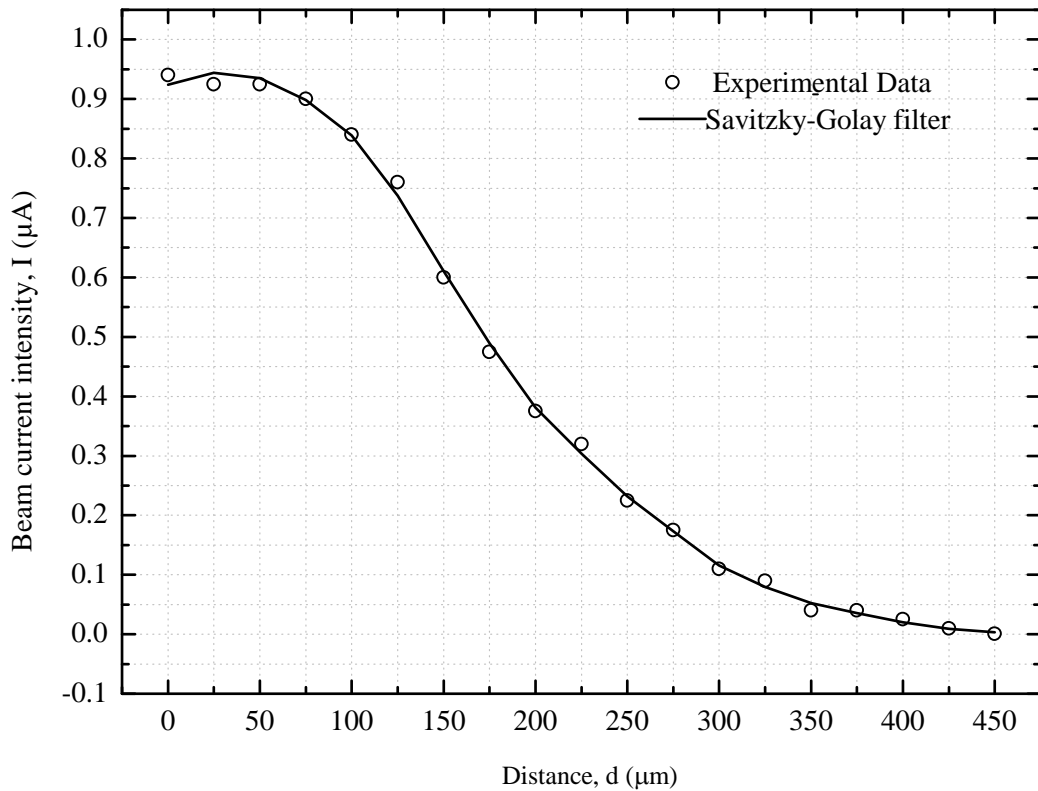


**Figure 7.9:** Electron beam current intensity as a function of distance scanned on the Faraday cup.

The data obtained for the electron beam current intensity as a function of distance scanned, was smoothed by applying the Savitzky-Golay filter of grade 2 and width 6. This ensured that a smooth curve was obtained which can be differentiated without the occurrence of spikes. Differentiation of the Savitzky-Golay curve in figure 7.9 resulted in a graph, figure 7.10, from which the beam diameter can be calculated using the full width half maximum method (FWHM).

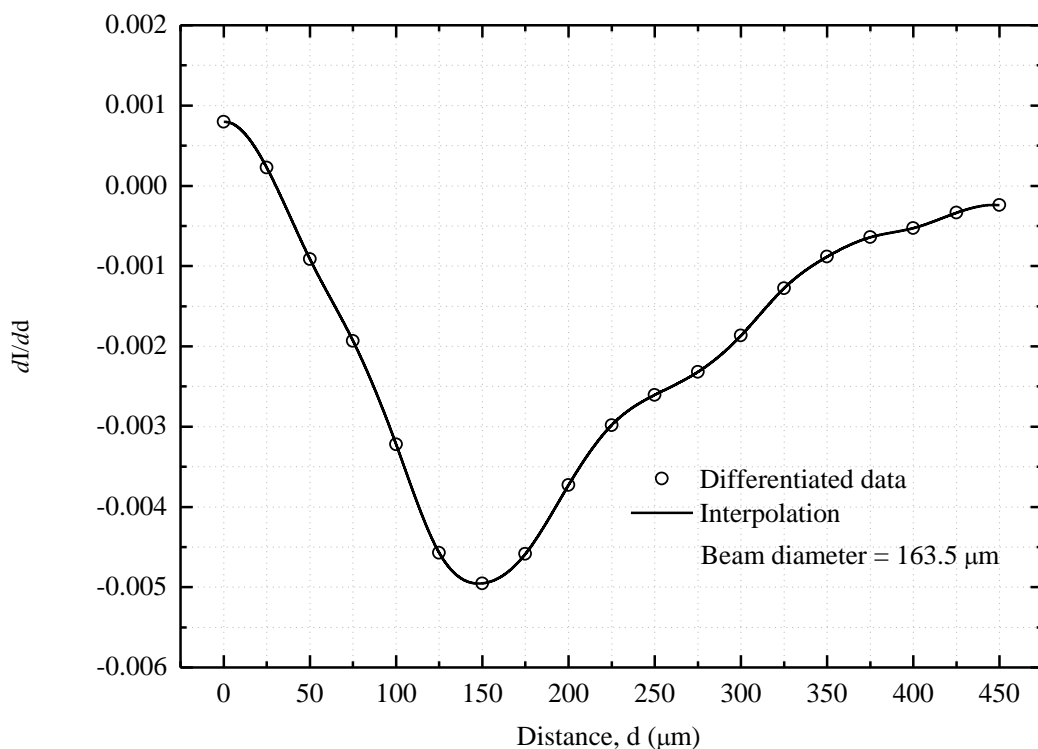


**Figure 7.10:** Differentiated electron beam current intensity as a function of distance scanned on the Faraday cup.

The above method was used to determine the beam sizes of both Auger spectrometers used in this study. For the SAM 590 Auger system a beam diameter of 163.5  $\mu\text{m}$  was obtained using the settings described in table 7.2. For the PHI 700 Auger Nanoprobe a beam diameter of 20 nm was obtained using the settings described in table 7.3.

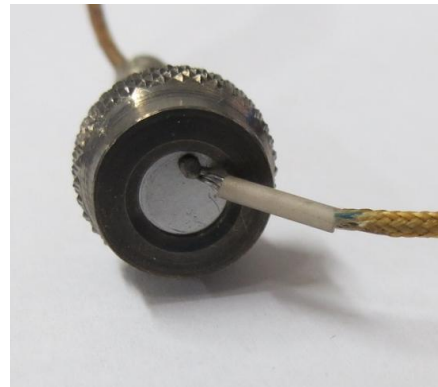
### 7.3.5. Temperature measurements

In the study of surface segregation, the Fe samples were mounted onto a heating stage located onto the sample stage of the SAM 590 Auger system. The required temperature was obtained by applying a high electrical current to the tungsten filament of the heating stage. The temperature was measured by a type K thermocouple located underneath the sample, between the sample and the

heater, and controlled using a PID control unit. This thermocouple does not give an accurate value for the temperature of segregation. Large amounts of heat are lost through the Fe surface due to radiation. Considering that the segregated atoms come from the near surface layers, it is more correct to use the surface temperature as the temperature for segregation. Thus the temperature measured by the computer during data capturing needs to be scaled to obtain the true segregation temperature. In order to obtain the relationship between the measured temperature at the back of the sample and the segregation temperature (surface temperature), a type K thermocouple was spot welded to the surface of a test sample. Figure 7.11 illustrates the thermocouples connected beneath the sample and on the surface of the test sample respectively.



(a)



(b)

**Figure 7.11:** (a) Thermocouple placed beneath the sample to measure the temperature during surface segregation experiments. (b) A thermocouple spot welded to the surface of a test sample.

The relationship between the surface temperature and the temperature measured by the thermocouple beneath the sample is given in figure 7.12.

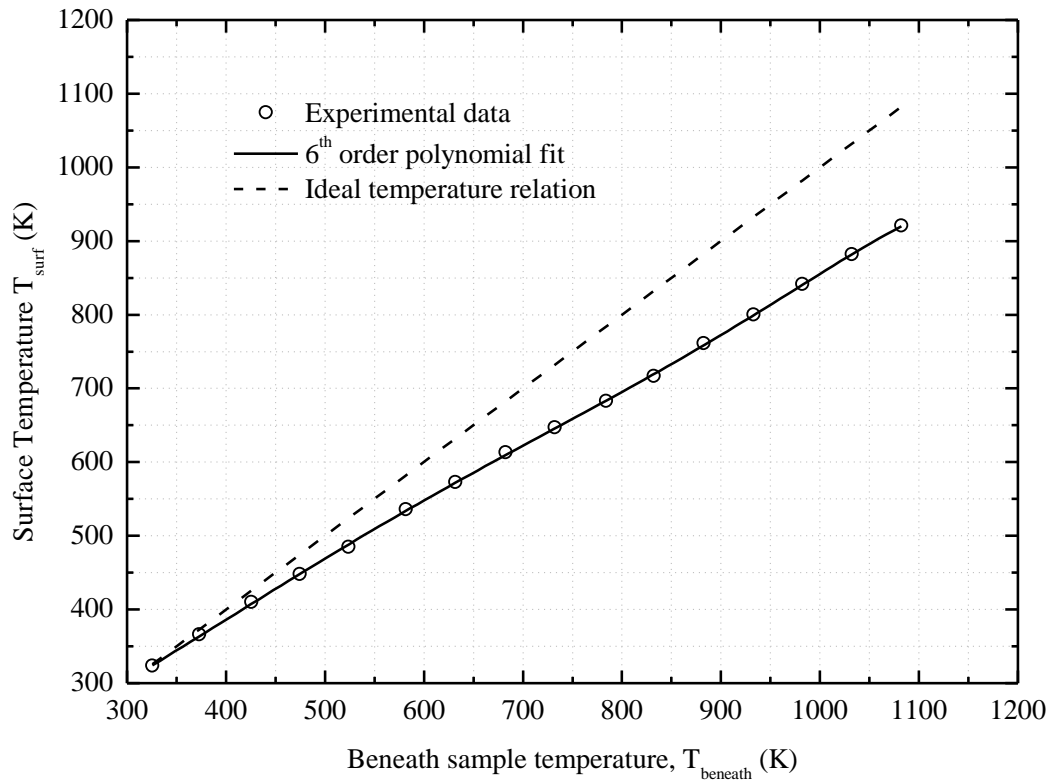


**Figure 7.12:** Relationship between the surface temperature and the temperature beneath the Fe sample mounted onto the heating stage of the SAM 590.

Fitting of a 6<sup>th</sup> degree polynomial gave an accurate descriptions of the relationship between the surface temperature and the temperature beneath the sample. This polynomial model was used to obtain the segregation temperature (surface temperature) for all the segregation experiments performed in this study.

## 7.4. Auger quantification

In order to obtain the atomic concentrations of the elements in the system under study, the measured Auger peak-to-peak heights (APPH) need to be quantified. Depending on the system under study, various quantification methods exist. Three different methods of Auger quantification will be discussed here: the basic Palmberg method, the quantification of atoms segregated onto a surface using the layer approach and the quantification of depth profiles using the method for homogeneous samples.

### 7.4.1. Palmberg method

The method of Palmberg is the most basic form of Auger quantification. Equation 7.5 gives the mathematical expression for the Palmberg quantification formula [3; 4]

$$C_i = \frac{\frac{I_i}{I_i^*}}{\sum_j^n \frac{I_j}{I_j^*}} \quad (7.5)$$

where  $I_i$  is the Auger intensity,  $I_i^*$  is the sensitivity factor and  $C_i$  is the fractional concentration of element  $i$ . The denominator in equation 7.5 performs a summation over all  $n$  elements in the system. The formula neglects the matrix factors of the system under study and cannot be used to provide a final answer for the elemental concentrations. It is frequently used as a first approximation to the quantification of Auger data, as is done in this study.

## 7.4.2. Segregated layer/monolayer quantification

For the quantification of elements segregated to the surface of a material, the system can be considered as an infinite number of layers. This enables the quantification of elements as a function of their escape depth in the sample. This is called the layer approach and is described by du Plessis [7].

The Auger yield for element A is given by equation 7.6 [4; 7]

$$I_A = I_0 T(E_A) D(E_A) \sigma_A(E_p) R_A \sum_{n=0}^{\infty} N_A(nd) \exp[-nd / \lambda_A \cos \theta] \quad (7.6)$$

Where  $I_0$  is the primary electron beam current,  $T(E_A)$  is the transmission efficiency of the electron spectrometer and  $D(E_A)$  is the efficiency of the electron detector. The ionization cross section of the core level responsible for the Auger transition with an electron energy of  $E_p$ , is given by  $\sigma_A(E_p)$ . To account for the backscattering of electrons the term  $R_A$  is included. The atomic density of element A at a distance of  $nd$  from the surface is given by the symbol  $N_A(nd)$ , with  $d$  as the layer thickness and  $n$  the atomic layer of interest. The distance travelled by an Auger electron from where it is generated in the material to the surface of the material is given by  $\lambda_A \cos \theta$ , where  $\lambda_A$  is the inelastic mean free path and  $\theta$  is the angle of emission relative to the surface normal. For the pure element A, the Auger intensity is given by equation 7.7

$$I_A^* = \text{const} \sigma_A(E_p) R_A^* \sum_{n=0}^{\infty} N_A^*(nd^*) \exp[-nd_A^* / \lambda_A^* \cos \theta] \quad (7.7)$$

where the symbol \* is used to indicate the use of a pure element. The primary electron beam current, the transmission efficiency of the spectrometer and the efficiency of the electron detector were taken as constants (const) in equation 7.7. The Auger yield for element A in the alloy is given by equation 7.8

$$I_A = \text{const } \sigma_A(E_p) R_A^M N^M \left[ X_A^\phi + \sum_{n=1}^{\infty} X_A^{bulk} \exp(-nd^M / \lambda^M \cos \theta) \right] \quad (7.8)$$

where  $X_A^\phi$  is the surface concentration of element A and  $X_A^{bulk}$  is the bulk concentration of element A in the alloy. Solving equation 7.7 for  $\sigma_A$  and substituting the result into equation 7.8 delivers equation 7.9

$$I_A = \frac{I_A^* R_A^* N_B^M}{R_A^* N_A^* \sum_{n=0}^{\infty} \exp(-nd_A^* / \lambda_A^* \cos \theta)} \left[ X_A^\phi + \sum_{n=1}^{\infty} X_A^{bulk} \exp(-nd^M / \lambda^M \cos \theta) \right]. \quad (7.9)$$

For element B a similar expression is obtained, given by equation 7.10

$$I_B = \frac{I_B^* R_B^* N_A^M}{R_B^* N_B^* \sum_{n=0}^{\infty} \exp(-nd_B^* / \lambda_B^* \cos \theta)} \left[ X_B^\phi + \sum_{n=1}^{\infty} X_B^{bulk} \exp(-nd / \lambda^M \cos \theta) \right]. \quad (7.10)$$

Taking the ratio of the Auger yields for the two elements in the alloy, results in equation 7.11

$$\frac{I_A}{I_B} = \frac{I_A^* R_A^M R_B^* N_B^M \sum_{n=0}^{\infty} \exp(-nd_B^* / \lambda_B^* \cos \theta)}{I_B^* R_B^M R_A^* N_A^M \sum_{n=0}^{\infty} \exp(-nd_A^* / \lambda_A^* \cos \theta)} \times \frac{\left[ X_A^\phi + \sum_{n=1}^{\infty} X_A^{bulk} \exp(-nd^M / \lambda^M \cos \theta) \right]}{\left[ X_B^\phi + \sum_{n=1}^{\infty} X_B^{bulk} \exp(-nd^M / \lambda^M \cos \theta) \right]}. \quad (7.11)$$

The first term of equation 7.11 is defined by equation 7.12

$$\alpha_{AB} = \frac{I_A^* R_A^M R_B^* N_B^M \sum_{n=0}^{\infty} \exp(-nd_B^* / \lambda_B^* \cos \theta)}{I_B^* R_B^M R_A^* N_A^M \sum_{n=0}^{\infty} \exp(-nd_A^* / \lambda_A^* \cos \theta)}. \quad (7.12)$$

The sensitivity factors  $I_A^*$  and  $I_B^*$  were determined for the spectrometer using elemental standards. For the exponential expressions in the second term, the symbols  $\beta_A$  and  $\beta_B$  can be defined as given by equations 7.13 and 7.14

$$\beta_A = \sum_{n=1}^{\infty} \exp(-nd^M / \lambda^M \cos \theta) \quad (7.13)$$

$$\beta_B = \sum_{n=1}^{\infty} \exp(-nd^M / \lambda^M \cos \theta). \quad (7.14)$$

Substituting equations 7.12-7.14 into equation 7.11 results in the final expression, equation 7.15

$$\frac{I_A}{I_B} = \alpha_{AB} \frac{X_A^\phi + \beta_A X_A^{bulk}}{X_B^\phi + \beta_B X_B^{bulk}}. \quad (7.15)$$

Equation 7.15 is not limited to a binary system and can be expanded to  $m-1$  expressions in  $X^\phi$  for a system consisting of  $m$  components.

The backscattering coefficients,  $R$ , were calculated using the expression of Shimizu [3; 8], equation 7.16

$$R = 1 + (0.462 - 0.777 Z^{0.20})U^{-0.32} + (1.15 Z^{0.20} - 1.05). \quad (7.16)$$

where  $Z$  is the atomic number for the element of interest and  $U$  is the ratio of the primary electron beam voltage over the binding energy of the core electron responsible for the Auger transition. The layer thickness,  $d$ , for each element was calculated as the sum of the atomic diameter for the respective elements plus the atomic diameter of Fe. The value of the atomic diameter,  $a$ , was calculated using equation 7.17

$$1000 \rho N_A a^3 = M \quad (7.17)$$

where  $\rho$  is the density,  $N_A$  is Avogadro's number with a value of  $6.022 \times 10^{23}$  [9] and  $M$  is the atomic mass for the element of interest.

For the calculation of the inelastic mean free path the TPP-2 method proposed by Tanuma, Powell and Penn [10], equation 7.18, was used

$$\lambda = \frac{E}{\left\{ E_p^2 \left[ \beta \ln(\gamma E) - \left( \frac{C}{E} \right) + \left( \frac{D}{E^2} \right) \right] \right\}} \quad (7.18)$$

where  $E$  is the electron energy and  $E_p$  is the free-electron plasmon energy. Each of the symbols used in equation 7.18 are defined by the expressions given below

$$E_p = 28.8 \left( \frac{N_v \rho}{M} \right)^{\frac{1}{2}}$$

$$\beta = -0.0216 + \frac{0.944}{E_p} + 7.39 \times 10^{-4} \rho$$

$$\gamma = 0.191 \rho^{-0.50}$$

$$U = \frac{N_v \rho}{M}$$

$$C = 1.97 - 0.91U$$

$$D = 53.4 - 20.8U$$

In the above equations  $N_v$  is the number of valance electrons of an element. The values for the matrix, denoted by the superscript  $M$  are calculated as a weighed sum of the elements in the matrix. For an alloy consisting of  $n$  elements the matrix values are calculated by:

$$\rho^M = \sum_i^n X_i^{bulk} \rho_i$$

$$M^M = \sum_i^n X_i^{bulk} M_i$$

$$Z^M = \sum_i^n X_i^{bulk} Z_i$$

$$d^M = \sum_i^n X_i^{bulk} d_i$$

The atomic density,  $N$ , were taken to be the same for all elements, since 95 % of Auger electrons originates from the first three atomic layers [5] where the atomic density of the segregating element and the matrix are assumed to be equal.

To illustrate the Palmberg and the layer approach of quantification, a segregation profile was quantified using both methods. The segregation profile giving the APPH vs. temperature is shown in figure 7.13. The respective spectrums for the Palmberg and layer quantification methods are given in figures 7.14 (a) and 7.14 (b).

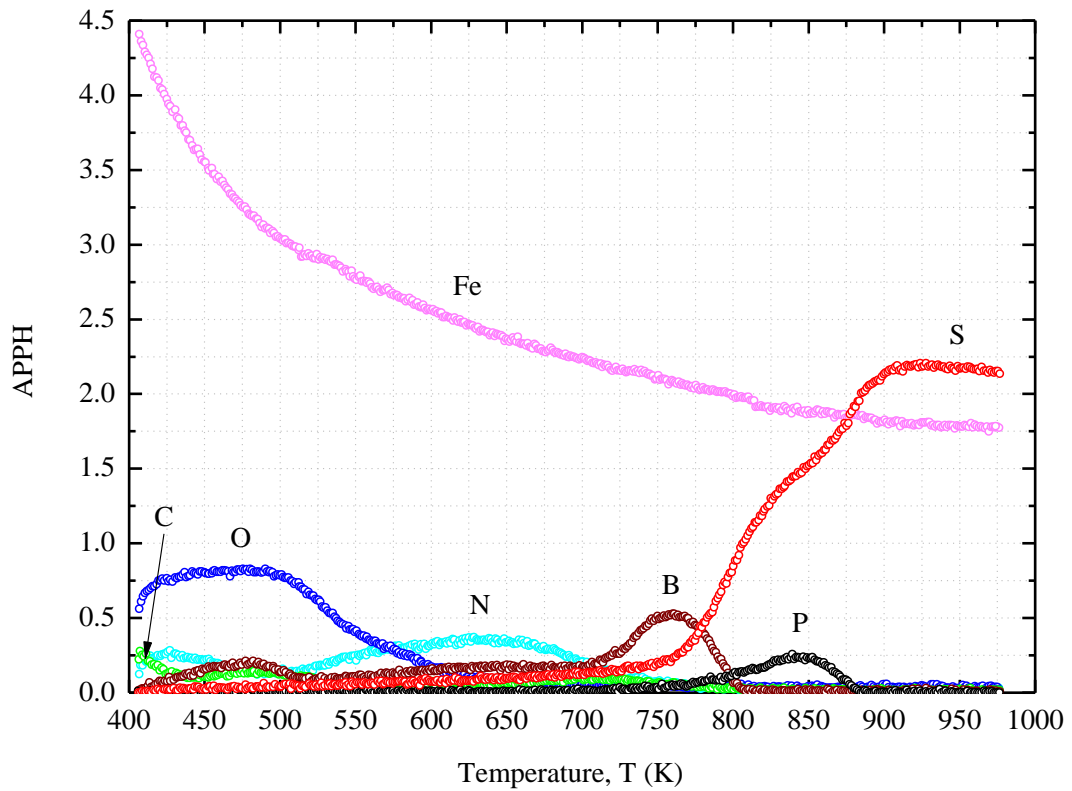


**Figure 7.13:** Auger data of a linear programmed heating segregation experiment performed on the polycrystalline Fe sample

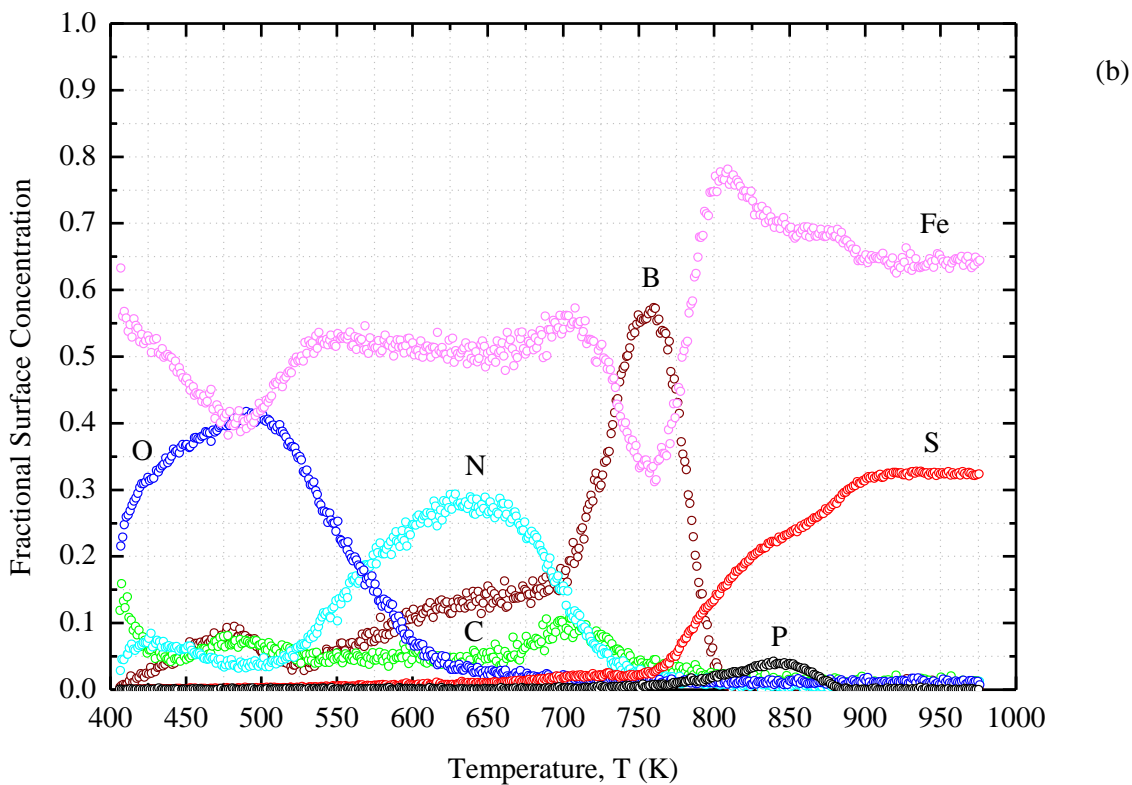
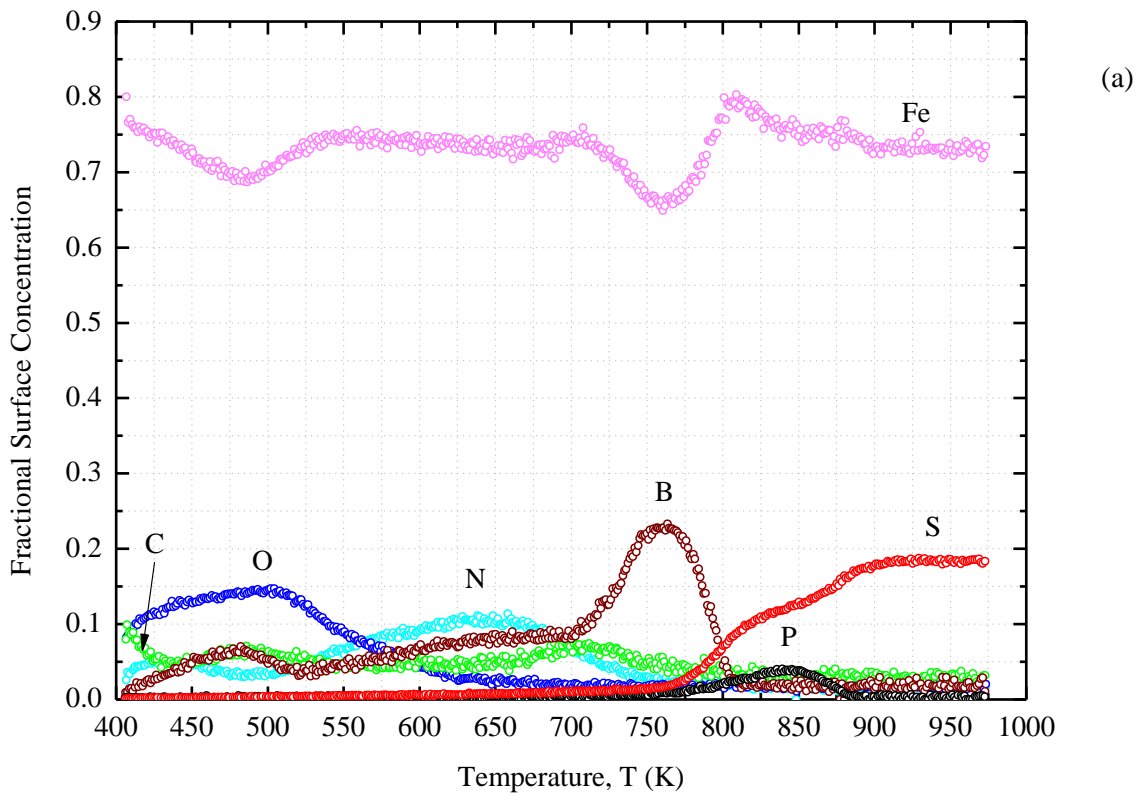


**Figure 7.14:** Fractional concentration of segregated atoms on the bcc polycrystalline Fe surface as determined by (a) the Palmberg and (b) the layer approach of quantification.

Comparing figures 7.14(a) and 7.14(b) shows that using the Palmberg method to quantify Auger data can result in differences of more than 14 % in the concentration for S. This is due to the neglect of the matrix factors in the Palmberg method. The layer approach is used throughout this study for the quantification of surface segregation data.

### 7.4.3. Quantification of homogenous samples

For an alloy consisting of elements which are distributed homogeneously throughout the matrix, the method described in this section can be used. This applies to the depth profiles performed in chapter 8, Experimental results. Equation 7.2 gives the Auger yield for element A, a similar expression can be obtained for the Auger yield of element B. To derive an expression with which the Auger data for a homogenous solid can be quantified, two assumptions are made. The first assumption is that the atomic density in the matrix is constant throughout resulting in equation 7.6 becoming equation 7.19 [4]

$$I_A = I_0 T(E_A) D(E_A) \sigma_A(E_p) R_A N_A \lambda_A \cos \theta \quad (7.19)$$

and for the pure element A, the Auger yield is give by equation 7.20

$$I_A^* = I_0 T(E_A) D(E_A) \sigma_A(E_p) R_A^* N_A^* \lambda_A^* \cos \theta. \quad (7.20)$$

Solving  $\sigma_A(E_p)$  for equation 7.19 and substituting the result in equation 7.20, results in equation 7.21

$$\frac{I_A}{I_A^*} = \frac{R_A N_A \lambda_A \cos \theta}{R_A^* N_A^* \lambda_A^* \cos \theta} \quad (7.21)$$

A similar expression can be derived for element B, and by taking the ratio of these two equations results in equation 7.22 [4]

$$\frac{I_A}{I_B} = \frac{I_A^* R_B^* N_B^* N_A \lambda_B^*}{I_B^* R_A^* N_A^* N_B \lambda_A^*}. \quad (7.22)$$

Using equation 7.23 [4]

$$\frac{N_B^* N_A}{N_A^* N_B} = \frac{X_A}{X_B} \left( \frac{a_A}{a_B} \right)^3 \quad (7.23)$$

Where  $a$  is given by equation 7.17. Equation 7.23 can be written as

$$\frac{I_A}{I_B} = \frac{I_A^* R_B^* \lambda_B^*}{I_B^* R_A^* \lambda_A^*} \frac{X_A}{X_B} \left( \frac{a_A}{a_B} \right)^3$$

$$\frac{I_A}{I_B} = \alpha_{AB} \frac{X_A}{X_B} \quad (7.24)$$

where the term,  $\alpha_{AB}$ , is given by equation 7.25

$$\alpha_{AB} = \frac{I_A^* R_B^* \lambda_B^*}{I_B^* R_A^* \lambda_A^*} \left( \frac{a_A}{a_B} \right)^3. \quad (7.25)$$

Equation 7.24 was derived here for components A and B, but is not limited to a binary system. If a multi-component system is studied consisting of  $m$  elements,  $m-1$  equations can be obtained in  $X$ . For the calculation of the backscattering coefficients,  $R$ , the method of Shimizu, given by equation

7.16, described earlier was used and for the calculation of the inelastic mean free path,  $\lambda$ , the TPP-2 method was used.

For the quantification methods described in sections 7.4.2 and 7.4.3, the Nelder-Meads optimization method was used to solve the system of linear equations. The Palmberg method was used to provide initial values for the optimization process.

To illustrate the quantification of Auger data using the method described here for homogenous samples, the depth profile of S diffused into Fe in figure 7.15 was quantified using both the Palmberg method and the method for homogenous samples. The results are respectively given by figures 7.16(a) and 7.16(b).

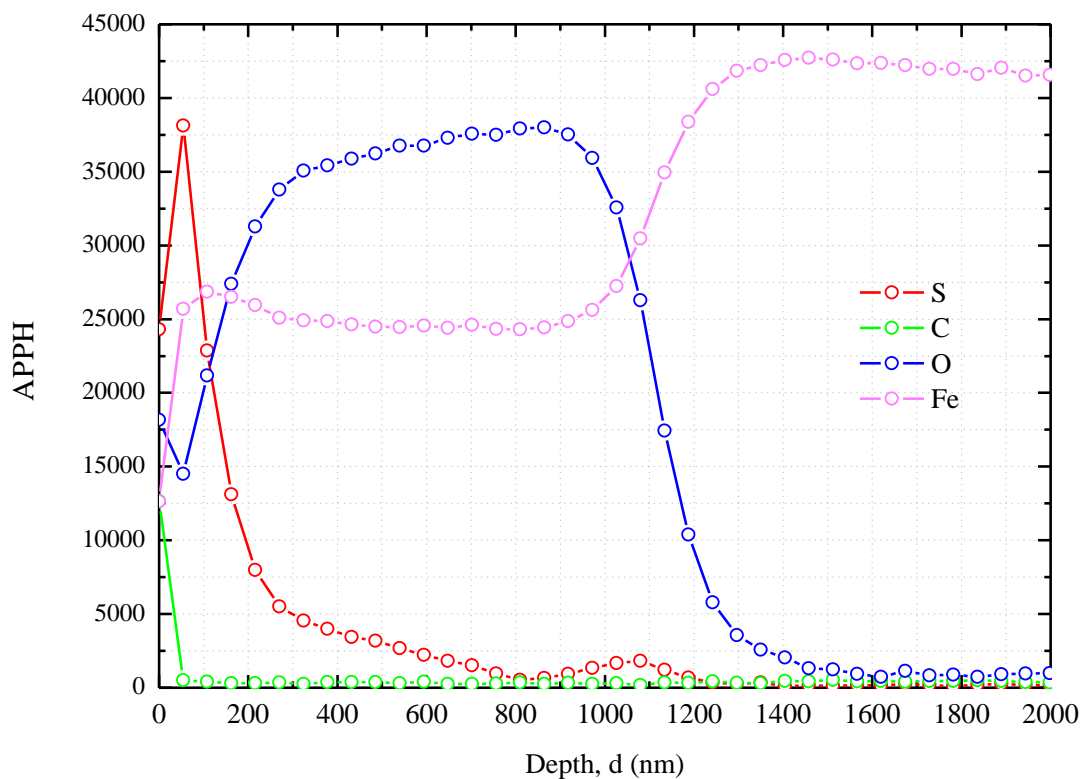


**Figure 7.15:** Depth profiles of a S doped Fe sample given as the Auger peak-to-peak height as a function of depth (

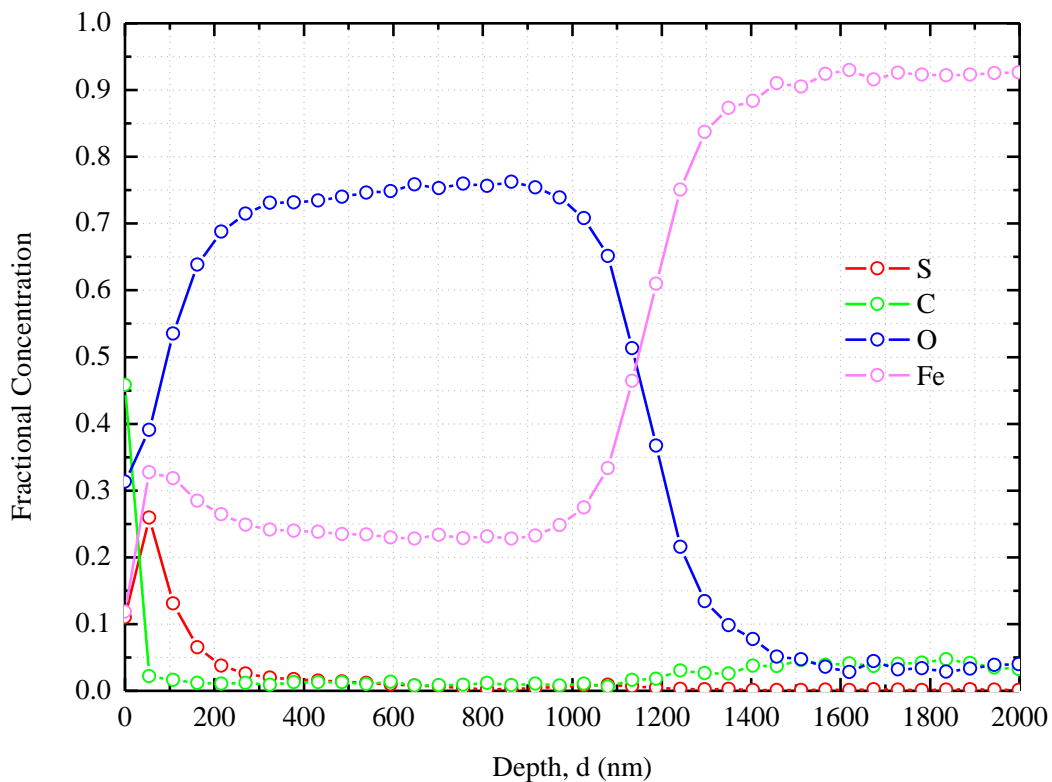
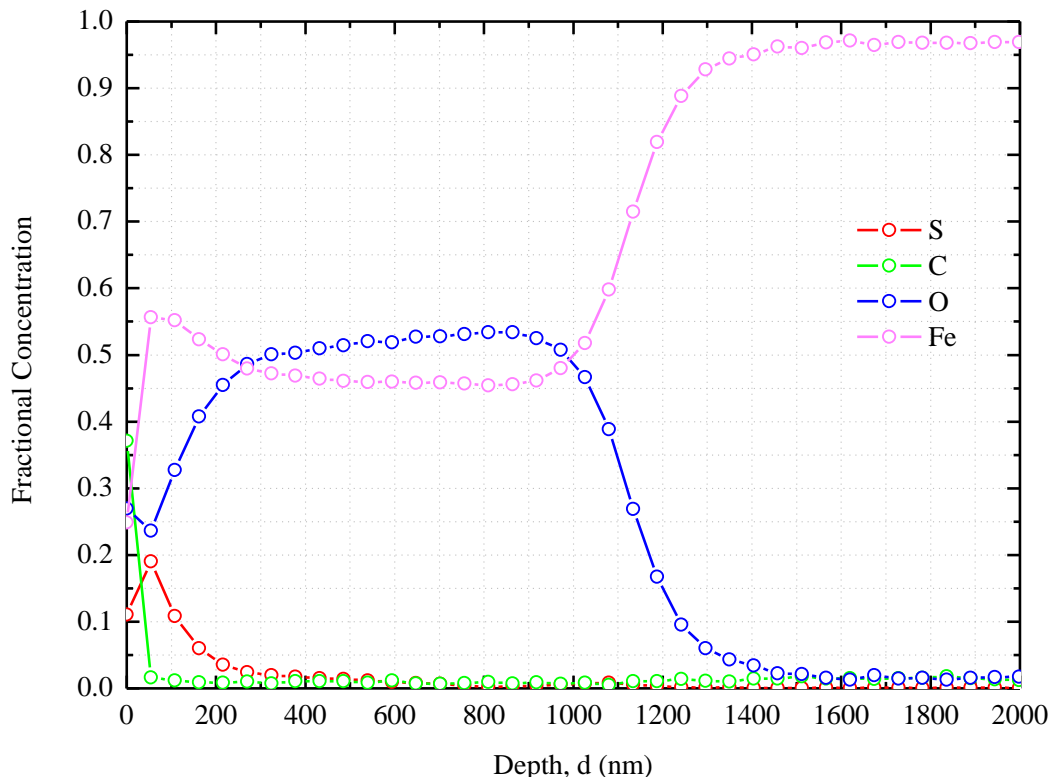


**Figure 7.16:** Depth profile of the S doped Fe sample, showing the concentration of elements as determined by the quantification method for (a) Palmberg and (b) homogenous samples.

Comparing the depth profiles given by figure 7.16(a) and figure 7.16(b), shows that by neglecting the matrix factors results in concentration differences of up to 30 % for O and 7 % for S. The use of Palmberg to describe the elemental concentrations of segregated atoms results in larger differences compared to the quantification of homogenous samples. The method described here for homogenous samples were used to quantify the depth profiles of the Fe samples in chapter 8, Experimental results.

## 7.5. Experimental procedure for segregation measurements

The segregation of non-metal impurities in bcc Fe was studied by increasing the temperature linearly in the range 410-975 K in increments of 0.01 K/s.

1. Before measurements were performed on the crystal for the first time, the sample was annealed for 24 hours at 915 K to ensure that no depletion regions were present in the sample.
2. After the 24 hour annealing process the sample was allowed to cool to 488 K at a rate of -0.05 K/s. Thereafter the sample was allowed to cool uncontrolled to room temperature (298 K).
3. For segregation measurements the sample was preheated to 410 K, until the heating unit reached a stable temperature.
4. The sample was then sputter cleaned for 10 min using  $\text{Ar}^+$  ions to remove any surface contaminants.
5. After sputter cleaning the surface, the recording of data was started immediately. The Ar gas in the system was pumped out.
6. Segregation profiles were recorded while the temperature was linearly increased at a rate of 0.01 K/s
7. Once the sample reached its maximum temperature of 975 K, the sample was linearly cooled to 488 K at a rate of -0.05 K/s and then cooled to room temperature uncontrolled.

8. The sample was then annealed at 915 K for 12 hours to ensure that depletion regions that occurred during the previous segregation run were restored. After the 12 hours the sample was linearly cooled to 488 K at a rate of -0.05 K/s. It was then allowed to cool to room temperature at an uncontrolled rate.
9. Steps 3-8 were repeated for the next segregation run

The results obtained using the above experimental procedure are given in chapter 8, Experimental results.

## 7.6. Summary

This chapter described the experimental techniques used in this study with the emphasis on the equipment used. For XRD measurements the D8 ADVANCE diffractometer from BRUKER is described. Auger Spectroscopy was the primary experimental technique used throughout this study and was performed by the PHI 700 Auger Nanoprobe and the SAM 590 from the Physical Electronics Company. To obtain elemental concentrations from Auger data, Auger quantification was described in detail.

## 7.7. References

- [1]. B.D. Cullity, S.R. Stock, Elements of X-Ray diffraction, Prentice Hall, New Jersey, 2001.
- [2]. BRUKER, D8 ADVANCE highlights at a glance, BRUKER.
- [3]. D. Briggs, J.T. Grant, (Eds.), Surface analysis by Auger and X-Ray Photoelectron Spectroscopy, IM Publications and SurfaceSpectra Limited, United Kingdom, 2003.
- [4]. D. Briggs, M.P. Seah, (Eds.), Practical surface analysis by auger and Photoelectron spectroscopy, John Wiley & Sons, New York, 1983.

- [5]. J.M. Walls, (Ed.), *Methods of surface analysis*, Cambridge University Press, Cambridge, 1989.
- [6]. *Scanning auger Nanoprobe*, Tsinghua University Analysis Center, 2010.
- [7]. J. du Plessis, *Surface Segregation*, Sci-Tech Publications, Bloemfontein, 1990.
- [8]. R. Shimizu, *JPN. J. APPL. PHYS.* 22 (1983) 1631.
- [9]. K.J. Laidler, J.H. Meiser, B.C.Sanctuary, *Physical chemistry*, Houghton Mifflin company, 2003.
- [10]. S. Tanuma, C.J. Powell, D.R. Penn, *Surf. Interface Anal.* 20 (1993) 77.



Part III  
Results and discussion



# Chapter 8: Experimental results

## 8.1. Introduction

This chapter presents the experimental findings for the study of S segregation and diffusion in polycrystalline bcc Fe. Results for the preparation of Fe-S samples, using the method described in chapter 6, Sample preparation, are presented here which confirms the successful doping of Fe with S using the newly proposed doping method and experimental set-up. The segregation of the non-metal impurities O, N, C, B, S and P in polycrystalline bcc Fe are discussed. Using the model of Fick for the case of linear programmed heating and the model of Guttmann which describes equilibrium segregation in ternary alloys, the segregation parameters of S and P in polycrystalline bcc Fe were extracted.

## 8.2. Sample composition

All the experimental results were performed on polycrystalline bcc Fe samples of purity 99.99+ %, supplied by the Goodfellows company in the U.K. The composition of the samples as specified by the manufacturer is given in table 8.1.

**Table 8.1:** Composition of the polycrystalline bcc Fe samples used in all experiments performed in this study.

<b>Element</b>	<b>Concentration, <i>C</i> (ppm)</b>
Aluminium (Al)	1.60
Arsenic (As)	0.12
Boron (B)	2.30
Carbon (C)	12.0
Cobalt (Co)	15.0
Chromium (Cr)	3.20
Copper (Cu)	2.00
Gallium (Ga)	0.29
Germanium (Ge)	5.90
Potassium (K)	0.23
Manganese (Mn)	0.87
Molybdenum (Mo)	0.28
Oxygen (O)	60.0
Phosphorus (P)	10.0
Sodium (Na)	0.25
Nitrogen (N)	10.0
Niobium (Nb)	<0.10
Nickel (Ni)	16.0
Silicon (Si)	36.0
Sulfur (S)	6.00
Tantalum (Ta)	<10.0
Titanium (Ti)	0.41
Vanadium (V)	0.49
Tungsten (W)	0.18
Zinc (Zn)	0.19

The concentration of S was determined as <6 ppm by set-point laboratories using LECO analysis and a concentration value of 6 ppm was used for S during this study.

### 8.3. Doping of Fe with S

This section gives the experimental findings obtained by the PHI 700 Auger Nanoprobe for the diffusion of S into Fe during the doping procedure. A polycrystalline Fe sample was doped for 50 s using the method described in chapter 6, Sample preparation. When the electrical current to the heater filaments was switched off and the sample allowed to cool, some S vapour were deposited onto the Fe surface forming a thin S layer. During annealing some of this thin S layer was observed to have evaporated off the Fe surface and into the quartz tube of the annealing oven. This statement is valid, considering that there is an amount of S deposited onto the Fe surface with a melting point of 393 K [1].

The doped sample, after removal from the doping chamber is shown in figure 8.1, with figure 8.2 showing a SED image of the structure of the deposited S layer on the Fe surface.

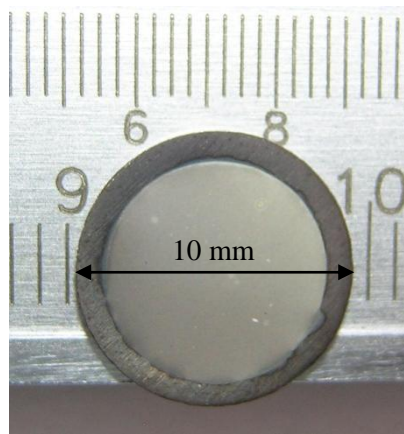


*Figure 8.1: Polycrystalline bcc Fe sample after being doped with S for a period of 50 seconds.*

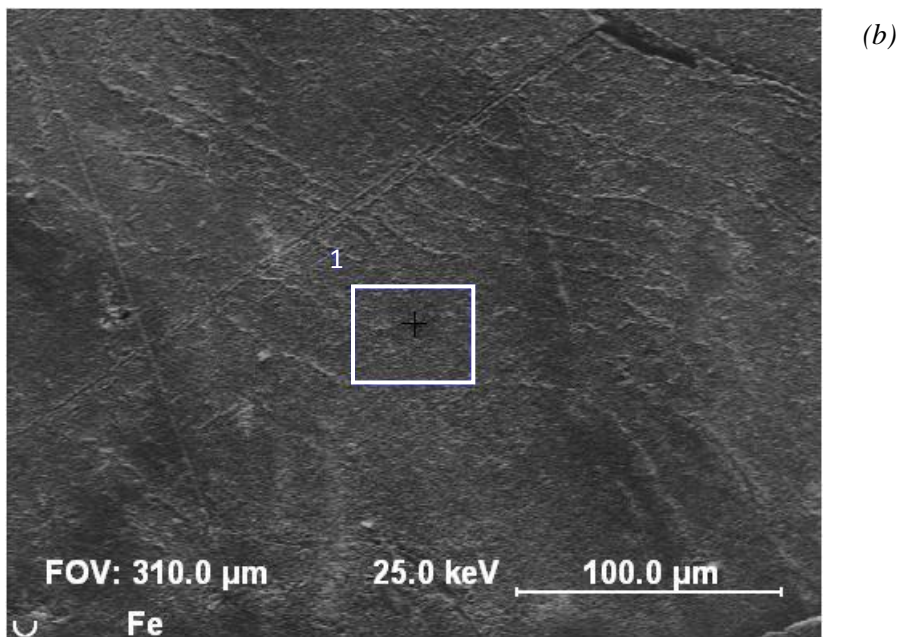
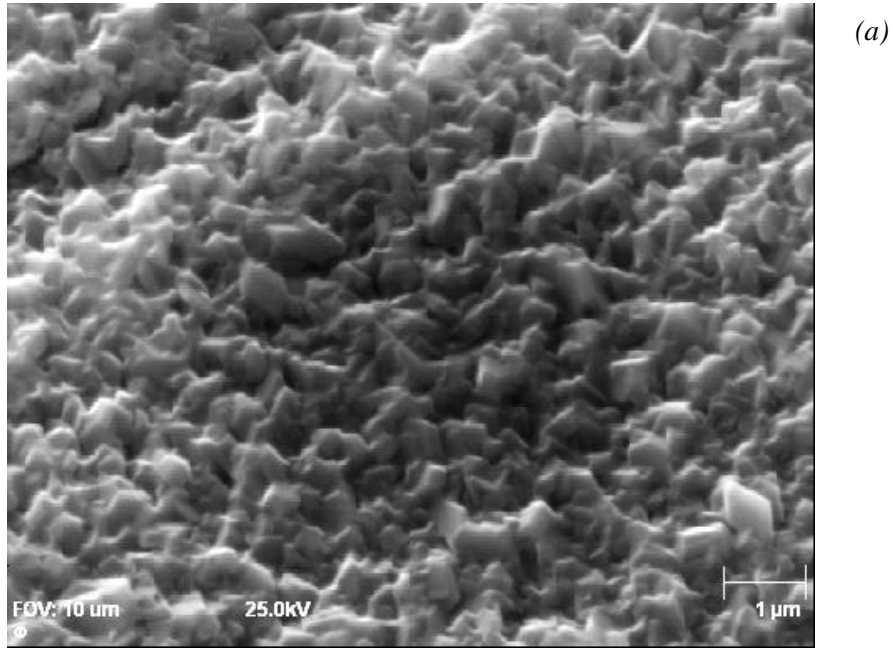


**Figure 8.2:** SED image showing the structure of the deposited S layer on the Fe sample surface, after the sample was doped with S for 50 seconds. (a) 10 μm field of view (b) 310 μm field of view.

The cap of the heater used to keep the sample in place prevented S from being deposited onto the outer ring of the sample shown in figure 8.1. The fraction of the Fe sample deposited with S was calculated by measuring the respective diameters of the Fe and S areas in figure 8.1. It was

calculated that a fraction of 0.65 was deposited with S during the doping process. This value along with the sample thickness of 0.38 mm is used later in this section to calculate the total S concentration of two differently doped Fe samples.

To establish this doping method as a viable method for the doping of Fe with S, two requirements had to be met. The first requirement was that experimental evidence for the diffusion of S into Fe had to be obtained and secondly it had to be shown that the concentration of S can be doubled by doubling the doping time. To achieve this, two samples were doped for respectively 25 s and 50 s. Auger depth profiling was performed on each of the samples to determine the diffusion profile of S in Fe. To avoid obtaining information from a local area such as a grain boundary, two areas of  $4 \mu\text{m}^2$  each were selected at a distance of  $22 \mu\text{m}$  apart as shown in the SED image of figure 8.3.

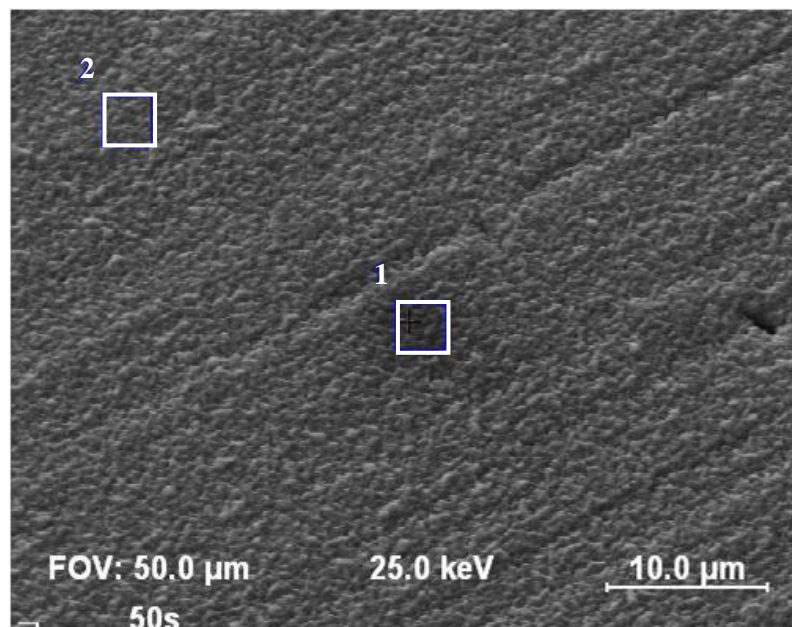


**Figure 8.3:** SED image showing the two areas selected for Auger depth profile analysis with dimensions of  $4 \mu\text{m}^2$  each, separated by a distance of  $22 \mu\text{m}$ .

The samples were eroded with  $\text{Ar}^+$  ions in intervals of 2 min at a rate of 27 nm/min for a total of 75 minutes. The results of the depth profiles performed on the two areas of the samples doped respectively for 25 s and 50 s are given by figures 8.4 and 8.5. Quantification of the depth profiles were performed using the method for homogeneous samples described in chapter 7, Experimental techniques.

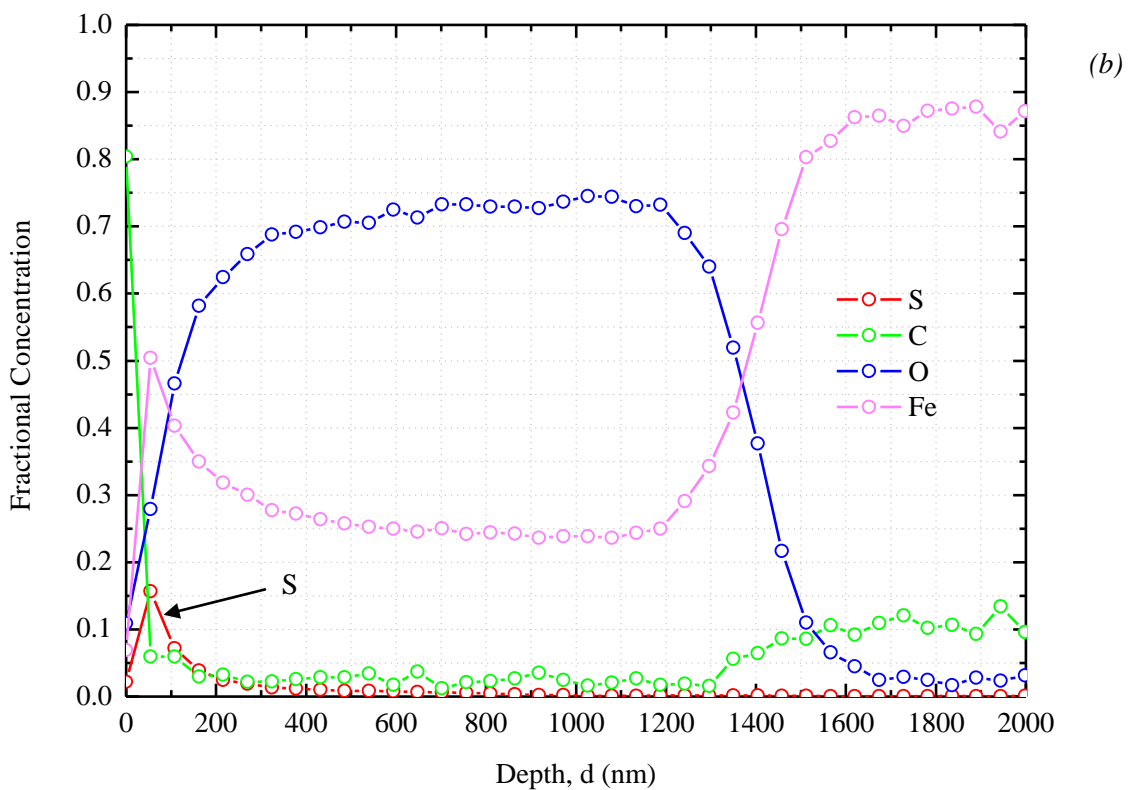
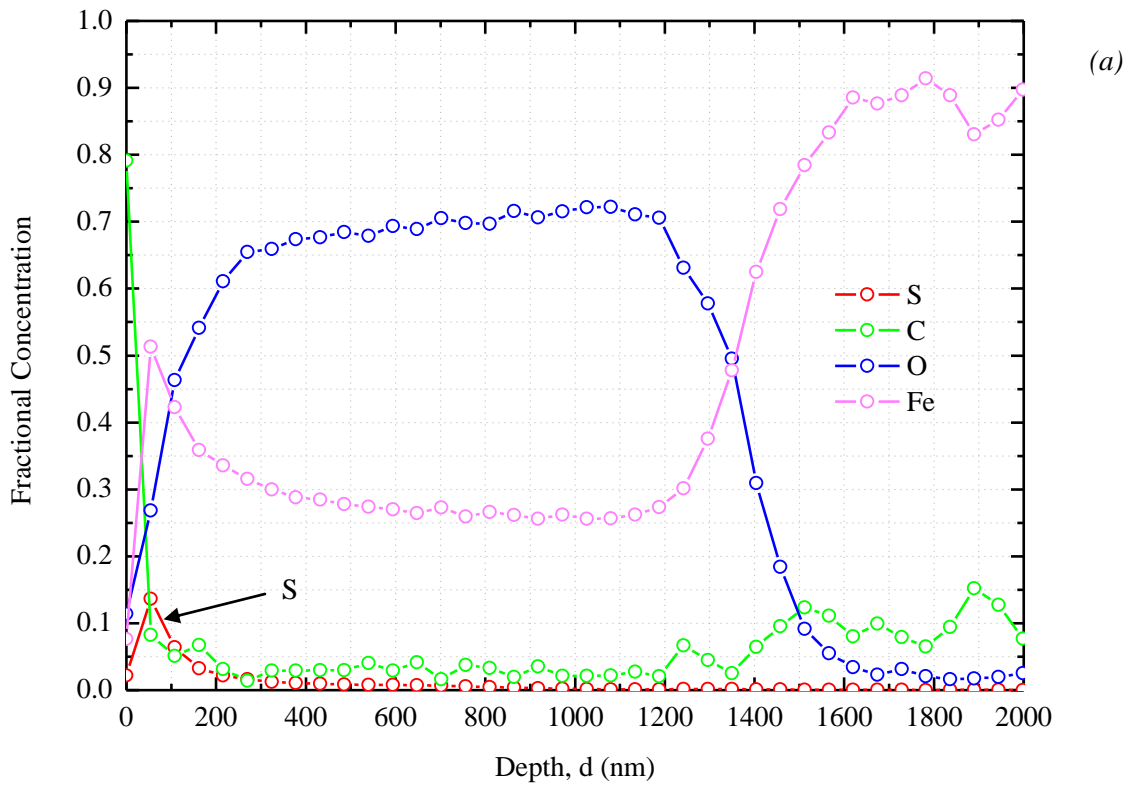


**Figure 8.4:** Auger depth profiles of the Fe sample doped with S for 25 seconds, showing the diffusion of S to a depth of 1026 nm (1.026  $\mu\text{m}$ ). (a) Area 1 (b) Area 2.

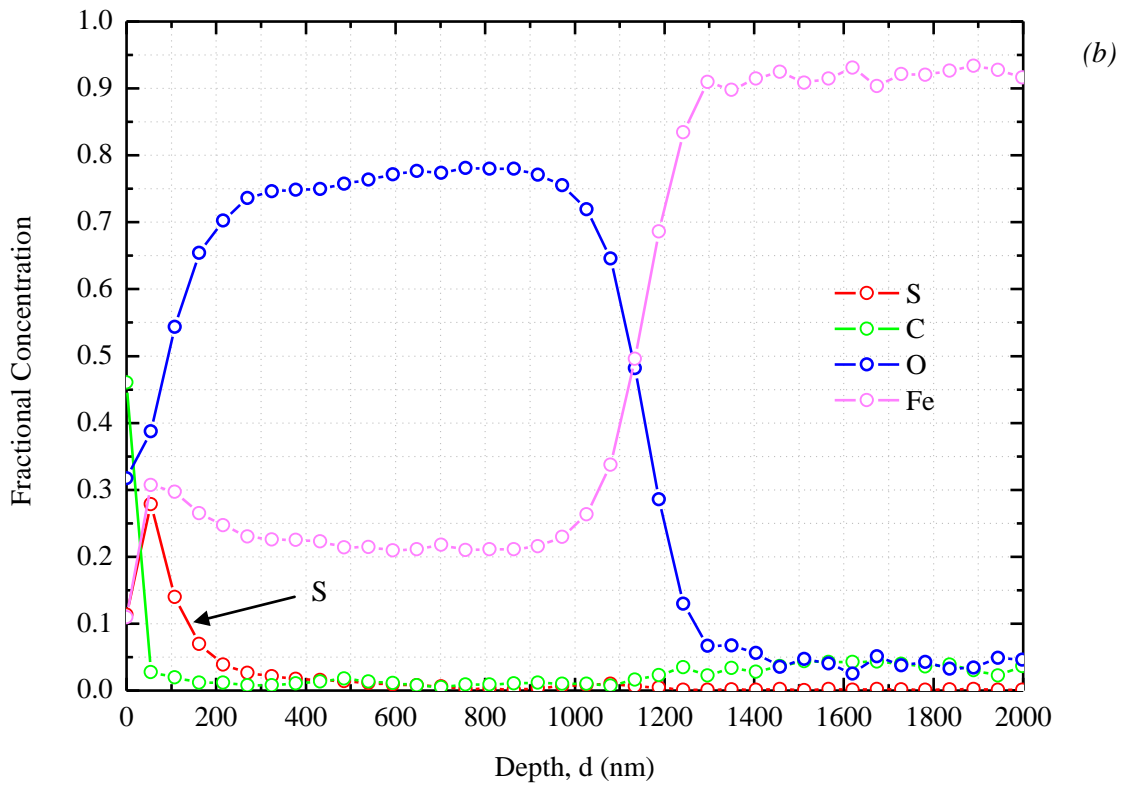
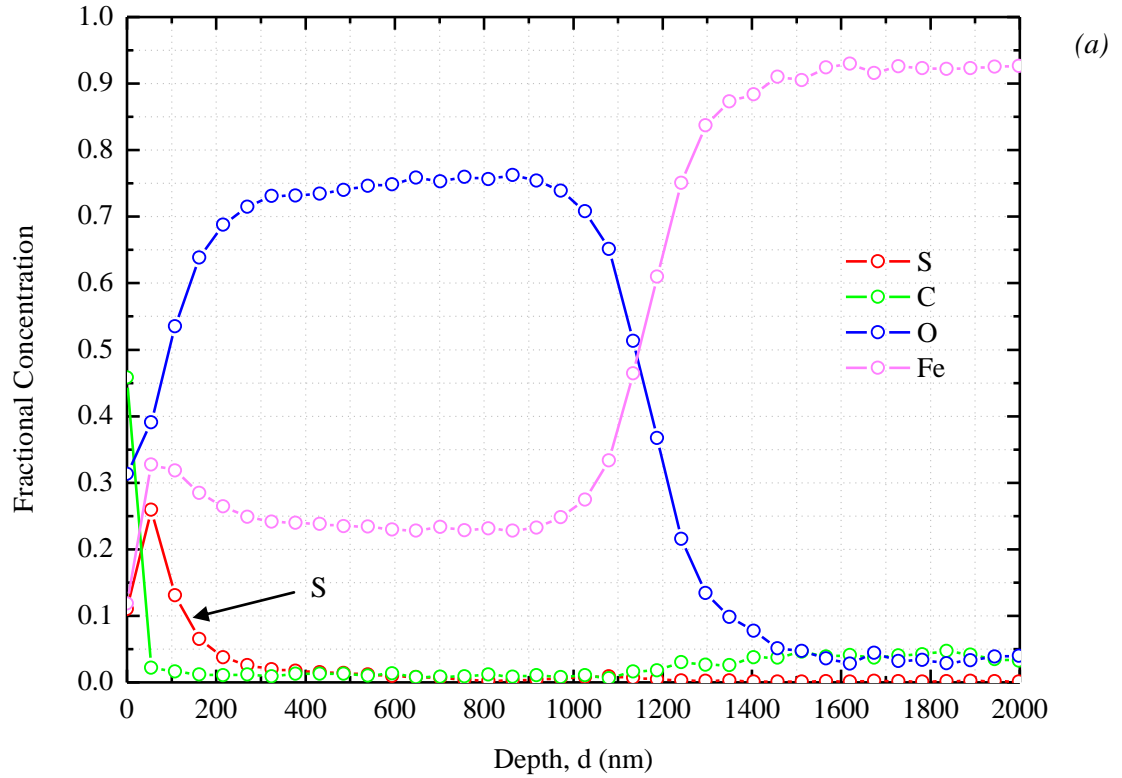


**Figure 8.5:** Auger depth profiles of the Fe sample doped with S for 50 seconds, showing the diffusion of S to a depth of 1242 nm (1.242  $\mu\text{m}$ ). (a) Area 1 (b) Area 2.

Figure 8.4 and 8.5 confirms that S has diffused into Fe to a total depth of 1026 nm (1.026  $\mu\text{m}$ ) for the sample doped for 25 s and to a depth of 1242 nm (1.242  $\mu\text{m}$ ) for the sample doped for 50 s. The presence of C were detected as a surface contaminant with a layer of thickness <50 nm, which were quickly removed by  $\text{Ar}^+$  ion sputtering. As the S concentration decreased with depth into the sample some C were once again observed at a depth of  $\sim 1300$  nm (1.300  $\mu\text{m}$ ) for the sample doped for 25 s and at a depth of  $\sim 1100$  nm (1.100  $\mu\text{m}$ ) for the sample doped for 50 s. This C region is a result of C that were present on the Fe surface before S doping, which diffused into the Fe sample during the preheating step of the doping process.

A strong O presence was observed in the samples which illustrates the ability of O to bind to Fe despite the fact that the samples were doped under clean conditions. The total thickness of the O layer for the two samples are 1350 nm (1.350  $\mu\text{m}$ ) for the sample doped for 25 s and 1134 nm (1.134  $\mu\text{m}$ ) for the sample doped for 50 s. Thus for the sample containing more S, less O was observed and it is concluded that the presence of S prevents the adsorption of O onto the Fe surface. This is in agreement with the observations made by Fujita *et. al.* [2], whom observed that the segregation of S to the Fe surface prevents the initial oxidation of Fe. The amount of O can be decreased by fitting a titanium (Ti) filament into the preparation chamber which can absorb the O impurities. The use of Ti as an absorber for O was employed during sample annealing which has shown to decrease the effect of sample oxidation. Figure 8.6 shows the average value of the two areas measured on the two samples doped for respectively 25 s and 50 s.

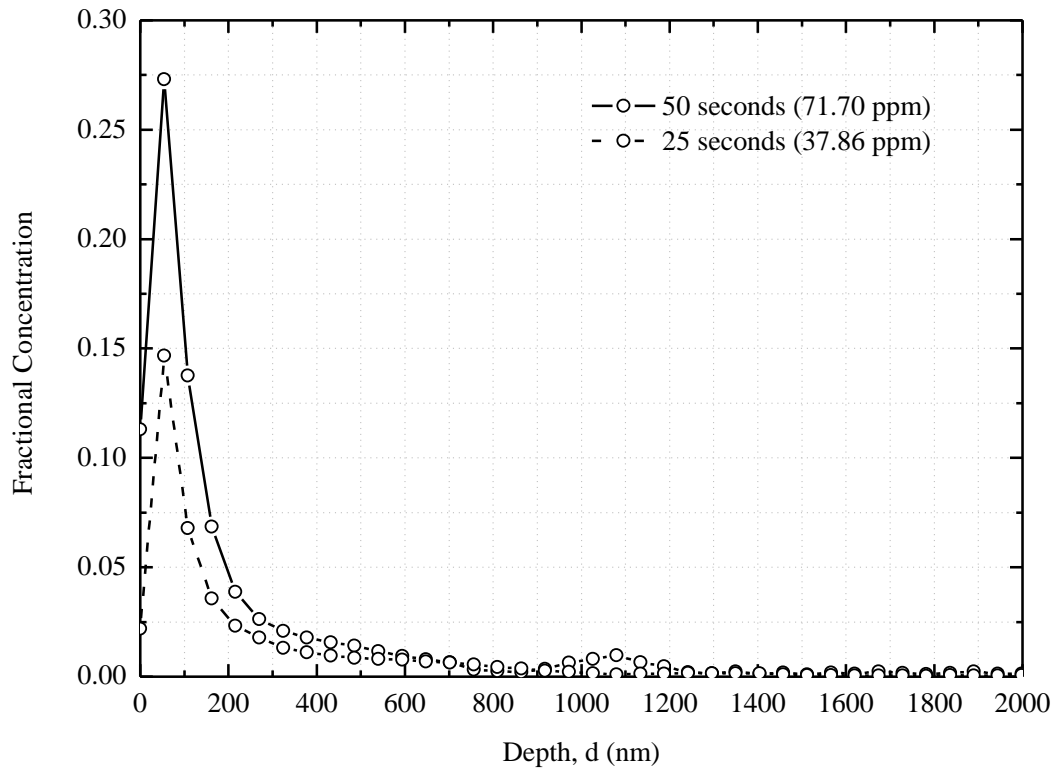


**Figure 8.6:** Comparison between the S diffusion profiles obtained during depth profile analysis of the Fe samples doped for 25 s and 50 s respectively.

The concentrations of the two differently doped Fe samples were calculated by integrating each of the S profiles in figure 8.6 which provided the total S area in the respective samples. Dividing this area by the total area of the Fe sample and multiplying this result by the fraction of the sample deposited with S (0.65), calculated earlier, resulted in the total S concentration of each sample. For the sample doped for 25 s a concentration of 37.86 ppm was calculated and for the sample doped for 50 s a concentration of 71.70 ppm was calculated. This proves that the new method of doping Fe with S proposed in chapter 6, Sample preparation, can be repeated for different time periods resulting in almost double (89.38 %) the S concentration. Table 8.2 contains all the values used in the calculation of the S concentration for the respective samples.

*Table 8.2: Values used in the calculation of the total S concentration which have diffused into the Fe samples doped at respectively 25 seconds and 50 seconds.*

	<b>S area, <math>A_S</math> (Fractional concentration.nm)</b>	<b>Fe area, <math>A_{Fe}</math> (Fractional concentration.nm)</b>	<b>Fraction of sample deposited with S</b>	<b>Concentration, C (ppm)</b>
<b>25 s</b>	22.13	380000.00	0.65	37.86
<b>50 s</b>	41.92	380000.00	0.65	71.70

## 8.4. Grain growth and surface effects of polycrystalline Fe

This section covers the effects observed on the surface of a S doped Fe sample after being annealed for 40 days at a temperature of 1073 K. Figure 8.7 shows the image of the S doped Fe sample after being removed from the annealing oven.

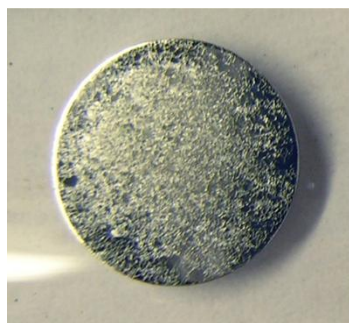


*Figure 8.7: The S doped Fe sample after being annealed for 40 days at a temperature of 1073 K.*

On careful inspection two different regions can be seen on the surface of the sample shown in figure 8.7, the region deposited with S (region A) and the outer ring of the sample not deposited with S (region B). The sample was placed in the PHI 700 Auger Nanoprobe to investigate the influence of S on the size of the Fe grains. An SED image of the sample is shown in figure 8.8, where the two regions of different grain sizes can be seen.

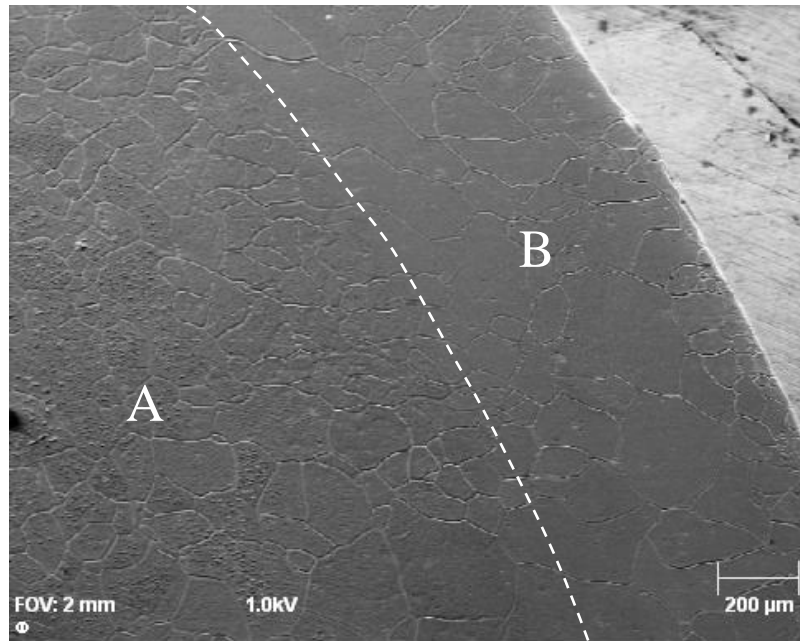


**Figure 8.8:** SED image of the S doped Fe sample after being annealed for 40 days at a temperature of 1073 K. Two regions can be identified on the Fe surface, the region deposited with S, region A, and the outer ring of the Fe sample not deposited with S, region B.

The two regions of the sample, region A and B can respectively be seen in figures 8.9 and 8.10.

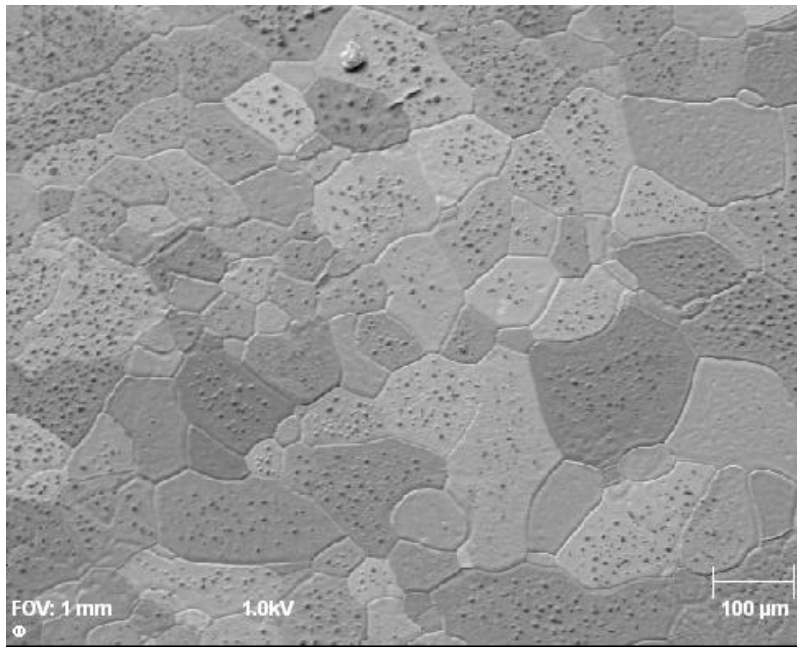


**Figure 8.9:** SED image of the S deposited region, region A, on the Fe sample after being annealed for 40 days at 1073 K.

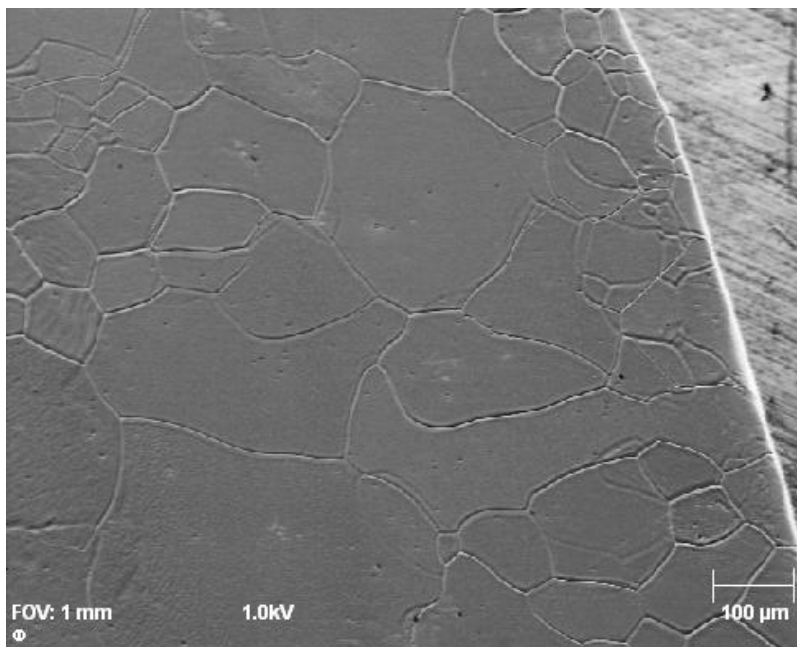


**Figure 8.10:** SED image of the region on the Fe sample not deposited with S, region B, after being annealed for 40 days at 1073 K.

From images 8.8-8.10 it is clear that region A have grains which are smaller in size compared to the grains found in region B. An area ( $\sim 1 \times 1$  mm) was selected in each of the two regions in order to determine the grain sizes. Line segments were constructed across these areas and the number of grains in the length of each of the line segment were counted. The average grain size for grains along the line segments were determined. To obtain an average value for the grain sizes of the respective areas on the sample, ten such line segments were constructed for each area. The average grain size of region B was calculated as  $140 \pm 8$   $\mu\text{m}$ , while a average grain size of  $90 \pm 8$   $\mu\text{m}$  was calculated for region A. Thus from the calculated grain sizes it can be concluded that the presence of S in bcc polycrystalline Fe caused a  $36 \pm 11$  % decrease in the grain sizes of Fe.

The initial stages of annealing consists of three steps [3], the first step is rapid recovery which eliminates the residual stresses on the metal and leads to the formation of a polygonised dislocation structure. The second step is nucleation which results in the formation of new grains at the grain boundaries which formed during recovery. During nucleation the majority of the dislocations in the material are eliminated leading to a material with low strength but high ductility [3]. The third step is grain growth where the more favoured grains will consume the smaller grains. All three of the above stages of annealing were observed in the region of the Fe sample deposited with S.

Both the S deposited region and region not deposited with S are observed to have a polygonised structure where sub grains have formed. The S layer (figure 8.2) on the Fe surface leads to the formation of FeS in small areas on the Fe surface during annealing. The FeS phase was identified by the plateau region in the Auger depth profile of the S doped Fe sample shown in figure 8.24. These FeS areas in the S deposited region acts as a tracer, which makes it easy to identify the second and third steps of the annealing process. The second step, nucleation, is marked by the grains which are completely free from FeS, indicating that these grains are the newly formed grains. The third step in the annealing process, grain growth, is marked by the grains which only contain FeS in the centre of the grain. The regions close to the grain boundary where the FeS is absent are the newly grown regions of the grains.

It is concluded that the large S concentration in the area of the Fe sample deposited with S causes a decrease in the thermal energy required by the three annealing steps, resulting in the effects of annealing being more dramatic in this region. The observed decrease in grain sizes of the S deposited region is in agreement with the experimental findings of Tacikowski *et. al.* [4], whom observed grain size decrease of Fe samples containing S. This observed effect of grain size decrease will result in a decrease of the mechanical strength and an increased ductility of the Fe sample [3].

To determine which crystal orientations of Fe were present in the S doped polycrystalline Fe sample, the sample was analysed using XRD. The results obtained for the doped sample were compared to results of an un-doped Fe sample of the same batch that was used in segregation measurements. The results for the un-doped Fe sample are shown in figure 8.11 with the results of the doped sample shown in figure 8.12.

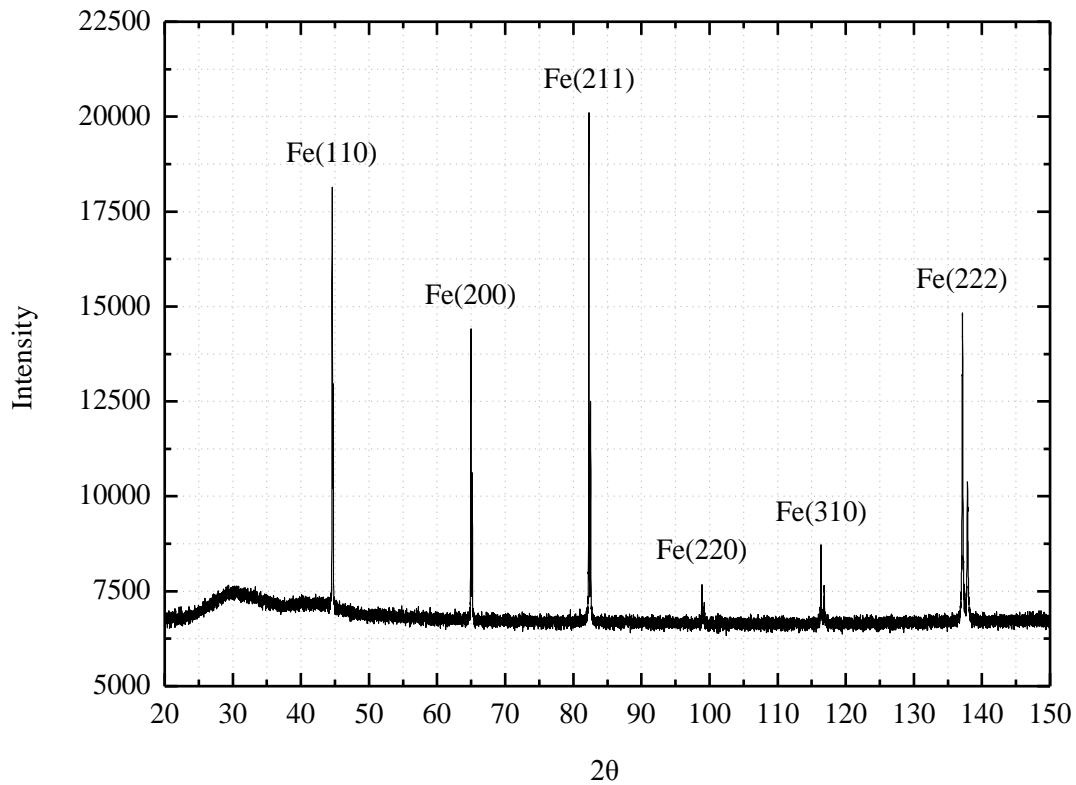


**Figure 8.11:** XRD spectra of the un-doped polycrystalline bcc Fe sample measured after surface segregation measurements were performed at temperatures in the range 400-975 K.

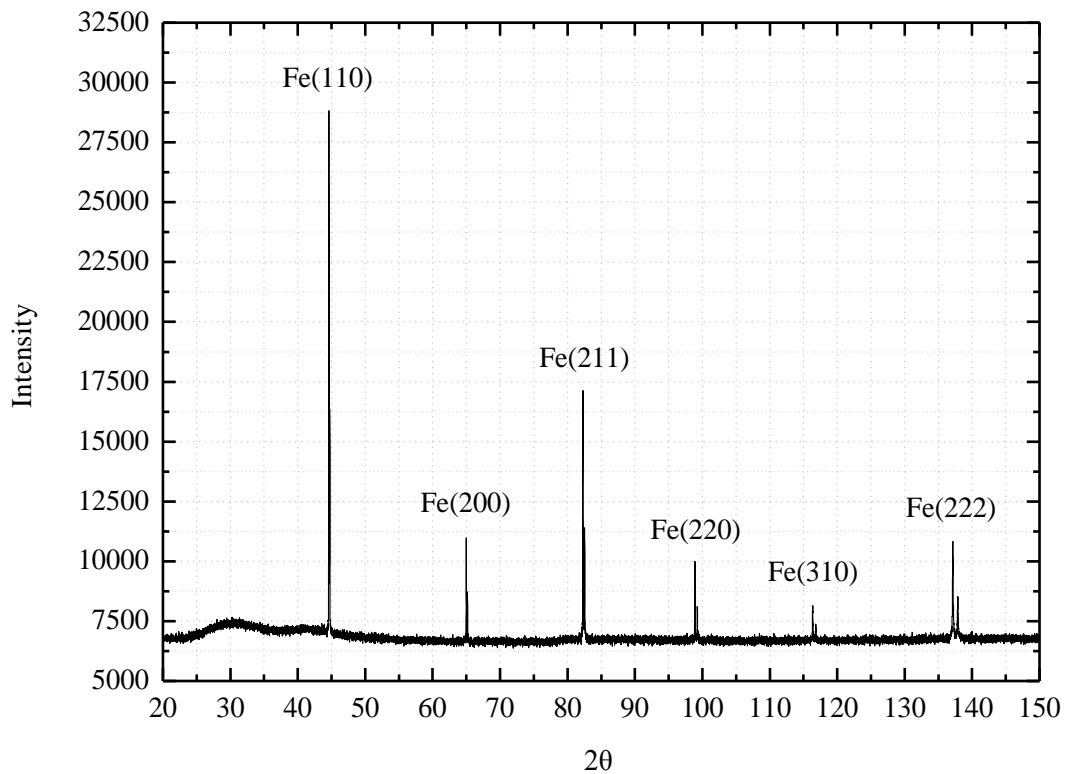


**Figure 8.12:** XRD spectra of the doped polycrystalline bcc Fe sample after being annealed for 40 days at a temperature of 1073 K.

Figures 8.11 and 8.12 show the various orientations of Fe that were detected for the un-doped and doped Fe samples. The presence of doublet peaks are seen and are especially visible for the higher diffraction angles. These doublet peaks are due to the presence of both the  $K_{\alpha 1}$  and the  $K_{\alpha 2}$  Cu X-Rays with wavelengths of respectively 1.541 Å and 1.544 Å.

The following orientations were detected in both the un-doped and doped Fe samples: Fe(110), Fe(200), Fe(211), Fe(220) Fe(310) and Fe(222). The Fe(220) peaks are due to diffraction occurring from the Fe(110) crystal planes. This effect is caused by the constructive interference of X-Rays with different whole number of wavelengths, see chapter 7. The effect also occurs for the Fe(200) and Fe(100) orientations as well as for the Fe(222) and Fe(111) orientations.

Equation 8.1, was used to calculate the fractional concentration,  $C$ , of each orientation in the polycrystalline Fe samples. Since the Fe(220) and Fe(110) peaks describe the same crystal plane, only the Fe(220) peak intensities were used to quantify the Fe samples. Similarly for the Fe(100) and Fe(111) peaks only the Fe(200) and Fe(222) peak intensities were used for quantification.

$$C_i = \frac{\frac{I_i}{I_i^\infty}}{\sum_j^n \frac{I_j}{I_j^\infty}} \quad (8.1)$$

where  $I_i$  is the XRD intensity of orientation  $i$  and  $I_i^\infty$  is the calculated XRD relative integrated intensity for orientation  $i$ . The denominator in equation 8.1 performs a summation over all  $n$  orientations in the system. The expression used for the calculation of the relative integrated intensity is given by equation 8.2 [5]

$$I^\infty = |F|^2 p \left( \frac{1 + \cos^2 2\theta}{\sin^2 \theta \cos \theta} \right) \exp^{-2M} \quad (8.2)$$

where  $F$ , is the structure factor given by equation 8.3 for the bcc crystal structure

$$F = 2f . \quad (8.3)$$

In equation 8.2,  $p$  is the multiplicity factor,  $\theta$  the angle between the X-Ray source and the detector and  $\exp^{-2M}$  is the temperature factor. The term  $M$  in the temperature factor is given by equation 8.4 [5]

$$M = \frac{6h^2T}{mk\Theta^2} \left[ \phi(x) + \frac{x}{4} \left( \frac{\sin \theta}{\lambda} \right)^2 \right] \quad (8.4)$$

where  $h$  is Planck's constant,  $T$  is the absolute temperature in Kelvin,  $m$  the mass of the vibrating atom,  $k$  is Boltzmann's constant,  $\Theta$  is the Debye characteristic temperature of the substance in Kelvin and  $\lambda$  is the wavelength with a value of 1.541 Å ( $K_{\alpha 1}$ ) for the copper X-Ray source used. The peaks which were generated by the  $K_{\alpha 1}$  X-Rays of the Cu source resulted in the largest peak

intensities and was thus used for the quantification of the Fe samples. The symbol  $x$  is given by equation 8.5

$$x = \frac{\Theta}{T} . \quad (8.5)$$

Values for the function  $\phi(x)$ , along with values of  $p$  and  $f$  were obtained from the book: Elements of X-Ray diffraction [5]. For completeness these values are given in table 8.3.

**Table 8.3:** Values of  $\phi(x)$ ,  $p$  and  $f$  used for the calculation of the relative integrated intensity for the orientations present in the polycrystalline Fe samples.

	$\phi(x)$	$p$	$f$
<b>Fe(200)</b>	1.42	6	14.36
<b>Fe(211)</b>	1.42	24	12.69
<b>Fe(220)</b>	1.42	12	11.60
<b>Fe(310)</b>	1.42	24	10.80
<b>Fe(222)</b>	1.42	8	10.15

Table 8.4 gives the weighted fractional values of the peak intensities for the un-doped and doped Fe samples, along with the weighted calculated relative integrated intensities.

**Table 8.4:** Weighted values for the measured X-Ray diffraction intensities of the Fe un-doped and doped samples. The last column contains the weighed calculated relative integrated intensities for the different orientations.

<b>Orientation</b>	<b>Weighed intensity of un-doped sample</b>	<b>Weighed intensity of Doped sample</b>	<b>Weighed calculated relative integrated intensity</b>
<b>Fe(100)</b>	0.24	0.18	0.17
<b>Fe(211)</b>	0.42	0.44	0.34
<b>Fe(110)</b>	0.03	0.14	0.12
<b>Fe(310)</b>	0.06	0.06	0.25
<b>Fe(111)</b>	0.25	0.17	0.11

The percentage of each orientation present in the un-doped and doped samples are given in table 8.5, along with the percentage difference between the different orientations of the two samples.

**Table 8.5:** Quantified data giving the percentage of each orientation in the un-doped and doped Fe samples, with the percentage difference given in the last column.

<b>Orientation</b>	<b>% Un-doped sample</b>	<b>% Doped sample</b>	<b>% Difference</b>
<b>Fe(100)</b>	26.25	21.07	-5.180
<b>Fe(211)</b>	22.74	24.77	+2.030
<b>Fe(110)</b>	4.748	21.16	+16.41
<b>Fe(310)</b>	4.825	5.221	+0.396
<b>Fe(111)</b>	41.45	27.78	-13.67

From table 8.5, the biggest decrease is observed for the Fe(111) crystal orientation with a value of -13.67 % while the Fe(100) crystal orientation showed a -5.180 % decrease. The largest increase was observed for the Fe(110) crystal orientations with a value of 16.41 %. From the results presented in table 8.5 it can be concluded that the more favoured crystal orientations of Fe(110), Fe(211) and Fe(310) have grown during annealing and have consumed the less favourite Fe(111) and Fe (100) crystal orientations.

In chapter 9 calculations were performed for the Fe(100), Fe(110) and Fe(111) surfaces to determine the surface stability of each surface. Results showed that the most stable surface is that of the Fe(110) crystal orientation, with Fe(100) being the second most stable surface and Fe(111) being the most unstable surface. It was shown that the most stable surface of Fe(110) was bulk terminated with no lattice relaxation occurring. The Fe(111) surface was shown to relax the most with little relaxation occurring in the Fe(100) surface. The stability of the surfaces are also seen in the experimental results presented in table 8.5. The unstable crystal orientations Fe(100) and Fe(111) have decreased, while the stable Fe(110) crystal orientation have increased in concentration. Thus it can be concluded that a stable surface structure is expected for the Fe(211) and Fe(310) crystal orientations. The different crystal orientations of the polycrystalline Fe samples can thus be arranged in order from most stable to unstable as Fe(110)>Fe(211)>Fe(310)>Fe(100)>Fe(111).

An investigation of the S doped Fe surface was performed in order to determine which elements are present on a selected area of the sample. Figure 8.14 shows an SED image of the area on the sample chosen for elemental mapping analysis. The elemental maps of the 4 elements S, C, O and Fe are shown in figures 8.15-8.18. The combined elemental maps of Fe, S and C are shown in figure 8.19 and the combined elemental maps of Fe, S and O are shown in figure 8.20.

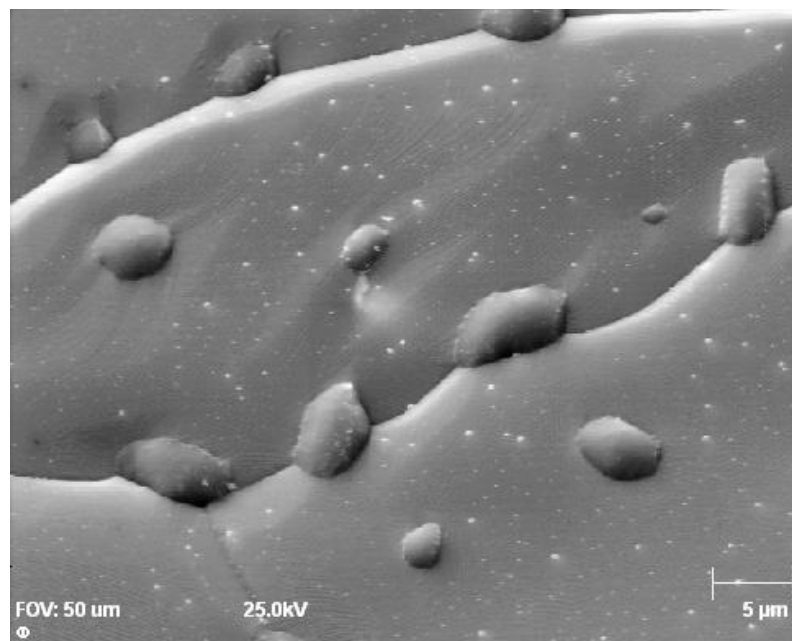


**Figure 8.14:** SED image of the area on the S doped Fe sample selected for elemental mapping.

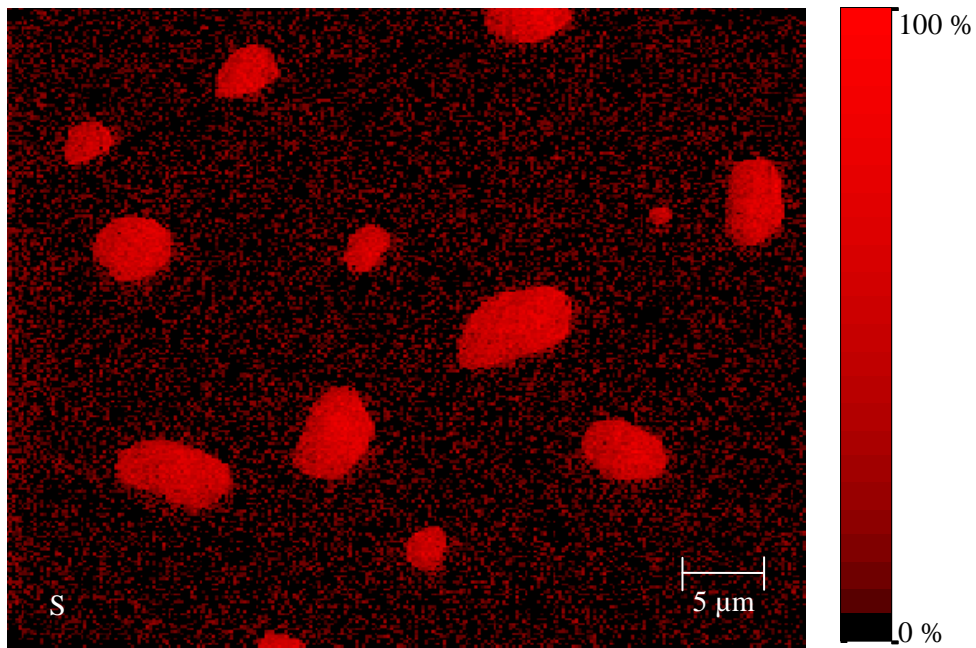


*Figure 8.15: Elemental map of S on the surface of the annealed Fe sample.*

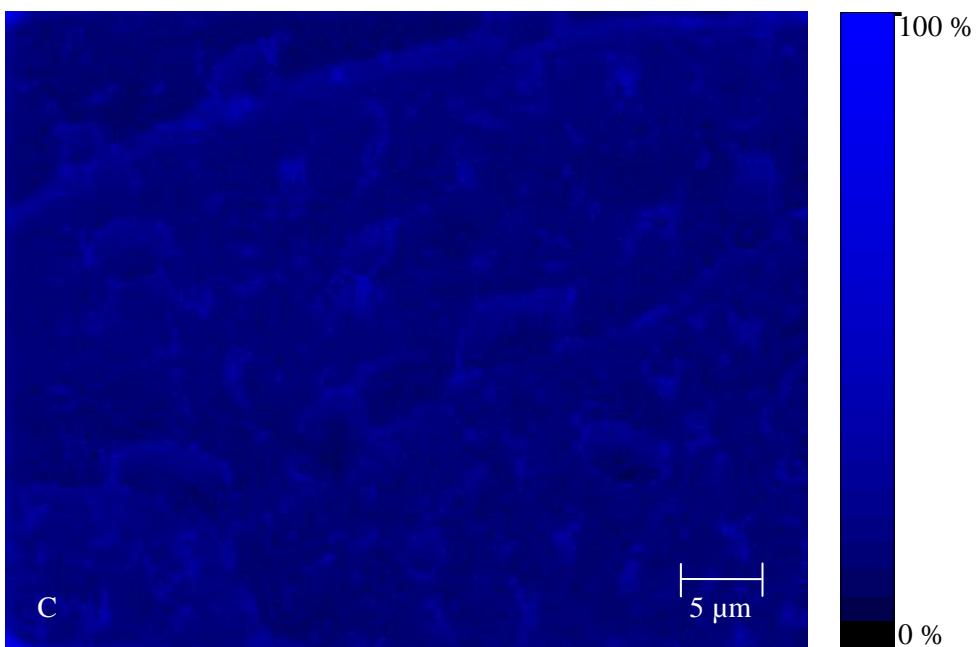


*Figure 8.16: Elemental map of C on the surface of the annealed Fe sample.*

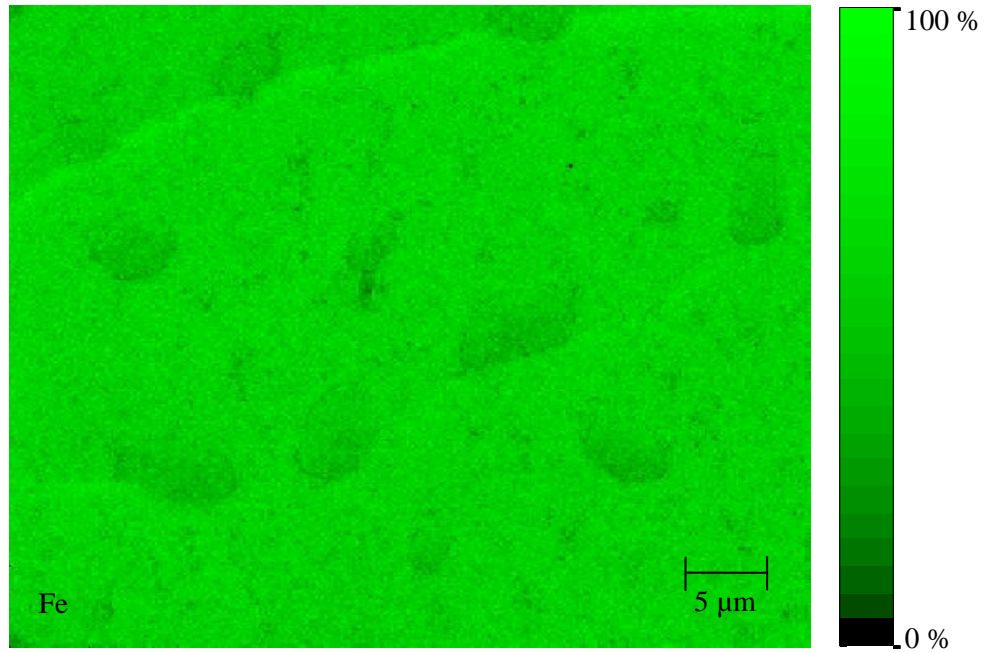


*Figure 8.17: Elemental map of Fe on the surface of the annealed Fe sample*

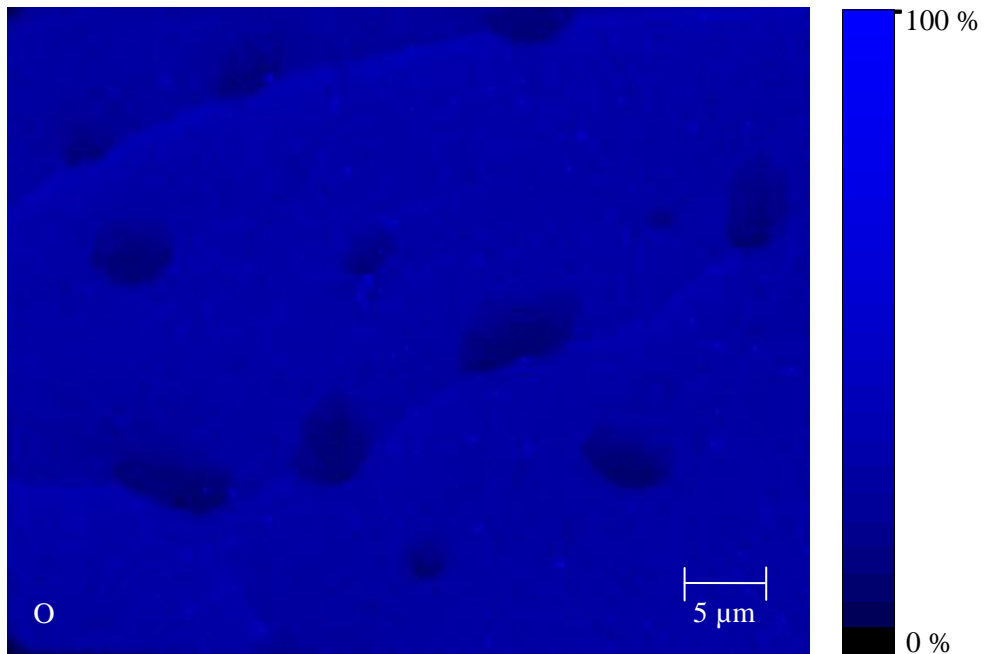


*Figure 8.18: Elemental map of O on the surface of the annealed Fe sample*

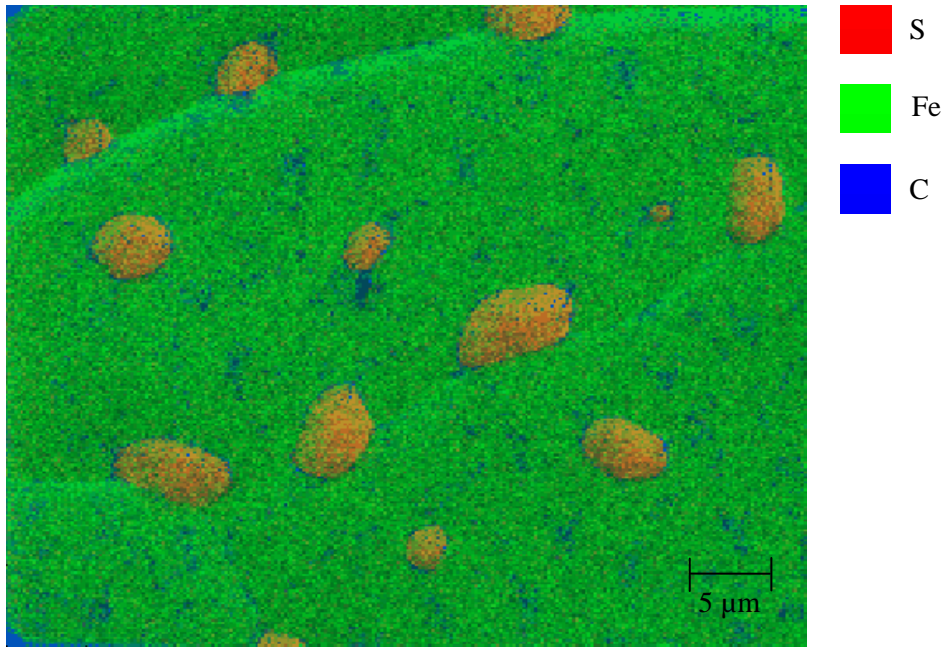


*Figure 8.19: Elemental map of the three elements S, C and Fe on the surface of the annealed Fe sample*

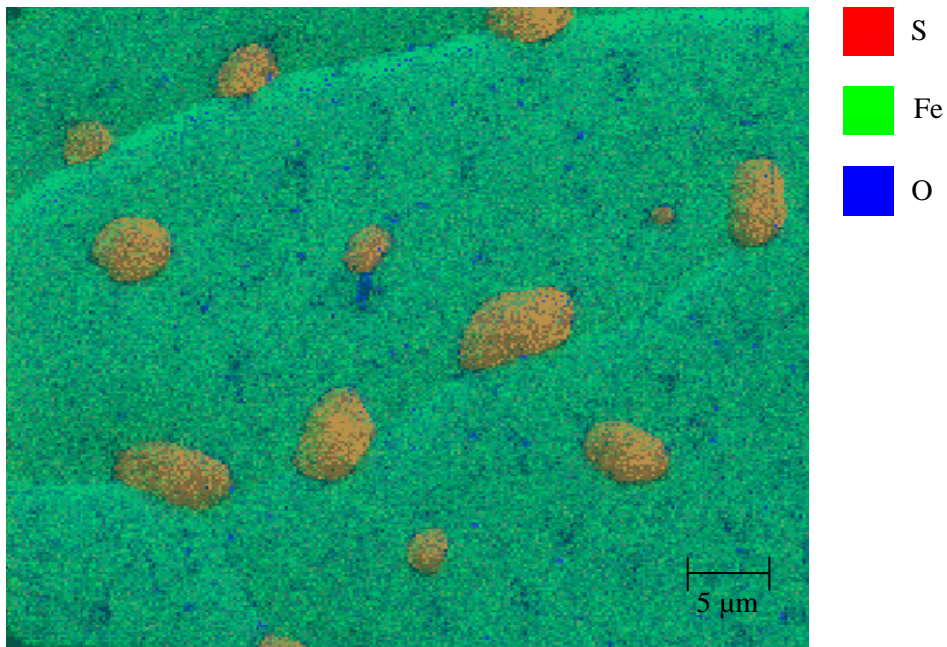


*Figure 8.20: Elemental map of the elements O, S and Fe on the surface of the annealed Fe sample*

The elemental maps of figures 8.15-8.20 shows the S doped Fe surface to be dominated by Fe, with the exception of a number of areas where FeS has formed on the surface, referred to as FeS blobs from here on. Small quantities of both C and O can also be seen as surface contaminants. S has been observed to rapidly segregate via the grain boundaries [6], but looking at the elemental map of S in figure 8.15, no S is observed in the grain boundaries. This is explained by performing model calculations using the Guttman model described in chapter 4, Segregation theory. Figure 8.21 shows the segregation curves of S and P with segregation energies of respectively -60 kJ/mol (0.6 eV) and -50 kJ/mol (0.5 eV). The interaction parameter for Fe/S was chosen as 8 kJ/mol (0.08 eV) which was obtained for the segregation of S in the doped Fe sample of section 8.5. For Fe and P a 0 kJ/mol interaction parameter was chosen and for S and P an interaction parameter of 5 kJ/mol (0.05 eV) was chosen. This was a valid choice since a positive interaction parameter is expected between S and P as concluded from the surface segregation measurements in section 8.5. The maximum surface concentration for the calculations were chosen as 34 % for S and 1 % for P. Little P is seen in the equilibrium segregation region of the segregation profiles shown in figure 8.26, section 8.5, making the low concentration of P chosen here a valid choice.

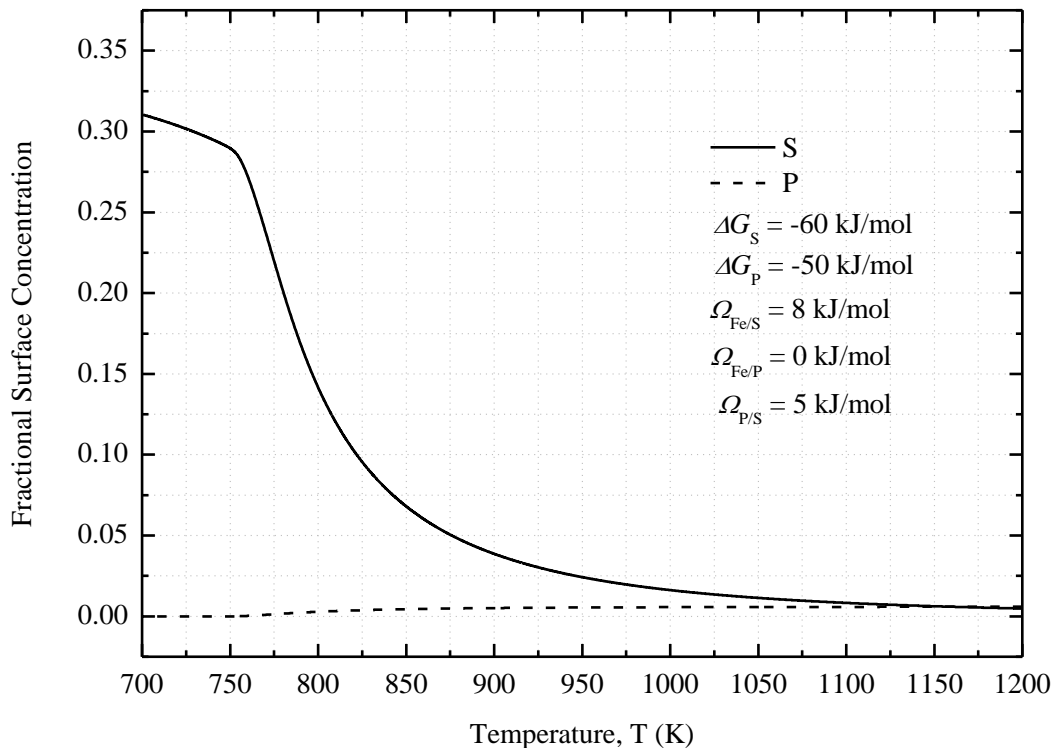


**Figure 8.21:** Model calculations of S and P equilibrium segregation using the Guttman model.

Using the same interaction parameters, profiles for a range of segregation energies for S and P were calculated. From literature the segregation energies of S and P in Fe(100) differed by a value of 10 kJ/mol [7], this difference was maintained between the segregation energies of S and P for all the calculations performed here. Figure 8.22 shows only the S profiles calculated using the Guttman model. The P profiles were omitted since the concentration of P in the equilibrium region is negligible.

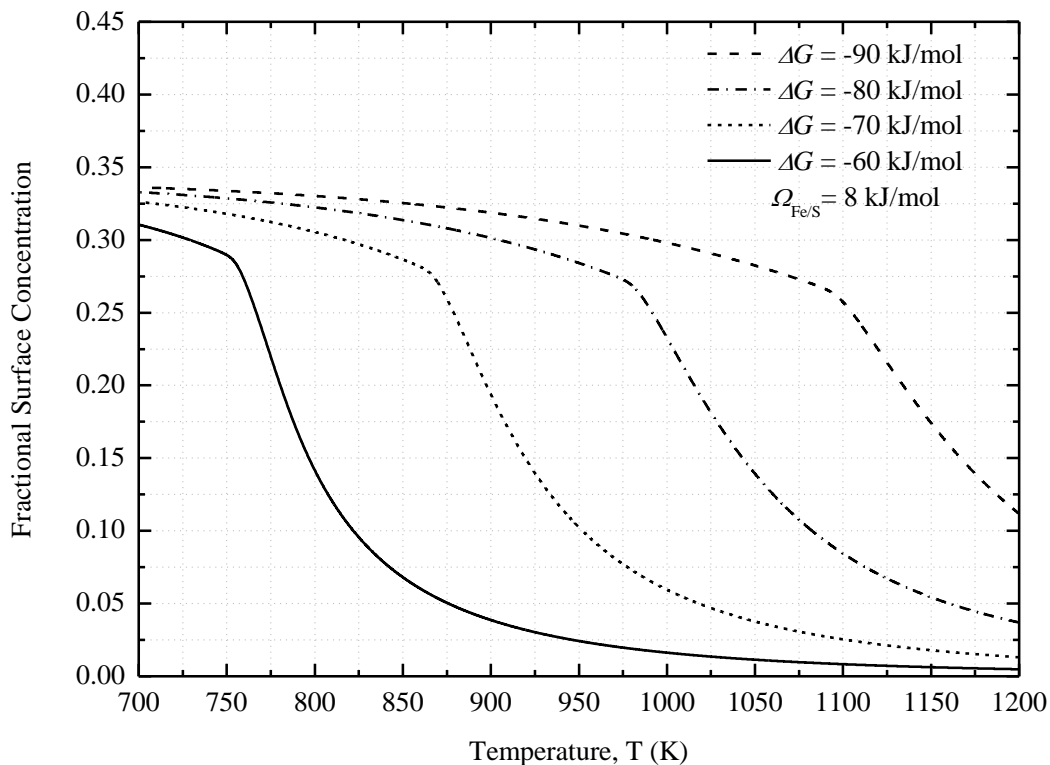


**Figure 8.22:** Model calculations for equilibrium surface segregation of S using the Guttman model.

From figure 8.22 it is observed that very little S will be present in the grain boundaries at the annealing temperature of 1073 K for a segregation energy  $>-60$  kJ/mol (0.6 eV). Thus it is concluded that the absence of S in the grain boundaries of figure 8.15 is due to a low grain boundary segregation energy of -60 kJ/mol (0.6 eV) at least

No specific pattern is observed for the position of the FeS blobs on the Fe surface in figures 8.9 and 8.14. It was calculated that the FeS blobs are approximately 5.5  $\mu\text{m}$  in diameter. This was done by

constructing a line segment both horizontally and vertically across 10 blobs to obtain an average value for the diameter of the blobs. To determine the thickness of one such blob, Auger depth profile analysis was performed. The surface was sputtered in intervals of 2 min at a rate of 27 nm/min for a total of 114 min. Point 1 in figure 8.23 shows the point on the blob chosen for depth profile analysis and point 2 shows the point on an area of the clean Fe surface chosen for depth profile analysis. Point 2 was chosen to obtain experimental evidence that S has diffused homogeneously throughout the sample.

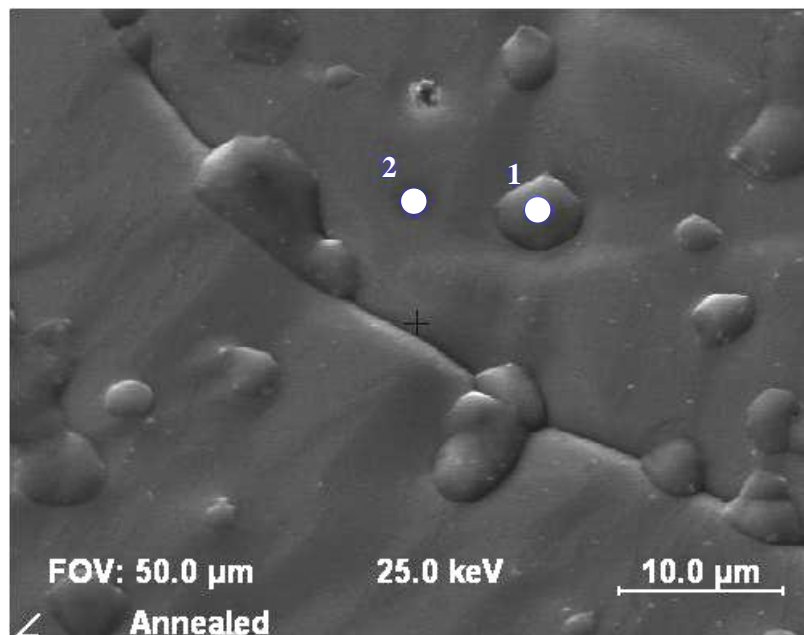


**Figure 8.23:** SEM image of the surface area chosen for depth profile analysis. Point 1 shows the FeS blob chosen for depth analysis. Point 2 was chosen to confirm that S has diffused homogeneously throughout the sample.

The results of the depth profile performed on point 1 is shown in figures 8.24.

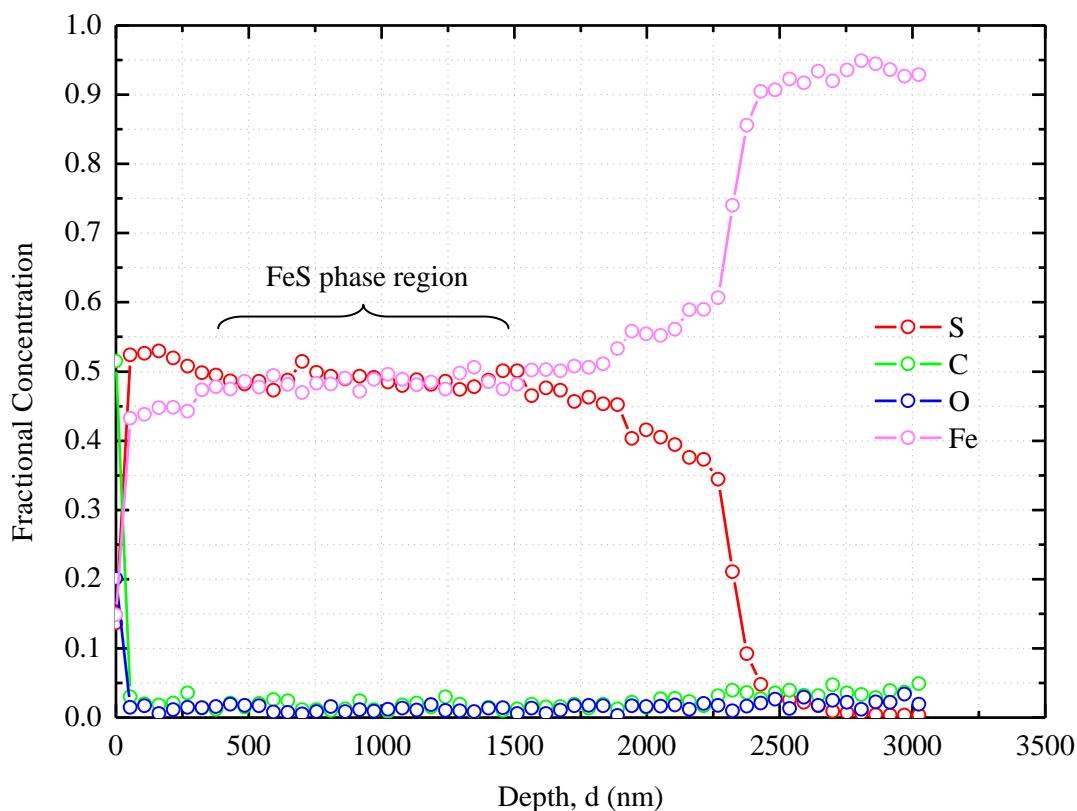


**Figure 8.24:** Depth profile of the FeS blob which have formed during the annealing of the S doped Fe sample.

From figure 8.24 it is observed that C and O with a layer thickness of <50 nm are present as surface contaminants which were easily removed by Ar<sup>+</sup> ion sputter cleaning. From 50 nm the concentration of S is seen to decrease until the FeS phase region is entered. The plateau region of both the elements S and Fe indicates that a Fe-S phase has formed on the surface, and by noting that they both have a ~50 % concentration in this region it can be concluded that a FeS (50 % Fe, 50 % S) phase has formed. The FeS blob was found to be 2268 nm (2.268 μm) in thickness. The results of the depth profile performed on point 2 is shown in figures 8.25.

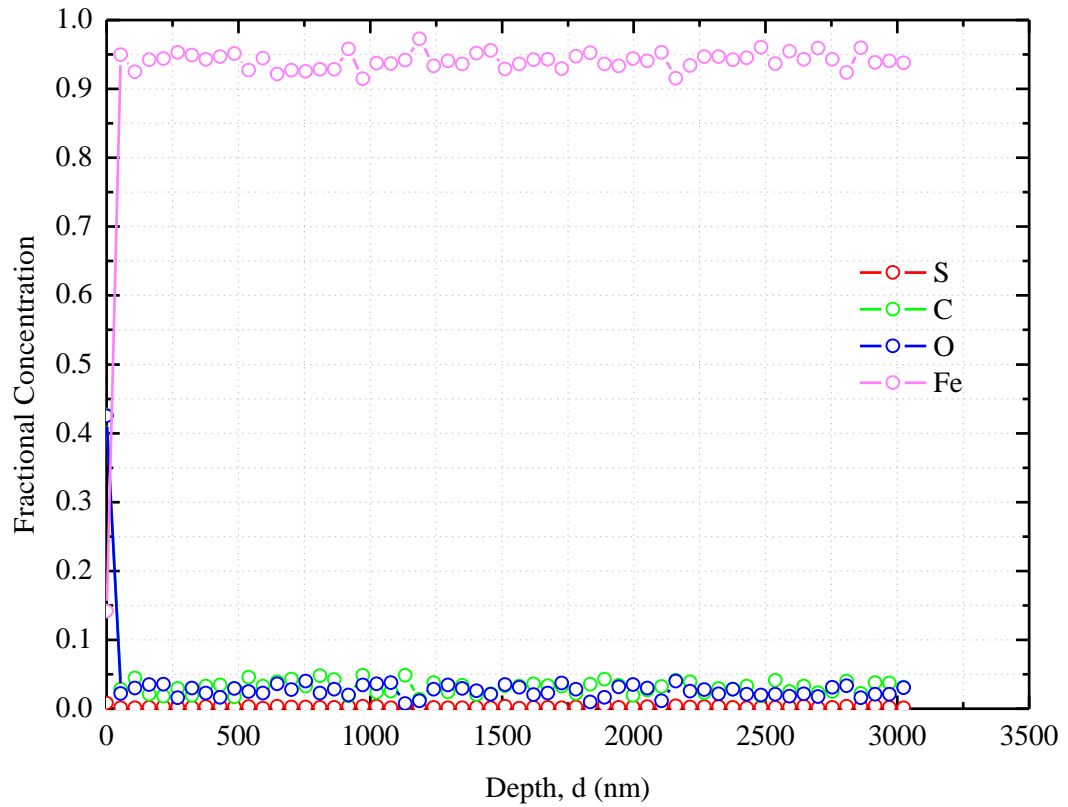


**Figure 8.25:** Auger depth profile on the clean area of the S doped Fe sample after the sample was annealed for 40 days at a temperature of 1073 K.

The Auger depth profile on the clean area of the S doped Fe surface, point 2, in figure 8.25 shows that C and O are present as contaminants on the surface. No S were detected, indicating that a homogeneous distribution of S in Fe was obtained during annealing.

## 8.5. Surface segregation measurements

The surface segregation results of the non-metal impurities O, N, B, C, S and P in polycrystalline bcc Fe obtained using the SAM 590 Auger system are presented in this section. The experimental procedure described in chapter 7, Experimental techniques, was used to obtain all the segregation profiles presented here. Two samples were analysed, the first is a pure polycrystalline Fe sample without any added S. The second sample measured was doped with 71.70 ppm S, using the method described in chapter 6, Sample preparation. In order to obtain the elemental concentrations of the segregated elements, the segregation profiles were quantified using the method for thin layers described in chapter 7, Experimental techniques.

Fick's linear programmed heating and Guttmann's equilibrium models described in chapter 4, Segregation theory, were used to extract the segregation parameters for S and P. The linear programmed heating segregation profile of the un-doped and doped samples heated at a rate of 0.0078 K/s are given in figure 8.26.

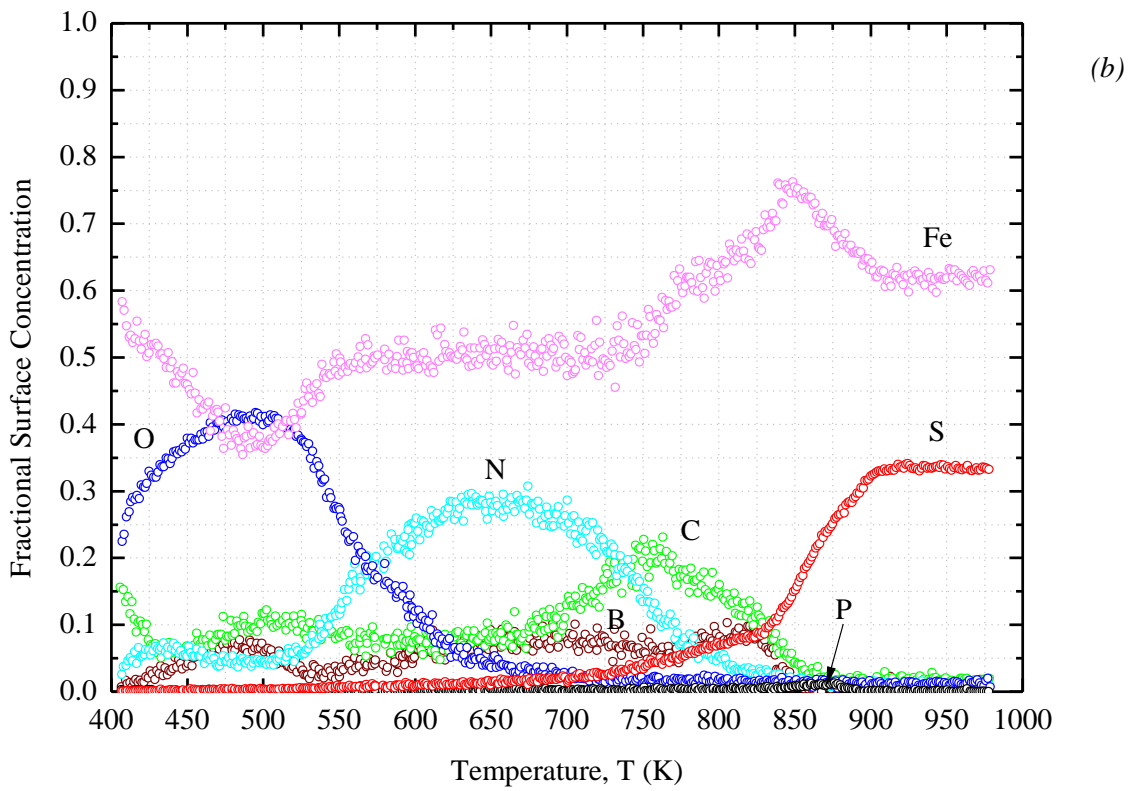
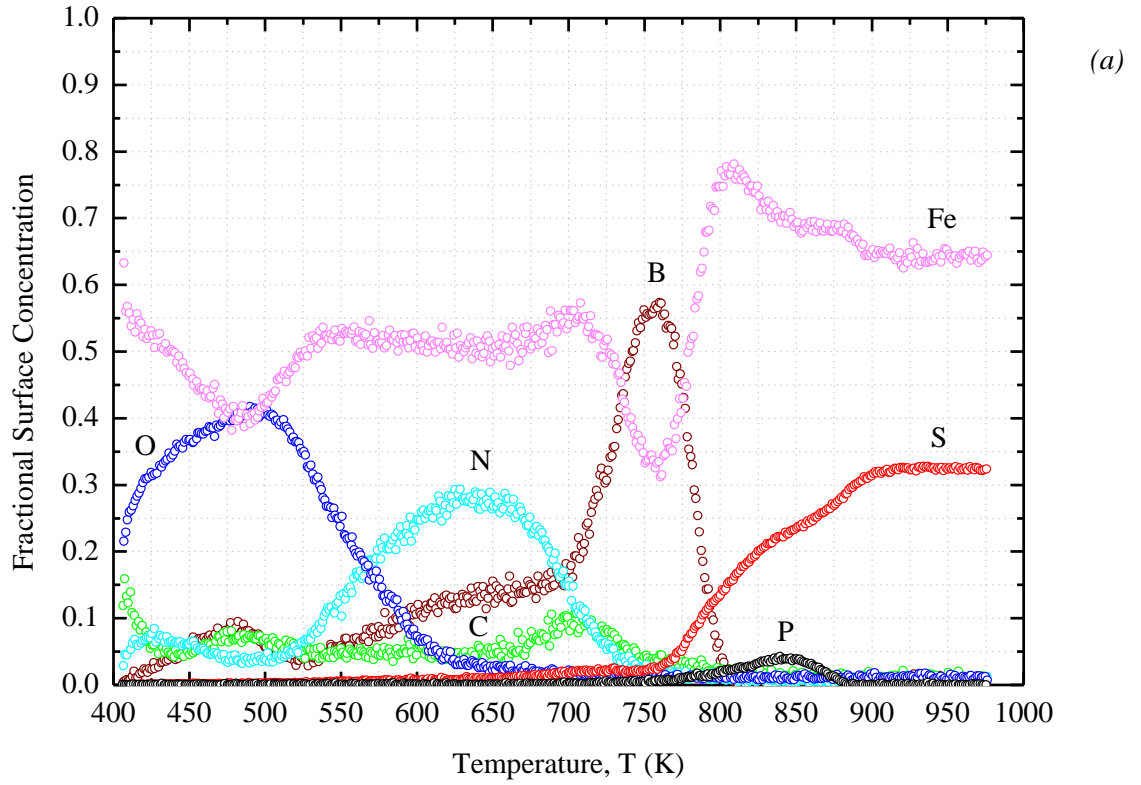


**Figure 8.26:** Segregation profiles of the elements O, N, C, B, S and P in polycrystalline bcc Fe samples heated linearly at a rate of 0.0078 K/s. (a) Un-doped sample (b) Doped sample.

Figure 8.26 shows the segregation of 6 non-metal impurities from the polycrystalline bcc Fe samples. For the un-doped sample the presence of O on the surface is not due to segregation alone, but due to O from the surroundings adsorbed onto the heated Fe surface. It is not possible from the results presented here to determine the respective amounts of O adsorbed and O segregated onto the surface. At 500 K a maximum surface concentration of 40 % is seen for O in both samples. Above 500 K O starts to desegregate due to the segregation of N which obtains a maximum surface concentration of 28 % at a temperature of 640 K. Above 550 K B and C is observed to be in competition to segregate to the surface. In the un-doped sample, B is the dominant element of the two and is observed to rapidly segregate at temperatures above 700 K. In the doped sample C seems to be the dominant element and segregates to a maximum surface concentration of 22 % at a temperature of 750 K. In both samples it is observed that the segregation of C causes N to desegregate. For the un-doped sample, the desegregation of C leads to the rapid segregation of B to reach a maximum surface concentration of 57 % at a temperature of 760 K.

S is observed to start segregating very slowly in both samples at a temperature of 600 K, at 750 K in the un-doped sample the segregation of S causes B to desegregate. Both C and B is seen to desegregate due to the segregation of S in the doped sample. Very little P is seen to segregate in the un-doped sample at temperatures above 770 K reaching a maximum surface concentration of 4 % at 850 K before S causes the P to desegregate. This effect of S being able to dominate the Fe surface leading to the desegregation of all other impurity elements suggest that S has the largest segregation energy. The elements can be arranged from the first to the last to segregate as: O, N, B/C, S, P with S dominating the surface. The segregation of N is in good agreement with the observations by M.M. Eisl *et. al.* [8] and E.C. Viljoen *et. al.* [9] who observed N to segregate in the temperature region 523-673 K. Fujita *et. al.* [2] observed the segregation of C in the temperature range 573-673 K in Fe(100) and the segregation of S to occur at temperatures above 673 K.

The dominance of an element on the surface is determined by the segregation energy of that element. The segregation energy is the amount of energy by which the total energy of the crystal is lowered when an atom is removed from the subsurface of the material and placed onto the surface. This is confirmed by the dominance of S, with a segregation energy of -134 kJ/mol (1.39 eV) for the un-doped sample, on the Fe surface. Thus the segregation of S resulted in the lowering of the Fe structures total energy by -134 kJ/mol (1.39 eV). Table 8.6 gives literature values for the segregation energies of some non-metal impurities considered here, obtained from Fe single crystals.

**Table 8.6:** Segregation energies of the non-metal impurities N, C, S and P in Fe single crystals as obtained from literature.

Element	Segregation energy, $\Delta G$ (kJ/mol)
N	-110 [7]
C	-85 [7]
P	-180 [7]
S	-190 [7]

The fitting of Fick's linear programmed heating model to the segregation profile of S obtained for the un-doped Fe sample is shown in figure 8.27, resulting in a pre-exponential factor,  $D_0$ , of  $4.90 \times 10^{-2} \text{ m}^2/\text{s}$  and an activation energy,  $Q$ , of 190.8 kJ/mol (1.978 eV).

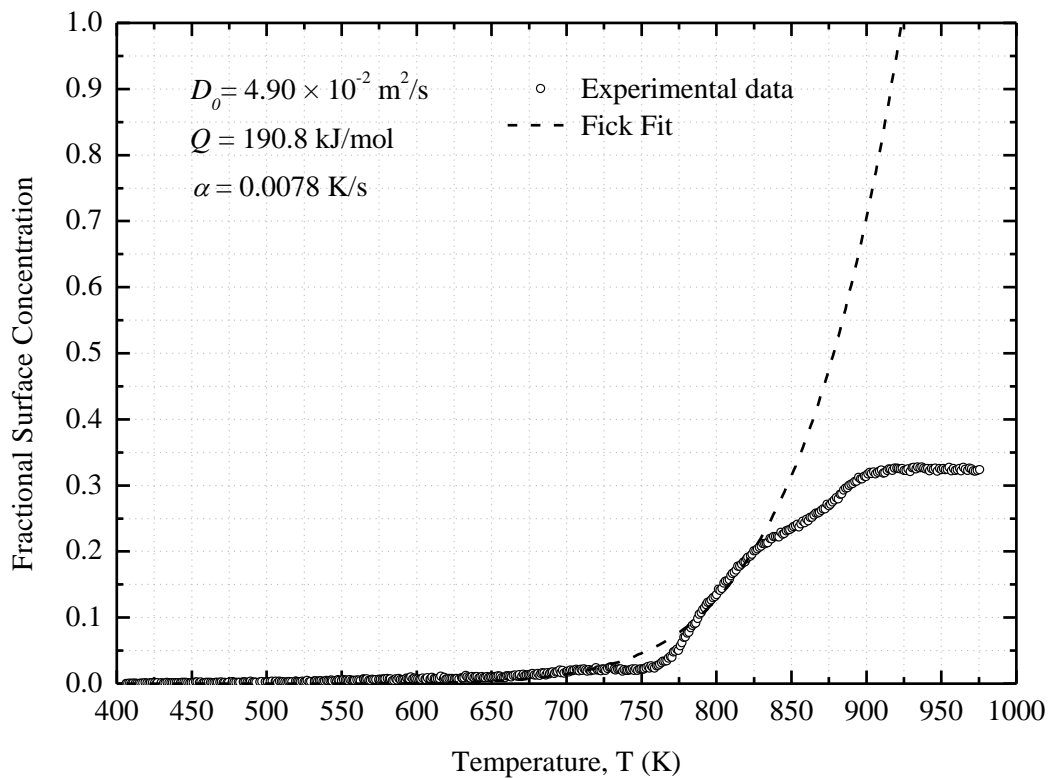


**Figure 8.27:** Fit of Fick's linear programmed heating model to the segregation profile of S, resulting in a pre-exponential factor,  $D_0$ , of  $4.90 \times 10^{-2} \text{ m}^2/\text{s}$  and an activation energy,  $Q$ , of 190.8 kJ/mol (1.978 eV).

In figure 8.27, two discrepancies between the model of Fick and the experimental data is observed, the first occurs in the temperature range  $\sim 725-785$  K and the second occurs between the temperatures  $825-900$  K. Looking at figure 8.26(a), the deviations between the model of Fick and the experimental data can be explained by a strong interaction occurring between S and one of the other segregating elements. At temperatures below  $725$  K the segregation curve of S can be described by Fick's model, but above  $700$  K B segregates rapidly causing the segregation curve of S to deviate from Fick's model. The experimental data has a lower segregation rate as what is predicted by the model of Fick, caused by a positive interaction energy leading to a repulsive force between S and B. Similarly the second discrepancy in the temperature range  $\sim 825-900$  K can be explained by the interaction of S and P. Here the segregation of P causes the segregation rate of S to decrease as a result of a positive interaction parameter leading to a repulsive force between S and P. Thus the presence of other elements in the Fe causes local changes in the segregation rate of S and thus the fit shown in figure 8.27 provides an average segregation rate for S in the un-doped Fe sample.

To provide a description of the equilibrium segregation region the model of Guttman was fitted to the segregation profiles of the elements S, P and Fe. Figure 8.28 shows the fitting of the Guttman model to the experimental data of S. Since the concentration of P is  $\sim 0$  in the equilibrium region the fit for P is omitted from figure 8.28. For S a segregation energy,  $\Delta G$ , of  $-134$  kJ/mol ( $-1.39$  eV) and a interaction parameter,  $\Omega_{\text{Fe/S}}$ , of  $20$  kJ/mol ( $0.2$  eV) was obtained.

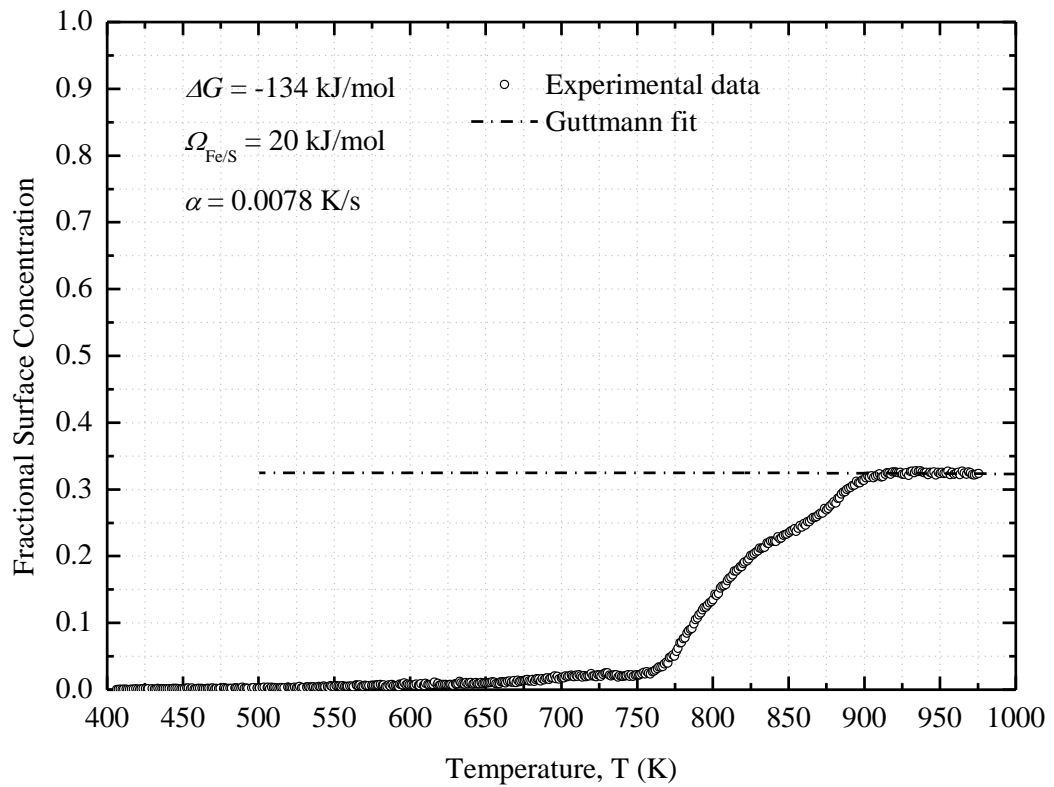


**Figure 8.28:** Fit of Guttman's model describing the equilibrium region of the S segregation profile. A segregation energy of  $-134 \text{ kJ/mol}$  ( $1.39 \text{ eV}$ ) and a interaction parameter of  $20 \text{ kJ/mol}$  ( $0.2 \text{ eV}$ ), describing the interaction between Fe and S, was obtained.

Figure 8.29 shows the combination of Fick's linear programmed heating model describing the kinetics of surface segregation and Guttman's model describing the equilibrium region of surface segregation.

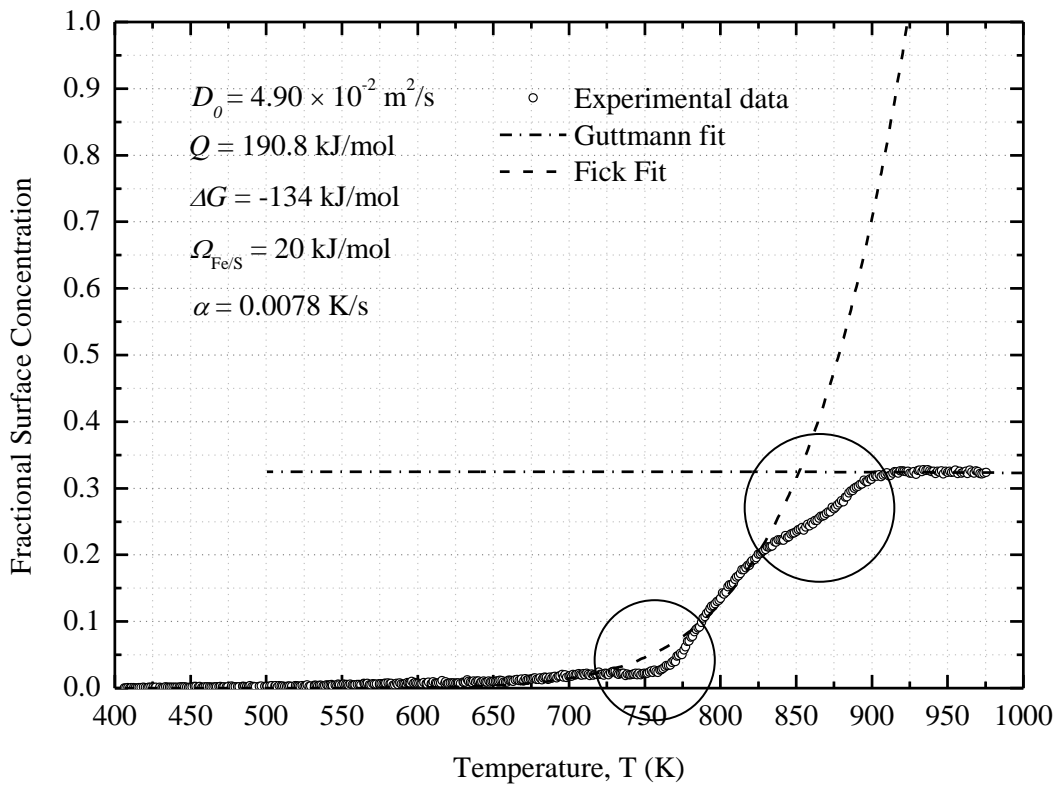


**Figure 8.29:** Combination of Fick's linear programmed heating model and Guttman's model to the segregation profile of S in a un-doped polycrystalline bcc Fe sample. The circles indicate the regions in which Fick's model failed to describe the kinetics of S segregation due to a positive interaction parameter between S and B and S and P respectively.

Figure 8.29 provides a complete picture of the two models used to respectively describe the kinetics and equilibrium regions of surface segregation. The circles in image 8.29 indicates the regions where the S segregation profile deviates from Fick's model due to a positive interaction parameter between S and B and S and P respectively.

Fitting of Fick's linear programmed heating model to the segregation profile of P is shown in figure 8.30. The pre-exponential factor,  $D_0$ , and activation energy,  $Q$ , were respectively determined as  $0.129 \text{ m}^2/\text{s}$  and  $226.5 \text{ kJ/mol}$  ( $2.348 \text{ eV}$ ).

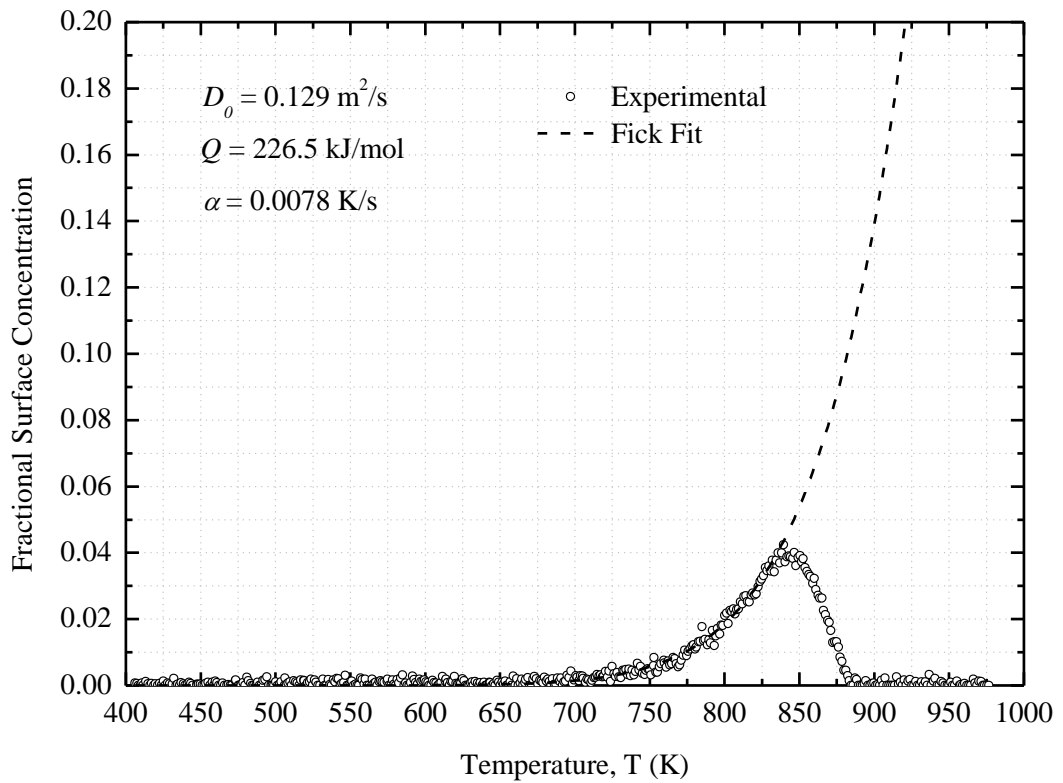


**Figure 8.30:** Fit of Fick's linear programmed heating model to the segregation profile of *P* for the un-doped Fe sample which delivered a pre-exponential factor,  $D_0$ , of  $0.129 \text{ m}^2/\text{s}$  and a activation energy,  $Q$ , of  $226.5 \text{ kJ/mol}$  ( $2.348 \text{ eV}$ ).

A good description of the experimental data is given by the model of Fick with no deviations observed between the experimental data and the fitting of Fick's model.

The results obtained for the segregation of S in the doped Fe sample are presented in the remainder of this section. The fitting of Fick's linear programmed heating model to the doped sample having a total S concentration of 77.70 ppm is shown in figure 8.31. The sample had an initial S concentration of 6 ppm, together with the amount with which the sample was doped, 71.70 ppm, resulted in a total S concentration of 77.70 ppm.

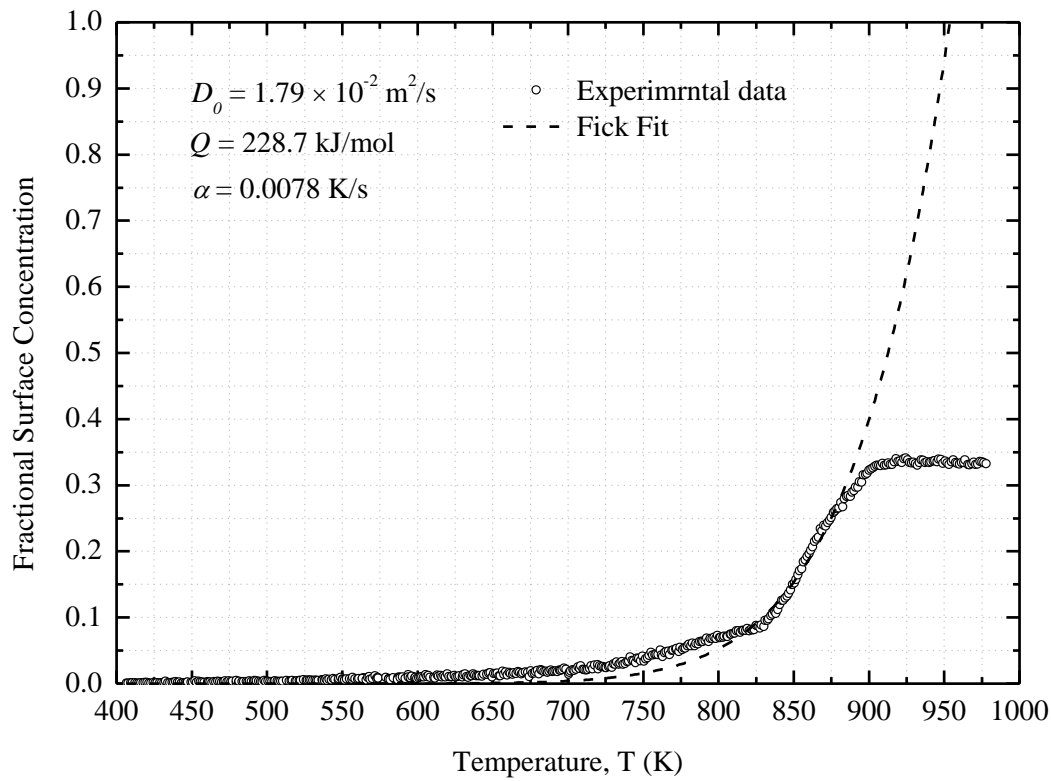


**Figure 8.31:** Fit of Fick's linear programmed heating model to the segregation profile of S for the doped Fe sample, resulting in a pre-exponential factor,  $D_0$ , of  $1.79 \times 10^{-2} \text{ m}^2/\text{s}$  and a activation energy,  $Q$ , of 228.7 kJ/mol (2.370 eV).

Similar behaviour for the kinetics of segregation is observed for the doped sample as was observed for the un-doped sample presented in figure 8.27. Due to the increased bulk S concentration very little P is observed to segregate, nevertheless a kink in the S segregation profile can be seen due to the interaction of S and P at temperatures above 875 K. A large interaction between C and S is also observed, which is evident in the large kink of the S segregation profile at a temperature of 830 K. The results obtained by fitting Fick's model to the segregation curve of S resulted in a pre-exponential factor,  $D_0$ , of  $1.79 \times 10^{-2} \text{ m}^2/\text{s}$  and an activation energy,  $Q$ , of 228.7 kJ/mol (2.370 eV). Literature values of  $D_0 = 0.16 \text{ m}^2/\text{s}$  and  $Q = 231 \text{ kJ/mol}$  (2.39 eV) was obtained by Reichl *et al.* [6] and a good agreement is seen between the literature and experimental values measured in the two samples.

Figure 8.32 shows the fitting of the Guttman model to the equilibrium region of the segregation profile. The values for the segregation energy,  $\Delta G$ , and the interaction parameter,  $\Omega$ , obtained are respectively -145 kJ/mol (-1.50 eV) and 8 kJ/mol (0.08 eV).

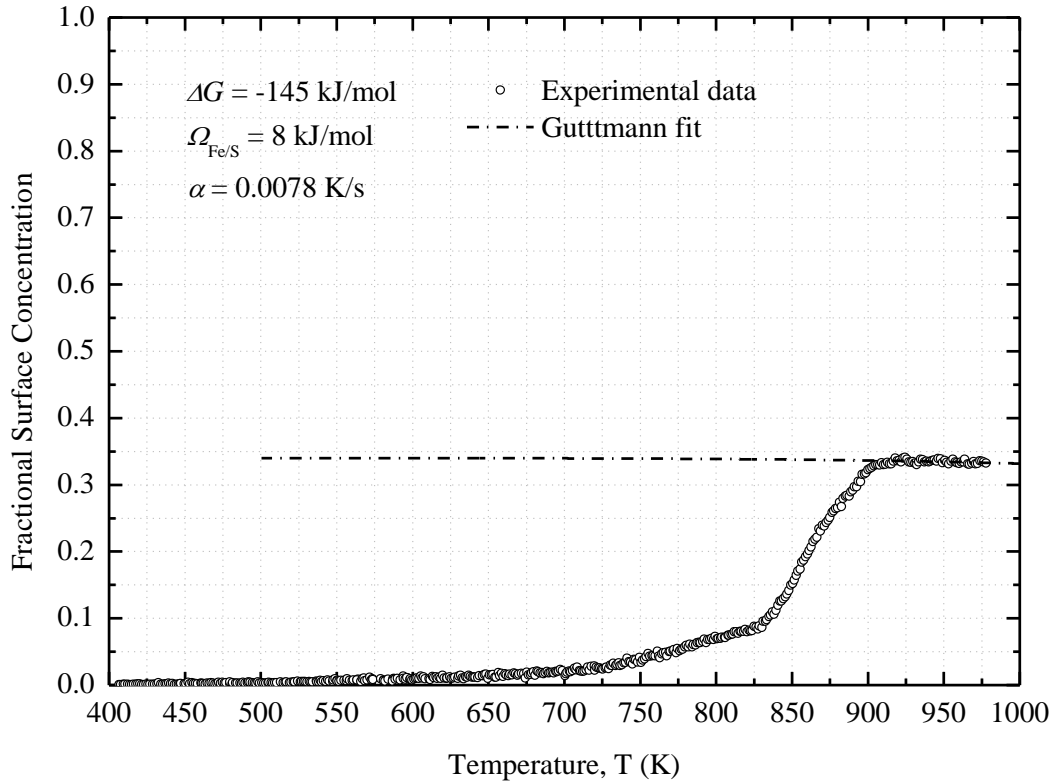


**Figure 8.32:** Fit of Guttman's model to the equilibrium region of the segregation profile of S for the doped Fe sample which delivered a segregation energy of -145 kJ/mol (-1.50 eV) and a interaction parameter of 8 kJ/mol (0.08 eV).

Comparing the segregation energy and interaction parameter of S obtained for the un-doped sample to the values obtained for the doped sample, differences are seen to occur. These differences are caused by the difference in the crystal orientations of the samples measured. The segregation energy is calculated as the difference in the binding energy of a impurity atom in the subsurface layer minus the binding energy of that atom on the surface of the material. Since S will have different surface binding energy values for different surface orientations, different segregation energies are expected. In chapter 9, section 9.4.3 the segregation energy of S in Fe(100) was calculated using this method with a value of -179.4 kJ/mol (-1.859 eV) compared to the experimental value of -190.0 kJ/mol (-1.969 eV) obtained by Grabke and Viehhaus [10]. The mathematical expression for the interaction parameter is given by equation 8.6 [11].

$$\Omega_{12} = Z \left[ \varepsilon_{12} - \frac{1}{2}(\varepsilon_{11} - \varepsilon_{22}) \right] \quad (8.6)$$

where  $\varepsilon$  is the binding energy for the elements of interest and  $Z$  is the number of nearest neighbour atoms. The binding energy of Fe,  $\varepsilon_{11}$  is not expected to change, but for different surface orientations different binding energies of S,  $\varepsilon_{22}$  and S to Fe,  $\varepsilon_{12}$  is expected. This is caused by the different positions in which the S atoms will bind onto the Fe surface. This statement is confirmed by the literature information which shows that S will form a c(2×2) structure on the Fe(100) surface and a p(1×1) structure on the Fe(111) surface. Thus the decrease in the interaction parameter is due to different surface orientations for the un-doped and doped Fe samples.

The combined fits of Fick's linear programmed heating and Guttman's model on the segregation profile for the doped Fe sample is shown in figure 8.33.

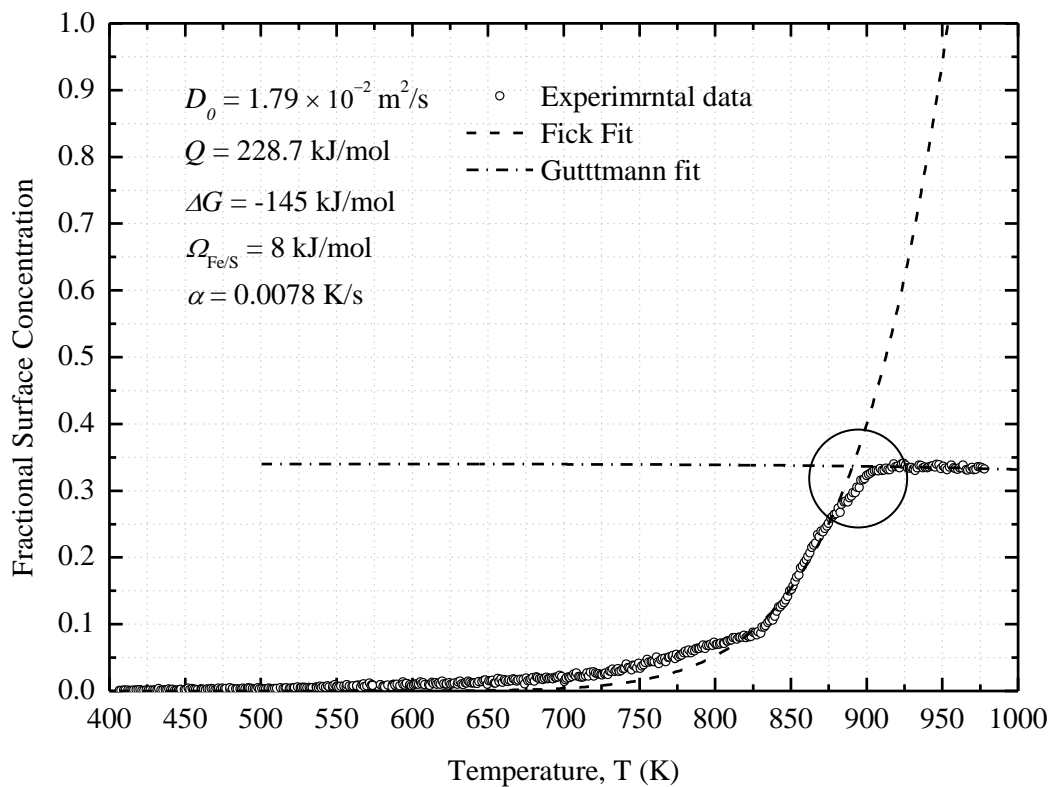


**Figure 8.33:** Combined fit of Fick's linear programmed heating model and Guttman's model on the segregation profile of S obtained for the doped Fe sample.

The circle in figure 8.33 indicates the deviations in the experimental data and the model of Fick, caused by the interaction of S and P.

Figure 8.34 shows the plot of the segregation profiles of S for both the un-doped and the doped Fe samples with the model of Fick fitted to the data.

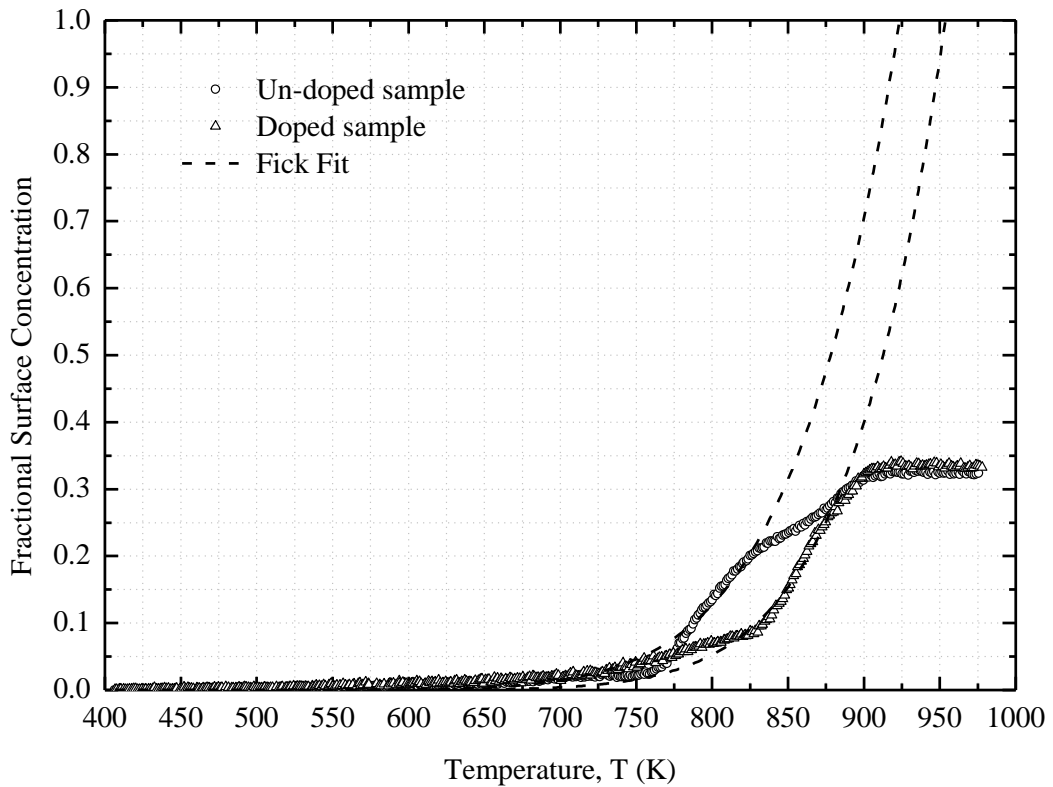


**Figure 8.34:** Combined plot of the S segregation profiles for the un-doped and doped samples of Fe along with the fits of Fick's linear programmed heating model.

The initial segregation of S in the two samples are the same up to a temperature of 700 K where the profiles start to follow different paths. Another confirmation that the crystal orientations of the samples measured are different is given by the difference in the two profiles for temperatures above 700 K. Different crystal orientations will have different activation energies as was shown in the calculation of chapter 9. In section 8.4 it was determined that the two samples, the un-doped and doped samples have different concentrations of the different crystal orientations. The increase in concentration of the stable Fe(110) surface with a theoretical activation energy of 277.4 kJ/mol (2.875 eV) and a decrease of the Fe(100) and Fe(111) orientations with theoretical activation energies of respectively 266.8 kJ/mol (2.765 eV) and 188.1 kJ/mol (1.950 eV) contributed to the activation energy of the doped sample to increase. The above theoretical values for the activation energies were obtained from chapter 9, Computational results.

## 8.6. Summary

Auger depth profile analysis performed on two differently doped Fe samples confirmed the successful doping of Fe with S using the newly proposed method and experimental set-up. It was found that by doubling the diffusion time, resulted in a 89.38 % increase of the S concentration. SED images of the annealed sample surface revealed that the presence of S caused a  $36\pm 11\%$  decrease in the grain sizes of the Fe sample. It was concluded that the presence of S caused an increased rate in the 3 steps of annealing: recovery, nucleation and grain growth.

X-ray diffraction revealed the following crystal orientations for the un-doped Fe sample and the Fe sample doped with 71.70 ppm S: Fe(100), Fe(211), Fe(110) Fe(310) and Fe(111). The percentage of each crystal orientation present in the samples and their differences are summarized in the table below.

<b>Orientation</b>	<b>% Un-doped sample</b>	<b>% Doped sample</b>	<b>% Difference</b>
<b>Fe(100)</b>	26.25	21.07	-5.180
<b>Fe(211)</b>	22.74	24.77	+2.030
<b>Fe(110)</b>	4.748	21.16	+16.41
<b>Fe(310)</b>	4.825	5.221	+0.396
<b>Fe(111)</b>	41.45	27.78	-13.67

The largest percentage changes in concentration for the S doped Fe sample was observed for the three low-index planes of Fe. In order from largest to smallest concentration change, the three orientations can be arranged as: Fe(110)>Fe(100)>Fe(111). The activation energies for the three low-index orientations of Fe, calculated in chapter 9, can be arranged from most stable to least stable as: Fe(110)>Fe(100)>Fe(111). Thus it can be concluded that the more stable surfaces have grown during annealing, consuming the unstable orientation of Fe. Thus two effects were observed to have occurred in the S doped Fe sample when annealed, the first is the decrease in grain sizes caused by the presence of S in the sample. Secondly is the grain growth of the more stable orientations of Fe which consumed the more unstable orientations of Fe.

Elemental mapping of the Fe-S surface revealed the presence of C and O as surface contaminants and the presence of FeS phase areas which have formed on the surface. No S was observed in the grain boundaries due to a low grain boundary segregation energy of -60 kJ/mol (0.6 eV) at least, at which the S would desegregate into the bulk. The formation of FeS blobs were observed in certain areas on the Fe surface with a diameter of 5.5  $\mu\text{m}$  and a thickness of 2.268  $\mu\text{m}$ . The thickness of the FeS phase was measured by Auger depth profile analysis, from which the formation of a FeS phase could be identified.

Results for the segregation of S in the un-doped polycrystalline bcc Fe delivered the following segregation parameters:  $D_0=4.90\times 10^{-2}$  m<sup>2</sup>/s,  $Q=190.8$  kJ/mol (1.978 eV),  $\Delta G=-134$  kJ/mol (-1.39 eV) and  $\Omega_{\text{Fe/S}}=20$  kJ/mol (0.2 eV). For the segregation of P in the un-doped Fe sample a  $D_0$  value of 0.129 m<sup>2</sup>/s and a  $Q$  value of 226.5 kJ/mol (2.348 eV) were obtained. For the segregation measurements on the doped Fe sample, the segregation parameters of S was determined as:  $D_0=1.79\times 10^{-2}$  m<sup>2</sup>/s,  $Q=228.7$  kJ/mol (2.370 eV),  $\Delta G=-145$  kJ/mol (-1.50 eV) and  $\Omega_{\text{Fe/S}}=8$  kJ/mol (0.08 eV). The difference in the activation energies, segregation energies and interaction parameter values were explained at the hand of different crystal orientations of the un-doped and doped Fe samples.

## 8.7. References

- [1]. R.C. Weast, M.J. Astle, W.H. Beyer, (Eds.), CRC Handbook of chemistry and Physics, CRC Press, Boca Raton, Florida, 1983-1984.
- [2]. D. Fujita, T. Ohgi, T. Homma, Appl. Surf. Sci. 200 (2002) 55.
- [3]. D.R. Askeland, The science and engineering of materials, Stanley Thornes, Cheltenham, 1998.
- [4]. M. Tacikowski, M.W. Grabski, J. Driver, A. Kobylanski, (1996).
- [5]. B.D. Cullity, S.R. Stock, Elements of X-Ray diffraction, Prentice Hall, Inc., New Jersey, 2001.
- [6]. B.M. Reichl, M.M. Eisl, T. Weis, H.Störi, Surf. Sci. 331-333 (1995) 243.
- [7]. P.A. Dowben, A. Miller, (Eds.), Surface segregation phenomena, CRC Press, Boca Raton, Florida, 1990.
- [8]. M.M. Eisl, B.M. Reichl, H. Stori, Surf. Sci. 336 (1995) 377.

- [9]. E.C. Viljoen, J. du Plessis, Surf. Sci. 431 (1999) 128.
- [10]. H.J. Grabke, H. Viehhaus, Surface segregation on nonmetal atoms on metal surfaces. in: P.A. Dowben, A. Miller, (Eds.), Surface segregation phenomena, CRC press, Boca Raton, Florida, 1990, pp. 233.
- [11]. C.H.P. Lupis, Chemical thermodynamics of materials, North-Holland, New York, 1983.

# Chapter 9: Computational results

## 9.1. Introduction

The computational results for the diffusion and segregation of sulfur (S) in bcc iron (Fe) are presented in this chapter. The bulk binding energies were calculated for pure Fe and for the substitutional, octahedral interstitial and the tetrahedral interstitial sites of S in bcc Fe. Using the optimized lattice positions, the climbing image nudged elastic band (CI-NEB) method was used to calculate the migration energy for the diffusion of S in the respective lattice sites. Considering the formation of vacancies as the formation of a Schottky defect in the lattice, vacancy formation energies were calculated for the three low-index planes, Fe(100), Fe(110) and Fe(111), of bcc Fe. The activation energy for the respective surfaces for each of the diffusion mechanism were calculated and compared to literature values. It was found that S diffuses throughout bcc Fe via a nearest neighbour substitutional diffusion mechanism. For the Fe(100) surface the equilibrium position of segregated S was determined as the hollow site with a segregation energy which was found to be in good agreement with the literature value.

## 9.2. Computational details

All calculations were performed using the QUANTUM Espresso code [2], which performs fully self-consistent DFT calculations to solve the Kohn–Sham equations [3]. The Kohn-Sham equations were solved for the generalized-gradient approximation (GGA), using the functional of Perdew and Wang (PW91) [1]. The electronic wave functions were expanded as linear combinations of plane waves, truncated to include only plane waves with kinetic energies below the energy cut-off,  $E_{cut}$ , of 381 eV. Core electrons were replaced by ultrasoft pseudopotentials (USPP) [4] in order to increase the efficiency of the calculations. k-space sampling was performed using a Monkhorst-Pack mesh [5] of dimension  $8 \times 8 \times 8$  for all single unit cell ( $1 \times 1 \times 1$ ) calculations and a mesh of dimension  $3 \times 3 \times 3$  for all calculations on the  $3 \times 3 \times 3$  bulk supercell. For all surface calculations, the

size of the k-point mesh was reduced to  $3 \times 3 \times 1$ , where the smaller dimension is in the direction of the surface. For metallic smearing, the scheme of Methfessel and Paxton [6] with a smearing width of 0.54 eV was used. A fractional spin up state of 0.4 was used for the starting magnetization which resulted in the ground state energy of the system. To ensure that the calculations for the supercells are reliable, the total energy have been converged to  $4.23 \times 10^{-4}$  eV/atom with respect to the computational parameters. The ground state properties of bcc Fe for a  $(1 \times 1 \times 1)$  unit cell are summarized in table 9.1.

**Table 9.1:** Ground state properties of bcc Fe, calculated using the GGA functional of Perdew and Wang (PW91) [1].

Parameter	This work	Experimental [7]	Theory (PW91) [8]
Lattice parameter, $a$ (Å)	2.861	2.866	2.869
Bulk modulus, $B_0$ (GPa)	149.5	168.0	140.0
Magnetic moment, $B$ ( $\mu\text{B}$ )	2.48	2.22	2.37

For all structural relaxation calculations the total energy was converged to  $1 \times 10^{-3}$  eV and the forces have been converged to  $1 \times 10^{-2}$  eV/Å. For all surface structures a vacuum spacing of 14.81 Å was used, which was determined efficient to avoid the interaction of periodically repeated cells. This value corresponds well to literature values of 10-14 Å [8; 9; 10; 11; 12; 13]. All surfaces consisted of 9 atomic layers, with 4 atomic layers to simulate the surface and 5 atomic layers, that were kept frozen, to represent the bulk of the material. The choice for using nine atomic layers was based on literature information, where depending on the information required structures of 4-17 atomic layers have been used [8; 9; 10; 11; 12; 13]. The climbing image nudged elastic band (CI-NEB) [14] method was used to calculate the minimum energy paths (MEP) and migration energy barriers for the diffusion of S in bcc Fe. To ensure that the CI-NEB calculations are fully optimized, the Broyden optimization scheme was used to relax all images to  $<0.05$  eV/atom. To ensure that a high resolution is obtained at the transition state, a variable elastic constant was used in all CI-NEB calculations. A minimum elastic constant value of  $0.017 \text{ N/Å}$  and a maximum value of  $1.166 \text{ N/Å}$  was used. These values were determined by the software as the most appropriate values that would allow the elastic band to relaxed unconstrained. The detailed calculations of the parameter optimizations are given in Appendix B.

## 9.3. Bulk Fe calculations

### 9.3.1. Binding energy

In order to establish by which mechanism S diffuses in bcc Fe, the lattice site where S bonds most strongly and the corresponding binding energy of that lattice site is needed. To determine the equilibrium lattice site of S, the damped dynamics structural relaxation algorithm was used to relax all crystal structures. A substitutional lattice site and the two interstitial sites, the tetrahedral and octahedral sites were considered as equilibrium positions for S in the bcc Fe lattice. The binding energy of pure bcc Fe was also calculated to serve as a reference value for binding energies calculated using the computational parameters specified in section 9.2. The binding energy,  $E_B$ , for an atom in the  $3 \times 3 \times 3$  bcc Fe structure was calculated using equation 9.1 [15; 16]

$$E_B = \frac{E_{Fe} - NE_{FeAtom}}{N} \quad (9.1)$$

where,  $E_{Fe}$ , is the total energy of the  $3 \times 3 \times 3$  bcc Fe supercell structure,  $N$  is the number of Fe atoms in the supercell and  $E_{FeAtom}$  is the energy of a single Fe atom in the gas phase.  $E_{FeAtom}$  was calculated by performing a total energy calculation for a single Fe atom in a  $14.81 \text{ \AA}$  cubic cell. Equation 9.1 gives an average value for the binding energy of an Fe atom, but since the cell is symmetrical the value accurately describes the binding energy of any one atom in the  $3 \times 3 \times 3$  Fe structure. The value calculated was  $-4.878 \text{ eV/atom}$  which is in good agreement with the calculated value of  $-4.89 \text{ eV/atom}$  found in literature [17], see table 9.2. From literature, the experimental binding energy  $-4.28 \text{ eV/atom}$  [18], differing with the value calculated in this work by  $0.60 \text{ eV}$  or  $12.26 \%$ . This difference is acceptable considering that binding energies are overestimated by DFT [19].

For the S atom to diffuse via a substitutional mechanism a vacant lattice site is required. The energy needed to accommodate this vacant site in the lattice is termed  $E_{defect}$ , where the vacant site is considered as a defect in the lattice. It should be noted that this energy term,  $E_{defect}$  is not the amount of energy that is needed to create a vacancy in a perfect bcc Fe crystal structure, it is only

the amount of energy that is needed by the Fe lattice to accommodate a vacant lattice site. Equation 9.2 is used to calculate the energy of the defect,  $E_{defect}$ , in the pure bcc Fe crystal

$$E_{defect} = E_{Fe} - E_{Fe+vacancy} - (E_{FeAtom} + E_B) \quad (9.2)$$

where  $E_{Fe+vacancy}$  is the total energy of the  $3 \times 3 \times 3$  bcc Fe supercell structure containing one vacant lattice site. This statement is in contradiction to literature, where it is believed that the vacancy formation energy is indeed given by the term  $E_{defect}$  [20; 21; 22]. The difference arises due to the approach used in this work to calculate the vacancy formation energy as opposed to how it is commonly done in literature. According to literature, the formation of a vacancy is seen as the removal of an atom from the system, thus an atom is placed in the gas phase. This is unlikely to occur at temperatures below the melting point of bcc Fe. In this work, the formation of a vacancy is considered as the formation of a Schottky defect [23] in the crystal. An atom is removed from the bulk of the crystal and placed on top of the surface leaving a vacant site in the bulk material. This is the approach followed by Terblans [24; 25], whom was able to successfully calculate the formation of vacancies in both aluminium (Al) and copper (Cu) single crystals. A complete discussion on how vacancy formation energies are calculated using the method proposed by Terblans is done in section 9.4.2.

The term in brackets of equation 9.2 is calculated by dividing the total energy of the  $3 \times 3 \times 3$  bcc Fe structure by the number of Fe atoms,  $N$ , in order to get an average energy per Fe atom, equation 9.3. This value includes the energy of the Fe atom itself (an Fe atom in the gas phase) as well as the average binding energy of an Fe atom in the lattice

$$(E_{FeAtom} + E_B) = \frac{E_{Fe}}{N} \quad (9.3)$$

Equation 9.4 which is similar to equation 9.2 is used to calculate the binding energy of the substitutional S atom in the Fe lattice

$$E_B = E_{Fe-S} - E_{Fe+vacancy} - E_S - E_{defect} \quad (9.4)$$

where  $E_{Fe-S}$  is the total energy of the Fe-S structure and  $E_S$  is the total energy for a single S atom in the gas phase. The value of  $E_S$  was calculated for a single S atom in a 14.81 Å cubic box. The value of  $E_{defect}$  is the value calculated using equation 9.2. A binding energy of -3.605 eV was calculated for S, which is in good agreement with the calculated literature value of -3.10 eV [26]. Figure 9.1, shows the optimized position of S (purple atom) in the substitutional lattice site of the 3×3×3 bcc Fe crystal.

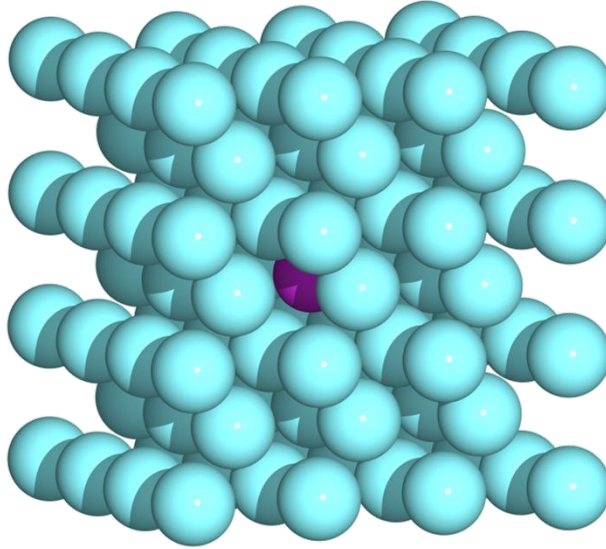


**Figure 9.1:** Substitutional position of S (purple atom) in a 3×3×3 bulk bcc Fe crystal structure.

The binding energy,  $E_B$ , for the tetrahedral and octahedral interstitial positions of S were calculated using equation 9.5

$$E_B = E_{Fe-S} - E_{Fe} - E_S . \quad (9.5)$$

The calculation of the binding energy for the octahedral site resulted in a value of -1.660 eV, while a value of -1.464 eV was found for the tetrahedral lattice site of S. Thus if the S atom is to occupy an interstitial lattice site in the Fe lattice, then the octahedral site with a higher binding energy resulting in a lower total energy of the structure would be favoured. The octahedral interstitial position of S (purple atom) in bcc Fe is illustrated in figure 9.2 and figure 9.3 illustrates the

tetrahedral interstitial position of S in bcc Fe. For illustration purposes the crystal cells were cut in half in order to display the position of the S atom inside the respective Fe lattices.

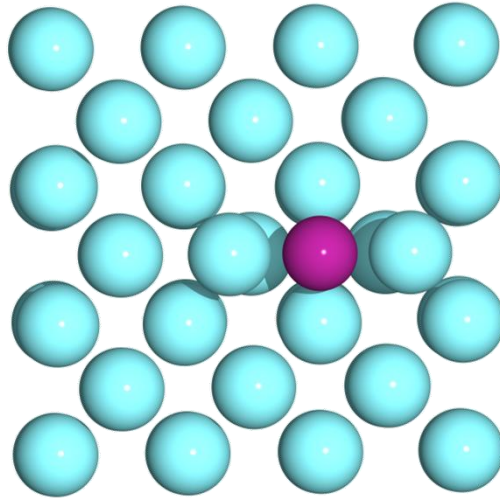


**Figure 9.2:** Octahedral interstitial position of S (purple atom) in bulk bcc Fe. For illustration purposes the front view of a Fe cell cut in half is displayed in order to provide a clear view of the S atoms' position.

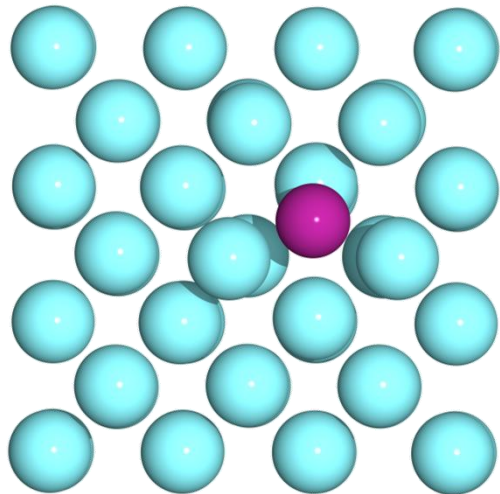


**Figure 9.3:** Tetrahedral interstitial position of S (purple atom) in bulk bcc Fe. For illustration purposes the front view of a Fe cell cut in half is displayed in order to provide a clear view of the S atoms' position.

Table 9.2 summarizes the binding energy values for the bulk Fe, Fe-S (substitutional S), Fe-S (octahedral interstitial S) and Fe-S (tetrahedral interstitial S) structures.

**Table 9.2:** Calculated binding energy values in units of electron volts per atom for Fe and the substitutional and interstitial positions of S in bcc Fe. Also the experimental binding energy value of Fe obtained from literature is given. The last column contains the percentage deviation in the values calculated in this work as compared to the experimental values found in literature.

	This work	Theory	Experimental	% Deviation
<b>Pure bcc Fe</b>	-4.878	-4.89 [17]	-4.28 [18]	12.26
<b>Substitutional</b>	-3.605	-3.10 [26]	-	-
<b>Interstitial (octa)</b>	-1.660	-	-	-
<b>Interstitial (tetra)</b>	-1.464	-	-	-

### 9.3.2. Lattice strain

Looking at figures 9.2 and 9.3, it is evident that the interstitial S atom causes the Fe lattice to become distorted, due to the strain caused on the lattice by the presence of the S atom. To determine the amount of lattice strain caused by the S atom in the respective substitutional and interstitial positions, equation 9.6 [27] was used

$$\varepsilon = \frac{a_{Fe-S} - a_{Fe}}{a_{Fe}} \quad (9.6)$$

where  $a_{Fe}$  is the equilibrium lattice parameter of the Fe  $3 \times 3 \times 3$  supercell and  $a_{Fe-S}$  is the lattice parameter of the  $3 \times 3 \times 3$  supercell of Fe containing a S atom. Table 9.3 gives the values for the percentage strain experienced by the Fe lattice due to the presence of the S atom in the respective interstitial and substitutional lattice sites.

**Table 9.3:** Percentage strain experienced by the bcc Fe  $3\times 3\times 3$  supercell structure due to the presence of S in the respective interstitial and substitutional lattice sites.

<b>S atom position</b>	<b>% Strain</b>
<b>Interstitial (octahedral)</b>	1.818
<b>Interstitial (tetrahedral)</b>	1.818
<b>Substitutional</b>	0

The results in table 9.3 indicates that the interstitial positions of S in bcc Fe causes the Fe structure to become strained. This will cause the total energy of the structure to increase by a value of approximately 1.945-2.141 eV; the difference in binding energy between the substitutional and interstitial sites of S. Under normal circumstances this energy increase would be an unlikely event. Thus taking into consideration the weak binding energy of S in the interstitial positions and the strain caused by the S atom in the interstitial positions, the most probable position for S in bcc Fe would be a substitutional position.

### 9.3.3. Charge density

To obtain a deeper understanding regarding the behaviour of the S impurity in the different lattice sites, charge density plots of the respective structures were constructed. In figure 9.4(a) the S impurity is shown in the substitutional lattice site of bcc Fe with the corresponding charge density plot given in figure 9.4(b). It is seen in figure 9.4(b) how the delocalized charge of the metal is drawn towards the electronegative S atom, which has a value of 2.58 on the Pauling scale [28]. Due to the accumulation of charge on the S atom, a S ion is formed with an ionic radius larger than that of the neutral S atom. From the current calculations it is not possible to give the exact ionic state of the S ion and further analysis is required. The charge accumulation on the S atom causes a charge poor or a charge depleted region on the outside of the S ion. Charge transfer effects due to the presence of S in Fe was also observed by Nelson *et al.*[11]. They investigated the change in the work function of the Fe(100) surface upon adsorption of S and found an increase in the work function due to the electronegative S atom withdrawing charge from the surface. Panzner *et al.* conducted XPS measurements and found from core level analysis that the electron binding energies

of the S 2p peak are in the range 162.2 eV to 161.7 eV, which indicates that the S atoms are negatively charged as a result of the charge transfer from Fe to S.

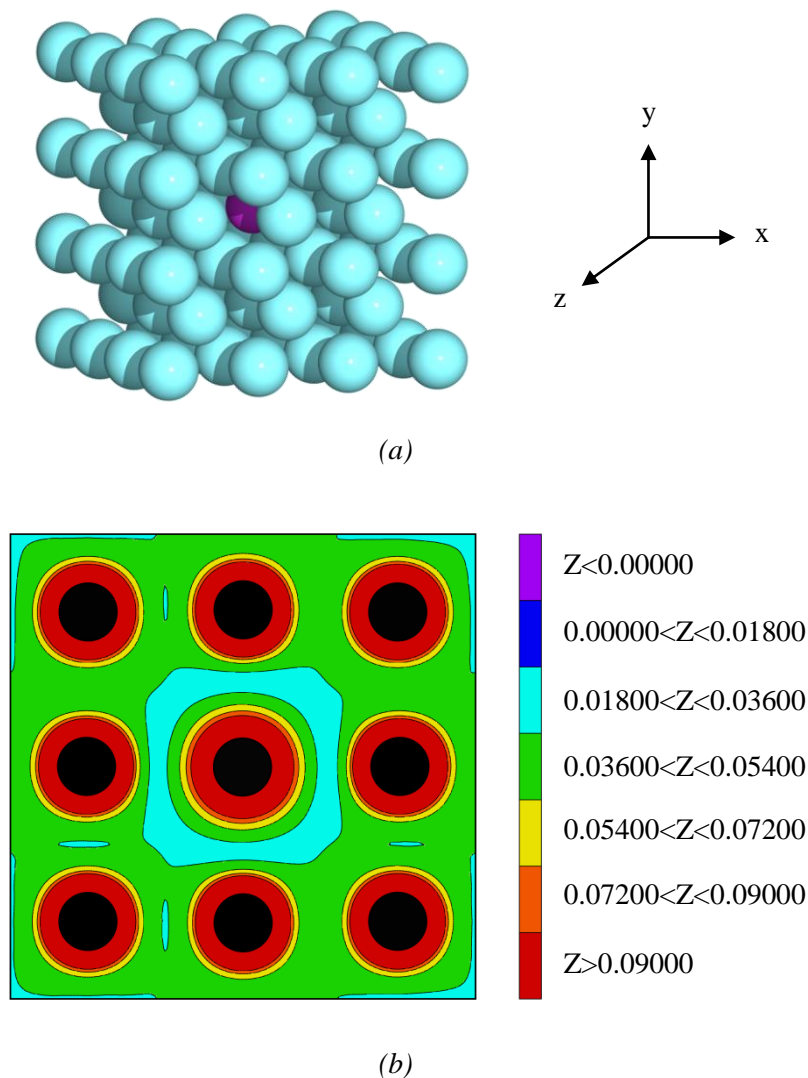


**Figure 9.4:** (a) Substitutional position of S (purple atom) in bulk bcc Fe. (b) The charge density plot in the x-plane of the Fe-S crystal structure. An increase in the size of the S atom is observed as a result of charge accumulating on the electronegative S atom.

The same charge effects as seen for the substitutional position of S in bcc Fe is observed for the interstitial positions of S in bcc Fe, shown in the charge density plots of figures 9.5(b) and 9.6(b). Figures 9.5(a) and 9.6(a) shows the respective octahedral and tetrahedral interstitial sites of S in bcc Fe. As before the S atom is observed to increase in size due to the accumulation of charge on the S atom, which leads to the formation of a S ion with a larger ionic radius as compared to the

neutral S atom. Unlike the case of a substitutional S atom, no depletion region is observed outside of the S ion for either of the two interstitial S structures. This can be contributed to the structures being strained resulting in a larger bulk modulus and thus a more confined space is observed for the S ion in the interstitial sites. Rather than a depletion region around the S ion, bonding between the S ion in the interstitial sites. Rather than a depletion region around the S ion, bonding between the S atom and the Fe atoms is observed.

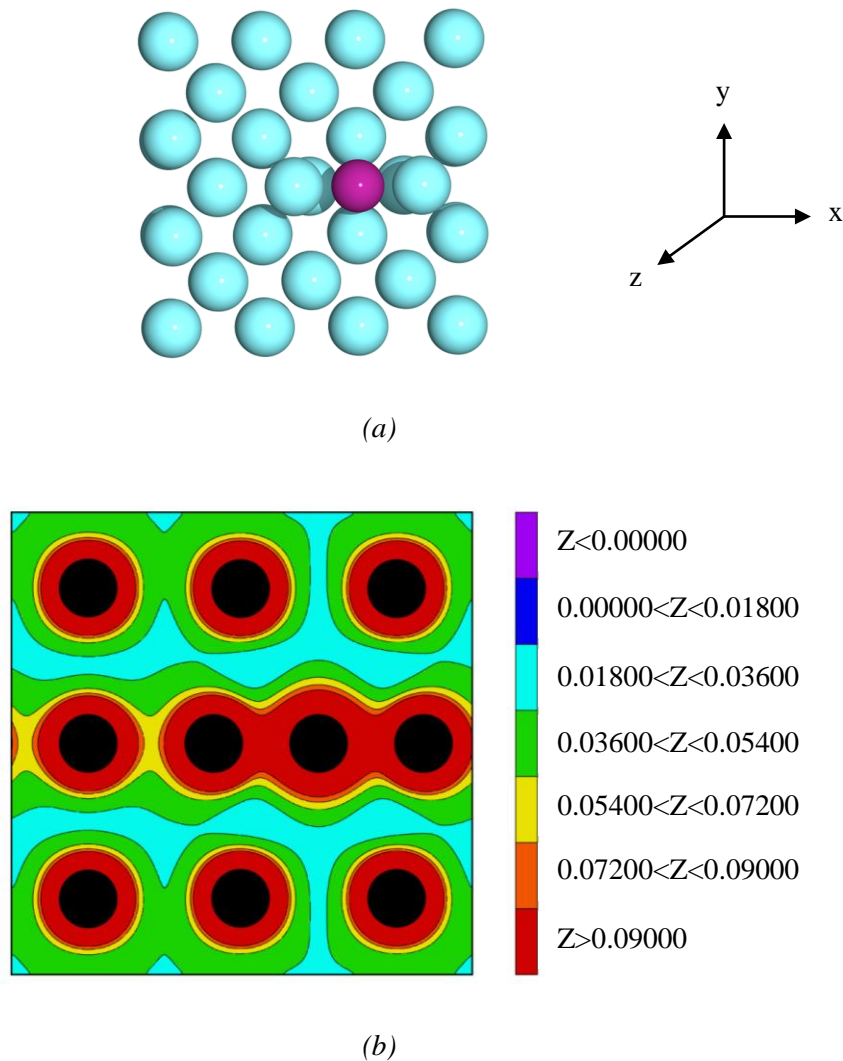


**Figure 9.5:** (a) Octahedral interstitial position of S (purple atom) in bulk bcc Fe. (b) The charge density plot in the x-plane of the crystal structure. The increased size of the S atom as a result of the electronegative character of S is evident.

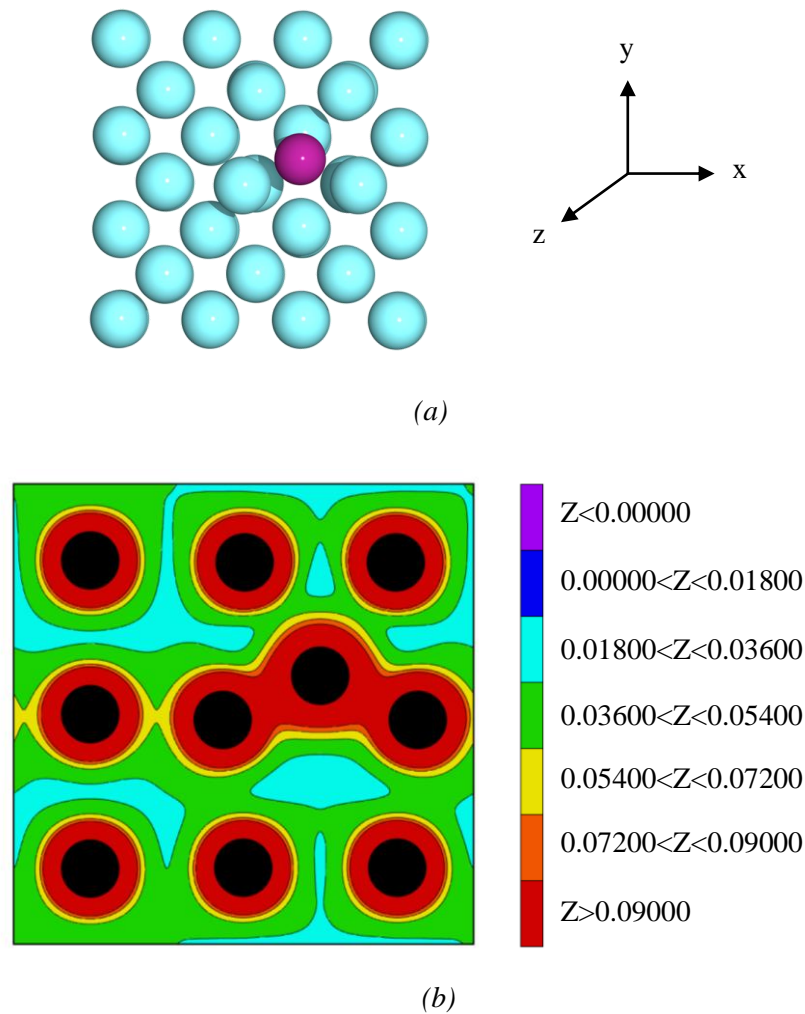


**Figure 9.6:** (a) Tetrahedral interstitial position of S (purple atom) in bulk bcc Fe. (b) The charge density plot in the x-plane of the crystal structure. The increased size of the S atom as a result of the electronegative character of S is evident.

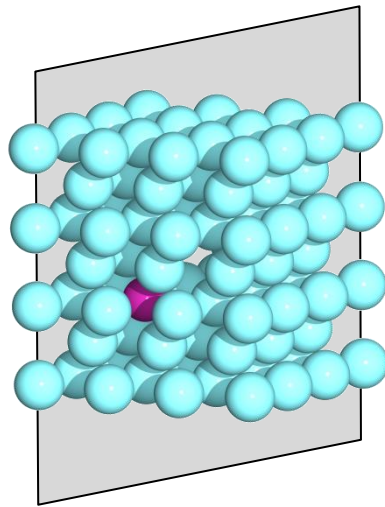
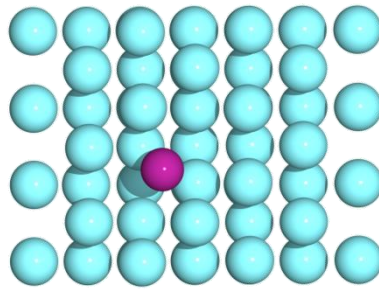
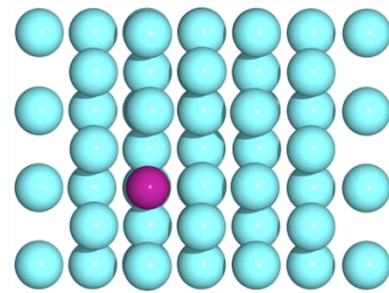
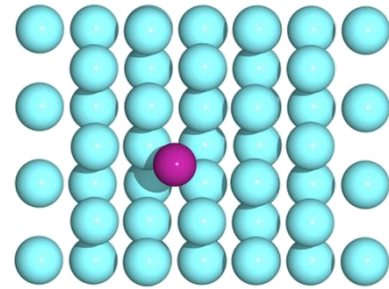
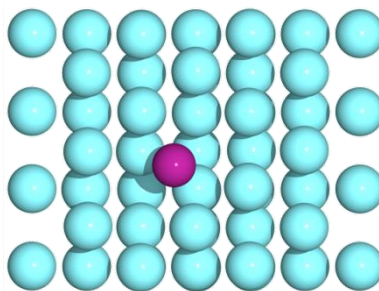
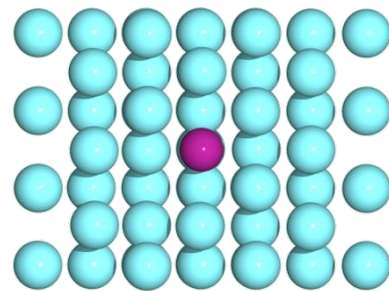
The larger ionic radius of the S ion agrees with the binding energy findings which indicates that the most stable position for the S atom would be in a substitutional lattice site. This section provided information regarding the binding of S in the three possible lattice sites of a bcc Fe crystal. The more favourable site was determined to be the substitutional site due to a larger binding energy value and the fact that for a substitutional S atom there is no strain on the crystal. The strain for the interstitial positions of S is caused by the large ionic radius of S resulting from the transfer of charge from the Fe structure to the S atom. This section states that if a substitutional position is available in the lattice, the probability of S occupying that position is higher than the probability of S occupying an interstitial position. This does not mean that S will never occupy an interstitial

lattice site, only that the probability of that occurring is smaller compared to a substitutional position and that such an event is unlikely to occur. The next section looks at the energy requirements for the migration of S in bcc Fe.

### **9.3.4. Reaction pathways and activation energy calculations**

The different diffusion paths of S in bulk bcc Fe are studied in this section by employing the climbing image nudged elastic band (CI-NEB) method. The minimum energy paths and corresponding migration energy barriers for the different diffusion mechanisms of S in bcc Fe are presented. According to the binding energy calculations from a previous section, section 9.3.1, S prefers to bind in a substitutional lattice site within the bcc Fe lattice. For this site, two possible diffusion mechanisms are considered, namely a nearest neighbour (nn) substitutional diffusion mechanism and a next nearest neighbour (nnn) substitutional diffusion mechanism. Despite the small probability that exist for S to occupy an interstitial lattice site due to the small binding energy and the strain it causes on the Fe lattice, both octahedral and tetrahedral interstitial diffusion mechanisms are also investigated.

Figure 9.7 illustrates the nn substitutional diffusion mechanism of S (purple atom) in bcc Fe, here S diffuses from a substitutional lattice site to a nearest neighbour substitutional vacancy in the crystal. For illustration purposes the crystal cells were cut diagonally in order to provide a clear view of the diffusion process, this is illustrated in the first image of figure 9.7. The CI-NEB method with a 14 image linear path was used in the calculation in order to provide a high resolution of the migration energy barrier. The climbing image was automatically determined by the software as image 8, see figure 9.8. Due to the small distance over which the S atom needs to diffuse and the configuration and symmetry of the atoms, the possibility of a non-linear path was not considered. In figure 9.8, the first image is positioned at a reaction coordinate of 0 and the last image is located at a reaction coordinate of 1. To give a complete energy profile of the substitutional diffusion process, the migration energy barrier was extrapolated to higher and lower reaction coordinates. It can be seen from the images in figure 9.7 that a very open structure is formed by the presence of the vacancy, making the diffusion of S via this mechanism energetically favourable. This is evident in the low migration energy barrier of 0.103 eV shown in figure 9.8.

*Image 1**Image 4**Image 8**Image 11**Image 14*

**Figure 9.7:** Illustration of the nearest neighbour substitutional diffusion of S in bcc Fe. The S atom (purple atom) diffuses from one substitutional lattice site to a nearest neighbour vacancy site.

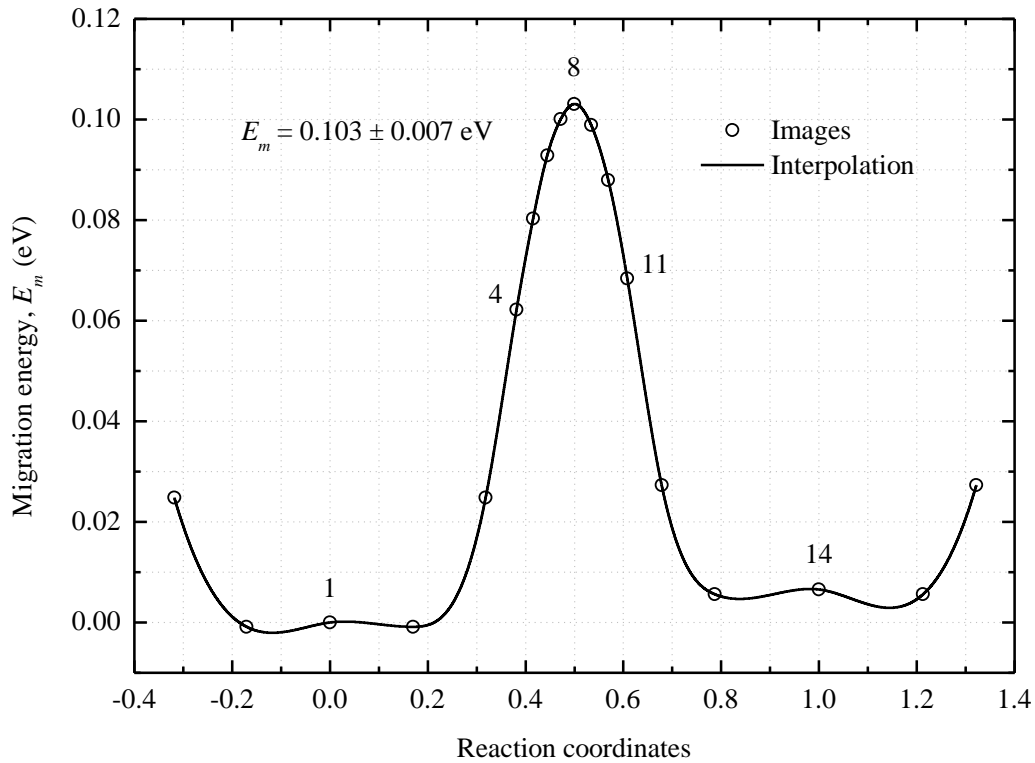


**Figure 9.8:** Migration energy barrier for the diffusion of S via the nearest neighbour substitutional diffusion mechanism, whereby a substitutional S atom diffuses into a nearest neighbour vacancy.

Figure 9.8 shows that there exist a relatively large area in the Fe crystal were the S atom is located in a minimum energy position, which is separated by the small energy barrier of  $0.103 \pm 0.007$  eV. The small energy difference in the initial and final images, images 1 and 14, results in the error of 0.007 eV for the migration energy barrier.

In section 9.4.2 the vacancy formation energy is calculated, and it is proposed that the vacancy formation energy is dependent on the surface orientation of the crystal. For completeness the vacancy formation energy results are also given in table 9.4

**Table 9.4:** Calculated vacancy formation energies of the three low-index Fe surfaces, Fe(100), Fe(110) and Fe(111).

Crystal orientation	Calculated vacancy formation energy, $E_{vac}$ (eV)
<b>Fe(100)</b>	2.662
<b>Fe(110)</b>	2.772
<b>Fe(111)</b>	1.847

The assumption was made that the migration energy barrier of S is predominantly determined by the bulk of a material and thus would be the same for the three crystal orientations Fe(100), Fe(110) and Fe(111). Equation 9.7 is used to determine the activation energy,  $Q$ , for the substitutional diffusion of S

$$Q = E_m + E_{vac}. \quad (9.7)$$

The activation energy is calculated as the sum of the migration energy barrier,  $E_m$ , and the vacancy formation energy,  $E_{vac}$ . Table 9.5 gives the activation energies of the three low-index Fe orientations for the nn substitutional diffusion mechanism.

**Table 9.5:** Calculated activation energies for the nearest neighbour substitutional diffusion of S in the three Fe surfaces: Fe(100), Fe(110), Fe(111).

Crystal orientation	Calculated activation energy, $Q$ (eV)
<b>Fe(100)</b>	2.765
<b>Fe(110)</b>	2.875
<b>Fe(111)</b>	1.950

As previously mentioned a vacancy is required for S to diffuse via a substitutional mechanism. From the results of the substitutional diffusion mechanism it is seen that the presence of a vacancy

in a nearest neighbour lattice site provides a low migration energy path for S diffusion. It is important to also consider the case where the vacancy is not located in the nearest neighbour (nn) lattice site, but in the next nearest neighbour (nnn) lattice site. Thus if the S atom follows this diffusion path it will need to diffuse from a substitutional lattice site through a interstitial (octahedral) lattice site and into the nnn vacancy site. This nnn substitutional diffusion mechanism of S was studied using the CI-NEB method with a 10 image linear path as an initial guess. The calculation was also performed for a non-linear path of 10 images to ensure that the symmetry of the cell did not contribute to the MEP. The image of highest energy, the climbing image, was automatically determined by the software as image 5. The diffusion process is illustrated in figure 9.10, with the migration energy barrier shown in figure 9.9.

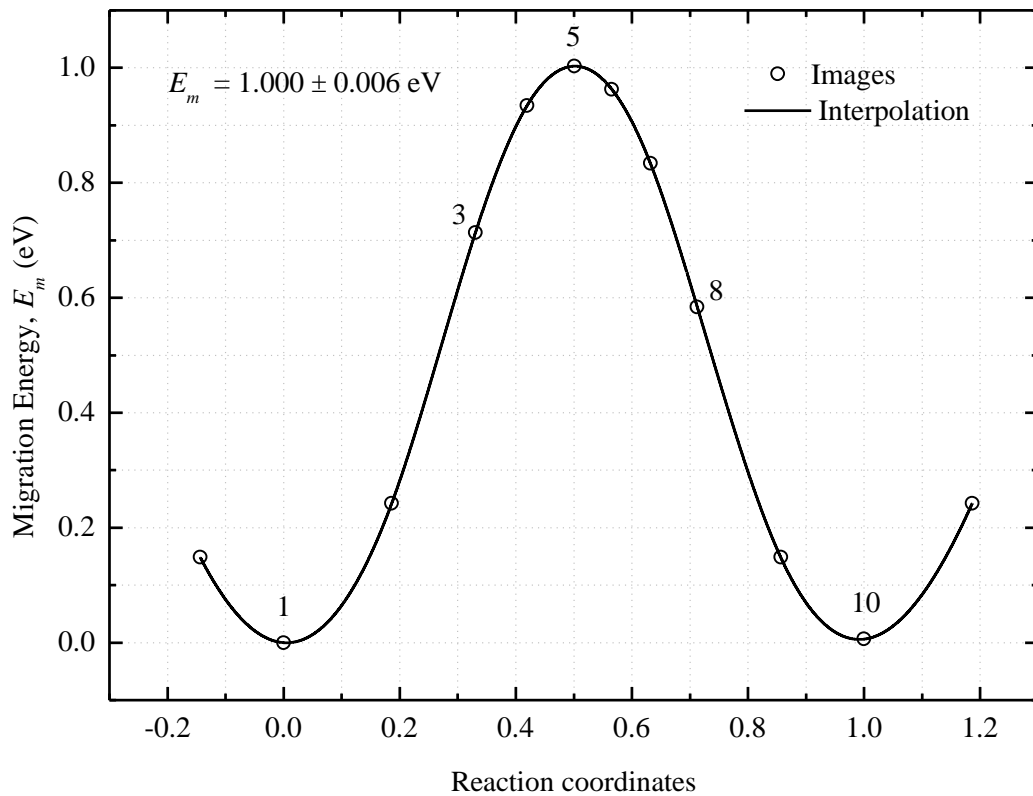


**Figure 9.9:** Migration energy barrier for the diffusion of S via the next nearest neighbour substitutional diffusion mechanism, whereby a S atom diffuses into a next nearest neighbour vacancy.

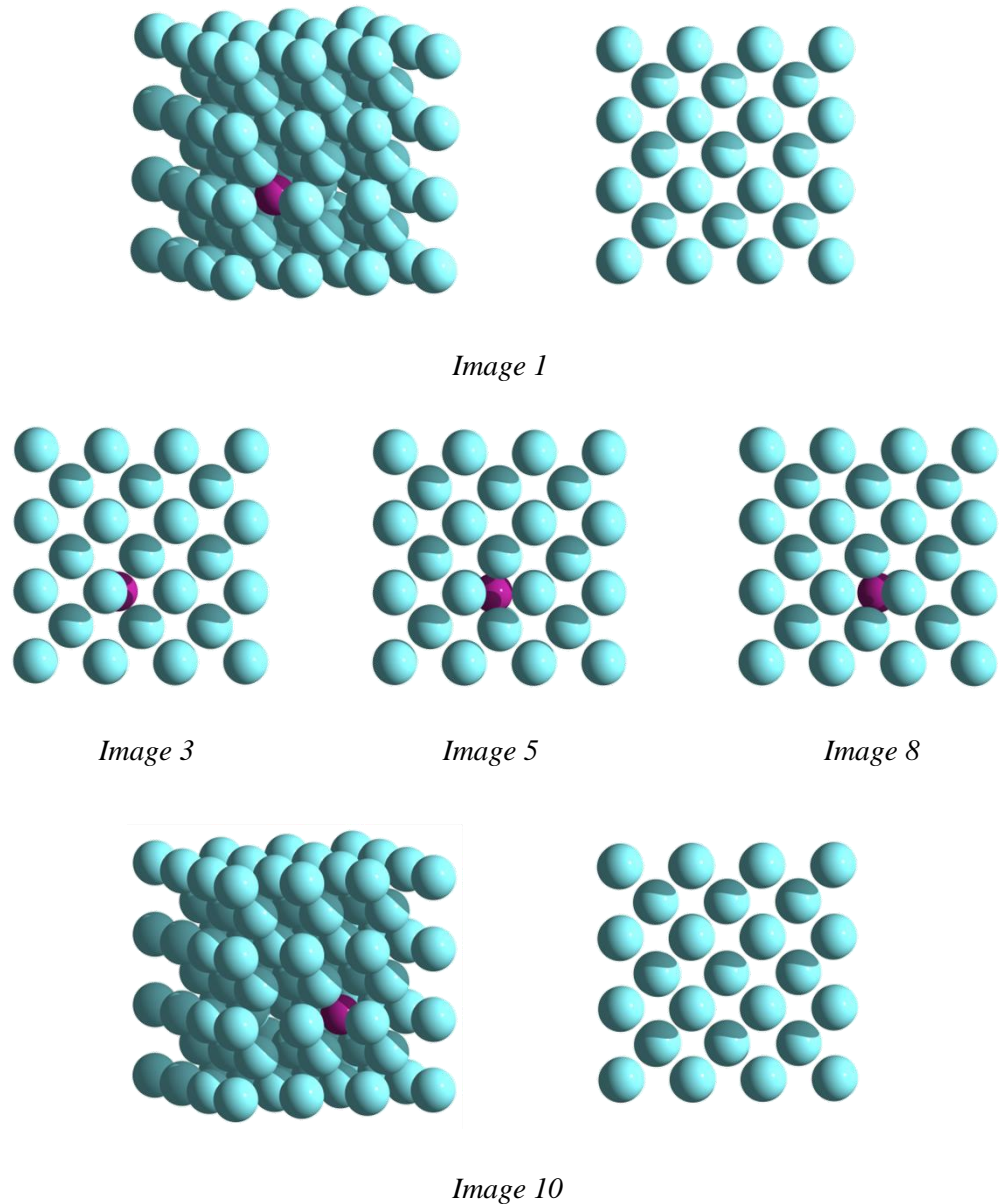


**Figure 9.10:** Illustration of the next nearest neighbour substitutional diffusion mechanism of S (purple atom) in bcc Fe.

Unlike the substitutional mechanism where the presence of the vacancy provided a open structure, here an amount of energy is required to distort the lattice in order to provide a channel by which the S atom can diffuse. Using the vacancy formation energies provided in table 9.4 together with equation 9.7, the activation energy for each of the three surfaces were calculated and are tabulated in table 9.6.

**Table 9.6:** Calculated activation energies for S diffusing via the next nearest neighbour substitutional diffusion mechanism in the three bcc Fe surfaces, Fe(100), Fe(110) and Fe(111).

Crystal orientation	Calculated activation energy, $Q$ (eV)
Fe(100)	3.662
Fe(110)	3.772
Fe(111)	2.847

The large migration energy for this mechanism makes it very unlikely to occur. Considering that the self-diffusion of Fe has a calculated migration energy barrier of 0.558-0.83 eV [29; 30]. Thus the more likely process to occur if a nearest neighbour vacancy is not present for substitutional diffusion is for the Fe atoms in the crystal to self-diffuse until a nearest neighbour vacancy becomes available to the S atom.

Although the interstitial diffusion of S in bcc Fe is an unlikely event due to the strain caused by an interstitial S atom in the Fe lattice and also due to the weak bonding of the S atom in either of the two interstitial sites. There is a certain probability, however small, that such an event can occur and thus the migration energy for these processes needs to be considered. The CI-NEB algorithm with a 32 image linear path was chosen in order to provide a high resolution of the migration energy path. Due to the complex migration energy path of this mechanism, the climbing images were manually chosen as images 5, 15 and 28. For the interstitial diffusion of S, the atom was allowed to diffuse from one octahedral to a nearest neighbour octahedral site. Figure 9.11 illustrates some images of the CI-NEB calculation with the activation energy barrier given in figure 9.12.

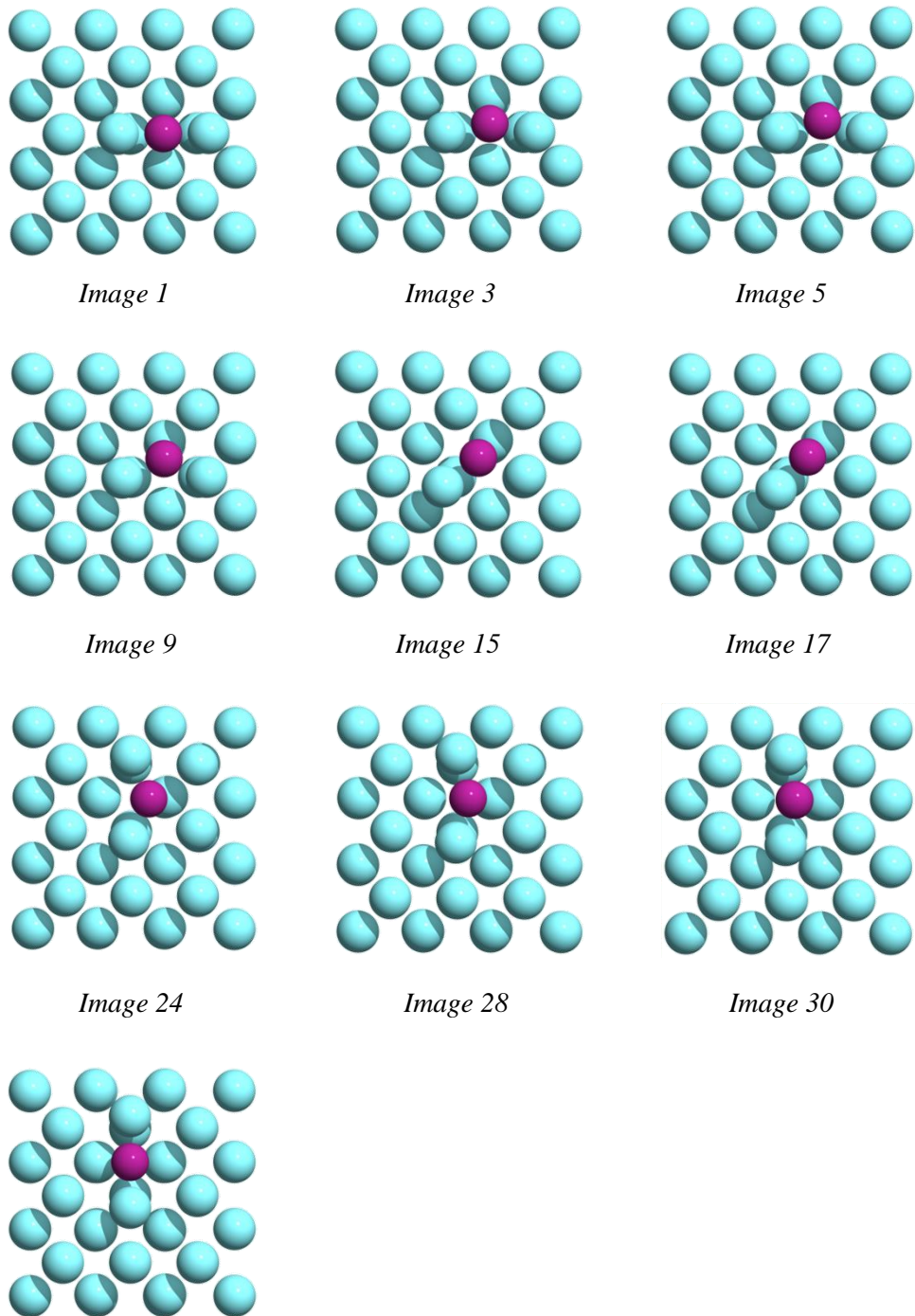


**Figure 9.11:** Illustration of the interstitial diffusion mechanism of S in bcc Fe. The S atom diffuses from a octahedral interstitial site to a nearest neighbour octahedral interstitial site via the tetrahedral interstitial sites.

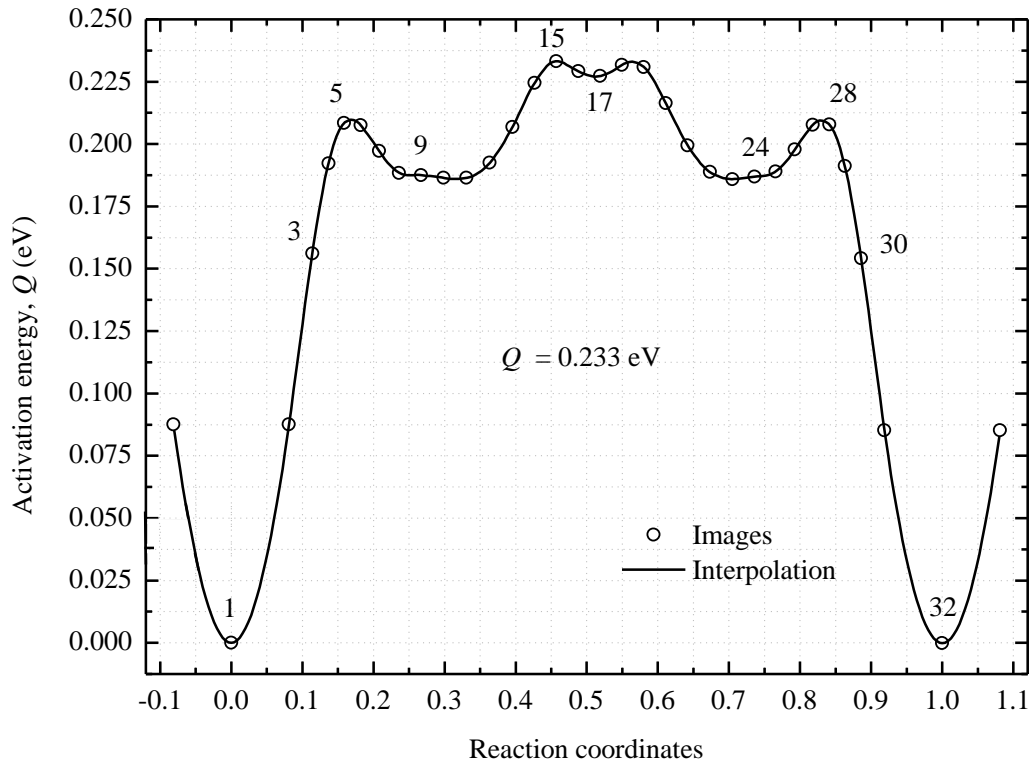


**Figure 9.12:** Activation energy barrier for the diffusion of S via the interstitial diffusion mechanism, whereby a S atom diffuses from one octahedral interstitial site through the tetrahedral sites to a nearest neighbour octahedral site.

The interstitial diffusion of S can be separated into two individual processes, the diffusion of S from an octahedral site to a tetrahedral site and the diffusion of S from one tetrahedral site to the nearest neighbour tetrahedral site. Using the activation energy profile in figure 9.12, the activation energy for the diffusion of S from a octahedral site to an tetrahedral site was calculated as 0.208 eV. For the diffusion of S from one tetrahedral site to the nearest neighbour tetrahedral site an activation energy of 0.046 eV was obtained.

All the possible diffusion mechanisms for S in bcc Fe have been considered in this section. From the binding energy calculations in section 9.3.1 it is most probable that S will occupy a substitutional lattice site. The two possible diffusion mechanisms for this site have been investigated, the nn substitutional diffusion and the nnn substitutional diffusion mechanisms. The nn substitutional diffusion path was found to be the most likely diffusion mechanism. For the interstitial diffusion mechanism both the octahedral and tetrahedral sites of S in bcc Fe were considered and a activation energy of  $0.233 \pm 0.0002$  eV was found for the diffusion of S from one

octahedral site to the next. Unlike the substitutional diffusion mechanism, no vacancy is required for interstitial diffusion and thus the migration energy is equal to the activation energy of diffusion. The activation energies of diffusion for the different mechanisms that were considered are summarized in table 9.7

**Table 9.7:** Activation energies for all the possible diffusion mechanisms of S in bcc Fe.

<b>Mechanism</b>	<b>Calculated activation energy, <math>Q</math> (eV)</b>
<b>Interstitial (octa-tetra)</b>	0.208
<b>Interstitial (tetra-tetra)</b>	0.046
<b>Interstitial (octa-octa)</b>	0.233
<b>Next nearest neighbour Substitutional Fe(100)</b>	3.662
<b>Nearest neighbour Substitutional Fe(100)</b>	2.765

To summarize the results presented up to this stage, figure 9.13 shows a schematic of the energy profile for the diffusion of S via the substitutional and the interstitial (octahedral to octahedral site) diffusion mechanisms. The solid black lines represent the equilibrium lattice sites of S in bcc Fe, while the red curves give the energy required for activation of the diffusion process.

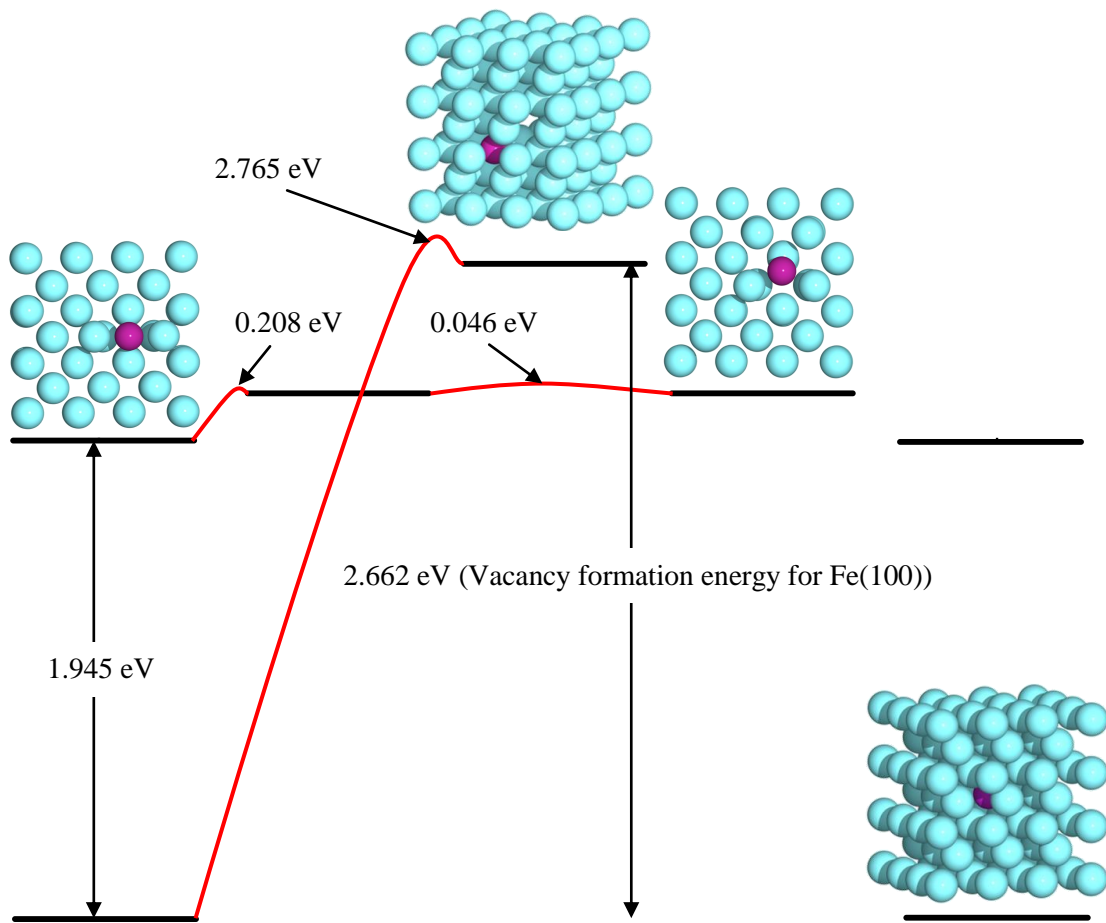


**Figure 9.13:** Energy diagram showing the equilibrium binding sites (solid black lines) of the interstitial and substitutional atoms in bcc Fe along with the activation energies of diffusion, indicated by the red lines.

From figure 9.13 the possibility of an interstitial mechanism looks plausible with 1.945 eV which is required by a substitutionally bonded S atom to jump into a octahedral interstitial site. This is lower than the energy required to form a vacancy in both the Fe(100) and Fe(110) crystal orientations. However if the concentration of the S atoms in the crystal is taken into account, a very small amount of events for the movement of a substitutional S atom to an tetrahedral interstitial site is observed. The remainder of the S atoms will be available to diffuse substitutionally. All of the Fe atoms are evenly probable to take part in the formation of a vacancy and thus the substitutional mechanism remains the dominant mechanism. This is illustrated in figure 9.14, where the probability for the respective processes, including the formation of vacancies in Fe(111), was calculated by equation 9.8

$$\text{number of events} = X \exp\left(\frac{-E}{RT}\right) \quad (9.8)$$

where  $E$  is the energy in J/mol required for the respective processes,  $X$  is the number of atoms which can undergo the specified process,  $R$  is the universal gas constant and  $T$  the temperature in K.

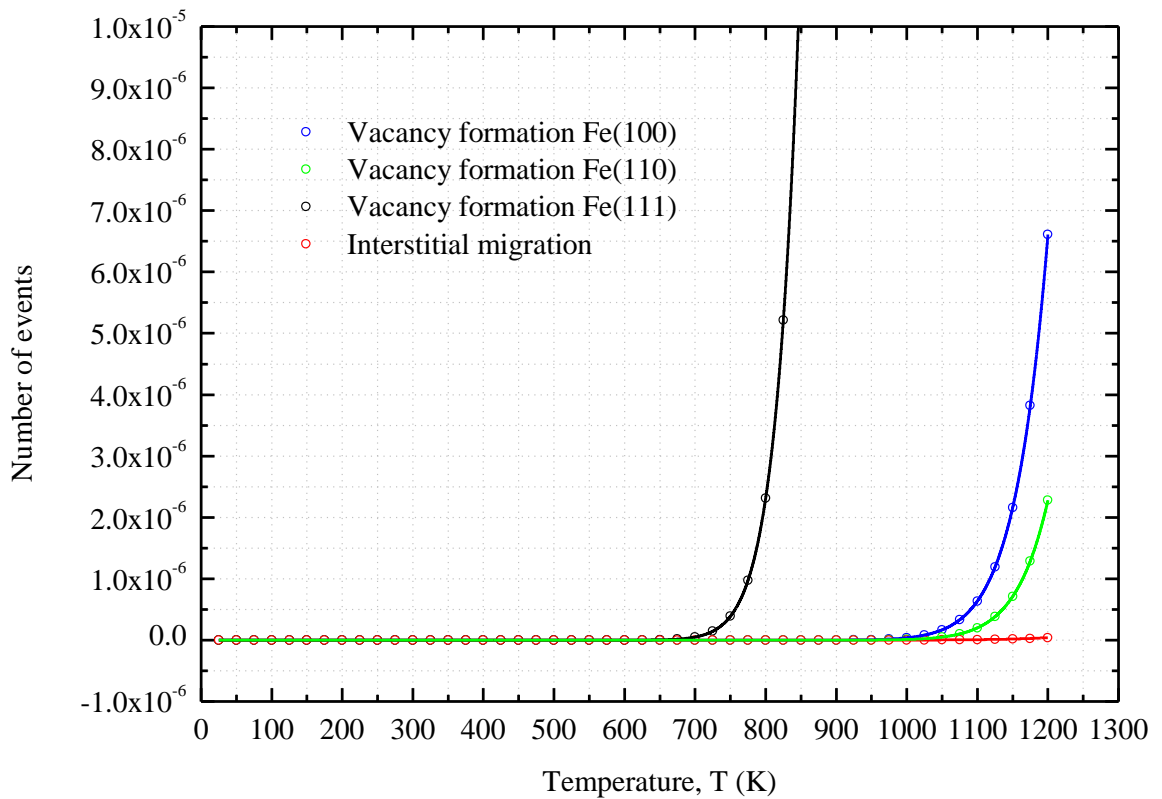


**Figure 9.14:** Number of substitutional S atoms that will jump into a octahedral interstitial position along with the number of vacancies being created in each of the low index orientations of Fe.

From literature the activation energy required for the diffusion of S in bcc Fe is reported as 2.40 eV [31], no indication is given to the crystal structure in which this value was obtained. Arabczyk *et. al.* [32] obtained a activation energy of 2.13 eV for S diffusion to the Fe(111) crystal orientation. Comparing these literature values to the calculated values shows good agreement between the values calculated for the nn substitutional mechanism and the literature values. No experimental

evidence could be obtained that indicates different values for the activation energies of diffusion for different crystal orientations.

## **9.4. Fe(100), Fe(110) and Fe(111) surface calculations.**

The previous sections focused on the bulk properties of bcc Fe and Fe-S, the remainder of this chapter will focus on properties related to the surfaces of bcc Fe. The three low-index surfaces of bcc Fe, Fe(100), Fe(110) and Fe(111) were chosen for the calculation of surface relaxation and vacancy formation energies. The equilibrium positions of segregated S on Fe(100) was determined and compared to experimental results obtained from literature. Using the equilibrium position of the segregated S atom, the segregation energy of S in Fe(100) was calculated.

The surface supercells for the 3 low-index surfaces of Fe used in all surface calculations are shown in figures 9.15, 9.16 and 9.17.

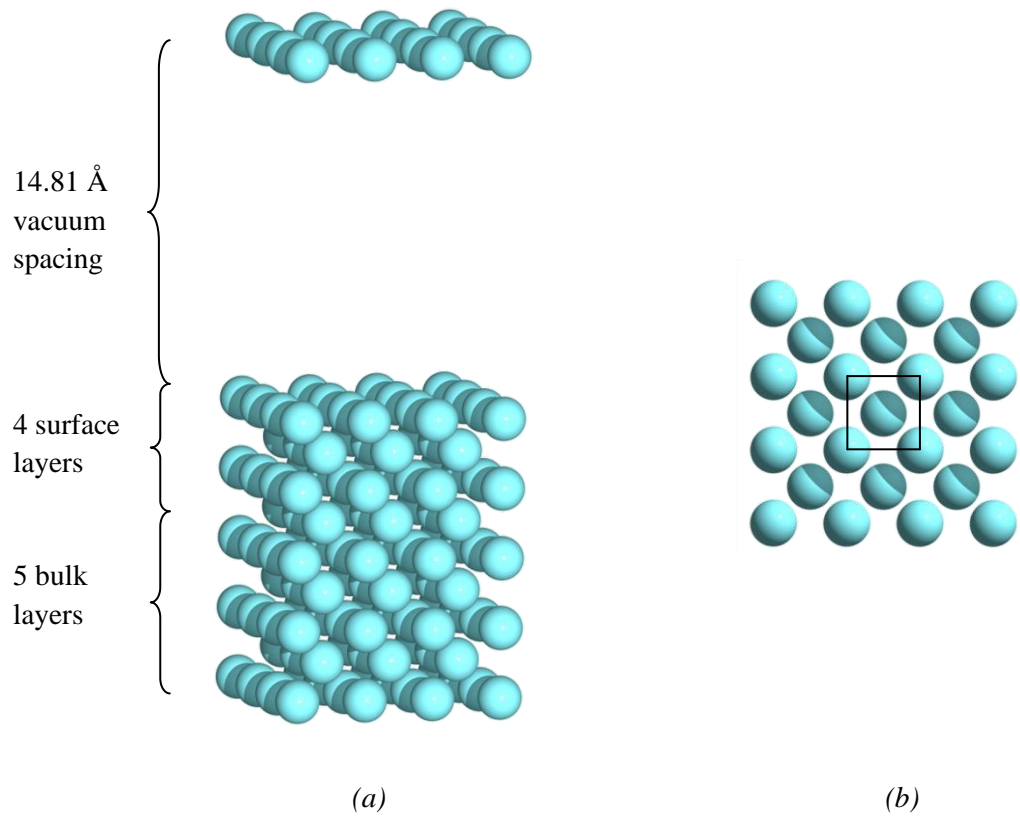
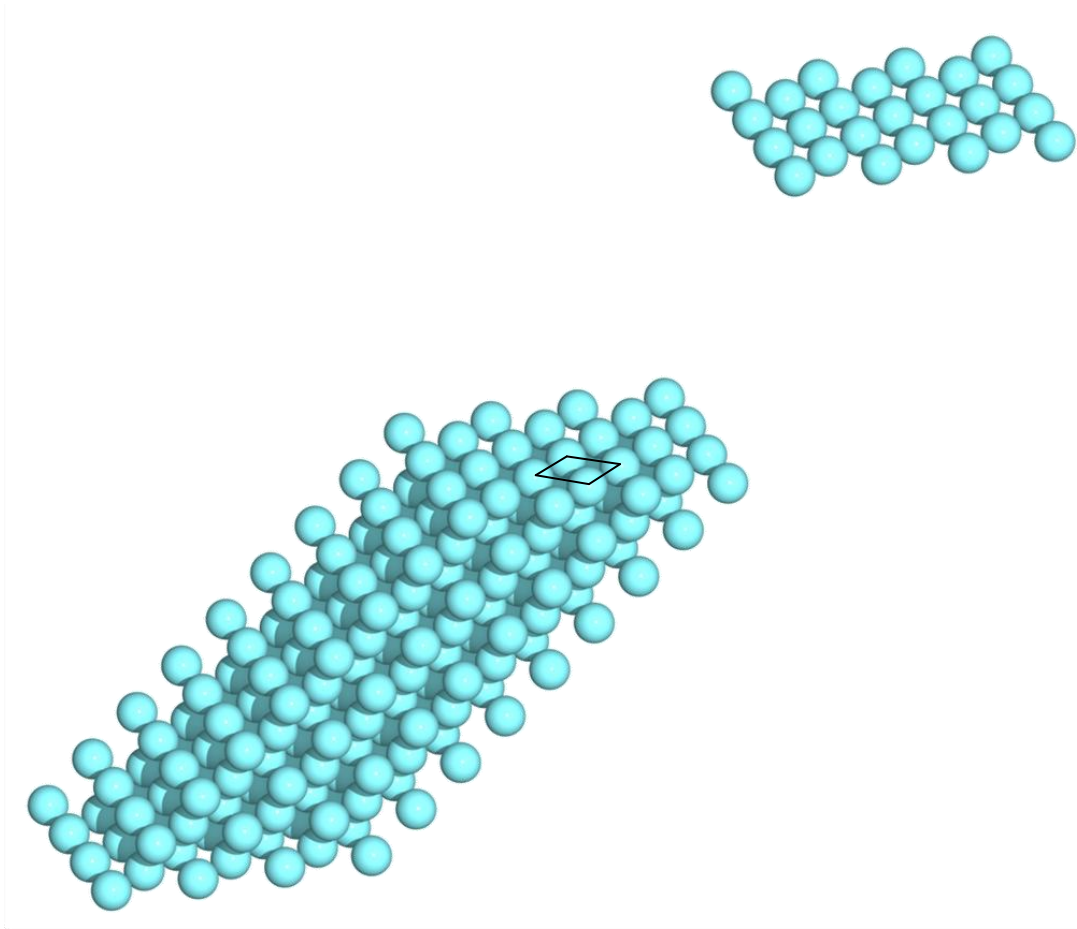
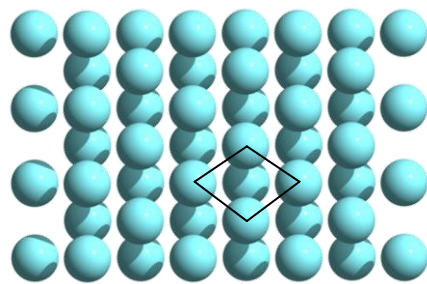


**Figure 9.15:** (a) Side view of the Fe(100) supercell structure. (b) Top view of the Fe(100) surface.



(a)



(b)

**Figure 9.16:** (a) Side view of the Fe(110) supercell structure. (b) Top view of the Fe(110) surface.

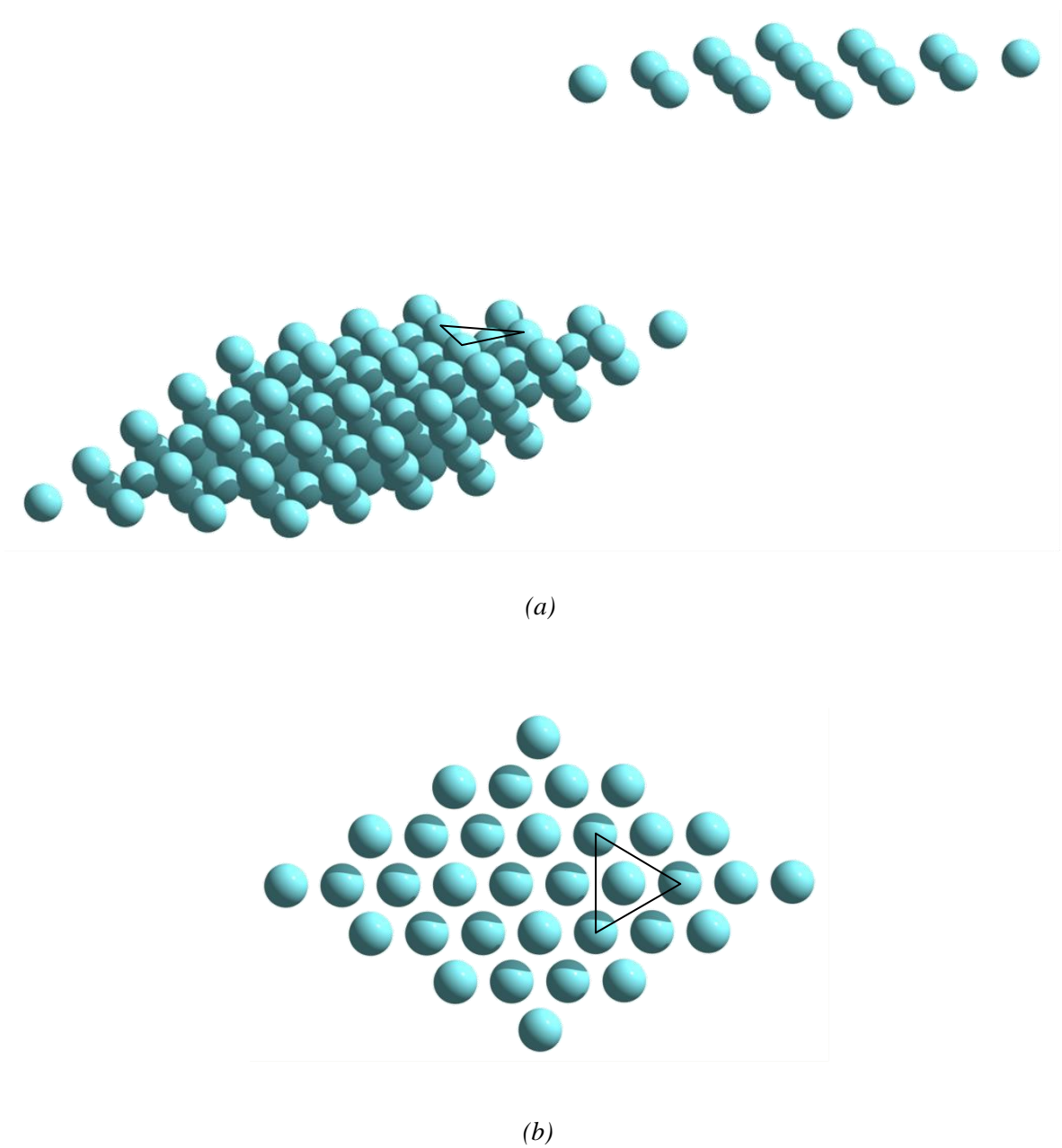


**Figure 9.17:** (a) Side view of the Fe(111) surface showing the step-like character of the surface. (b) Top view of the Fe(111) surface.

From figure 9.17 it can be seen how corrugated the Fe(111) surface is as opposed to the flat surfaces of Fe(100) and Fe(110). The Fe(111) surface has an almost step-like structure.

### 9.4.1. Relaxation of pure Fe surfaces

The relaxation of the first 4 atomic layers of the three low-index surfaces of Fe, Fe(100), Fe(110) and Fe(111) were carried out by means of damped dynamics structural relaxation calculations. Tables 9.8, 9.9 and 9.10 contain the results for the respective surfaces, the tables also include values calculated by other authors and experimentally determined values found in the literature. The relaxation of the surfaces are well documented in literature and the calculations were repeated here to ensure that the structures used in calculations to follow are accurate. Equation 9.9 was used to calculate the relaxation of all surfaces [9; 13]

$$\Delta_{ij} = 100(d_{ij} - d) / d \quad (9.9)$$

where  $d_{ij}$  is the inter lattice spacing between the layers of interest and  $d$  is the inter lattice spacing of the bulk material.

**Table 9.8:** Surface relaxation data for the first 4 atomic layers of the Fe(100) surface.

Fe(100)	$\Delta_{12}$	$\Delta_{23}$	$\Delta_{34}$	$\Delta_{45}$	
	-2.921	+3.068	+0.299	-0.438	This work
	-3.09	+2.83	+1.93	-	Theory [9]
	-1.89	+2.59	+0.21	-0.56	Theory[10]
	-3.6	+2.3	+0.4	-0.4	Theory [13]
	-5±2	+5±2	-	-	Experiment (LEED) [33]
	-1.4±3	-	-	-	Experiment (LEED) [34]

The results obtained in this study compares well to values calculated by other authors. In comparison to the experimental values, obtained by LEED experiments, deviations are observed to be more significant, but still in an acceptable range of the calculated values. Of importance is the trend observed in all the calculated and experimental values for the contraction and expansion of the inter atomic layers. For the first inter atomic layer a contraction is observed, the second and

third inter atomic layers are observed to expand while the fourth inter atomic layer contracts. Thus the trend in surface relaxation of the Fe(100) surface can be summarized as -, +, +, -, where + refers to the expansion of inter atomic layers and - refers to the contraction of inter atomic layers .

**Table 9.9:** Surface relaxation data for the first 4 atomic layers of the Fe(110) surface.

<b>Fe(110)</b>	$\Delta_{12}$	$\Delta_{23}$	$\Delta_{34}$	$\Delta_{45}$	
	0	+0	0	0	This work
	-0.11	+1.16	+1.14	-	Theory [9]
	-0.13	+0.197	-0.06	-	Theory [10]
	-0.1	+0.3	-0.5	-0.2	Theory [13]
	+1±2	+0.5±2			Experiment (MEIS) [35]

Looking at the literature values of table 9.9 it can be seen that very little relaxation occurs for the Fe(110) surface, indicating that this surface is extremely stable. This is also the findings of this study, where the Fe(110) structure was observed not to relax at all with geometrical parameters the same as that of the bulk. The stability of the Fe(110) structure is also confirmed by experimental data obtained from MEIS experiments. Unlike the Fe(100) surface, no definitive pattern is observed for the expansion and relaxation of inter atomic layers. Although from the theoretical values it seems like the first and third inter atomic layers are always contracting, while the second inter atomic layer is expanding, giving a -, +, - pattern.

**Table 9.10:** Surface relaxation data for the first 4 atomic layers of the Fe(111) surface.

<b>Fe(111)</b>	$\Delta_{12}$	$\Delta_{23}$	$\Delta_{34}$	$\Delta_{45}$	
	-1.722	-8.726	9.256	-1.989	This work
	-6.74	-16.89	12.4	-	Theory [9]
	-13.3	-3.6	13.3	-1.2	Theory[10]
	-17.7	-8.4	11.0	-1.0	Theory [13]
	-16.9±3	-9.8±3	4.2±3.6	-2.2±3.6	Experiment (LEED) [36]

The Fe(111) shows large values for both the contraction and expansion of inter atomic layers, indicating that this surface is very unstable compared to the stable Fe(110) and Fe(100) surfaces. Here a definite trend is once again seen in the expansion and contraction of the inter atomic layers, it is -, -, +, -. Based on the relaxation data, the three surfaces can be arranged from most stable to least stable: Fe(110)>Fe(100)>Fe(111). This stability of the surfaces are in agreement with the surface energy calculations of Błonski *et. al.* [9] and Spencer *et. al.* [10].

### 9.4.2. Vacancy formation energy, $E_{vac}$

The amount of vacancies in the crystal structure is very important when it comes to the substitutional diffusion of impurities, since the S atom can only diffuse if a vacancy is available in the lattice. The activation energy,  $Q$ , for substitutional diffusion comprises out of the vacancy formation energy,  $E_{vac}$ , in the Fe lattice plus the migration energy barrier,  $E_m$ . Thus the well known Arrhenius relation [27] can be written in terms of these two energy terms, equation 9.10

$$D = D_0 \exp \left( \frac{-(E_{vac} + E_m)}{RT} \right). \quad (9.10)$$

Two possible mechanisms exist by which a vacancy in a crystal can be formed, namely the Frenkel defect [23] and the Schottky defect [23] mechanisms. Figure 9.18 illustrates the formation of a vacancy by these two respective mechanisms.

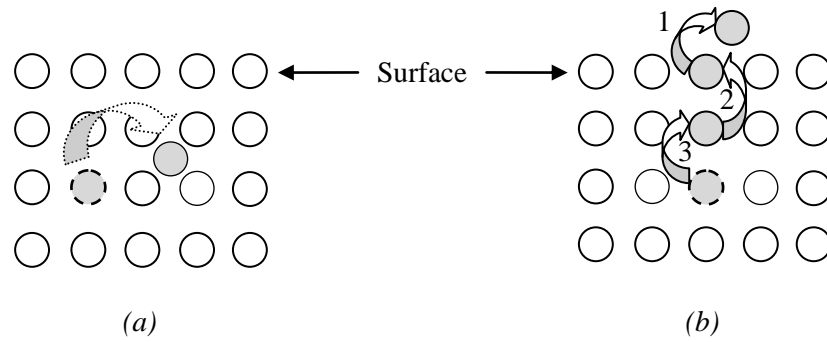


**Figure 9.18:** Illustration of vacancy formation in crystals via (a) the Frenkel defect mechanism and (b) the Schottky defect mechanism.

The Frenkel mechanism requires a large amount of energy, due to the large distortion of the lattice caused by an interstitial atom. The energy requirements of the Frenkel mechanism is significantly larger than that of the Schottky defect mechanism. The Schottky mechanism can be considered as a multistep process, whereby the atom in the surface layer is placed on top of the surface and the empty site created in the surface layer is filled by an atom from the atomic layer below. This process continues until eventually a bulk vacancy is created in the material. As a simplification, the mechanism can be seen as the removal of an atom from the bulk of the material and the placing of that atom onto the surface. Thus the vacancy formation energy can be seen as the difference in binding energy of an atom on the surface of the material minus the binding energy of an atom in the bulk of a material [37]. Mathematically it is given by equation 9.11

$$E_{vac} = E_{B(Surf)} - E_{B(Bulk)}. \quad (9.11)$$

Inserting this expression into equation 9.10 results in the Arrhenius expression for substitutional diffusion, equation 9.12

$$D = D_0 \exp\left(\frac{-(E_{B(Surf)} - E_{B(Bulk)} + E_m)}{RT}\right). \quad (9.12)$$

Considering the formation of vacancies by this mechanism where the surface binding energy comes into consideration, makes this mechanism surface orientation dependant. Thus for the three different orientations of Fe considered in this work, different vacancy formation energies were calculated and the results are given in table 9.11.

**Table 9.11:** Vacancy formation energy values calculated for the three low-index surfaces of Fe, by considering the formation of vacancies to occur via a Schottky defect mechanism.

<b>Crystal orientation</b>	<b>Calculated vacancy formation energy, <math>E_{vac}</math> (eV)</b>
<b>Fe(100)</b>	2.662
<b>Fe(110)</b>	2.772
<b>Fe(111)</b>	1.847

For the calculation of the vacancy formation energy the equilibrium position of the Fe atom placed on top of the surface was determined by performing structural relaxation calculations using the damped dynamics algorithm. For the Fe(100) and Fe(111) surfaces the Fe atom placed onto the surface was found to be most stable in a hollow site on the surface, while the atom on the Fe(110) surface was most stable in the long bridge site. Figures 9.19, 9.20 and 9.21 shows the atom on the Fe surfaces which was removed from the bulk to form the vacancy.

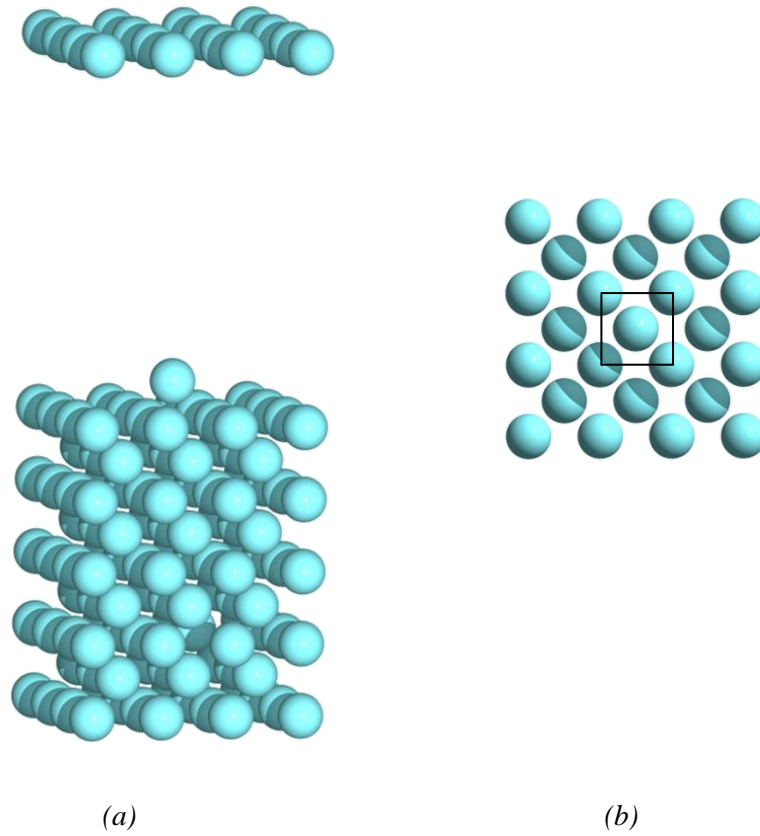


**Figure 9.19:** (a) Side view of the Fe(100) surface showing the position of the Fe atom (placed on the surface which was removed from the bulk material to create a vacancy). (b) Top view showing the Fe atom in the hollow site of the Fe(100) surface.

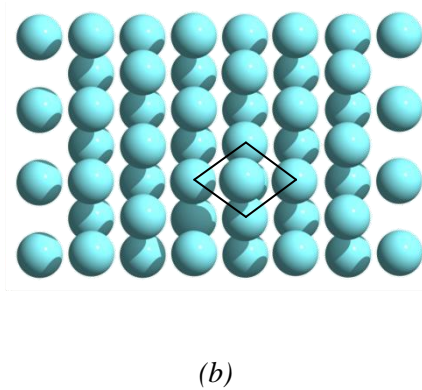
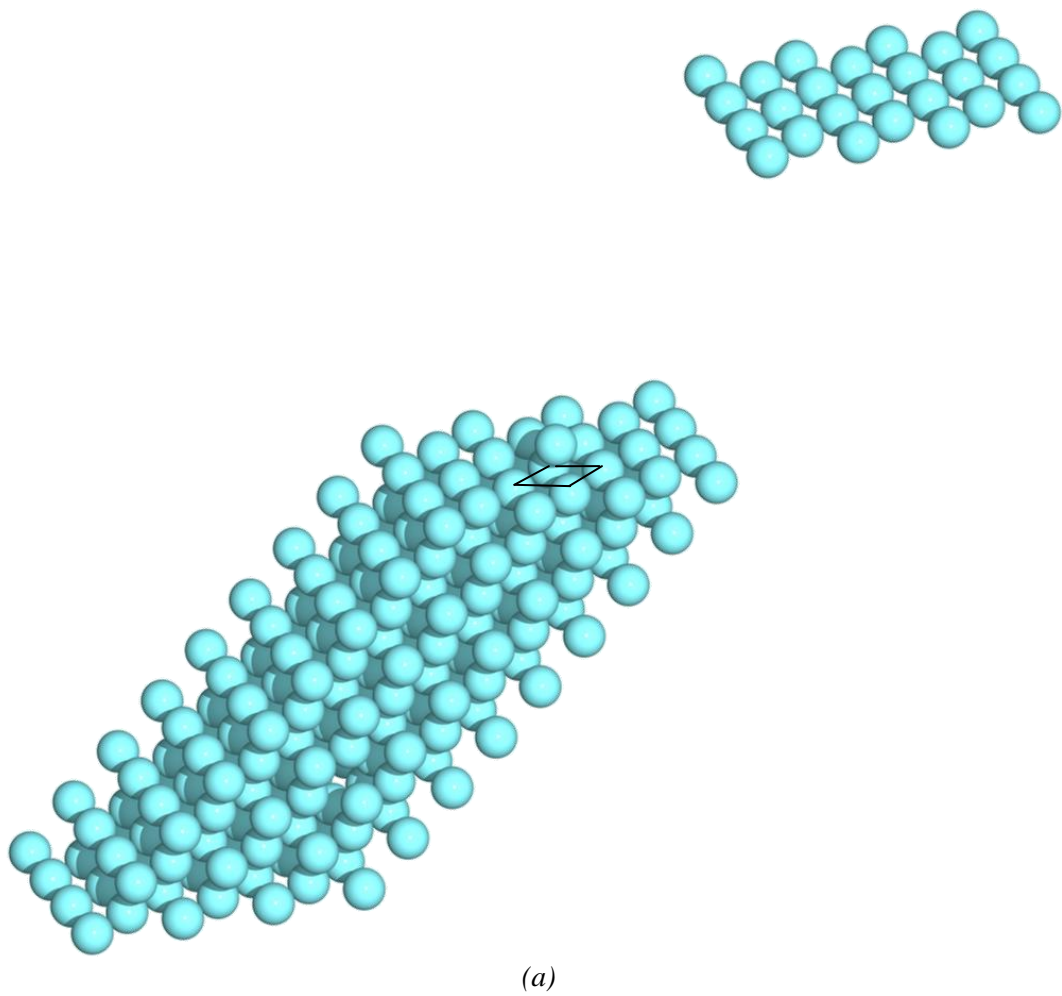


**Figure 9.20:** (a) Side view of the Fe atom placed in the long bridge site of the Fe(110) surface. (b) Top view showing the Fe atom in the long bridge site on the surface of Fe(110).

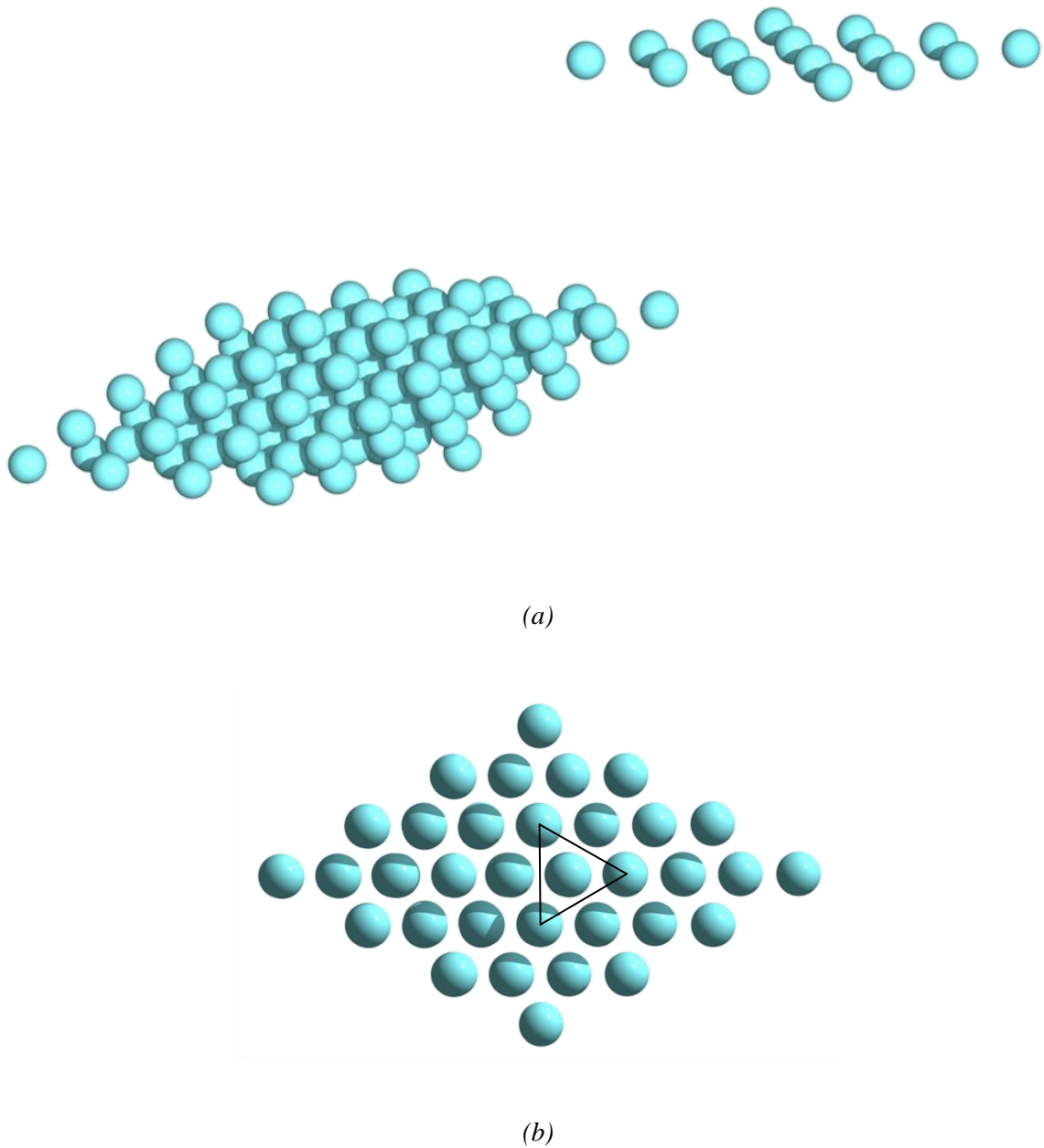


**Figure 9.21:** (a) Side view of the Fe atom placed in the hollow position of the Fe(111) surface. (b) Top view illustrating the position of the Fe atom placed in the hollow site of the Fe(111) surface.

From the results presented in table 9.11 a more rapid diffusion of S in Fe(111) is expected as compared to the other two surfaces based on the small value for the vacancy formation energy of this surface. Thus the conclusion can be made that the orientation of the crystal determines the stability of the structure and for the low-index surfaces of Fe, that the more stable structures have

higher vacancy formation energies. This is expected since the more unstable a surface is, the less energy is required to remove a surface atom which is the initial step in the formation of vacancies.

No literature data could be found where the orientation of the surface was taken into account for the calculation of the vacancy formation energies in bcc Fe as was done in this study. Calculated values found in literature was determined for bulk structures, where the orientation of the surface was not taken into account. Experimental data from literature also neglected to taken into account the influence of the surface orientation on the formation of vacancies. Table 9.12 summarizes the values calculated here and those found in literature.

**Table 9.12:** Summary of vacancy formation energies calculated in this work and values found in literature. All energies are given in units of electron volts per atom (eV/atom).

	<b>Fe(100)</b>	<b>Fe(110)</b>	<b>Fe(111)</b>	<b>Bulk</b>
<b>This work</b>	2.662	2.772	1.847	
<b>Theory(ab- initio)</b>				2.17 [38]
<b>Theory (molecular dynamics)</b>				1.863 [20]
<b>Theory (ab- initio)</b>				2.16 [39]
<b>Experimental</b>				1.8-2.0 [40]
<b>Experimental</b>				2.0±0.2 [41]

### 9.4.3. Segregation energy of Fe(100)

In section 9.3.4, the diffusion mechanism of S in bcc Fe was found to be the nn substitutional mechanism, where a S atom diffuses from a substitutional lattice site to a nearest neighbour vacancy. Thus in principle if the S atom is located just beneath the surface and a vacancy becomes available in the surface layer, the S atom should diffuse into that vacancy. The question is whether this would be the most stable position for the S atom or whether the S atom would diffuse onto the surface. To determine the most stable position for a segregated S atom in the Fe(100) surface, a position in the surface and the hollow site on the Fe(100) surface was considered as the two

possible equilibrium positions. From literature the most stable position for adsorbed S on the Fe(100) surface is found to be the hollow site [11; 12]. Figure 9.22 shows the initial and final positions if the final position of the segregated atom is taken to be in the surface layer. Figure 9.23 shows the initial and final positions of the S atom if the final position is taken to be in the hollow site of the Fe(100) surface.

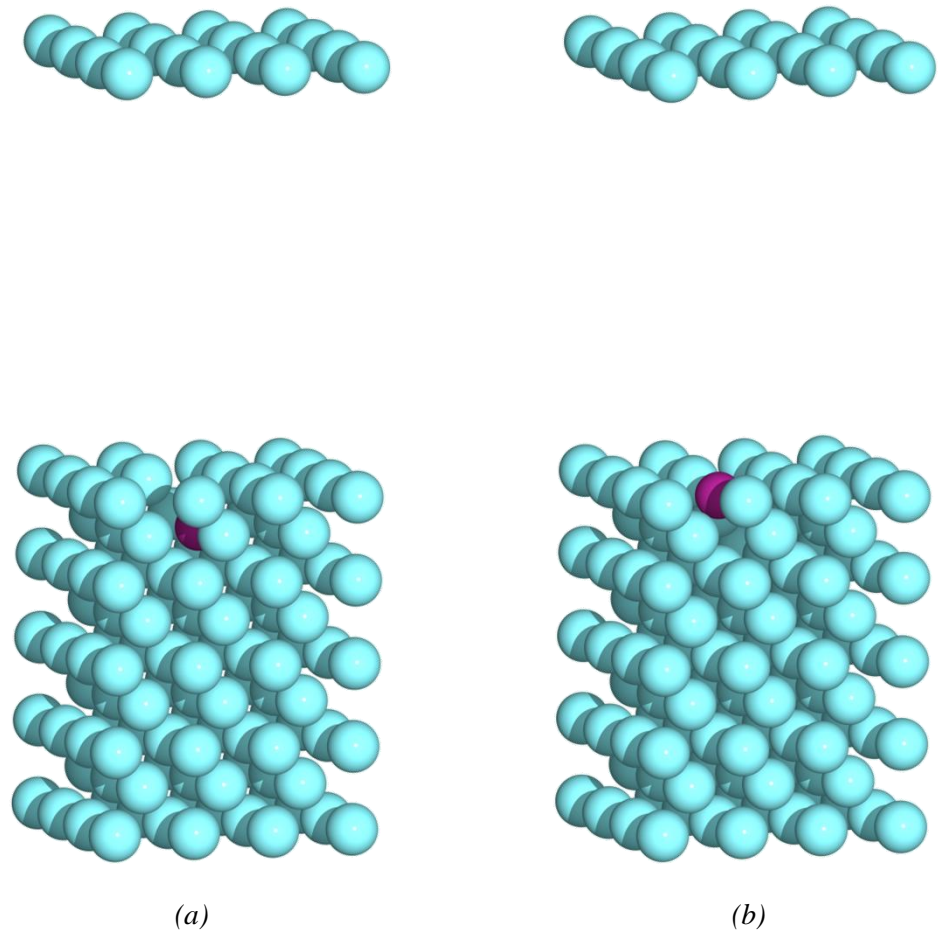


**Figure 9.22:** Images showing the (a) initial and (b) final position of the segregation process if the final position is taken to be in the surface layer of the material. The purple atom represents the S atom.

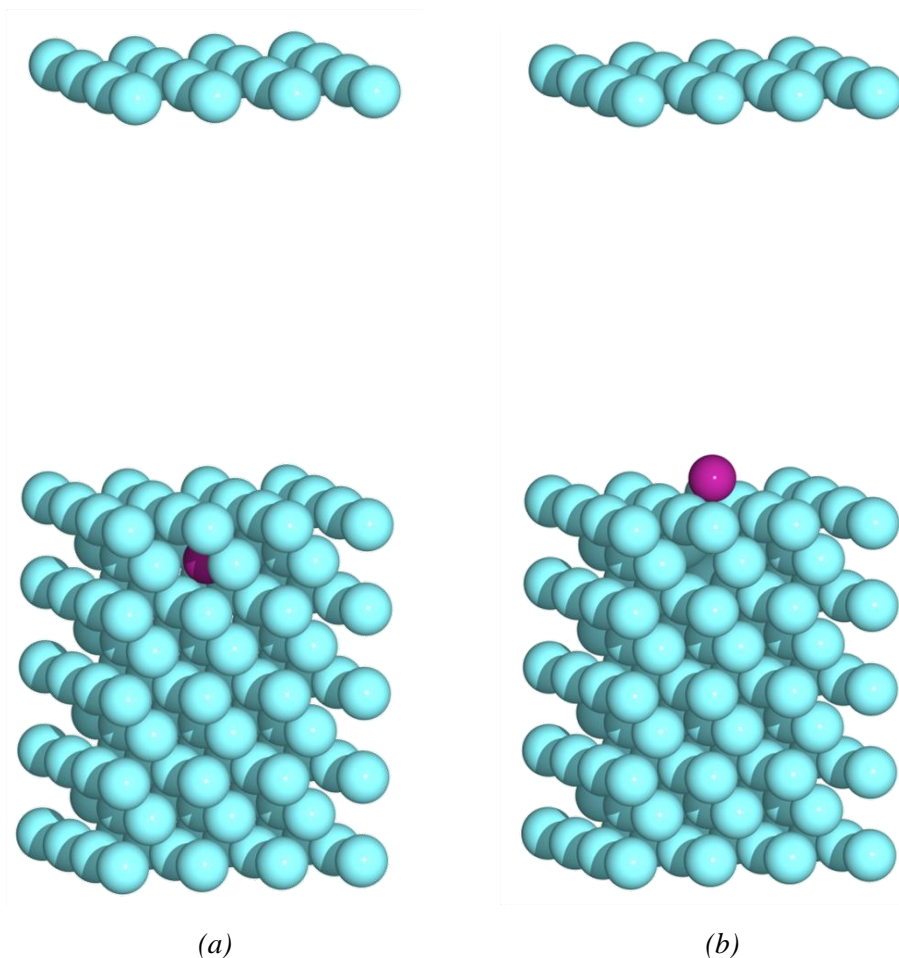


**Figure 9.23:** Images showing the (a) initial and (b) final position of the segregation process if the final position is taken to be in the hollow site of the Fe(100) surface. The purple atom represents the S atom.

The segregation energies were calculated as the energy difference between the binding energy of a S atom in the final position minus the binding energy of the S atom in the initial position. The results indicated that the diffusion of a S atom from beneath the surface to a position in the surface layer would result in a segregation energy of -0.643 eV (62.04 kJ/mol). If the atom diffuses to the hollow site onto the Fe surface a segregation energy of -1.859 eV (-179.4 kJ/mol) is obtained. The value of -1.859 eV (179.4 kJ/mol) is in good agreement with the experimental value of -1.969 eV (-190.0 kJ/mol) reported by Grabke and Viehhaus [42] with a 5.58 % deviation. Thus the most stable position of a segregated S atom in Fe(100) would be in the hollow site onto the surface.

## 9.5. Summary

A systematic study was conducted to investigate the diffusion of S in the low-index surfaces of bcc Fe namely the Fe(100), Fe(110) and Fe(111) surfaces. Calculations of the binding energies revealed that the S atom would bind most favourably in a substitutional lattice site with a binding energy of -3.605 eV as opposed to the interstitial binding energies of -1.660 eV and -1.464 eV for the octahedral and tetrahedral sites respectively. Charge density plots were constructed to investigate the effect of charge transfer in the Fe-S system due to the presence of the electronegative S atom. Results indicated that charge accumulated onto the S atom causing it to increase in size. The S ion with an atomic radius larger than that of the neutral S atom confirmed the strain calculations which showed that the larger S ion in the interstitial sites causes the Fe lattice to become strained.

From the CI-NEB calculations the diffusion mechanism of S was determined to be the nn substitutional mechanism with a migration energy barrier of 0.103 eV, whereby the substitutional S atom diffuses into a nearest neighbour vacancy. If a nearest neighbour vacancy is not available to the S atom, self-diffusion of Fe with an migration energy barrier of 0.558-0.83 eV as obtained from literature, will occur as opposed to the S atom diffusing to a next nearest neighbour vacancy. The vacancy formation energy was calculated by considering the formation of vacancies to occur via the Schottky defect mechanism. For Fe(100) a vacancy formation energy of 2.662 eV (256.8 kJ/mol) was calculated, while Fe(110) and Fe(111) have vacancy formation energies of 2.772 eV (267.4 kJ/mol) and 1.847 eV (178.2 kJ/mol) respectively. The migration energy was considered to be surface independent and the activation energies were calculated as 2.765 eV (277.4 kJ/mol) for Fe(100), 2.875 eV (266.8 kJ/mol) for Fe(110) and 1.950 eV (188.1 kJ/mol) for Fe(111). Experimental values for the activation energy of S in bcc Fe was given as 2.40 eV (231.6 kJ/mol) [31] for an unknown crystal orientation and 2.13 eV (205.5 kJ/mol) [32] for Fe(111), which is in good agreement with the activation energies calculated here. These values confirm a nn substitutional diffusion mechanism for S in bcc Fe.

It was found that the stability of the surfaces from most to least stable are: Fe(110)>Fe(100)>Fe(111). It was concluded that the more unstable surfaces have the lowest vacancy formation energy and thus the lowest activation energy. The segregation of S in the Fe(100) surface was investigated and it was found that the most stable position of a segregated S atom is located in the hollow site on the surface and not in the surface layer of the material. Results revealed a

segregation energy of -1.859 eV (-179.4 kJ/mol) which is in good agreement with the experimental value of -1.969 eV (-190.0 kJ/mol) found in literature.

## 9.6. References

- [1]. J.P. Perdew, Y. Wang, Phys. Rev. B 45 (1992) 13244.
- [2]. P. Giannozzi, et al., Cond. Mat. 21 (2009) 1.
- [3]. W. Kohn, L.J. Sham, Phys. Rev. B. 140 (1965) 1133.
- [4]. D. Vanderbilt, Phys. Rev. B 41 (1990) 5188.
- [5]. H.J. Monkhorst, J.D. Pack, Phys. Rev. B 13 (1976) 5188.
- [6]. M. Methfessel, A.T. Paxton, Phys. Rev. B 40 (1989) 3616.
- [7]. H.C. Herper, E. Hoffman, P. Entel, Phys. Rev. B 60 (1999) 3839.
- [8]. A. Hung, I. Yarovsky, J. Muscat, S.R. Russo, I. Snook, R.O. watts, Surf. Sci. 501 (2002) 261.
- [9]. P. Błonski, A. Kiejna, Vacuum 74 (2004) 179.
- [10]. M.J.S. Spencer, A. Hung, I.K. Snook, I. Yarovsky, Surf. Sci 513 (2002) 389.
- [11]. S.G. Nelson, M.J.S. Spencer, I.K. Snook, I. Yarovsky, Surf. Sci. 590 (2005) 63.
- [12]. N. Todorova, M.J.S. Spencer, I. Yarovsky, Surf. Sci 601 (2007) 665.
- [13]. P. Błonski, A. Kiejna, Surf. Sci 601 (2007) 123.
- [14]. G. Henkelman, B.P. Uberuaga, H. Jónsson, J. Chem. Phys. 113 (2000) 9901.
- [15]. Y. Ouyang, H. Chen, X. Zhong, Theor. Chem. Acc 115 (2006) 32.
- [16]. S.S. Pundlik, K. Kalyanaraman, U.V. Waghmare, J. Phys. Chem-US 115 (2011) 3809.
- [17]. W. Coa, Theoretical and experimental studies of surface and experimental interfacial phenomena involving steel surfaces, Dissertation, Stockholm, 2010.
- [18]. C. Kittel, Introduction to solid state physics, John Wiley & sons, 2005.
- [19]. D.S. Sholl, J.A. Steckel, Density functional theory - a practical introduction, John Wiley & Sons, Inc., Hoboken, Jew Jersey, 2009.
- [20]. C.Q. Wang, Y.X. Yang, Y.S. Zhang, Y. Jia, Comp. Mater. Sci. 50 (2010) 291.
- [21]. O.Y. Vekilova, D.I. Bazhanov, S.I. Simak, I.A. Abrikosov, Phys. Rev. B. 80 (2009) 024101.
- [22]. K. Sato, T. Ihara, H. Sakurai, T. Yoshiie, Q. Xu, Comp. Mater. Sci. 47 (2009) 521.
- [23]. M.A. Omar, Elementary solid state physics, Addison-Wesley, 1975.
- [24]. J.J. Terblans, Surf. Interface Anal. 33 (2002) 767.
- [25]. J.J. Terblans, Surf. Interface Anal. 35 (2003) 548.

- [26]. S.Y. Hong, A.B. Anderson, *Phys. Rev. B* 38 (1988) 9417.
- [27]. D.R. Askeland, *The science and engineering of materials*, Stanley thornes, Cheltenham, 1998.
- [28]. K.J. Laidler, J.H. Meiser, B.C.Sanctuary, *Physical chemistry*, Houghton Mifflin company, 2003.
- [29]. J.-M. Zhang, G.-X. Chen, K.-W. Xu, *Physica B* 390 (2007) 320.
- [30]. P.A.T. Olsson, *Comp. Mater. Sci.* 47 (2009) 135.
- [31]. S. Mrowec, *Defects and diffusion in solids: an Introduction*, Elsevier, Amsterdam, 1980.
- [32]. W. Arabczyk, M. Militzer, H.-J. Müssig, J. Wieting, *Scripta Metall. Mater.* 20 (1986) 1549.
- [33]. Z.Q. Wang, Y.S. Li, F. Jona, P.M. Marcus, *Solid State Commun.* 61 (1987) 623.
- [34]. K.O. Legg, F.Jona, D.W.Jepsen, P.M. Marcus, *Surf. Sci.* 66 (1977) 25.
- [35]. C. Xu, D.J. O'Connor, *Nucl. Instrum. Meth. B* 53 (1991) 315.
- [36]. J. Sokolov, F. Jona, P.M. Marcus, *Phys. Rev. B.* 33 (1986) 1397.
- [37]. J.J. Terblans, *Modellering en Eksperimentele ondersoek van Sb-oppervlaksegregasie in Cu-enkelkristalle*, Dissertation, Bloemfontein, 2001.
- [38]. T. Ohnuma, N. Soneda, M. Iwasawa, *Acta Mater.* 57 (2009) 5947.
- [39]. G. Lucas, R. Schäublin, *Nucl. Instrum. Meth. B* 267 (2009) 3009.
- [40]. P. Ehrhart, H.U. (ed.), 2.1.1. General remarks, *SpringerMaterials-The Landolt-Börnstein Database*.
- [41]. L. de Schepper, D. Segers, G. Knuyt, L. Dorikens-Vanpraet, M. Dorikens, L. Stals, P. Moser, *Phys. Lett. A* 95 (1983) 121.
- [42]. H.J. Grabke, H.Viefhaus, *Surface segregation on nonmetal atoms on metal surfaces*. in: P.A. Dowben, A. Miller, (Eds.), *Surface segregation phenomena*, CRC press, Boca Raton, Florida, 1990, pp. 233.



## Chapter 10: Conclusion

During this study the diffusion mechanism of S in bcc Fe was determined as the nearest neighbour substitutional diffusion mechanism, whereby a S atom would diffuse from a substitutional lattice site to a nearest neighbour vacancy. The influence of the surface orientation on the vacancy formation and thus the activation energy of diffusion were investigated by performing calculations on the three low-index orientations of Fe: Fe(100), Fe(110) and Fe(111). The different Fe orientations considered can be arranged from highest to lowest vacancy formation energy as Fe(110)>Fe(100)>Fe(111), with activation energies of 277.4 kJ/mol (2.875 eV), 266.8 kJ/mol (2.765 eV) and 188.1 kJ/mol (1.950 eV) respectively. Structural relaxation calculations revealed that the Fe(110) surface is the most stable surface of Fe, with Fe(100) being the second most stable surface and Fe(111) being the most unstable surface. For the Fe(100) orientation a segregation energy of -1.859 eV (-179.4 kJ/mol) was calculated comparing well to the literature value of -190.0 kJ/mol (-1.969 eV). Experimental values for the activation energy of S in bcc Fe (232 kJ/mol (2.40 eV) and 205 kJ/mol (2.13 eV)) were obtained from literature confirming the nearest neighbour substitutional diffusion mechanism of S in bcc Fe. No indication is given regarding the orientation of the crystals in which these experimental values were measured.

For the experimental confirmation of the above results which shows different activation energies for different orientations, a new method for doping Fe with S was developed. A new doping system was build for the experiment which was used successfully in the preparation of Fe-S samples. It was shown that the S concentration in the Fe sample was increased by 47.20 % when the doping time was doubled from 25s to 50s.

The calculated trend in activation energies for the low-index planes of Fe are in agreement with the AES results which showed that the activation energy of the polycrystalline samples increased when the grains consisting of the stable orientations increased and the grains consisting of unstable orientations in the samples decreased. For the un-doped polycrystalline sample the segregation parameters are;  $D_0=4.90\times 10^{-2}$  m<sup>2</sup>/s,  $Q=190.8$  kJ/mol (1.978 eV),  $\Delta G=-134$  kJ/mol (-1.39 eV) and  $\Omega_{Fe/S}=20$  kJ/mol (0.20 eV). The segregation parameters of P obtained for the un-doped Fe sample are:  $D_0=0.129$  m<sup>2</sup>/s,  $Q=2.348$  eV (226.5 kJ/mol). The sample doped with S and annealed for 40 days at 1073 K had diffusion parameters of;  $D_0=1.79\times 10^{-2}$  m<sup>2</sup>/s and  $Q=228.7$  kJ/mol (2.370 eV) ,

$\Delta G = -145$  kJ/mol (-1.50 eV) and  $\Omega_{\text{Fe/S}} = 8$  kJ/mol (0.08 eV). The table below gives the concentrations of the different crystal orientations in the two samples.

<b>Orientation</b>	<b>% Un-doped sample</b>	<b>% Doped sample</b>
<b>Fe(100)</b>	26.25	21.07
<b>Fe(211)</b>	22.74	24.77
<b>Fe(110)</b>	4.748	21.16
<b>Fe(310)</b>	4.825	5.221
<b>Fe(111)</b>	41.45	27.78

Experimental results showed that the more stable Fe(110) orientation have grown during annealing and consumed the less stable Fe(100) and unstable Fe(111) orientations. It can be concluded that the stability of a crystal orientation determines the activation energy of diffusion as well as the energy required for that orientation to grow during high temperature annealing of the crystal.

## Future work

The study presented here forms the foundation for future work on S diffusion and segregation in bcc Fe. The segregation behaviour of S was established by this study and future work will focus on finding an element that can inhibit the segregation of S in bcc Fe. This will include the experimental techniques AES, XPS and SIMS, the doping chamber developed in this study will be modified to combat the effects of oxidation. Future work will also include the computational techniques DFT, kMC and the Darken rate equations. A Darken model capable of solving a 7 component system will be developed with a large emphasis on increasing the speed of the Darken model.

Part V  
Appendix



# Appendix A: Density Functional Theory

## A.1. Introduction

The aim of this appendix is to present theoretical concepts supplementary to chapter 5, density functional theory fundamentals. The Hohenberg-Kohn theorems are stated in chapter 5, here the full derivation of these two theorems are given. Also the derivation of the Hellmann-Feynman force theorem is given, in order to explain how forces are calculated in DFT.

## A.2. Hohenberg-Kohn theorems

**Theorem 1:** For any system of interacting particles in an external potential  $V_{ext}(\vec{r})$ , the potential  $V_{ext}(\vec{r})$  is determined uniquely, except for a constant, by the ground state electron density  $n(\vec{r})$ .

**Corollary 1:** Since the Hamiltonian is thus fully determined, except for a constant shift in the energy, it follows that the many body wave function for all states (ground and excited) are determined. Therefore all properties of the system are completely determined given only the ground state electron density  $n(\vec{r})$  [1].

**Proof of theorem 1:** Suppose that the two potentials  $V_{1,ext}(\vec{r})$  and  $V_{2,ext}(\vec{r})$  differing by more than a constant lead to the same ground state electron density  $n(\vec{r})$ . Thus each potential will have its own Hamiltonian and its own wave function according to Schrödinger's equation, equation A.1

$$\hat{H}\psi = E\psi \tag{A.1}$$

The Hamiltonian in equation A.1 is given by equation A.2

$$\hat{H}_i = -\frac{\hbar^2}{2m_e} \sum_i \nabla_i^2 - \sum_{i,J} \frac{Z_I e^2}{|\bar{r}_i - \bar{R}_I|} + \frac{1}{2} \sum_{i \neq j} \frac{e^2}{|\bar{r}_i - \bar{r}_j|} - \sum_I \frac{\hbar^2}{2M_I} \nabla_I^2 + \frac{1}{2} \sum_{I \neq J} \frac{Z_I Z_J e^2}{|\bar{R}_I - \bar{R}_J|}. \quad (\text{A.2})$$

where,  $\frac{\hbar^2}{2m_e} \sum_i \nabla_i^2$  is the kinetic energy of the electrons and can be represented by the kinetic energy operator  $\hat{T}$ . The second term,  $\sum_{i,J} \frac{Z_I e^2}{|\bar{r}_i - \bar{R}_I|}$ , is the potential acting on the electrons due to the nuclei which can be represented by the operator  $\hat{V}_{ext}$ . The electron-electron interaction is given by  $\frac{1}{2} \sum_{i \neq j} \frac{e^2}{|\bar{r}_i - \bar{r}_j|}$ , which can be represented by the operator  $\hat{V}_{int}$ . Using the Born-Oppenheimer approximation, which states that the mass of the ions are large compared to the mass of the electrons and thus  $\frac{1}{M_I}$  is a negligible quantity leading to a zero value for the fourth term. The final term,  $\frac{1}{2} \sum_{I \neq J} \frac{Z_I Z_J e^2}{|\bar{R}_I - \bar{R}_J|}$ , is the classical nuclei-nuclei interaction given by  $E_{II}$ . Each of the two external potentials,  $V_{1,ext}(\bar{r})$  and  $V_{2,ext}(\bar{r})$ , lead to a Hamiltonian and a wave function associated with it as given by equation A.3

$$\begin{aligned} V_{1,ext}(\bar{r}) &\rightarrow \hat{H}_1 \rightarrow \psi_1 \\ V_{2,ext}(\bar{r}) &\rightarrow \hat{H}_2 \rightarrow \psi_2. \end{aligned} \quad (\text{A.3})$$

The wave functions are hypothesized to have the same ground state electron density, but the two wave functions are not equal to one another. Since  $\psi_2$  is not the ground state for  $\hat{H}_1$  it follows that

$$E_1 = \langle \psi_1 | \hat{H}_1 | \psi_1 \rangle < \langle \psi_2 | \hat{H}_1 | \psi_2 \rangle. \quad (\text{A.4})$$

For a non-degenerate ground state, the second term in equation A.4 can be expanded as

$$\langle \psi_2 | \hat{H}_1 | \psi_2 \rangle = \langle \psi_2 | \hat{H}_2 | \psi_2 \rangle + \langle \psi_2 | \hat{H}_1 - \hat{H}_2 | \psi_2 \rangle \quad (\text{A.5})$$

with the last term in equation A.5 given by equation A.6

$$\langle \psi_2 | \hat{H}_1 - \hat{H}_2 | \psi_2 \rangle = \int \psi_2^* (\hat{H}_1 - \hat{H}_2) \psi_2 d^3r. \quad (\text{A.6})$$

Using the Hamiltonian in equation A.2, the difference in the two Hamiltonians,  $\hat{H}_1$  and  $\hat{H}_2$ , is given by equation A.7

$$\begin{aligned} \hat{H}_1 - \hat{H}_2 &= -\frac{\hbar^2}{2m_e} \sum_i \nabla_i^2 - \frac{1}{2} \sum_{i \neq j} \frac{e^2}{|\bar{R}_i - \bar{R}_j|} + \sum_i V_{1,ext}(\bar{r}_i) + \frac{1}{2} \sum_{I \neq J} \frac{Z_I Z_J e^2}{|\bar{R}_I - \bar{R}_J|} \\ &- \left( -\frac{\hbar^2}{2m_e} \sum_i \nabla_i^2 - \frac{1}{2} \sum_{i \neq j} \frac{e^2}{|\bar{R}_i - \bar{R}_j|} + \sum_i V_{2,ext}(\bar{r}_i) + \frac{1}{2} \sum_{I \neq J} \frac{Z_I Z_J e^2}{|\bar{R}_I - \bar{R}_J|} \right) \\ &= \sum_i V_{1,ext}(\bar{r}_i) - \sum_i V_{2,ext}(\bar{r}_i). \end{aligned} \quad (\text{A.7})$$

Substituting equation A.7 into equation A.6 results in equation A.8

$$\begin{aligned} \langle \psi_2 | \hat{H}_1 - \hat{H}_2 | \psi_2 \rangle &= \int \psi_2^* \left( \sum_i V_{1,ext}(\bar{r}_i) - \sum_i V_{2,ext}(\bar{r}_i) \right) \psi_2 d^3r \\ \langle \psi_2 | \hat{H}_1 - \hat{H}_2 | \psi_2 \rangle &= \int (V_{1,ext}(\bar{r}_i) - V_{2,ext}(\bar{r}_i)) |\psi_2|^2 d^3r \\ &= \int (V_{1,ext}(\bar{r}_i) - V_{2,ext}(\bar{r}_i)) n(\bar{r}) d^3r. \end{aligned} \quad (\text{A.8})$$

Substituting equation A.8 into equation A.5 results in equation A.9

$$\langle \psi_2 | \hat{H}_1 | \psi_2 \rangle = E_2 + \int (V_{1,ext}(\bar{r}_i) - V_{2,ext}(\bar{r}_i)) n(\bar{r}) d^3 r . \quad (\text{A.9})$$

Inserting equation A.9 into equation A.4 leads to equation A.10

$$E_1 < E_2 + \int (V_{1,ext}(\bar{r}_i) - V_{2,ext}(\bar{r}_i)) n(\bar{r}) d^3 r . \quad (\text{A.10})$$

Following the same procedure starting with equation A.4, but with indices 1 and 2 exchanged it can be proven that

$$E_2 < E_1 + \int (V_{2,ext}(\bar{r}_i) - V_{1,ext}(\bar{r}_i)) n(\bar{r}) d^3 r . \quad (\text{A.11})$$

The sum of equation A.10 and A.11 leads to equation A.12 [1; 2; 3]

$$E_1 + E_2 < E_2 + E_1 . \quad (\text{A.12})$$

Equation A.12 cannot be a valid statement, therefore there cannot be two different external potentials giving rise to the same ground state electron density. The electron density uniquely determines the external potential and thus also the Hamiltonian. From this the corollary follows, if the Hamiltonian is known then the wave function can be obtained by solving Schrödinger's equation, equation A.1 [1].

**Theorem 2:** A universal functional in terms of the energy  $E(n)$  in terms of the density can be defined, valid for any external potential  $V_{ext}(\bar{r})$ . For any particular  $V_{ext}(\bar{r})$  the exact ground state energy of the system is the global minimum value of this functional, and the density  $n(\bar{r})$  that minimizes the functional is the exact ground state electron density  $n(\bar{r})$ .

**Corollary 2:** The functional  $E(n)$  alone is sufficient to determine the exact ground state energy and electron density. In general, excited states of the electron must be determined by other means. Thermal equilibrium properties such as specific heat are determined directly by the free-energy functional of the density [1].

**Proof of theorem 2:** The original proof is restricted to densities  $n(\bar{r})$  which are ground state densities of the electron Hamiltonian with some external potential,  $V_{ext}(\bar{r})$ . This defines a space of possible densities in which functionals of the density can be constructed. Since all properties can be determined if the electron density is known (theorem 1), all properties can be given as a functional of the electron density. The total energy as a functional of the density is given by equation A.13 [1]

$$E_{HK}[n] = T[n] + E_{in}[n] + \int V_{ext}(\bar{r})n(\bar{r})d^3r + E_{II} \quad (\text{A.13})$$

where the subscript HK refers to the Hohenberg-Kohn. The first term in equation A.13 represents the kinetic energy of the electrons. The second term represents the interaction potential between electrons, the third term is the external potential between electrons and ions and the fourth term is the ion-ion interaction energy term. The total energy can be written in terms of the functional,  $F_{HK}[n]$  as given by equation A.14

$$E_{HK}[n] = F_{HK}[n] + \int V_{ext}(\bar{r})n(\bar{r})d^3r + E_{II} \quad (\text{A.14})$$

where the functional in equation A.14 is given by equation A.15

$$F_{HK}[n] = T[n] + E_{in}[n]. \quad (\text{A.15})$$

Consider now a ground state electron density  $n_1(\bar{r})$  with an associated wave function given by  $\psi_1$

$$E_1 = E_{HK}[n_1] = \langle \psi_1 | \hat{H}_1 | \psi_1 \rangle. \quad (\text{A.16})$$

Thus for a different density  $n_2(\bar{r})$  corresponding to a wave function,  $\psi_2$ , equation A.17 follows [1]

$$E_1 = \langle \psi_1 | \hat{H}_1 | \psi_1 \rangle < \langle \psi_2 | \hat{H}_1 | \psi_2 \rangle = E_2. \quad (\text{A.17})$$

Thus  $E_2$  is greater than  $E_1$ , if the functional  $F_{HK}[n]$  is minimized by varying the density, the exact ground state energy and electron density would be obtained. This is only valid for the ground state properties and no information is obtained for the excited states [1].

### A.3. Hellman-Feynmann force theorem

The total force and total energy acting on a system needs to be minimized in order to obtain the equilibrium positions of atoms in the system. The starting point is the expression for the force,  $\bar{F}$ , experienced by an atom, given by equation A.18

$$\bar{F} = -\frac{\partial E}{\partial \bar{R}} \quad (\text{A.18})$$

where,  $E$ , is the energy and  $\bar{R}$  the position vector of the nucleus. The energy can be written in terms of the energy operator,  $\hat{H}$ .

$$E = \frac{\langle \psi | \hat{H} | \psi \rangle}{\langle \psi | \psi \rangle}. \quad (\text{A.19})$$

Using the Hamiltonian given by equation A.2 leads to the fundamental expressions of the Hamiltonian which is central to the theory of electronic structure.

$$\hat{H} = \hat{T} + \hat{V}_{ext} + \hat{V}_{int} + E_{II} \quad (\text{A.20})$$

Each of the terms in equation A.2 have been presented in operator form in equation A.20. Equation A.20 remains valid if the nuclear coulomb interactions are replaced by a pseudopotential. Equation A.19 can also be written in terms of the electron density  $n(\vec{r})$ , resulting in equation A.21.

$$E = \frac{\langle \psi | \hat{H} | \psi \rangle}{\langle \psi | \psi \rangle} = \langle \hat{T} \rangle + \langle \hat{V}_{int} \rangle + \int \hat{V}_{ext}(\vec{r}) n(\vec{r}) d^3 r + E_{II} \quad (\text{A.21})$$

Making use of a normalized wave function i.e.

$$\langle \psi | \psi \rangle = 1 \quad (\text{A.22})$$

equation A.18 can be written as

$$\bar{F} = -\frac{\partial E}{\partial R} = -\frac{\partial}{\partial R} \langle \psi | \hat{H} | \psi \rangle. \quad (\text{A.23})$$

Equation A.23 can be simplified into equation A.24

$$\bar{F} = -\frac{\partial E}{\partial R} = \left\{ -\left\langle \frac{\partial \psi}{\partial R} \middle| E \middle| \psi \right\rangle - \left\langle \psi \middle| E \middle| \frac{\partial \psi}{\partial R} \right\rangle - \left\langle \psi \middle| \frac{\partial \hat{H}}{\partial R} \middle| \psi \right\rangle \right\}$$

$$\bar{F} = \left\{ -E \frac{\partial}{\partial R} \langle \psi | \psi \rangle - \left\langle \psi \middle| \frac{\partial \hat{H}}{\partial R} \middle| \psi \right\rangle \right\} \quad (\text{A.24})$$

Making use of equation A.22 for a normalized wave function reduces equation A.24 into equation A.25

$$\bar{F} = -\left\langle \psi \middle| \frac{\partial \hat{H}}{\partial R} \middle| \psi \right\rangle. \quad (\text{A.25})$$

Inserting equation A.21 into equation A.25 results in the Hellmann-Feynman theorem, equation A.26 [1; 2]

$$\bar{F} = -\int \frac{\partial \hat{V}_{ext}}{\partial R} n(\vec{r}) d^3 r - \frac{\partial E_{II}}{\partial R}. \quad (\text{A.26})$$

Any structure is optimized when equation A.26 is approximately equal to zero for all the atomic positions in the system. This means that all the energy is drained from the system and that all atoms are in their equilibrium lattice positions.

## A.4. References

- [1]. R.M. Martin, *Electronic structure: basic theory and Practical applications*  
Cambridge University Press, Cambridge, 2004.
- [2]. P. Giannozzi, *Density Functional Theory for electronic structure calculations Italy: Pisa*,  
2005.
- [3]. K. Burke, *The ABC of DFT*, Department of Chemistry, University of California Irvine, 2007.



# Appendix B: Optimization of computational parameters

## B.1. Introduction

For the accurate calculation of material properties such as the binding energy, migration energy etc. the system under study needs to be optimized with respect to the various computational parameters. These parameters include the energy cut-off,  $E_{cut}$ , which determines how many plane-waves will be used in the calculation and the k-point grid size over which brillouin zone summation will be performed. Using the optimized values for the above two mentioned parameters, an equilibrium lattice parameter,  $a$ , and corresponding bulk modulus,  $B_0$ , is calculated. These values needs to be compared to experimental values to evaluate the correct ground state of the system.

For metallic systems, optimization also needs to be performed with respect to the smearing scheme, the smearing width or degauss value and the magnetization of the system. Electrons are free to move across the Fermi surface in metals causing a continuous distribution of electrons. To account for this effect, the total energy of the system is computed by incorporating a distribution function for electrons across the Fermi surface, called the smearing scheme. Different schemes exist and the scheme`s convergence with respect to the degauss value needs to be determined. The width of smearing or the degauss value is determined by converging the total energy of the system with respect to the number of k-points for different degauss values. The spin of electrons, which is the cause of the magnetic character for the metallic system, needs to be determined for the ground state of the system. An initial value is needed to break the symmetry of the system and start the calculation. To determine the optimum value for magnetization, convergence of the total energy is performed with respect to different values for the starting magnetization.

It is important that all of the above mentioned parameters are determined as accurately as possible, since the accuracy of all other calculations depend upon them. However there is always a trade-off

between accuracy and computational time, and thus these parameters need to be as accurate as allowed by the computational resources available.

## B.2. Overview of computational parameters

Table B.1 gives a summary of the optimized parameters for the bcc Fe system. All calculations performed here were done on a  $1 \times 1 \times 1$  unit cell of bcc Fe. The interaction between the valence electrons and ionic cores were represented by ultrasoft pseudopotentials (USPP) [1]. Two generalized gradient spin approximation (GGSA) pseudopotentials were considered for the system, the PW91 [2] and PBE [3] pseudopotentials. Both pseudopotentials have shown to give an accurate description of the Fe, FeS and FeS<sub>2</sub> systems [4; 5; 6; 7; 8].

*Table B.1: Ground state properties of bulk bcc Fe as calculated by the PW91 and PBE pseudopotentials respectively. Experimental and calculated values from literature are also given for comparison.*

Property	PW91	PBE	Experimental Values [9]	Literature Values (PW91) [8]
<b>Cut-off energy, E-cut (eV)</b>	381	585	–	–
<b>k-point grid size</b>	8×8×8	9×9×9	–	–
<b>Lattice parameter, <math>a</math> (Å)</b>	2.861	2.855	2.866	2.869
<b>Bulk modulus, <math>B_0</math> (GPa)</b>	149.5	156.1	168	140
<b>Magnetic moment, <math>B</math> (<math>\mu_B</math>)</b>	2.48	2.45	2.22	2.37
<b>Metallic smearing scheme</b>	Methfessel-Paxton	Methfessel-Paxton	–	–
<b>Degauss/smearing width (eV)</b>	0.54	0.54	–	–
<b>Starting magnetization (fraction)</b>	0.40	0.20	–	–

Both pseudopotentials gave an accurate description of the ground state properties of bcc Fe with a 4.23 % difference in the bulk modulus of the two pseudopotentials. The three parameters that defines the ground state, the lattice parameter, bulk modulus and magnetic moment of the two pseudopotentials also compares well to experimental values. The last column in table B.1 contains values calculated by other authors using the PW91 pseudopotential, which compares well to the values calculated in this study. In comparison to the experimental values in column 3, there was found to be a difference of 0.17 % in the lattice parameter, 11.01 % in bulk modulus and 10.48 % difference in the magnetic moment values calculated for the PW91 pseudopotential. For the PBE pseudopotential a deviation of 0.38 % for the lattice parameter was found. While the deviation for the bulk modulus was 7.08 % and the magnetic moment deviated by 9.39 %. Since both pseudopotential give an accurate description of the ground state properties and considering that the PBE pseudopotential would be more expensive computationally. The PW91 functional was chosen to perform all subsequent calculations in order to shorten computational time. To illustrate how the system was optimized, optimization with respect to each of the parameters mentioned above are performed in this chapter.

### **B.3. Optimization of a single unit cell**

The procedure followed for the optimization of the ground state parameters was to perform a first estimate optimization for all the parameters of a single unit cell. Once all the values were obtained the cut-off energy was once again optimized using the optimized values of all other parameters to determine the energy convergence of the total energy with respect to the chosen parameters.

### B.3.1. Convergence of the total energy with respect to the energy cut-off $E_{cut}$

This section shows how the convergence of the total energy with respect to the energy cut-off was performed for the PW91 pseudopotential. The mathematical expression for the plane waves used in DFT calculations is given by equation B.1

$$\psi_{\bar{k}}(\bar{r}) = \frac{1}{\sqrt{\Omega}} \sum_{\bar{G}} C_{\bar{k}}(\bar{k} + \bar{G}) e^{i(\bar{k} + \bar{G})\bar{r}} \quad (\text{B.1})$$

In order to determine the amount of Fourier components,  $C_{\bar{k}}(\bar{k} + \bar{G})$ , that are required for the plane waves. The cut off value for the  $\bar{k} + \bar{G}$  vectors were determined by converging the Fe structures total energy with respect to the energy cut-off where the expression for  $E_{cut}$  is given by equation B.2.

$$E_{cut} \leq \frac{\hbar^2 (\bar{k} + \bar{G})^2}{2m} \quad (\text{B.2})$$

Figure B.1 shows the convergence of the total energy with respect to  $E_{cut}$ . The graph was constructed using the optimized values of all other parameters. The total energy of the Fe unit cell converged to 381 eV with a convergence criteria of  $4.23 \times 10^{-4}$  eV/atom. From figure B.1 it can be seen that the total energy is always decreasing for an increase in the energy cut-off value. The energy cut-off value of 381 eV was obtained from the initial convergence of the energy cut-off and was used in all subsequent calculations.

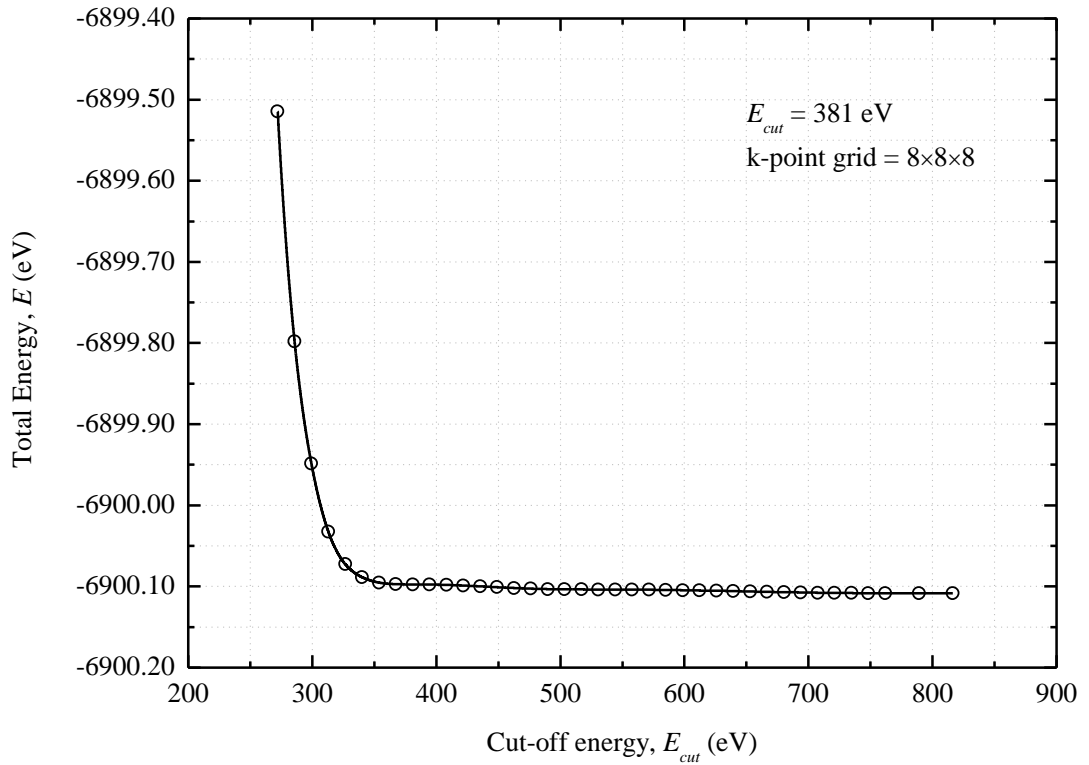


**Figure B.1:** Convergence of the total energy with respect to the energy cut-off value. For the Fe system the cut-off value was determined as 381 eV, where the total energy has converged to  $4.23 \times 10^{-4}$  eV/atom.

### B.3.2. Convergence of the total energy with respect to the k-point grid size

Summation over the Brillouin zone is performed for a number of special points in k-space in order to calculate the electron density and thus the total energy of the structure under study. The summation is performed over a number of special point, since summation over the whole of k-space would mean a summation over an infinite number of values for k. The Monkhorst-Pack scheme [10] was used to identify these special points. To determine the density of these special points, the convergence of the total energy with respect to the k-point grid size was determined and is shown in figure B.2.

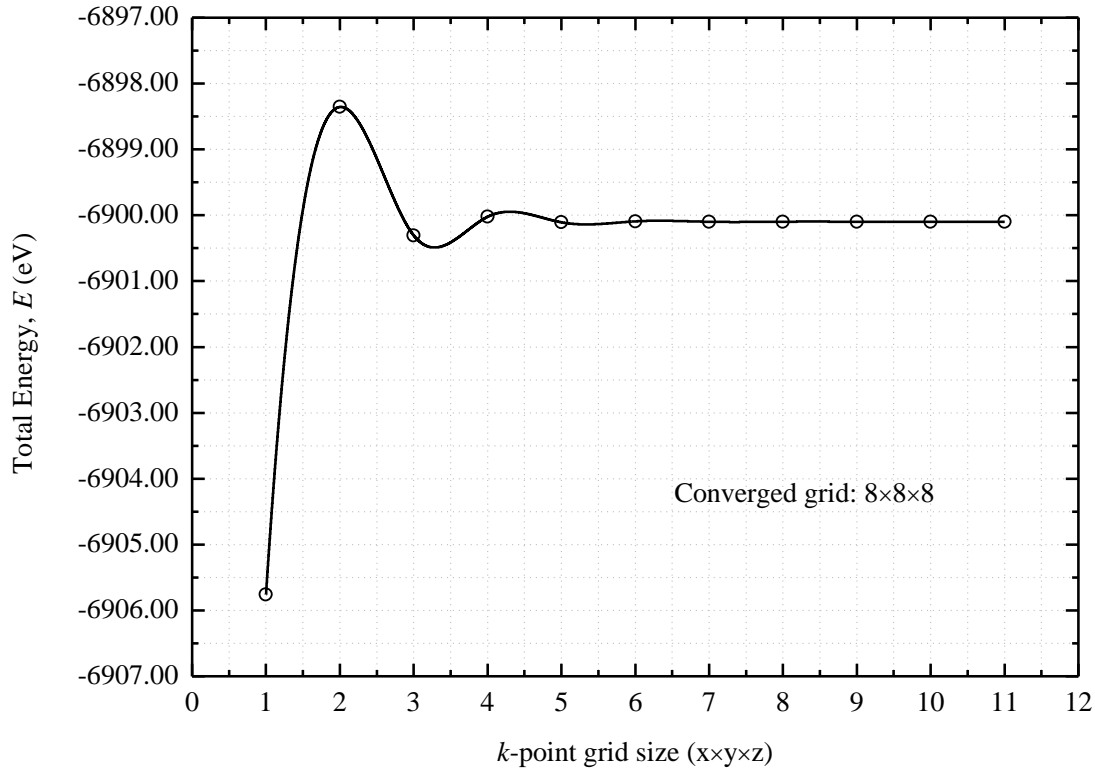


**Figure B.2:** Convergence of the total energy with respect to the size of the Monkhorst-Pack  $k$ -point grid used for summation over the Brillouin zone (BZ). For the Fe system it was determined that a  $8 \times 8 \times 8$  grid is sufficient with the total energy converged to  $1.38 \times 10^{-3}$  eV/atom

While the total energy is always decreasing with respect to the energy cut-off, for the  $k$ -point grid size the total energy can either increase or decrease, but will eventually converge to below the specified convergence criteria. The appropriate  $k$ -point grid for the Fe system was determined as a  $8 \times 8 \times 8$  grid with the total energy being converged to  $1.38 \times 10^{-3}$  eV/atom. For all subsequent calculations, the  $k$ -point grid size of  $8 \times 8 \times 8$  was used.

### B.3.3. Determination of the magnetic state

To incorporate the ferromagnetic properties of Fe, both spin up and spin down states were taken into account. To ensure that the symmetry is broken, as a starting point for the calculations, an

initial fraction of electrons are allocated a spin up state. To determine this fraction, the total energy was calculated for different fractions of spin up states, with the lowest energy describing the ground state of the system. The total energy as a function of the fraction of spin up states are shown in figure B.3.

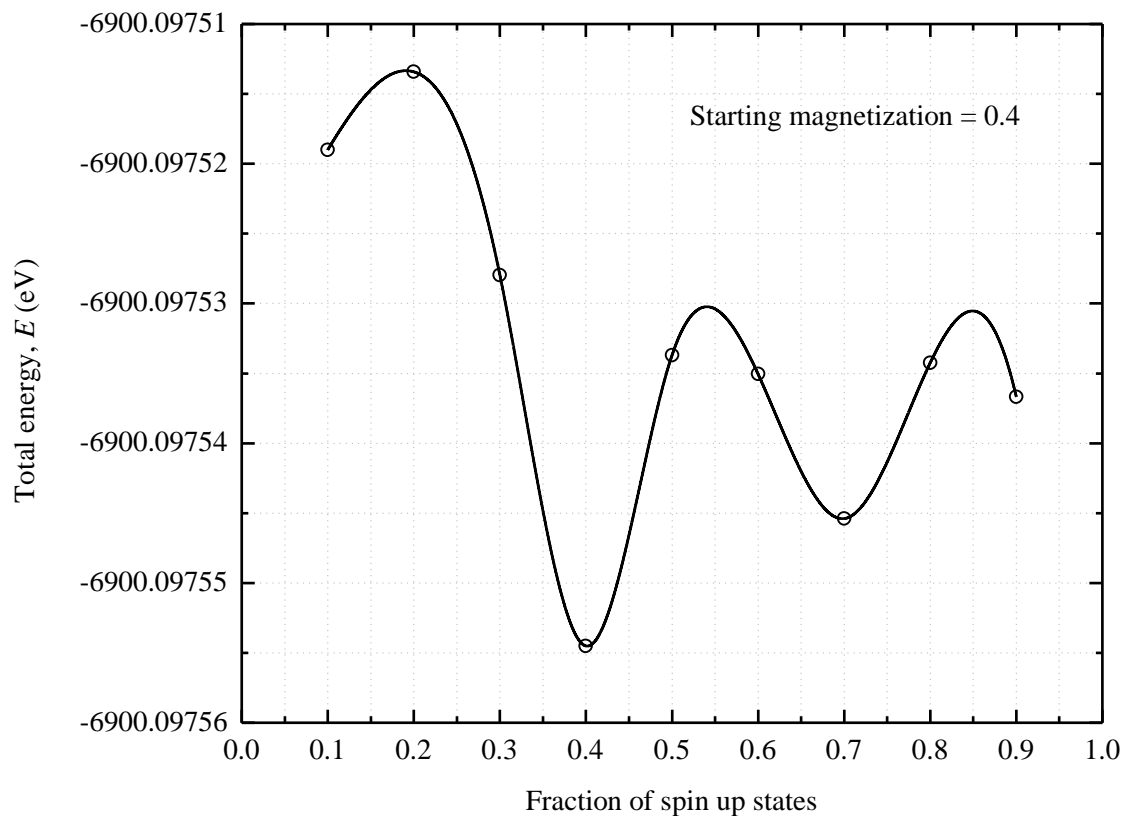


**Figure B.3:** Convergence of the total energy with respect to the fraction of spin up states. It was determined that the ground state energy is obtained at a fractional spin up of 0.4. This value is used for the starting magnetization in order to break the symmetry and start the calculation.

The ground state of the system was found at a fractional spin up state of 0.4. This value is used in all subsequent calculations in order to break the symmetry and start the calculations.

### B.3.4. Determination of the smearing scheme for metallic systems

In order to account for the continuous distribution of electrons across the Fermi level a fictitious electronic temperature is introduced, called metallic smearing. Different schemes have been devised, each capable of describing different systems. In order to obtain a smearing scheme that best describes the Fe system, different schemes were tested. This was done by plotting the total energy of the structure as a function of the different degauss values for each of the schemes as shown in figure B.4.

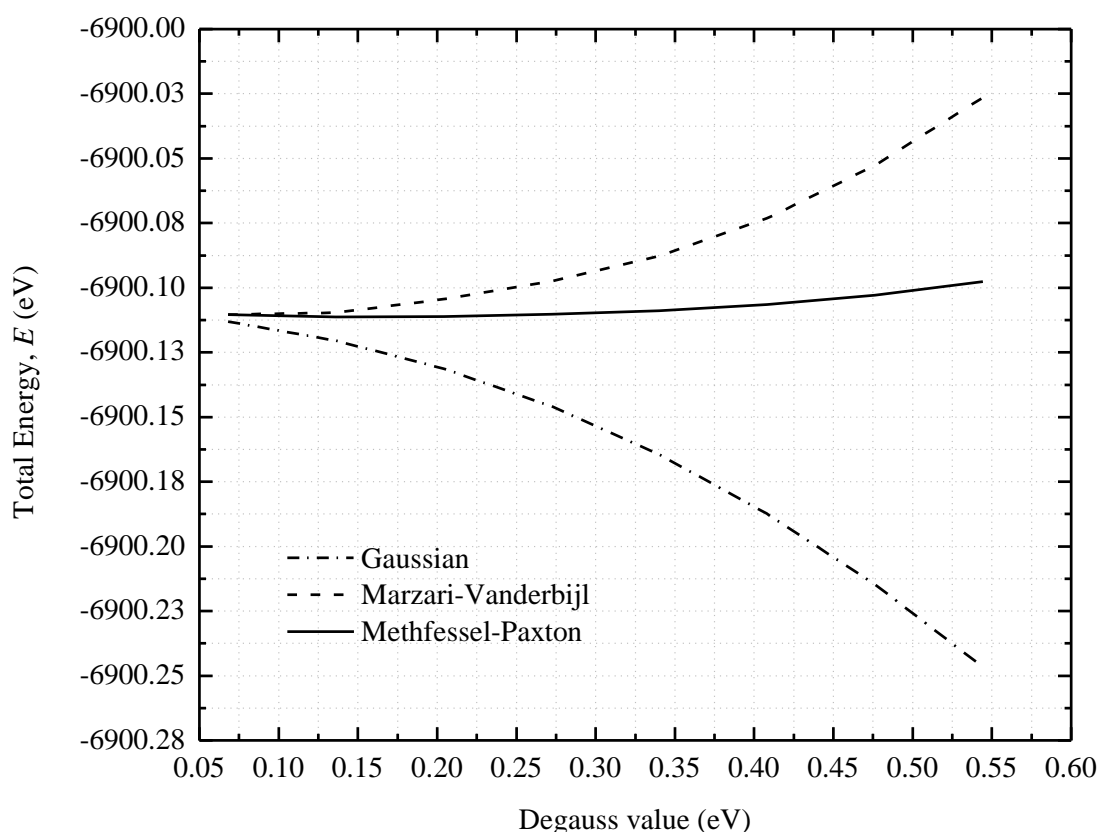


**Figure B.4:** The Methfessel-Paxton smearing scheme was determined as the most accurate scheme to account for the occupation of electrons in metals. Compared to the other schemes the Methfessel-Paxton scheme is the most stable with increasing degauss value.

The Gaussian distribution function follows the free energy of the system while the Marzari-Vanderbilt function follows the total energy of the system. The Methfessel-Paxton [11] scheme remained constant for a range of degauss values before following the total energy of the system. Thus to account for the continuous distribution of electrons across the Fermi level, the Methfessel-Paxton scheme was used.

### **B.3.5. Determination of the smearing width (degauss value)**

To determine the degree of smearing that is required by the Methfessel-Paxton smearing scheme different values were tested. This was done by converging the total energy for each of the degauss values with respect to the k-point grid size. Figure B.5 shows the convergence of the total energy with respect to the k-point grid for four different degauss values. The 0.54 eV value converged to  $<1.38 \times 10^{-3}$  eV/atom for a k-point grid size of  $8 \times 8 \times 8$  which was the choice made earlier for the k-point grid size.

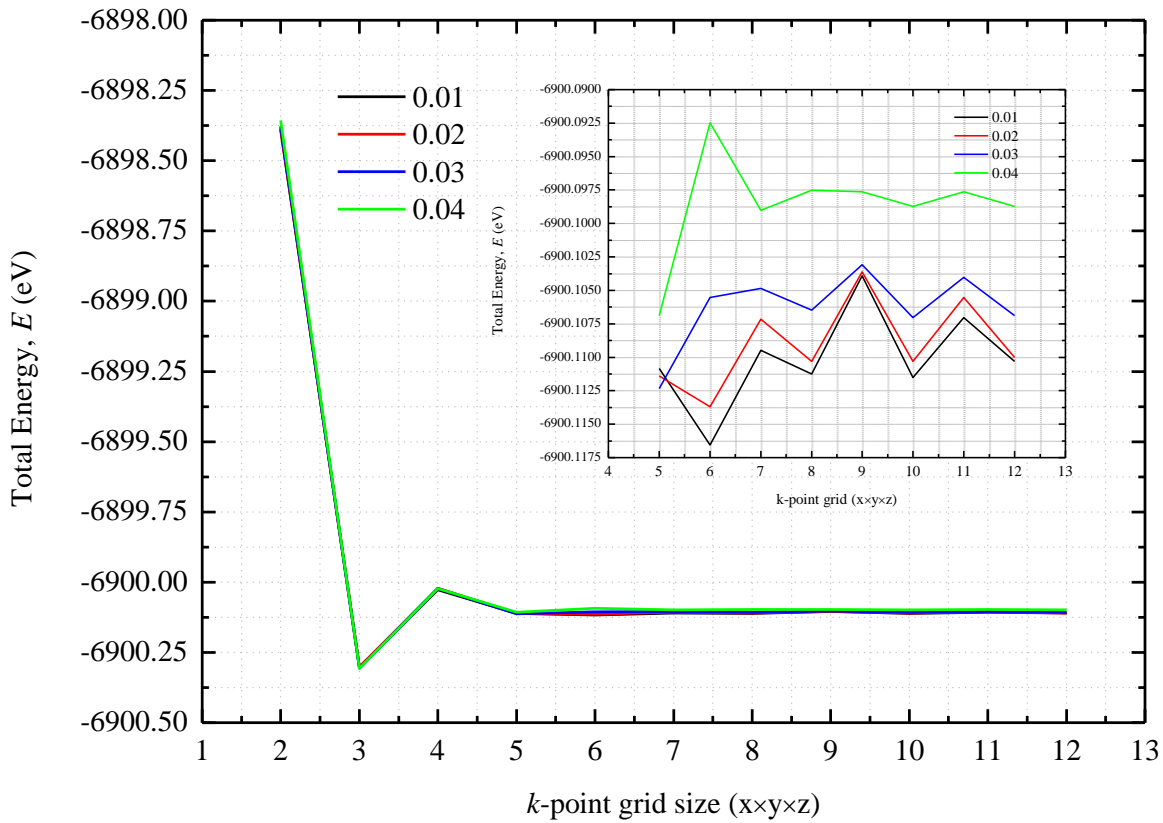


**Figure B.5:** The degree of smearing or the smearing width for the Methfessel-Paxton scheme was determined as 0.54 eV for a k-point grid size of  $8 \times 8 \times 8$  with the total energy converged to  $< 1.38 \times 10^{-3} \text{ eV/atom}$ .

### B.3.6. Determination of the equilibrium lattice parameter and bulk modulus

The last two parameters to be determined is the lattice parameter and the bulk modulus. This was done by calculating the total energy for a range of lattice parameter values and then fitting the Murnaghan equation of state to the data. It is important to note that both these values needs to be in agreement with experimental values, to ensure that there is no strain on the system and that the system is at its ground state. Figure B.6 gives the Murnaghan equation of state fitted to the calculated values.

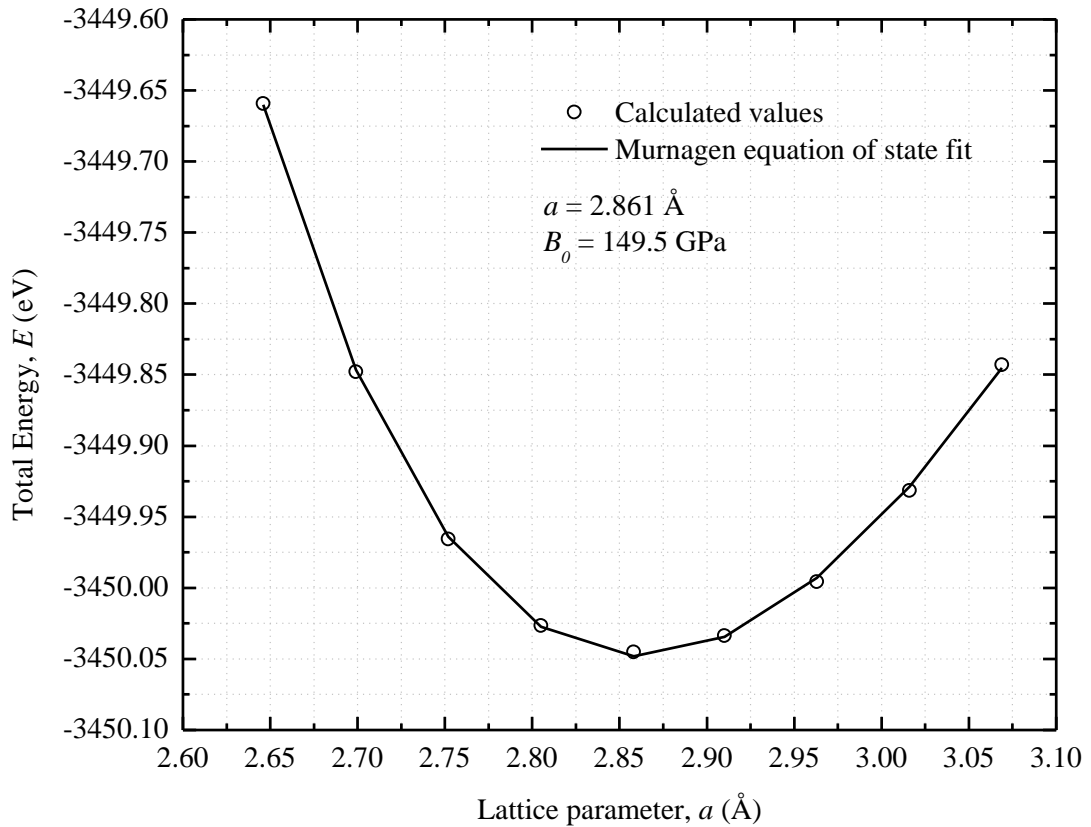


**Figure B.6:** A lattice parameter of 2.861 Å and a bulk modulus value of 149.5 GPa was obtained for bulk bcc Fe by fitting of the Murnaghan equation of state to the data.

The equilibrium lattice parameter was determined as 2.861 Å, and the bulk modulus as 149.5 GPa. The total energy values on the y-axis in figure B.6 differs from the total energy of the other parameters, since a bravais lattice of 3 was used for the lattice parameter optimization, as compared to the other parameters where atomic positions were assigned manually (a cell of two atoms in the bcc lattice was used).

## **B.4. Optimization parameters for Supercell Calculations**

In addition to the optimization parameters that were discussed in the previous sections, more parameters need to be considered if a supercell structure is studied. Supercells are used when large bulk cell structures or surface structures are studied. If a bulk structure is considered, the cell has to be large enough to avoid interaction of the impurity atom in one cell with its periodic repetition in the next cell. If a surface supercell is studied, the number of atomic layers and the size of the vacuum spacing need to be optimized. The number of atomic layers used, have to be large enough to give an accurate description of a surface with some atomic layers to represent the bulk of the structure. A vacuum spacing is introduced to simulate a surface and has to be large enough to prevent interactions between periodically repeated cells. The parameters mentioned above are optimized with respect to some physical property of the system. In the case of bulk supercells, the cell size is optimized with respect to the binding energy of an atom. For surface structures, the number of atomic layers are optimized by converging the surface energy with respect to the number of atomic layers. To optimize the vacuum spacing, a binding energy curve is constructed to determine the minimum distance of interaction between the atoms under consideration. This section presents the results for the optimization of a bulk Fe supercell and for the supercells of the three Fe surfaces, Fe(100), Fe(110) and Fe(111).

### **B.4.1. Cell size determination**

The binding energy of S in different lattice sites were calculated and compared in order to obtain the most stable position of S in bcc Fe. The details of how the binding energies were calculated are not discussed in this section, only the final results are used here to determine the optimum cell size. The binding energy calculations are done in chapter 9, Computational results. The equilibrium lattice positions of S in a substitutional, octahedral interstitial and tetrahedral interstitial lattice site were calculated by allowing a  $3\times 3\times 3$  supercell to relax according to the damped dynamics structural relaxation algorithm. Due to the low symmetry of the cell, the calculations were done for

the whole brillouin zone (BZ) and not reduced to the irreducible brillouin zone (IBZ) as is commonly done in DFT calculations. For the substitutional position of S a binding energy of -3.605 eV was calculated, compared to the octahedral interstitial binding energy of -1.660 eV and the tetrahedral interstitial binding energy of -1.464. This indicated that S favours a substitutional lattice site over an interstitial lattice site. To ensure that the size of the supercell does not contribute to the value of the binding energy, calculations on a larger cell were done. The binding energy of S in a  $4\times 4\times 4$  cell was calculated as -3.556 eV. Table B.2 summarizes the results and also contains the approximate time it took to complete the calculation for each of the cell sizes.

**Table B.2:** Binding energies of substitutional S for a  $3\times 3\times 3$  and a  $4\times 4\times 4$  cell. The estimated time of the calculations are included to show the increase in computational time as the cell is increased from a  $3\times 3\times 3$  to a  $4\times 4\times 4$  supercell.

Cell size	Binding energy, $E_b$ (eV)	Approximate CPU time of calculation (hours)
<b><math>3\times 3\times 3</math></b>	-3.605	50.76
<b><math>4\times 4\times 4</math></b>	-3.556	97.55

The  $3\times 3\times 3$  cell gives a value which compares well to the literature value of -3.10 eV [12] and a very small increase in binding energy, 1.36 %, is observed when a  $4\times 4\times 4$  cell is used. Considering the small increase in accuracy as opposed to the large increase, 47.96 %, in computational time, a  $3\times 3\times 3$  cell was used for all calculations. Figure B.7 illustrates the  $3\times 3\times 3$  cell containing a S atom in a substitutional lattice site

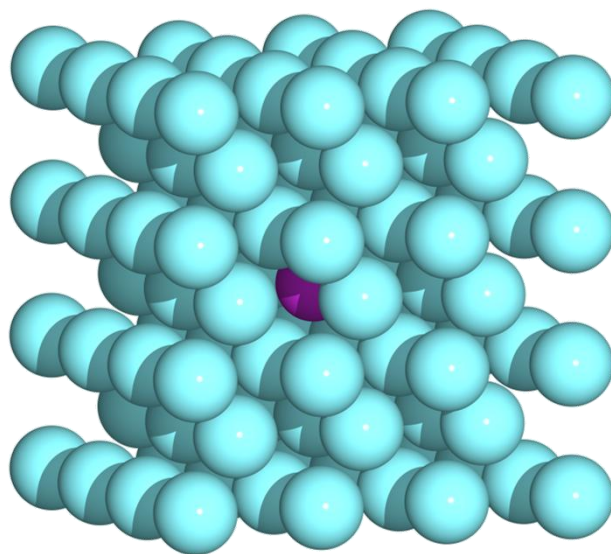


*Figure B.7: Substitutional position of S (purple atom) in a  $3\times 3\times 3$  bulk bcc Fe supercell.*

#### **B.4.2. Calculation of the required vacuum spacing for surface structures**

When performing surface calculations a certain vacuum spacing is required to simulate the surface of the material. This vacuum spacing needs to be large enough to prevent the interaction between periodically repeated cells, while effectively simulating the surface. To determine the minimum distance required to prevent the interaction of two Fe layers, a large unit cell of dimensions  $10.58 \text{ \AA} \times 10.58 \text{ \AA} \times 42.32 \text{ \AA}$  was constructed with only two atoms inside. Initially the atoms were separated by a distance of  $21.16 \text{ \AA}$  and then brought closer in increments of  $0.53 \text{ \AA}$  to a final distance of  $5.29 \text{ \AA}$ . From this data, plotted in figure B.7, the minimum distance required to avoid interaction between two Fe atoms were determined as  $14.81 \text{ \AA}$

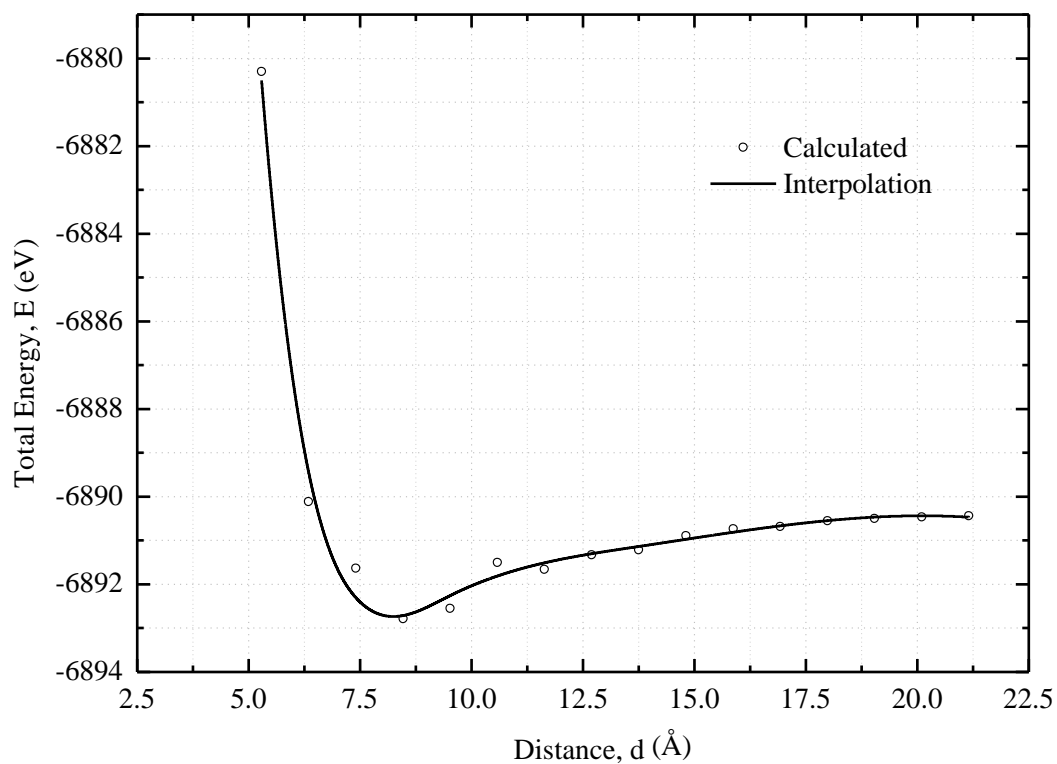


**Figure B.8:** Binding energy curve of two Fe atoms in the gas phase in a  $10.58 \times 10.58 \times 42.32$  Å cell. From this curve the minimum distance to avoid interaction of two atoms/layers were determined as 14.81 Å.

As an example of a surface supercell, figure B.9 illustrates the Fe(100) surface where a 14.81 Å vacuum spacing was used.

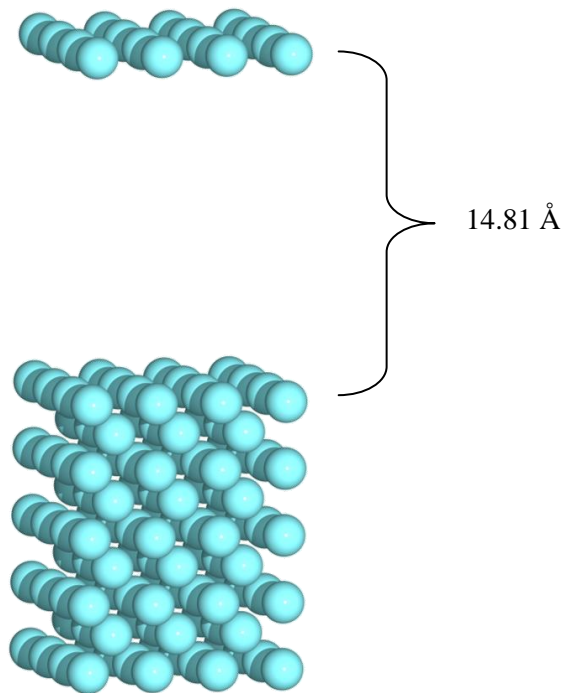


*Figure B.9: The Fe(100) surface supercell with a 14.81 Å vacuum spacing to prevent interaction between periodically repeated cells.*

## B.5. References

- [1]. D. Vanderbilt, Phys. Rev. B 41 (1990) 5188.
- [2]. J.P. Perdew, Y. Wang, Phys. Rev. B 45 (1992) 13244.
- [3]. J.P. Perdew, K. Burke, M. Ernzerhof, Phys. Rev. Lett. 77 (1996) 3865.
- [4]. A. Hung, J. Muscat, I. Yarovsky, S.P. Russo, Surf. Sci. 513 (2002) 511.
- [5]. S.G. Nelson, M.J.S. Spencer, I.K. Snook, I. Yarovsky, Surf. Sci. 590 (2005) 63.
- [6]. M.J.S. Spencer, A. Hung, I.K. Snook, I. Yarovsky, Surf. Sci. 513 (2002) 389.
- [7]. M.J.S. Spencer, A. Hung, I.K. Snook, I. Yarovsky, Surf. Sci. 540 (2003) 420.
- [8]. A. Hung, I. Yarovsky, J. Muscat, S.R. Russo, I. Snook, R.O. watts, Surf. Sci. 501 (2002) 261.
- [9]. H.C. Herper, E. Hoffman, P. Entel, Phys. Rev. B 60 (1999) 3839.
- [10]. H.J. Monkhorst, J.D. Pack, Phys. Rev B 13 (1976) 5188.
- [11]. M. Methfessel, A.T. Paxton, Phys Rev B 40 (1989) 3616.
- [12]. S.Y. Hong, A.B. Anderson, Phys. Rev. B 38 (1988) 9417.

# Appendix C: Publications and conference contributions

1. **Fe/S sample preparation: A method for the calculation of the S concentration required for doping Fe Crystals**  
P.E. Barnard, J.J. Terblans, H.C. Swart, M.J.H. Hoffman  
SAIP 2010
2. **Determining the bulk concentration of S in Fe-S: a Auger electron spectroscopy study**  
P.E. Barnard, J.J. Terblans, H.C. Swart, B.G. Anderson, M.J.H. Hoffman  
SAIP 2011
3. **Investigation of S diffusion in bulk Fe: a DFT study**  
P.E. Barnard, J.J. Terblans, H.C. Swart, B.G. Anderson, M.J.H. Hoffman  
SAIP 2011